Conformable transistors for bioelectronics

Claudia Cea

Submitted in partial fulfillment of the
requirements for the degree of
Doctor of Philosophy
under the Executive Committee
of the Graduate School of Arts and Sciences

COLUMBIA UNIVERSITY

2023

Abstract

Conformable, Implantable, Integrated Organic Material-Based systems for Neuroelectronics

Claudia Cea

The diversity of network disruptions that occur in patients with neuropsychiatric disorders creates a strong demand for personalized medicine. Such approaches often take the form of implantable bioelectronic devices that are capable of monitoring pathophysiological activity for identifying biomarkers to allow for local and responsive delivery of intervention. They are also required to transmit this data outside of the body for evaluation of the treatment's efficacy. However, the ability to perform these demanding electronic functions in the complex physiological environment with minimum disruption to the biological tissue remains a big challenge. An optimal fully implantable bioelectronic device would require each component from the front-end to the data transmission to be conformable and biocompatible. For this reason, organic material-based conformable electronics are ideal candidates for components of bioelectronic circuits due to their inherent flexibility, and soft nature. In this work, first an organic mixed-conducting particulate composite material (MCP) able to form functional electronic components and noninvasively acquire high–spatiotemporal resolution electrophysiological signals by directly interfacing human skin is presented. Secondly, we introduce organic electrochemical internal ion-gated transistors (IGTs) as a high-density, high-amplification sensing component as well as a low leakage, high-speed processing unit. Finally, a novel wireless, battery-free strategy for electrophysiological signal acquisition, processing, and transmission that employs IGTs and an ionic communication circuit (IC) is introduced. We show that the wirelessly-powered IGTs are able to acquire and modulate neurophysiological data *in-vivo* and transmit them transdermally, eliminating the need for any hard Si-based electronics in the implant.

Table of Contents

Chapter 1: Clinical Application of Neuroelectronics

To appropriately diagnose and treat disorders of the nervous system, it is critical to be able to accurately sense signals from the body that indicate the nature of the dysfunction and subsequently interact with the body to ameliorate the dysfunction and restore a physiologic state. Components of the nervous system communicate using electrical and chemical signals, which can be manipulated to achieve therapeutic effects. Therefore, the potential for use of bioelectronic devices to acquire, process, and alter neurophysiological signals is high. We will first briefly provide an overview of the electrical and chemical signals that contribute to diagnosis of neurologic disease and the current modalities available for treatment (Figure 1A–F). Advancements to all facets of these processes can improve clinical care of patients with neuropsychiatric diseases.

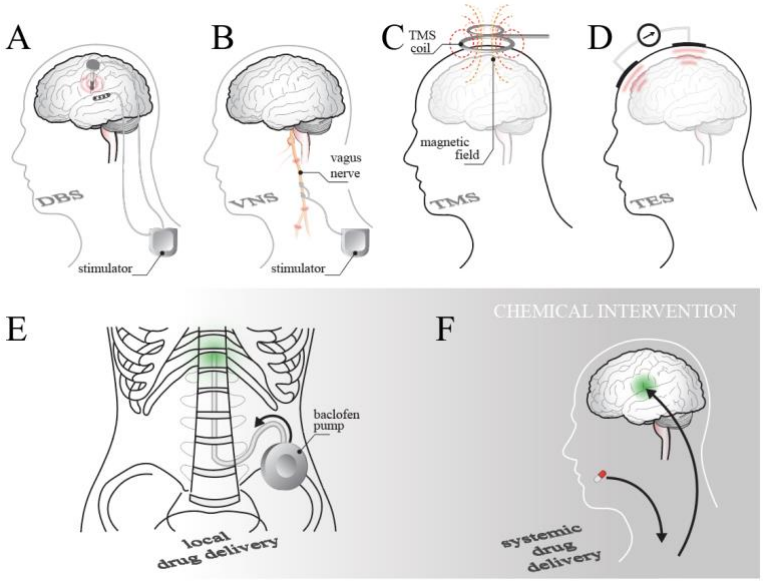

Figure 1: Common neurological clinical intervention approaches. A) Deep-brain stimulation (DBS) involves an implantable electrode connected to a remotely placed stimulator through leads routed subcutaneously. B) Vagal nerve stimulation (VNS) involves an electrode cuff wrapped around the vagus nerve and connected to an implanted stimulator. C) Transcranial magnetic stimulation (TMS) involves placement of magnetic coils above a brain region to be stimulated. D) Transcranial electrical stimulation (TES) involves placement of electrodes on the scalp over a brain region to be stimulated. E) Implantable pumps allow for localized, controlled drug delivery to the nervous system. F) Systemic drug delivery requires pharmacologic agents to undergo first pass metabolism and cross the blood–brain barrier before being able to modulate the central nervous system.

1.1 Diagnostics and Biomarkers

Understanding neurological disorders can be achieved using a range of biological indicators in different neurological systems. Though noninvasive diagnostics are possible, high-resolution information is often collected using invasive electrical and chemical measurements.

1.1.1 Brain

Although individual neurons in the brain communicate via action potentials, these signals can only be detected and their origin tagged to a specific neuron by miniaturized recording electrodes that are located within hundreds of micrometers from the cell.[1] The material and procedural requirements of acquiring such data on a scale that is relevant to brain function have thus far precluded its use in clinical diagnostics. Due to the organization of brain neurons into layers and nuclei, higher amplitude electrical signals are generated by incoming synaptic activity to a large population of neurons. Such signals undergo spatial summation and can be detected at much greater distances from the neurons as oscillatory patterns and waveforms ranging between 0.5 and 500 Hz.[2] Many characteristics of brain function can be gleaned from acquiring these electrical potentials, with the spatial and temporal resolution of the data dependent on whether it is recorded from the surface of the scalp, surface of the brain, or within brain tissue.

Noninvasive

Noninvasive methods of recording brain activity are frequently used in clinical neurology, and include electroencephalography (EEG) and magnetoencephalography (MEG). In the case of EEG, 19 electrodes are placed at standardized positions on the surface of the scalp to detect fluctuations in voltage in the range of 10–100 μV. Oscillatory activity with a frequency of greater than 40 Hz is typically difficult to resolve with EEG due to its restricted spatial distribution and low signal amplitude. With advanced signal processing techniques, it is sometimes possible to detect high

frequency patterns,[3] but these approaches are not yet commonly employed in clinical practice. In addition, electrical potentials that involve a small area of neural tissue, or are located deep within the brain, do not appear on EEG. It has been estimated that up to 6 cm^2 of neural tissue must be relatively synchronously active to generate patterns that are visible on EEG.[4] Because many different configurations of electrical potential patterns within the brain could generate a similar appearance on the surface, EEG also suffers from the "inverse problem" (whereby multiple combinations of a set of parameters may result in the same outcome), leading to the potential for inaccurate localization of EEG signals to brain structures.[5] Despite these limitations, EEG is a powerful tool for acquiring real-time information about brain function. The most common EEG diagnostic applications are in epilepsy, altered states of consciousness, and brain lesions. EEG is the first-line investigation when a diagnosis of epilepsy is considered, because the hypersynchronous neural firing patterns characteristic of this disease are often apparent.[6] Capturing epileptic activity on EEG facilitates classification of a patient's epilepsy and can guide the most appropriate treatment. However, EEG offers insufficient spatiotemporal resolution for localization of epileptic brain regions in a subset of patients who may require invasive monitoring (see below) to enable the most appropriate treatment. In patients with altered mental status, EEG can suggest brain structures most affected, provide clues as to the cause of the patient's symptoms, and in some cases provide prognostic information about how likely the patient is to recover from a neurologic insult.[7] Focal brain lesions result in slowing of oscillation frequencies on EEG, but the role of this diagnostic modality has decreased with the widespread availability of computerized neuroimaging. For all of these clinical scenarios, patients often require prolonged EEG monitoring (days to weeks) to capture appropriate diagnostic information, monitor response to treatment, and/or allow for early detection of neurologic complications in critical illness.[8] Therefore, the

ability to stably record high quality EEG without causing side effects, such as skin breakdown at sites of electrode placement, is highly clinically desirable.

MEG acquires the magnetic rather than electric signals generated by population activity of neurons in the brain. Because the magnetic field is orthogonal to the electric field, MEG is better able to detect signals arising from fields that are tangential to the scalp. It is also less attenuated by the structures, cerebrospinal fluid, dura, skull, subcutaneous tissue, located between neurons and recording electrodes. Clinically, MEG has been mainly used to supplement and refine the localization of epileptic foci within the brain.[9]

Invasive

Some patients with focal epilepsy that is refractory to treatment with medications have the potential to benefit from surgical resection of the brain tissue responsible for generating seizures. When the combination of seizure manifestations, noninvasive electrophysiologic studies, and neuroimaging are insufficient to clearly define where this tissue is located or its boundaries, invasive monitoring of brain signals is considered.[10] Intracranial EEG (iEEG) involves placing electrodes on the cortical surface, in the form of grid arrays or strips, and/or inserting electrodes in the form of a rigid shank with multiple contacts directly into brain tissue. These electrodes may be placed acutely for a short time during a neurosurgical procedure to guide tissue resection and allow intraoperative monitoring, or semichronically for a period of up to two weeks during which time the patient remains in the hospital. iEEG has the benefit of enhanced spatiotemporal resolution, and permits more precise localization of epileptic activity than noninvasive methods[11] and may help to characterize dysfunction of the interictal neural network.[12] Current clinical iEEG technology does not permit acquisition of action potentials despite the proximity to brain tissue, but high frequency oscillations (several hundred Hz) can be reliably detected and used

to aid localization of epileptic foci.[13] Evidence suggests that the ability to detect action potentials could improve this localization further, but no clinical trials of devices with this capacity have been performed, so the practical benefit to patients is unknown.[14] iEEG does carry more risk, with 1–4% of patients experiencing a complication related to the procedure such as bleeding, brain swelling, and infection.[15] As such, advancements that improve the spatiotemporal resolution of iEEG and decrease the associated morbidity are critical for improving care of patients who require this procedure.

1.1.2 Muscle

Muscle function is assessed by needle electromyography (EMG), a procedure that involves insertion of a concentric or monopolar needle through the skin and into a muscle to record muscle fiber action potentials. The amplitude, waveform duration and number of phases, firing rate and pattern, and stability of the action potentials identify when neurologic diseases involve motor neurons, motor nerves, or muscle. These properties typically identify the disease type, narrowing further investigations to establish a specific diagnosis.[16] In the case of a neuromuscular disorder, repeated studies over time can track disease progression or recovery.[17] Because sufficient spatiotemporal resolution can only be acquired by using penetrating electrodes, EMG is difficult to perform in patients who cannot tolerate the discomfort associated with it, such as children.

1.1.3 Nerve

Nerve function can be assayed by applying electrical stimulation through electrodes placed on the skin to elicit action potentials (nerve conduction studies, NCS). The combined action potential response is recorded using electrodes placed on the skin over muscle (motor nerves) or the course of a cutaneous nerve (sensory nerves). Analyzing the amplitude of the response provides insight into the number of axons that are conducting between the stimulating and recording points. The

latency of the response after stimulation provides an estimate of the conduction velocity of the nerve, and the duration of the waveform adds information regarding how action potentials are being conducted along the nerve.[18] NCS provide important diagnostic information when patients experience motor and sensory symptoms, identifying loss of nerve fibers or impaired ability to conduct action potentials. When a disease process affecting the nerves is diagnosed, such as a demyelinating condition or toxic exposure, NCS can also be used to track recovery over time.[19]

1.1.4 Spinal Fluid Examination

Direct examination of the cerebrospinal fluid (CSF), which protects and chemically communicates with brain and spinal cord tissue, has been critical for diagnosis and management of neurologic disease for over a century. It is most useful in identifying intracranial infection, bleeding, cancer, metabolic disorders, and changes in intracranial pressure. Because obtaining CSF requires performing an invasive procedure, lumbar puncture, the amount of fluid available for analysis and the capacity for serial sampling using current techniques is limited. Quantification of red and white blood cells, protein, and glucose within the CSF is typically performed, along with culture or immunologic studies looking for the presence of microorganisms. Studies aimed at identifying disorders of neurometabolism or autoimmunity can also be performed. Importantly, changes in these values over time are often critical to assay response to treatment, such as in patients receiving antivirals to treat encephalitis or those undergoing chemotherapy for brain cancer.[20] Bioelectronic devices capable of serially sampling small amounts of CSF and providing trends in quantification of key assays would prevent the requirement of performing multiple invasive procedures in these often critically ill patients.

1.2 Intervention and Treatment

1.2.1 Chemical Treatment

The majority of neurologic diseases are currently treated with medications. However, several challenges are encountered when trying to produce a desired pharmacologic response in the central nervous system. First, drug concentration within the brain is dependent upon the method of administration. Orally administered drugs can be extensively metabolized in the liver (first-pass metabolism) before reaching the brain, resulting in up to 75% of the administered dose never accessing systemic circulation.[20] Some drugs can be designed for sublingual, intranasal, or transdermal administration to avoid first-pass metabolism, but in order to reach brain tissue they still must cross the blood–brain barrier. The endothelial cells that make up the blood–brain barrier are tightly sealed to one another, preventing diffusion of most substances from blood into the brain. Drugs that are lipophilic, nonpolar, and have small molecular weight are most likely to cross the blood–brain barrier. Even if this barrier is crossed, the brain possesses carrier-mediated efflux systems that transport a wide variety of substances out of the brain, limiting drug accumulation.[21], [22] To bypass the blood–brain barrier, drugs can be injected intrathecally (directly into the cerebrospinal fluid). This approach requires a lumbar puncture to be performed, and the associated pain and procedural risks limit its use to life-threatening conditions, such as pediatric leukemia, that involve the central nervous system.

Implantable drug delivery systems can circumvent some of these challenges, and offer opportunities for application of bioelectronic devices. Programmable pumps, such as the SynchroMed Intrathecal Pump by Medtronic PLC, are used to chronically deliver medications for pain and spasticity management.[23] The pump is implanted subcutaneously in the abdomen, with a small tube placed in the intrathecal space. The drug is continuously administered at a low rate,

but some pumps can now be programmed by external magnetic signals to allow adjustment of flow. These pumps store 20–40 mL of drug and are refilled through a catheter access port. They also need to be surgically replaced every 4–7 years based on battery life.[24] Miniaturized, soft devices capable of providing localized, on-demand drug delivery could substantially improve care of patients requiring ongoing pharmacologic therapy.

1.2.2 Electromagnetic Treatment

Electromagnetic stimulation has been applied to treatment of various neuropsychiatric symptoms and conditions. Devices to provide electrical stimulation can be categorized as either open-loop or closed-loop. Open-loop stimulation is applied as per a predesigned protocol that is not modified by ongoing signals from the body, while closed-loop stimulation features are determined according to feedback provided from body signals.

Open Loop

Open-loop neurostimulation technologies are commonly employed to treat chronic pain, theoretically functioning by attenuating conduction of the pain signal or increasing local inhibition.[25] Stimulators can be implanted epidurally to target the spinal cord, as well as within or on the surface of subcutaneous tissue to target peripheral nerves. Substantial evidence supports the efficacy of these approaches in treating chronic, medically refractory pain related to cancer, neuropathy, and nerve injuries.[26] Vagus nerve stimulation (VNS), accomplished by an implanted device that applies pulses of stimulation to the axons of the nerve in the neck, has widespread effects on neuronal excitability and can decrease the occurrence rate of seizures in a select group of patients with medically refractory epilepsy.[27] Similar devices can be placed over the skin to pass current over a targeted muscle or group of muscles with the goal of contracting the

muscle and preventing disuse atrophy in conditions where the muscle must be immobilized, such as limb casting or hip replacement surgery.[28]

Noninvasive stimulation of the brain can be accomplished using either electrical or magnetic stimulation, with devices placed on the scalp over the brain region of interest during the epoch of treatment. Although the mechanisms underlying these stimulation approaches are incompletely understood, they are thought to activate or inhibit action potential generation depending on the parameters of stimulation applied.[29] Transcranial electrical stimulation (TES) is considered investigational for all purposes, but studies of its efficacy are ongoing for medical conditions including headaches, pain, insomnia, anxiety, and substance abuse treatment.[30] Transcranial magnetic stimulation is also under investigation for many of these disorders, but has only been approved for treatment of refractory major depressive disorder[31] (NeuroStar TMS Therapy System) and obsessive-compulsive disorder[32] (BrainsWay Deep TMS). Many studies employing TES and TMS have low numbers of subjects as well as heterogeneous technologies and protocols.

Deep brain stimulation (DBS) is an invasive approach that involves chronic implantation of a device that delivers electrical pulses to specific brain areas. Such devices are comprised of a pulse generator, usually implanted near the clavicle or in the abdomen, that is connected by subcutaneous wiring to leads that are inserted into the brain. The pulse generator can be programmed to deliver continuous or diurnally varying stimulation. Most conventional DBS systems use cylindrical electrodes that deliver omnidirectional stimulation and therefore affect neurons around the circumference of the electrode. More recently, directional electrodes have been developed in an attempt to minimize side effects caused by stimulation of off-target brain areas [33] (St. Jude Medical Infinity DBS System, Vercise DBS System). DBS that targets the basal ganglia, a key

center for motor control, results in clinically significant reduction in symptoms for patients with Parkinson's disease, essential tremor, and primary dystonia. [34]–[36] Studies are ongoing for patients with epilepsy, multiple sclerosis, treatment resistant depression, obsessive-compulsive disorder, Tourette's syndrome, and even drug addiction, but there is currently insufficient evidence for widespread clinical use.

In all cases, materials and devices that improve the efficacy of stimulation, decrease the cost per subject, minimize side effects, and simplify routine use of the technology would be expected to improve the quality of clinical studies and perhaps expand the applicability of these approaches to a broader range of disorders.

Closed loop

Closed-loop stimulation therapies have the advantage of providing treatment only when a biomarker of neurologic disease is detected. This type of approach potentially improves the efficacy of several open-loop interventions and decreases associated side effects.[37]

For instance, when the spinal cord stimulation parameters are tuned based on body posture information that is acquired by an accelerometer, patients with intractable neuropathic pain often experience improved pain relief.[38] Closed-loop vagal nerve stimulation (AspireSR) triggered by increases in heart rate associated with seizures is approved for clinical use, and may improve efficacy over conventional VNS in selected patients.[39] Automated triggering of DBS based on brain signals recorded from the basal ganglia in patients with Parkinson's disease (Activa, Medtronics PC+S neurostimulator) may also improve outcomes and increase device battery life.[40] Closed-loop therapy used to abort seizures based on intracranial detection of electrophysiologic seizure patterns (NeuroPace) has demonstrated clinical safety and efficacy in reduction of seizure frequency in selected patient populations, in contrast to open loop approaches

that have been mostly ineffective.[41], [42] Therefore, the ability to transform open- to closed-loop therapies holds promise for better patient outcomes. However, this process is beset by challenges related to accurate sensing of relevant biomarkers and implantation of electronic components capable of performing signal processing, most of which are non-biocompatible and therefore require strong encapsulation in physiological environments.

Substantial effort is also dedicated to devices aimed at facilitating patient movement rather than controlling neurologic symptoms. For many patients who have lost mobility due to injury of the limbs or spinal cord, amyotrophic lateral sclerosis, or brainstem stroke, closed-loop devices offer the possibility of restoring independence and improving quality of life. Here, electronics are interfaced with either the central or peripheral nervous system to translate movement intent into physical manifestation. Noninvasive approaches involve the use of microcomputer-controlled electrical pulses applied through electrodes placed on the skin over targeted nerves and muscles. For example, devices have been developed that assist gait abnormality due to dysfunction of a peripheral nerve in the leg by sensing onset of gait using a sensor worn in the shoe, triggering cutaneous nerve stimulation to increase dorsiflexion through a cuff worn below the knee (WalkAide, Bioness NESS L300). The Parastep ambulation system uses a similar approach to initiate a sequence of muscle contractions in the lower extremities that enable a patient with lower spinal cord injury to stand, sit, and take steps. Prostheses can also be integrated with functioning nerves or muscles in patients with limb amputations to restore distal motor function of the extremity.[43] To enable a greater diversity of controllable movements in patients with brain or spinal cord diseases, high spatiotemporal resolution brain signals are required, necessitating invasive implantation of devices into brain tissue. Typically, microelectrode arrays (96 channels, Blackrock Microsystems)[44] have been implanted into motor or parietal cortex, with acquired

signals used to control a variety of effectors, from a keyboard to robotic limb (LUKE arm, modular prosthetic limb)[45] or exoskeleton (CLINATEC BCI platform).[46] These systems encounter challenges in maintaining consistent, chronic recording of the brain signals required to operate the devices, require intensive training before effective use begins, and are difficult to operate outside of a clinical environment (e.g., in the home). Furthermore, the devices are currently unable to integrate sensory feedback, which is crucial for tuning and adjustment of motor movements.

As our understanding of the nervous system and its pathophysiology progress, potential applications for bioelectronic devices to diagnose and treat neuropsychiatric diseases are increasingly hypothesized. However, appropriate clinical testing of these hypotheses requires new approaches to the material design of bioelectronic devices to optimize efficacy and minimize potential risks. Here, each main component of bioelectronic devices is addressed advances that could improve translation to clinical use are discussed.

1.3 Clinical Development

The Food and Drug Administration (FDA) provides documentation outlining approval requirements for neurological devices. The basic process of neural device development for clinical use involves formalizing the device design and fabrication, establishing sterilization protocols, completing Institutional Review Board (IRB) approval at investigators' institutions (where the device is to be tested or used outside of FDA oversight), and ultimately acquiring FDA approval. Medical devices require stringent testing before commercialization, which is governed by the Center for Devices and Radiological Health (CDRH) within the FDA. Further, neurotechnology devices are primarily reviewed by the Division of Neurological and Physical Medicine Devices (DNPMD).[47] The process of registering a medical device involves regulation commensurate with risk associated with device use, classified as Class I, II, or III in order of escalating risk. Class

I devices are often simple in design and have minimal potential risk to the patient. Very few neurological devices hold this classification, though ventricular needles and anvils used to form skull plates fall in this category.[48] Noninvasive neurological devices such as biofeedback and diagnostic EEG sensors and some invasive devices such as neurostimulators fall under Class II devices because they require regulation beyond general controls. These special controls include labelling requirements, performance standards, and post market surveillance. Finally, devices that are implanted or life-sustaining fall under Class III, such as deep brain stimulators. These devices involve general controls and premarket approval activities that include clinical trials. The regulations that are associated with each class of device assure safety and effectiveness and are governed by Code of Federal Regulations (CFR) Title 21 for general device types and 21 CFR Part 882 and 890 for neurological and physical medicine devices, respectively.

References

[1] C. Gold, D. A. Henze, C. Koch, and G. Buzsáki, "On the origin of the extracellular action potential waveform: A modeling study," *J. Neurophysiol.*, vol. 95, no. 5, pp. 3113–3128, 2006, doi: 10.1152/jn.00979.2005.

[2] G. Buzsáki, C. A. Anastassiou, and C. Koch, "The origin of extracellular fields and currents-EEG, ECoG, LFP and spikes," *Nat. Rev. Neurosci.*, vol. 13, no. 6, pp. 407–420, 2012, doi: 10.1038/nrn3241.

[3] N. Kuhnke, J. Schwind, M. Dümpelmann, M. Mader, A. Schulze-Bonhage, and J. Jacobs, "High Frequency Oscillations in the Ripple Band (80–250 Hz) in Scalp EEG: Higher Density of Electrodes Allows for Better Localization of the Seizure Onset Zone," *Brain Topogr.*, vol. 31, no. 6, pp. 1059–1072, 2018, doi: 10.1007/s10548-018-0658-3.

[4] J. X. Tao, A. Ray, S. Hawes-Ebersole, and J. S. Ebersole, "Intracranial EEG substrates of scalp EEG interictal spikes," *Epilepsia*, vol. 46, no. 5, pp. 669–676, 2005, doi: 10.1111/j.1528-1167.2005.11404.x.

[5] M. Balish and R. Muratore, "The inverse problem in electroencephalography and magnetoencephalography.," *Adv. Neurol.*, vol. 54, no. May 2014, pp. 79–88, 1990.

[6] M. F. Selvitelli, L. M. Walker, D. L. Schomer, and B. S. Chang, "The relationship of interictal epileptiform discharges to clinical epilepsy severity: A study of routine electroencephalograms and review of the literature," *J. Clin. Neurophysiol.*, vol. 27, no. 2, pp. 87–92, 2010, doi: 10.1097/WNP.0b013e3181d64b1e.

[7] N. Maromi, J. M. Lee, V. L. Shanker, and M. R. Sperling, "The EEG and prognosis in status epilepticus," *Epilepsia*, vol. 40, no. 2, pp. 157–163, 1999, doi: 10.1111/j.1528-1157.1999.tb02069.x.

[8] D. Friedman, J. Claassen, and L. J. Hirsch, “Continuous electroencephalogram monitoring in the intensive care unit,” *Anesth. Analg.*, vol. 109, no. 2, pp. 506–523, 2009, doi: 10.1213/ane.0b013e3181a9d8b5.

[9] J. Cappell, C. Schevon, and R. G. Emerson, “Magnetoencephalography in epilepsy: Tailoring interpretation and making inferences,” *Curr. Neurol. Neurosci. Rep.*, vol. 6, no. 4, pp. 327–331, 2006, doi: 10.1007/s11910-006-0026-7.

[10] T. R. Henry, D. A. Ross, L. A. Schuh, and I. Drury, “Indications and outcome of ictal recording with intracerebral and subdural electrodes in refractory complex partial seizures,” *J. Clin. Neurophysiol.*, vol. 16, no. 5, pp. 426–438, 1999, doi: 10.1097/00004691-199909000-00004.

[11] I. S. Fernández and T. Loddenkemper, “Electrocorticography for seizure foci mapping in epilepsy surgery,” *J. Clin. Neurophysiol.*, vol. 30, no. 6, pp. 554–570, 2013, doi: 10.1097/01.wnp.0000436898.10125.70.

[12] P. Dahal *et al.*, “Interictal epileptiform discharges shape large-scale intercortical communication,” *Brain*, vol. 142, no. 11, pp. 3502–3513, 2019, doi: 10.1093/brain/awz269.

[13] A. Thomschewski, A. S. Hincapié, and B. Frauscher, “Localization of the epileptogenic zone using high frequency oscillations,” *Front. Neurol.*, vol. 10, no. FEB, 2019, doi: 10.3389/fneur.2019.00094.

[14] E. M. Merricks *et al.*, “Single unit action potentials in humans and the effect of seizure activity,” *Brain*, vol. 138, no. 10, pp. 2891–2906, 2015, doi: 10.1093/brain/awv208.

[15] E. Hedegärd, J. Bjellvi, A. Edelvik, B. Rydenhag, R. Flink, and K. Malmgren, “Complications to invasive epilepsy surgery workup with subdural and depth electrodes: A prospective population-based observational study,” *J. Neurol. Neurosurg. Psychiatry*, vol.

85, no. 7, pp. 716–720, 2014, doi: 10.1136/jnnp-2013-306465.

[16] J. R. Daube and D. I. Rubin, “Needle electromyography,” *Muscle and Nerve*, vol. 39, no. 2, pp. 244–270, 2009, doi: 10.1002/mus.21180.

[17] B. Katirji, “The clinical electromyography examination: An overview,” *Neurol. Clin.*, vol. 20, no. 2, pp. 291–303, 2002, doi: 10.1016/S0733-8619(01)00002-0.

[18] J. Kimura, “Facts, fallacies, and fancies of nerve conduction studies: Twenty-first annual Edward H. Lambert lecture,” *Muscle and Nerve*, vol. 20, no. 7, pp. 777–787, 1997, doi: 10.1002/(SICI)1097-4598(199707)20:7<777::AID-MUS1>3.0.CO;2-4.

[19] J. W. Albers, P. D. Donofrio, and T. K. McGonagle, “Sequential electrodiagnostic abnormalities in acute inflammatory demyelinating polyradiculoneuropathy,” *Muscle Nerve*, vol. 8, no. 6, pp. 528–539, 1985, doi: 10.1002/mus.880080609.

[20] M. Pollay, “Cerebrospinal fluid in diseases of the nervous system,” *Neurosurgery*, vol. 32, no. 2, p. 325, 1993, doi: 10.1097/00006123-199302000-00029.

[21] P. Ballabh, A. Braun, and M. Nedergaard, “The blood-brain barrier: An overview: Structure, regulation, and clinical implications,” *Neurobiol. Dis.*, vol. 16, no. 1, pp. 1–13, 2004, doi: 10.1016/j.nbd.2003.12.016.

[22] L. H. Jimison *et al.*, “Measurement of barrier tissue integrity with an organic electrochemical transistor,” *Adv. Mater.*, vol. 24, no. 44, pp. 5919–5923, 2012, doi: 10.1002/adma.201202612.

[23] K. Wesemann, R. J. Coffey, M. S. Wallace, Y. Tan, S. Broste, and A. Buvanendran, “Clinical accuracy and safety using the synchromed II intrathecal drug infusion pump,” *Reg. Anesth. Pain Med.*, vol. 39, no. 4, pp. 341–346, 2014, doi: 10.1097/AAP.0000000000000107.

[24] W. Ilias *et al.*, “Patient-controlled analgesia in chronic pain patients: Experience with a new device designed to be used with implanted programable pumps,” *Pain Pract.*, vol. 8, no. 3, pp. 164–170, 2008, doi: 10.1111/j.1533-2500.2008.00187.x.

[25] O. Sagher and D. L. Huang, “Mechanisms of spinal cord stimulation in ischemia.,” *Neurosurg. Focus*, vol. 21, no. 6, pp. 1–5, 2006, doi: 10.3171/foc.2006.21.6.5.

[26] C. A. Odonkor, S. Orman, V. Orhurhu, M. E. Stone, and S. Ahmed, “Spinal Cord Stimulation vs Conventional Therapies for the Treatment of Chronic Low Back and Leg Pain: A Systematic Review of Health Care Resource Utilization and Outcomes in the Last Decade,” *Pain Med. (United States)*, vol. 20, no. 12, pp. 2479–2494, 2019, doi: 10.1093/pm/pnz185.

[27] I. Orosz *et al.*, “Vagus nerve stimulation for drug-resistant epilepsy: A European long-term study up to 24 months in 347 children,” *Epilepsia*, vol. 55, no. 10, pp. 1576–1584, 2014, doi: 10.1111/epi.12762.

[28] J. E. Stevens-lapsley, J. E. Balter, P. Wolfe, D. G. Eckhoff, and W. M. Kohrt, “Arthroplasty : A Randomized,” vol. 92, no. 2, 2012.

[29] M. A. Nitsche and W. Paulus, “Excitability changes induced in the human motor cortex by weak transcranial direct current stimulation,” *J. Physiol.*, vol. 527, no. 3, pp. 633–639, 2000, doi: 10.1111/j.1469-7793.2000.t01-1-00633.x.

[30] N. E. O’Connell, B. M. Wand, L. Marston, S. Spencer, and L. H. Desouza, “Non-invasive brain stimulation techniques for chronic pain,” *Cochrane Database Syst. Rev.*, vol. 2014, no. 4, 2014, doi: 10.1002/14651858.CD008208.pub3.

[31] D. M. Blumberger *et al.*, “Effectiveness of theta burst versus high-frequency repetitive transcranial magnetic stimulation in patients with depression (THREE-D): a randomised

non-inferiority trial," *Lancet*, vol. 391, no. 10131, pp. 1683–1692, 2018, doi: 10.1016/S0140-6736(18)30295-2.

[32] A. P. Trevizol *et al.*, "Transcranial Magnetic Stimulation for Obsessive-Compulsive Disorder: An Updated Systematic Review and Meta-analysis," *J. ECT*, vol. 32, no. 4, pp. 262–266, 2016, doi: 10.1097/YCT.0000000000000335.

[33] T. A. Dembek *et al.*, "Directional DBS increases side-effect thresholds—A prospective, double-blind trial," *Mov. Disord.*, vol. 32, no. 10, pp. 1380–1388, 2017, doi: 10.1002/mds.27093.

[34] T. A. Zesiewicz *et al.*, "Evidence-based guideline update: Treatment of essential tremor: Report of the Quality Standards Subcommittee of the American Academy of Neurology," *Neurology*, vol. 77, no. 19, pp. 1752–1755, 2011, doi: 10.1212/WNL.0b013e318236f0fd.

[35] E. Moro *et al.*, "Efficacy of pallidal stimulation in isolated dystonia: a systematic review and meta-analysis," *Eur. J. Neurol.*, vol. 24, no. 4, pp. 552–560, 2017, doi: 10.1111/ene.13255.

[36] L. Perestelo-Pérez, A. Rivero-Santana, J. Pérez-Ramos, P. Serrano-Pérez, J. Panetta, and P. Hilarion, "Deep brain stimulation in Parkinson's disease: meta-analysis of randomized controlled trials," *J. Neurol.*, vol. 261, no. 11, pp. 2051–2060, 2014, doi: 10.1007/s00415-014-7254-6.

[37] E. Krook-Magnuson, J. N. Gelinas, I. Soltesz, and G. Buzsáki, "Neuroelectronics and biooptics: Closed-loop technologies in neurological disorders," *JAMA Neurol.*, vol. 72, no. 7, pp. 823–829, 2015, doi: 10.1001/jamaneurol.2015.0608.

[38] D. Schultz *et al.*, "Randomized Trial Sensor-Driven Position-Adaptive Spinal Cord Stimulation for Chronic Pain," *Pain Physician*, vol. 15, pp. 1–12, 2012, [Online]. Available:

www.painphysicianjournal.com

[39] P. Hamilton *et al.*, "Clinical outcomes of VNS therapy with AspireSR® (including cardiac-based seizure detection) at a large complex epilepsy and surgery centre," *Seizure*, vol. 58, pp. 120–126, 2018, doi: 10.1016/j.seizure.2018.03.022.

[40] C. Anidi *et al.*, "Neuromodulation targets pathological not physiological beta bursts during gait in Parkinson's disease," *Neurobiol. Dis.*, vol. 120, no. August, pp. 107–117, 2018, doi: 10.1016/j.nbd.2018.09.004.

[41] B. C. Jobst *et al.*, "Brain-responsive neurostimulation in patients with medically intractable seizures arising from eloquent and other neocortical areas," *Epilepsia*, vol. 58, no. 6, pp. 1005–1014, 2017, doi: 10.1111/epi.13739.

[42] E. B. Geller *et al.*, "Brain-responsive neurostimulation in patients with medically intractable mesial temporal lobe epilepsy," *Epilepsia*, vol. 58, no. 6, pp. 994–1004, 2017, doi: 10.1111/epi.13740.

[43] M. B. Lee *et al.*, "Clinical neuroprosthetics: Today and tomorrow," *J. Clin. Neurosci.*, vol. 68, pp. 13–19, 2019, doi: 10.1016/j.jocn.2019.07.056.

[44] A. B. Ajiboye *et al.*, "Restoration of reaching and grasping movements through brain-controlled muscle stimulation in a person with tetraplegia: a proof-of-concept demonstration," *Lancet*, vol. 389, no. 10081, pp. 1821–1830, 2017, doi: 10.1016/S0140-6736(17)30601-3.

[45] L. Resnik, F. Acluche, S. Lieberman Klinger, and M. Borgia, "Does the DEKA Arm substitute for or supplement conventional prostheses," *Prosthet. Orthot. Int.*, vol. 42, no. 5, pp. 534–543, 2018, doi: 10.1177/0309364617729924.

[46] A. L. Benabid *et al.*, "An exoskeleton controlled by an epidural wireless brain–machine

interface in a tetraplegic patient: a proof-of-concept demonstration," *Lancet Neurol.*, vol. 18, no. 12, pp. 1112–1122, 2019, doi: 10.1016/S1474-4422(19)30321-7.

[47] C. M. Loftus, M. Hoffmann, W. Heetderks, X. Zheng, and C. Peña, "Regulation of neurological devices and neurointerventional endovascular approaches for acute ischemic stroke," *Front. Neurol.*, vol. 9, no. JUN, pp. 1–5, 2018, doi: 10.3389/fneur.2018.00320.

[48] C. for D. and R. Health, "Neurological Devices - Regulatory Overview for Neurological Devices," vol. 510, pp. 1–3, 2019, [Online]. Available: https://www.fda.gov/MedicalDevices/ProductsandMedicalProcedures/NeurologicalDevices/ucm528786.htm

Chapter 2: Functional Pillars of Neuroelectronics

2.1 Acquisition Materials and Devices

The overall goal of acquiring neural signals is to be able to decode the neural syntax, detect dysfunction, and correct or even prevent this dysfunction. Complicating this goal is the fact that information is processed in the brain at different spatial and temporal resolutions. On the millisecond time scale, an action potential is the unit of communication between individual neurons. Action potentials are generated when a sufficient number of neurotransmitter-gated ion channels within the neuronal cell membrane are opened, resulting in a large change in the electric potential across the membrane in a spatially restricted region. This ion-mediated electrical potential becomes self-sustaining and propagates down the neuron's axon due to activation of adjacent voltage-gated ion channels. Action potentials induce neurotransmitter release at the neuron's presynaptic terminal, allowing communication with the postsynaptic neuron. The changes in ionic flux that result from action potentials can be detected using extracellular electrodes with sizes similar to the neuronal cell body at micrometer scale distances from the neuron. Similarly, changes in ionic flux that result from the opening of postsynaptic ion channels in a population of neurons can be detected as the local field potential (LFP).[1], [2] This synaptic activity is often in the form of brain oscillations at defined frequency bands, and is a result of interactions between excitatory and inhibitory neurons within microcircuits. These brain oscillations have a wide range of frequencies (a few milli-Hertz to several hundred Hertz) and are known to organize sequences of action potentials, establish communication between brain regions, play a causal role in several behavioral functions, and are used as biomarkers for various neurological conditions. Therefore, an ideal neural interface device would be able to acquire action potentials and LFP with high spatial and temporal resolution across large area of the brain simultaneously. The electrode size and

material are key parameters that define the spatial and temporal resolution of the acquired signal at a given location, whereas the density and geometrical distribution of the electrodes define the spatial scale of the recordings.

2.1.1 Materials at the Interface with Neural Tissue

The electric fields generated by nervous tissue are the result of ion movement. The efficiency of an electrode in converting ionic signals into electronic ones can be quantitively evaluated by the electrochemical impedance spectrum of the electrode across a physiologically relevant frequency band (0.1 Hz to 10 kHz). Typically, the electrochemical impedance of an extracellular electrode is reported at 1 kHz, which reflects the corresponding frequency of an action potential period (1 ms). The effective surface area of the electrode and the electrode material are the two key parameters defining this impedance value through the capacitance formed between the electrode and ions in the electrolyte, known as electric double layer capacitance. [3] The larger the electrode surface area, the larger the area of double layer electrical capacitance between electrolyte and the electrode, hence the lower the impedance. However, large electrodes will result in more spatially summated neural activity, limiting the spatiotemporal resolution of the electrode. Therefore, the optimal electrode size is defined by a trade-off between required resolution and electrochemical impedance of the electrode. For example, to be able to acquire an individual neuron's action potentials, the electrode size should be close to the size of the neuron's cell body and spaced to match the density of neurons within the tissue. This restricts the upper band of electrode geometry to ≈10–20 μm in the majority of brain regions, although denser regions with smaller neurons may require smaller electrodes, and similarly, larger electrodes may be used in areas with larger and less closely packed neurons.

Electrode material and its electrochemical properties define the capacitance value of the interface, and this capacitance is inversely related to the overall impedance of the electrode. In general, the neural electrode materials can be categorized as either polarizable or nonpolarizable based on their faradaic interactions with electrolyte. Although nonpolarizable electrode materials, such as Ag/AgCl, that can pass current across electrolyte-electrode interface with minimal resistance are preferred, the deposition of metal ions (such as AgCl) in vivo poses major biocompatibility concerns and precludes their use in high density implantable devices. These materials are often embedded into hydrogels that serve as ion-conductive physical barriers in noninvasive EEG, electrocardiography (ECG), and electro-oculogram (EOG) electrodes. On the, other hand, polarizable, chemically stable metals such as Au, Pt and stainless-steel have been extensively used as in vivo implantable electrode materials in both research and clinical applications. Several approaches have been employed to improve their capacitance and charge capacity, typically by increasing the electrode's effective surface area while maintaining the overall macroscopic geometry of the electrode.[4] These strategies include nanoscale surface patterning, deposition of the electrode material on rough surfaces, use of nanoparticles to form complex 3D nanostructures, and electrodeposition protocols with enhanced surface roughness. A prime example of this strategy is generation of platinum black, which has substantially larger surface area than conventional Pt. In addition to nanoscale enlargement of surface area, metal oxides and nitrides such as Ir/iridium oxide and TiN can further increase the charge capacity of the interface and have been used in several high-density neural interface devices (Figure 2A–C).[5]–[10]

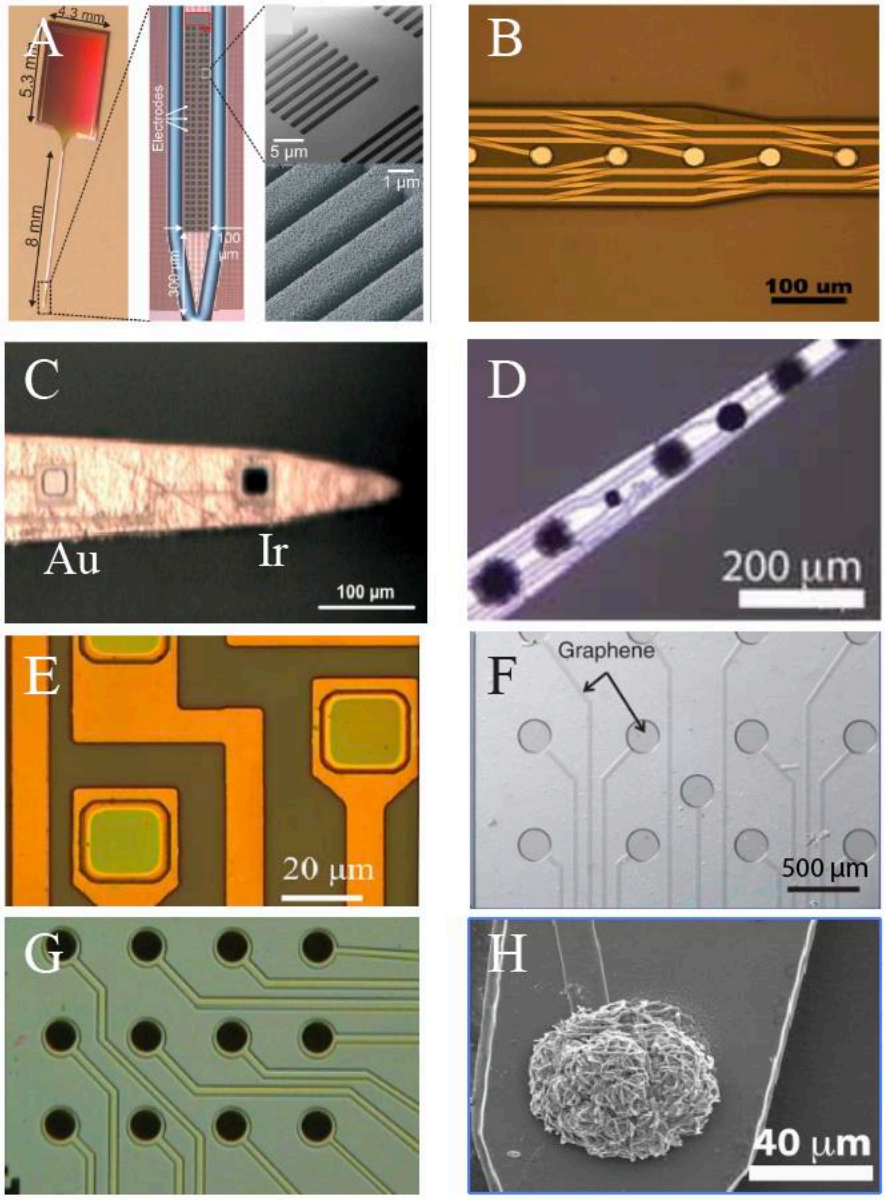

Figure 2: Neural interface electrode materials. A) TiN electrode used in a Neuropixel probe. Reproduced with permission.[11] Copyright 2018, Elsevier. B) Microscopy image demonstrating crossover of two metal sandwich layers (Ti/Pt/Ti) and exposed platinum electrode sites. Reproduced with permission.[12] Copyright 2008, Elsevier. C) Optical images of gold and Ir-plated electrode sites before the pulse test experiment. Reproduced with permission.[13] Copyright 2011, Elsevier. D) Electrochemical deposition of conducting polymer (PEDOT) on electrode sites and around electrospun PLLA nanofiber templates. Reproduced with permission.[14] Copyright 2010, Wiley-VCH. E) Photolithographically patterned conducting polymer electrodes. Reproduced with permission.[15] Copyright 2011, Wiley-VCH. F) High-magnification image of a surface array with transparent graphene electrode sites. Reproduced with permission.[16] G) Optical micrograph of a multielectrode array device made with carbon-nanotube-based pillars. Reproduced with permission.[17] Copyright 1991, Royal Society of Chemistry. H) SEM image of PPy nanotube outgrowth on silicon dioxide showing diameter outgrowth of 60 µm. Reproduced with permission.[14] Copyright 2010, Wiley-VCH.

In parallel to metal-based electrodes, [18]–[20] conducting polymers (a class of organic electronic materials) have gained substantial attention as an electrode coating material that improves the impedance of neural electrodes. Among these materials, the conducting polymer poly(3,4-ethylenedioxythiophene)–poly(styrenesulfonate) (PEDOT:PSS) has been highly used in a large variety of applications and scales due to its commercial availability, high conduction, and stability in physiological environments.[21]–[23] Originally, Martin et al. introduced PEDOT:PSS as polymer electrode coating for implantable silicon probes (Figure 2D,E). They used an electropolymerization technique to coat the existing metallic surface of silicon-based neural probe electrodes with PEDOT:PSS. Signal-to-noise ratio (SNR) and long-term stability in vivo was improved for chronically implanted PEDOT:PSS-based electrodes compared to conventional metal electrodes.[24]–[26] The simplicity and highly reliable electro-polymerization process for PEDOT:PSS was successfully deployed in several laboratories and industrial sectors as part of the electrode fabrication process.

While effective, the electrodeposition process of conducting polymers still poses two major challenges: i) the electrodeposition is limited to conducting surfaces and cannot be used to selectively coat nonconducting surfaces, and ii) the stability and adhesion of the conducting polymer is highly sensitive to deposition protocols and use of crosslinking agents is limited. To overcome these challenges, orthogonal photoresists combined with dry etching processes can be used to perform photolithographic patterning of PEDOT:PSS at high resolutions.[27], [28] This process allows modification of commercially available dispersions to achieve highly conducting patterned PEDOT:PSS. However, addition of crosslinking agents such as GOPS substantially slows the plasma etching process and limits the tractable thickness of the patterned polymer using this method. Instead, a photolithographic process involving patterning and delamination of an inert

sacrificial layer acting as a micropattern shadow mask can be used with many relevant polymers, including modified PEDOT:PSS, on a variety of surfaces (Figure 2E).[29], [30]

Beyond demonstrating improved impedances, organic material-based electrodes offer other unique advantages, including transparency (Figure 2F)[31] and higher surface areas (Figure 2G,H). Conductive polymer coated electrodes also demonstrate the ability to absorb and release biomolecules through swelling. For example, Cui et al. were able to successfully "load" graphene-based electrodes coated with an electrodeposited polymer film with anti-inflammatory drugs prior to insertion in the brain. After implantation, the hydrophilic nature of the polymer resulted in uptake of water and exchange of the drug with the surrounding tissue.[32]

2.1.2 Signal Amplification, Multiplexing and Processing

To obtain high-quality, multichannel neural recordings, signal amplification, multiplexing, and processing must be performed. Neural signal amplification is accomplished via biopotential amplifiers, which must amplify signals with high gain and low noise. Given that the external sources of interference (such as myoelectric potentials from muscle contractions, 50 or 60 Hz AC power, or environmental radio frequency signals) can be several orders of magnitudes larger than neural signals, recordings are performed using a differential setup. Such a setup requires grounding the subject, and performing recordings using at least two electrodes—one to record neural activity, and the other to serve as a reference. The interfering noise then appears as the common-mode signal to a differential amplifier, which if ideal (i.e., with infinite common-mode rejection ratio (CMRR), infinite input impedance, and zero electrode impedance) would completely suppress that common-mode signal. Typical neural amplifiers display CMRRs in the range of 70–120 dB.[33]

Because sampling each neural waveform to a distinct line would require an equal number of leads as electrodes and limit number of electrodes that could be used, multiplexing is applied to combine

several amplified signal lines into one data line.[34]–[39] In time division multiplexing (TDM), the multiplexer selects and forwards one slice of each line to its output line for a given time interval (the sampling window); by switching through all inputs, the multiplexer samples multiple channels into a single line. In turn, at the receiver a demultiplexer enables reconstruction of individual input signals from the multiplexed line.

In addition to multiplexing, neural acquisition systems must also digitize the amplified and multiplexed signal, a task accomplished by analog-to-digital converters (ADCs). This conversion usually occurs after multiplexing to reduce the total number of required ADC lines. In order to satisfy the Nyquist–Shannon sampling theorem (and enable perfect reconstruction of the continuous data from the discrete data), these converters must operate at a sampling rate greater than twice the bandwidth of the signal of interest.[40]

This section describes different approaches to amplifying, multiplexing, and processing signals for neural recordings, according to employed transistor material type.

Silicon Transistor-Based Devices

Silicon-transistor based devices incorporate amplification, multiplexing, and/or processing capacities into integrated-circuits or, more recently, flexible arrays. Silicon-based integrated-circuits are packaged, often implantable chips that receive neural signals from tissue-interfacing electrodes or probes as inputs, and yield amplified, multiplexed, and potentially further filtered signals as outputs. The first monolithic, microprocessor-based telemetry system for neurophysiological recordings, developed in 1985, was based on a micropower signal processor capable of amplifying, filtering, and multiplexing three neural action-potential waveforms detected by microwire electrodes.[41]While that chip interfaced with wire electrodes, ICs can also interface with silicon-based probes, like the Utah array (Figure 3A) or the Michigan probe (Figure 3B).

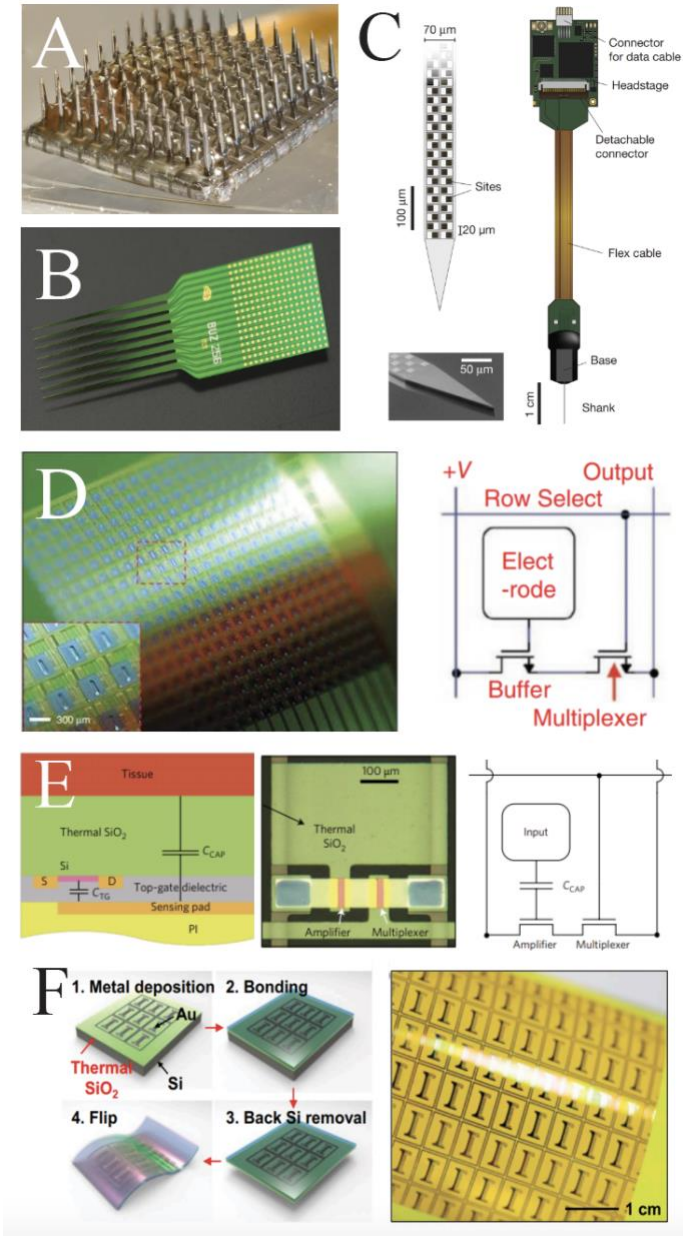

Figure 3: Silicon-based neural interface devices. A) A 10 by 10 Utah array. Reproduced with permission.[42] Copyright 2007, Society for Neuroscience.B) The Michigan probe, also known as an Si-probe. The image is of an 8-shank, 256-channel probe manufactured by NeuroNexus. Reproduced with permission. Image courtesy of NeuroNexus, Ann Arbor, USA. C) Probe tip (left) and packaging (right) of Neuropixel probe capable of recording of 384 channels simultaneously. Reproduced with permission.[5] Copyright 2017, Springer Nature. D) Flexible Si-based transistor used in a surface array to perform local buffering and multiplexing. Reproduced with permission.[39] Copyright 2011, Springer Nature. E) Capacitively coupled silicon nanomembrane transistor as an amplified sensing node. Circuit diagram (left) and optical microscopy image (middle) of a node. Mechanism for capacitively coupled sensing through a thermal SiO_2 layer (right). Reproduced with permission.[43] Copyright 2017, Springer Nature. F) Steps to thermally grow, transfer, and integrate ultrathin layers of encapsulating SiO2 onto flexible electronic platforms (left). Sample with 100 nm thick layer of thermal SiO2 on top surface (right). Reproduced with permission.[44] Copyright 2016, National Academy of Sciences.

IC-incorporating implantable probes have also been developed. The first probe, developed in 1986, included ten recording electrodes and corresponding on-chip electronics, namely, one preamplifier per electrode, an 11:1 multiplexer (driven by an 11-stage two-phase dynamic shift register), power-on-reset circuitry, and high-speed, unity-gain broad-band output buffer.[45] Further, the later-developed "Neuropixel" probe is comprised of a tissue-interfacing shank (tiled by low-impedance TiN sites) and base (on which voltage signals could be filtered, amplified, multiplexed, and digitized) for noise-free transmission of digital data (Figure 3C).[5] Digital signals are more resistant to noise interference, and can be protected from data corruption with a cyclic redundancy code (CRC) checksum. Therefore, such on-chip digitization, which was also employed by Muller et al. [46] in creating a 26400-microelectrode array, allowed for more robust data to be transmitted off-chip.

Multiplexed silicon-based neural interface arrays have also been developed (Figure 3D, E). Fang et al. produced a flexible array consisting of capacitive sensing nodes, whereby each node consisted of an NMOS source-follower amplifier with a capacitive input, and on-site NMOS multiplexer. [39], [44]This array was covered by an ultrathin, thermally-grown layer of SiO2, to act as a dielectric and enable capacitive coupling, as well as acting as a barrier to prevent penetration of biofluids (Figure 3F).[43]

Organic Transistor-Based Devices

Because silicon-based circuitry requires encapsulation in physiological environments, chronic, fully-implantable silicon-based devices are often bulky and display limited channel count and processing capabilities. Since biocompatible organic electronic materials can perform local amplification when used within transistor architectures, organic transistor-based devices have been explored for local amplification of neural signals.

Multiple organic transistor architectures have been applied for neural recordings. In the solution-gated field-effect transistor (SGFET, which is a type of electrolyte-gated OFET (EGOFET)) an organic semiconductor film connects the source and drain electrodes, and a liquid electrolyte separates the channel from the gate electrode. [47]–[49]Given their electrolyte-gating, SGFETs are well-suited to biosensing. Hess et al. used arrays of graphene SGFETs to detect action potentials from electrogenic cells (cardiomyocyte-like HL-1 cells).[50]Hebert et al. demonstrated that when taking recordings from the surface of the cortex, graphene SGFETs exhibit a similar SNR below 100 Hz as platinum black electrodes do, but cannot record signals above 1 kHz. They also successfully recorded slow-wave activity, synchronous activity, and potentials on the auditory and visual cortices.[51] Masvidal-Codina et al. further showed that graphene SGFETs arrays can be used to record a wide bandwidth of neural signals, ranging from infraslow frequencies (<0.1 Hz) to typical local field potential bandwidth (Figure 4A).[52] Cisneros-Fernandez et al. also established a scheme to enable large-scale µECoG recordings with SGFETs, via frequency-domain multiplexing (FDM). Their approach, involving use of SGFETs both as transconductance amplifiers and voltage mixers (with voltage mixing occurring a column voltage carrier and an µECoG signal), allows hybrid integration of SGFET arrays and read-out ICs.[38]

The organic electrochemical transistor (OECT) has also been widely used for bio-signal transduction. In the OECT, an electronic channel formed by patterning a conducting polymer between two electrodes is (de)-doped by injection of ions from an electrolyte. Conformable arrays of OECTs were therefore shown to enable the recording of brain activity, such as low-amplitude brain signals at the somatosensory cortex of rats[53] (Figure 4B,C). While capable of transducing such signals, OECTs, having transient characteristics that are controlled by the time needed for ions to travel between the electrolyte and polymeric channel, display slow switching speeds. To

overcome this limitation, internal ion-gated organic electrochemical transistors (IGTs) embed mobile ions in the conducting polymer defining the transistor channel. This design enables faster response times (τ = 2.6 μs) than observed in OECTs, for which the transient response is characterized by both the time constants for ionic transport in electrolyte (τ_i) and electronic transport (τ_e).[54] Spyropoulos et al showed that IGTs fabricated into a conformable ribbon structure could be applied to human EEG; their "μ-EEG IGTs" adhered directly to skin without additional chemicals, and enabled capture of alpha, beta, and low-gamma oscillations (Figure 4D).[55] In the same direction, Cea et al. developed conformable, implantable, enhancement mode IGTs for in vivo recording of neural action potentials, and circuitry for real-time detection of epileptic discharges[56] (Figure 4E).

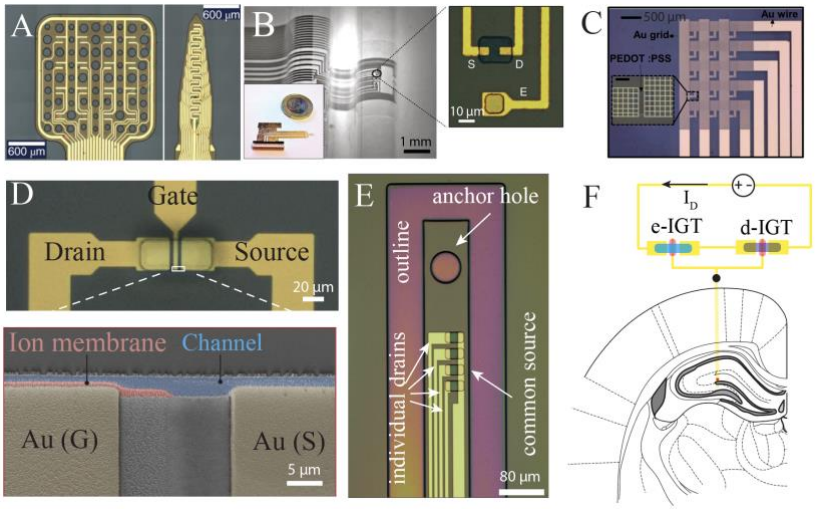

Figure 4: Materials and architectures of transistors used in neuroelectronics. A) Graphene-based transistors for surface and depth recordings. Reproduced with permission.[52] Copyright 2018, Springer Nature. B) OECT-based ECoG array, with inset showing an optical microscopy image of an OECT and adjacent conducting polymer electrode. Adapted with permission.[53] Copyright 2013, Springer Nature. C) An OECT-based surface array with mesh-like Au interconnects for optical transparency. Reproduced with permission.[57] Copyright 2017, National Academy of Sciences. D) Top view of an IGT (top), with cross-section SEM image of an IGT between gate and source electrodes (bottom). Reproduced with permission.[55] Copyright 2019, AAAS. E) Optical micrograph of an e-IGT-based device with 4 transistors for LFP and spike recording (left). The anchor hole facilitates insertion of the conformable device into deep layers of rat cortex. The potential generated by neurons serves as the small-signal VG. Reproduced with permission.[56] Copyright 2020, Springer Nature. F) Circuit diagram of two complementary IGTs used to record real-time detection in the rat hippocampus. The rat brain coronal slice schematic has the recording site indicated (red dot). Reproduced with permission.[56] Copyright 2020, Springer Nature.

The organic electrochemical transistor (OECT) has also been widely used for bio-signal transduction. In the OECT, an electronic channel formed by patterning a conducting polymer between two electrodes is (de)-doped by injection of ions from an electrolyte. Conformable arrays of OECTs were therefore shown to enable the recording of brain activity, such as low-amplitude brain signals at the somatosensory cortex of rats [53] (Figure 4B, C). While capable of transducing such signals, OECTs, having transient characteristics that are controlled by the time needed for ions to travel between the electrolyte and polymeric channel, display slow switching speeds. To overcome this limitation, internal ion-gated organic electrochemical transistors (IGTs) embed mobile ions in the conducting polymer defining the transistor channel. This design enables faster response times (τ = 2.6 μs) than observed in OECTs, for which the transient response is characterized by both the time constants for ionic transport in electrolyte (τ_i) and electronic transport (τ_e).[54] Spyropoulos et al showed that IGTs fabricated into a conformable ribbon structure could be applied to human EEG; their "μ-EEG IGTs" adhered directly to skin without additional chemicals, and enabled capture of alpha, beta, and low-gamma oscillations (Figure 4D).[56] In the same direction, Cea et al. developed conformable, implantable, enhancement mode IGTs for in vivo recording of neural action potentials, and circuitry for real-time detection of epileptic discharges[56] (Figure 4E).

2.2 Stimulation Materials and Devices

Neural stimulation enables modulation of brain activity, both for the purposes of understanding function of neural networks and treating dysfunction of these networks. In this section we aim to provide an overview of various stimulation methods based on their primary source of stimulation energy.

2.2.1 Electrical Stimulation

Materials

Electrical stimulation involves applying a constant or alternating pattern of voltage or current to the brain (intercranial) or scalp (transcranial) tissue. Noninvasive types of electrical stimulation, like transcranial (TES), are based on the use of skin-interfacing electrodes fabricated from metals, elastic carbon, hydrogels, and conducting polymers. Conventionally, metal electrodes have been used in both invasive and noninvasive stimulation procedures.

To ensure biocompatibility, electrodes are typically made from inert materials such stainless steel, Au, or Pt. A key defining factor in efficient delivery of charge from electrode to tissue is reliable electrode-skin contact through an interface providing the largest area possible, while ensuring homogeneous current density across the electrode. To improve metal electrodes' interface and mechanical stability with biological tissue, such electrodes are often coupled with an ion-conducting adhesive gel (or historically, covered with salt water saturated fabrics). In this setup, the electric current transforms into ionic current at the metal–electrolyte junction.[58] However, the rigidity of metal electrodes combined with their polarizable electrochemical characteristics, renders them nonideal for interaction with tissues. Hydrogel-based electrodes have replaced metal electrodes in many applications. Self-adhesive electrodes for transcutaneous stimulation can consist of two hydrogel layers: a base, conductive-gel layer made from polymerization-derived copolymers, like acrylic acid and N-vinylpyrrolidone, and another connecting the first layer to the conductive substrate such as carbon rubber, carbon film, or wire mesh. A scrim layer can also be incorporated between the two hydrogel layers to prevent slippage, or redistribute the stimulation current [58] (Figure 5A). Similar to strategies employed for recording electrodes, conducting polymer-based hydrogels have been used for transcranial as well as intercranial stimulation due to

their large volumetric capacitance and mixed ionic and electronic conduction (Figure 5B). [21], [59]–[64]

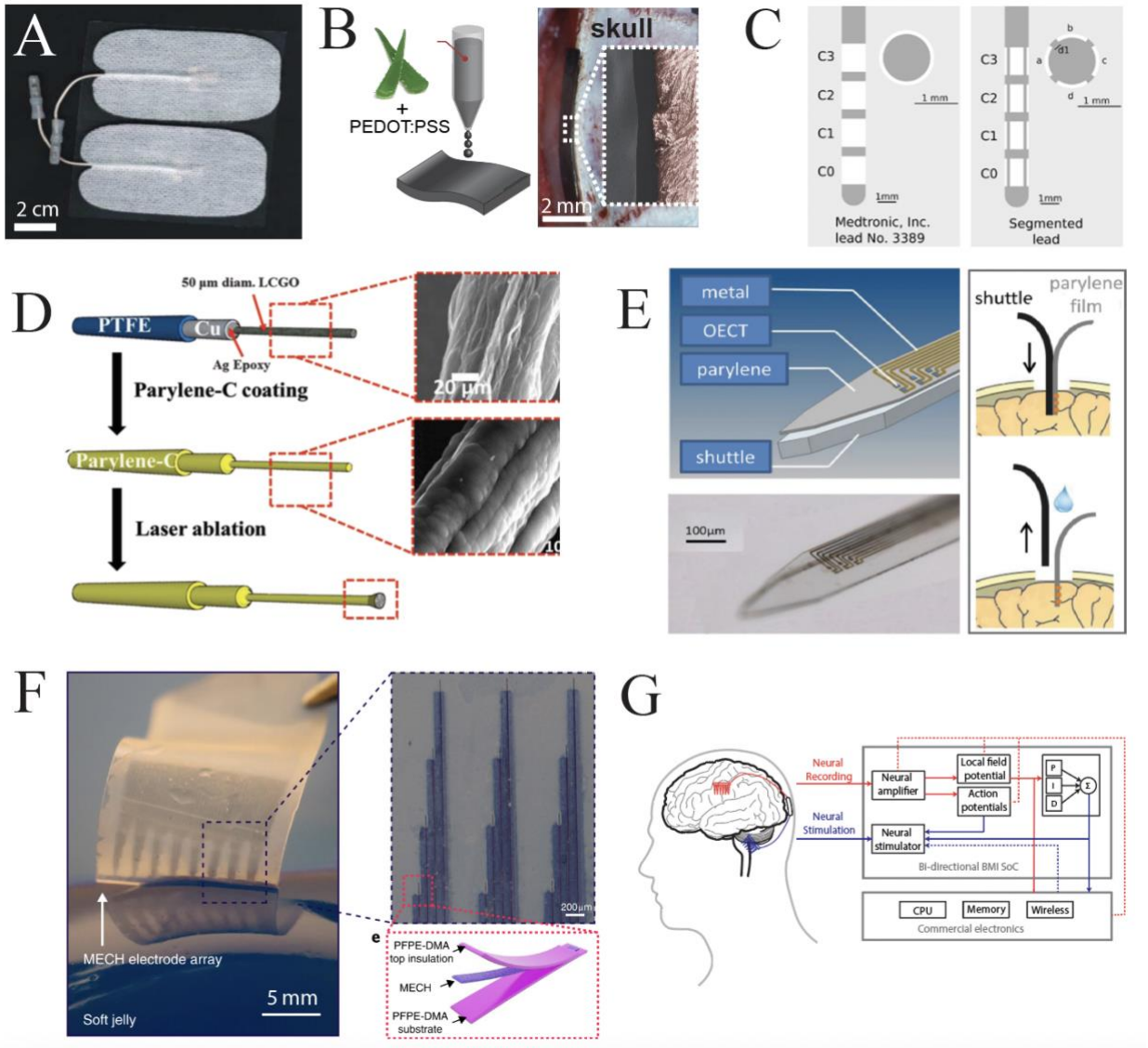

Figure 5: Electrical stimulation modalities. A) Self-adhesive electrode for transcutaneous stimulation. Reproduced with permission.[56] Copyright 2020, Springer Nature. B) Aloe vera conducting polymer film based on PEDOT:PSS and aloe vera hydrogel conforms on a rat skull (left). TES electrodes placed on the rat skull (right). Reproduced with permission.[59] Copyright 2019, Wiley-VCH. C) Unsegmented (left) versus segmented (right) deep-brain stimulation lead. Reproduced with permission.[65] D) "Brush" electrode composed of wet-spun liquid crystal graphene oxide for neural stimulation and recording. Reproduced with permission.[19] Copyright 2015, Wiley-VCH. E) Delaminating depth probes with organic electrochemical transistors penetrate the cortex and stimulate neurons. Reproduced with permission.[66] Copyright 2015, Wiley-VCH. F) Micropatterned electrically conductive hydrogel electrode array (left) consists of individual MECH electrodes (dark lines) encapsulated by fluorinated polymer PFPE-DMA (blue) (right). Reproduced with permission.[61] Copyright 2019, Springer Nature. G) Block diagram for bidirectional brain–machine interface system enabling closed-loop recording and stimulation.

Invasive electrical stimulation devices such as deep brain stimulation (DBS) electrodes usually incorporate smaller electrodes than those seen in noninvasive devices, are made out of inert material metals (e.g., platinum or platinum–iridium), and are inserted into the brain tissue to provide more local neural stimulation. DBS devices make use of unsegmented or segmented metal (e.g., platinum or platinum–iridium) electrodes (Figure 5C).[67]Retinal ganglion cell stimulation has been accomplished using “brush-like electrodes” formed from parylene-C coated, wet-spun liquid crystal graphene oxide (LCGO) fibers via laser ablation; implantation of these continuous, free-standing flexible probes was enabled by encapsulating them in a water-soluble sugar microneedle, which could be inserted into the tissue (Figure 5D).[19] Stimulation via transistors, rather than passive electrodes, has also been performed. Williamson et al. demonstrated that flexible, OECT-based depth probes could be implanted by aid of SU-8 shuttles (from which the probes delaminated after insertion). Application of monophasic current pulses to CA3 area of rat hippocampus pyramidal cell layer through OECTs was shown to be sufficient to evoke network and single cell responses (Figure 5E).[66]

Implantable arrays of electrodes have also been employed to achieve electrical stimulation. Liu et al. demonstrated that a thin-film elastic array of micropatterned electrically conductive hydrogel (MECH) electrodes could conformably wrap around the sciatic nerves of mice to stimulate muscle movements at low voltages (50 mV). This hydrogel was based on the conducting polymer PEDOT:PSS, and demonstrated an electrical conductivity of 47.4 ± 1.2 S cm^{-1}, as well as current density (under a bipolar pulsed voltage of 0.5 V at 50 Hz) that was orders of magnitude higher than that of electrodes made by a pure ionic conductor (Dulbecco's modified Eagle's media) or platinum electrodes (Figure 5F).[61]

Systems

Electrical stimulation involves applying a constant or alternating pattern of voltage or current to the brain (intracranial) or scalp (transcranial) tissue.

Traditionally, this has been performed in the form of an open-loop stimulation. However, closed-loop electrical stimulation has gained significant attention recently, and is being investigated for various neuropsychiatric disorders. Liu et al. demonstrated a fully-programmable, bidirectional neural interface system capable of i) acquiring 16-channel, low-noise neural amplifiers (based on 180 nm CMOS technology), ii) extracting neural waveform features, and iii) performing closed-loop electrical stimulation of neural circuits based on proportional-integral-derivative (PID) controllers (Figure 5G).[68] Whereas that system realized the closed-loop control on each channel through PID controllers, field-programmable gate arrays (FPGAs) have also been utilized to provide required computation for processing the ongoing feedback signal and controlling the stimulating circuitry. Zhou et al. develop a 128-channel, wireless neuromodulation device (WAND) that used an FPGA to run closed-loop algorithms, cancel residual artifacts (i.e., the large voltage transients resulting from stimulation), and detect neural biomarkers based on their waveform characteristics.[69] Park et al. employed an FPGA to develop a closed-loop, 128-channel spike-sorting system, which is the process of assigning neural spikes to an individual neuron (unit) for real time clustering of neural spikes into putative individual neurons.[70] Seu et al. used a reconfigurable FPGA-based processing system for low-latency preprocessing of spike data acquired by a 4096-electrode microelectrode array (MEA).[71]

2.2.2 Magnetic Stimulation

Magnetic stimulation, in the form of pulsed or low-radiofrequency alternating magnetic fields (100 kHz to 1 MHz), is applied for noninvasive (and to a lesser extent, invasive) excitation or inhibition

of specific brain areas. Magnetic stimulation can penetrate into the body without substantial attenuation (i.e., up to the MHz range). Although this method's stimulation is typically achieved via noninvasive procedures and devices, invasive methodologies are also being explored.

Transcranial magnetic stimulation (TMS) is a noninvasive approach that relies on passing current through a coil of wire (the “magnetic coil”) placed above the scalp, whereby the region of stimulation can be characterized through concurrent use of electrical recording (EEG) or imaging modalities.[72] Since coil geometry changes the resultant magnetic field, magnetic coils of specific sizes and shapes, including round, figure-of-eight (F8), or Hesed (H), are employed for targeted stimulated. F8-coils are more focal, with maximal current being produced at the intersection of the two round components.[73] By contrast, H-coils, which are larger and have more complex winding patterns, are used to stimulate deeper brain structures, though with less focality.[74]

For superficial cortical regions, the spatial limits of TMS stimulation can be well-defined: TMS-induced spiking activity of single neurons in an area of the macaque parietal cortex could be confined to a 2 mm diameter region through use of a 55 mm coil.[75] However, since TMS cannot achieve specific stimulation of deeper regions, smaller, penetrating devices have been developed. Bonmassar et al. produced micromagnetic stimulation coils that were small enough to be implanted within the brain parenchyma. Their coils were able to activate retinal ganglion cells both directly and indirectly (via activation of presynaptic neurons), with the activation respectively depending on whether neurons were near the end of the coil, or along its cylindrical length.[76] Targeted noninvasive stimulation (i.e., affecting specific subpopulations of neurons in a given brain region) can also be achieved through magnetic nanoparticles. Fe3O4 magnetic nanoparticles (MNPs), which dissipate heat generated by hysteresis when exposed to alternating magnetic fields, could be used to activate cells expressing the heat-sensitive capsaicin receptor TRPV1 both in vitro and

in vivo. Anikeeva and colleagues observed that the transfected neurons in mice could be activated up to one month after MNP injection, with the MNP injection site exhibiting lower macrophage accumulation and glial activation as well as a higher proportion of neurons compared to a similarly size stainless steel implant one month after surgery.[77]

2.2.3 Mechanical Stimulation

Mechanical stimulation uses continuous or repeated pulses of ultrasound (US) to modulate brain activity, either by stimulating the brain directly (via transcranial focused US, or tFUS), or by enabling the passage of molecular therapeutic agents into the brain (through transiently disturbing the blood–brain barrier). A single-element FUS transducer can focus 0.5 MHz ultrasound through the human skull and generate acoustic beam profiles with lateral and axial spatial resolutions of 4.9 mm and 18.0 mm from the focal distance, respectively. Such tFUS beams can modify the amplitudes of short-latency and late-onset somatosensory evoked potentials (SEPs).[78]

Low-pressure ultrasound has also been used to stimulate genetically targeted neurons directly. Misexpression of TRP-4, the pore-forming subunit of a mechanotransduction channel in Caenorhabditis elegans, sensitizes neurons to ultrasound; expressing the mechanosensitive channels within the mammalian brain therefore would form the basis for cell-type or region-specific ultrasound-based manipulation of neural activity ("sonogenetics").[79] Because ultrasound can be used in conjunction with piezoelectric materials to generate direct-current output,[80] neural stimulation via US and piezoelectric nanomaterials has also been explored. Marino et al. observed high-amplitude Ca2+ transients after ultrasound stimulation of SH-SY5Y-derived neurons that were treated with piezoelectric tetragonal barium titanate nanoparticles (BTNPs).[81] Functionalizing BTNPs with specific molecules could then eventually enable cell-type selective, in vivo neural stimulation.

FUS has also been used to open the blood–brain barrier (BB), an anatomic barrier through which only molecules <400 Da can pass.[82] Choi et al. demonstrated the feasibility of noninvasively opening the BBB in mice (i.e., through the intact skull and skin) using a single-element FUS transducer.[83] Marquet et al. then later showed that microbubble-enhanced, FUS (ME-FUS) enables BBB opening and subsequent recovery in nonhuman primates.[82] Temporally specific opening of the BBB has potential applicability to delivery of therapeutics as well as stimulation-enabling mediators (such as virus for subsequent expression of opto- or sonogenetic proteins).

2.2.4 Optical Stimulation

Optical stimulation is based on photosensitization and activation of neurons. Photosensitivity is most commonly achieved genetically, whereby cells are made to express light-sensitive proteins that depolarize (e.g., channelrhodopsin) or hyperpolarize (e.g., halorhodopsin) neurons after exposure to different wavelengths of light (blue or yellow, listed respectively for the previous examples).[84], [85] This optogenetic approach involves rapid and temporally precise control of neuronal activity in a cell-type specific manner.[86]

Silicon neural probes have been used for optogenetic applications. Schwaerzle et al. developed silicon-based neural probes with optical functionality ("optrodes") that contained platinum microelectrodes, base laser diode chips, and photographically patterned SU-8 waveguides[87] (Figure 6A). Yoon and colleagues designed a four-shank probe containing InGaN μLEDs and Ti/Pt/Ir recording electrodes; this probe could be used to independently control neurons localized ≈50 μm apart in the CA1 pyramidal layer of mice, and induce spikes at ultra-low optical power (≈60 nW, Figure 6B).[88] Mohanty et al. produced a reconfigurable visible-light nanophotonic platform based on waveguides defined in SiN, enabling light input from a single laser centered at 473 nm to be distributed across multiple localized emitters. They demonstrated their platform's

capacities by using it to control the flow of light to an implantable nanophotonic probe containing 8 independently switchable beams, and optically activate individual ChETA-expressing Gad2 interneurons in different layers of the visual cortex and hippocampus, with sub-millisecond precision (Figure 6C).[89] Lee et al. produced a "micro-optoelectrode array" from the optically transparent wide bandgap semiconductor ZnO. This device, which was a 4 × 4 array of electrically-isolated shanks with 400 μm pitch, triggered spiking in vivo at laser power levels of about 1 μW (Figure 6D).[90] Montgomery et al. developed a fully wireless implant consisting of a PCB-based powering circuit and an attached LED; this implant, which was powered via a resonant cavity, provided sufficient light power densities and pulse characteristics for optogenetic control of mouse brain, spinal, and peripheral circuits (Figure 6E).[91]

Stretchable electronics (which apply elastic conductors as electrical interconnects between rigid or bendable active devices,[92], [93] such as in a stretchable active-matrix display that used dispersed elastic conductors of single-walled nanotubes (SWNTs) in fluorinated copolymer rubber[94] and flexible fibers are being explored for optical stimulation, too. Park et al. presented an optogenetic device that combined thin, mechanically soft neural interfaces with implantable, stretchable wireless radio power and control systems. The different form factors of this device enabled specific and reversible activation of pain circuits in freely moving, untethered mice via an integrated light emitting diode (LED) (Figure 6F).[86] Lu et al. have shown that all-polymer neural fiber probes (comprised of a polycarbonate core, cyclic olefin copolymer cladding, conductive polyethylene electrodes) exhibit low-loss light transmission, even after deformation, for optogenetic stimulation of spinal cord neural activity (Figure 6G).[95]

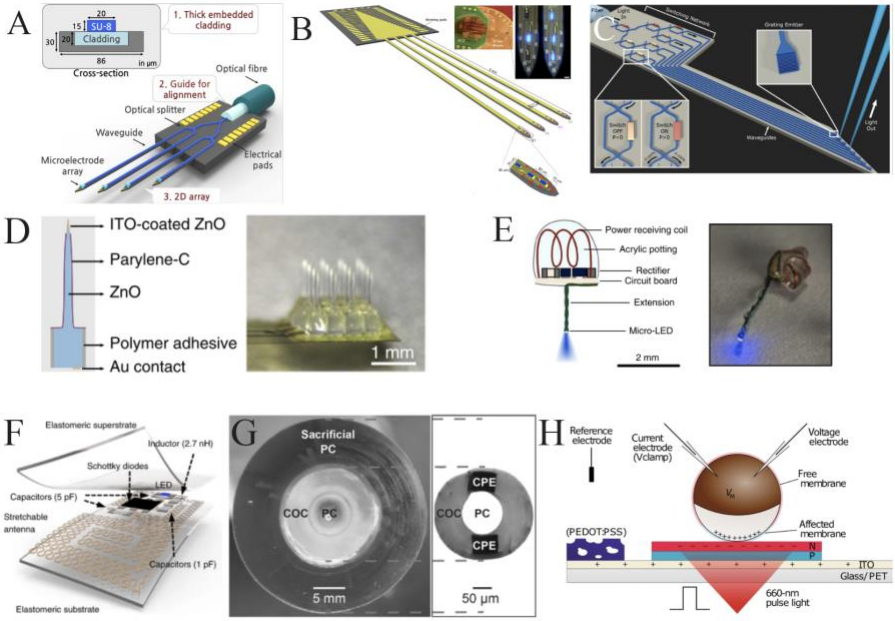

Figure 6: Optical stimulation modalities. A) Silicon-based neural probe ("optrode") monolithically integrated with SU-8 optical waveguides and microelectrode arrays. Reproduced with permission.[96] Copyright 2015, Springer Nature. B) Four-shank probe for high-resolution optogenetic manipulations. Each shank contains eight recording sites and three µLEDs. Adapted with permission.[88] Copyright 2015, Elsevier. C) Implantable silicon-based probe for optogenetic neuromodulation. Visible light entering a single waveguide is sent to a switching network, then emitted at the probe tip via grating emitters. Reproduced with permission.[89] Copyright 2020, Springer Nature. D) Micro-optoelectrode array based on optically transparent wide bandgap semiconductor ZnO. Reproduced with permission.[90] Copyright 2015, Springer Nature. E) Fully implantable wireless optogenetic device. Device is powered via a resonant cavity (not shown).[91] F) Energy harvesting unit of soft, wireless, implantable optoelectronic system. Reproduced with permission.[86] Copyright 2015, Springer Nature. G) All-polymer neural optical fiber with sacrificial polycarbonate layer. Reproduced with permission.[95] Copyright 2014, Wiley-VCH. H) Organic electrolytic photocapacitor capacitively coupling with an adjacent oocyte in electrolyte. Reproduced with permission.[97] Copyright 2019, AAAS.

Optogenetic approaches are not the only means of achieving photosensitivity in cells; cells have also been made photosensitive through nanomaterials, quantum-dots, or organic photocapacitors. Yoo et al. used near-infrared irradiated gold nanorods (GNRs) functioning as photothermal transducers bound to the plasma membrane of neurons to modulate action potentials of cultured hippocampal cells.[98] Further, Carvalho-de-Souva et al. employed gold nanoparticles (AuNPs), which are also photothermal transductors (with a plasmon absorption band peak near 523 nm) to enable optical triggering of action potentials. Since their particles were conjugated to ligands of dorsal root ganglion neuron (DRG) membrane proteins, their AuNP conjugates enabled selective

binding to and stimulation of DRG neurons.[99] CdSe quantum dots have also been used to produce illumination-triggered changes in membrane potentials and ionic currents of cortical neurons in vitro.[100] Jakešová et al. recently developed organic electrolytic photocapacitors (OEPCs), which function as optoelectronic-to-ionic transducers, or light-activated external voltage-clamp electrodes. They found that when excited by short impulses of light, OEPCs produce electrolytic charging currents that can perturb the membrane potentials of nearby cells in vitro (Figure 6H). [97], [101]

2.2.5 Chemical Stimulation

Chemical stimulation relies on use of pharmacological or chemogenetic methods for perturbing neural activity.[8] Delivery of chemical or biological agents can be accomplished via infusion, injection, or ingestion (Figure 7A). To further improve the localization and more targeted delivery can be accomplished through microfluidic, or ion pump-based neural implants. Isaksson et al. developed an electrophoretic ion pump, based on PEDOT:PSS, that functioned as actuator to pump cations (Ca2+, K+) from a reservoir electrolyte to a target electrolyte. This ion pump was able to stimulate individual cells, such that a cell located on a microchannel demonstrated an induced Ca2+ response, but distal cells did not (Figure 7B).[102] Jonsson et al. designed “neural pixels,” consisting of conducting polymer electrodes for sensing and organic electrochemical ion pumps (OEIP) for drug delivery. Their neural pixel-based device could stop externally induced hippocampal epileptic activity by delivering the inhibitory neurotransmitter GABA to seizure foci (Figure 7C).[103]

Chemical stimulation can also be integrated into training paradigms. Van den Brand et al. intraperitoneally administered selected serotonin and dopamine receptor agonists to rats afflicted with paralyzing lesions prior to training the rats (via a training paradigm that relied on

electrochemically enabling motor states while forcing rats to use their paralyzed hindlimbs through a robotic postural interface). This chemical stimulation and training triggered remodeling of cortical projections to restore voluntary control over locomotor movements in the rats.[104]

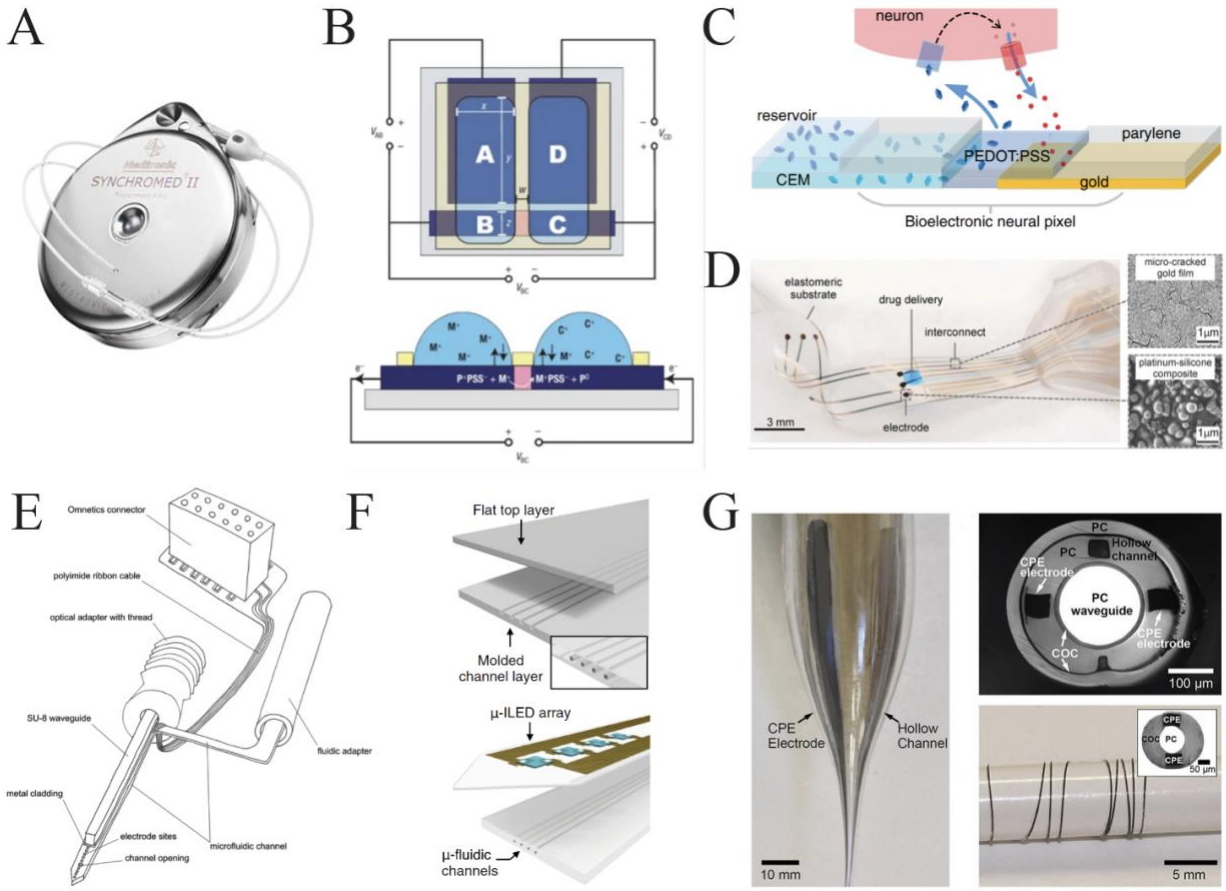

Figure 5: Chemical or multiple stimulation modalities. A) Intrathecal pump for infusion of medication into spinal fluid. Reproduced with permission.[105] Copyright 2008, Springer Nature. B) Top view (top) and cross-sectional view (bottom) of an organic electronic ion pump consisting of four PEDOT:PSS electrodes, labeled A to D. VBC drives ion transport, while VAB and VCD regenerate B and C electrodes. Reproduced with permission.[102] Copyright 2007, Springer Nature. C) Bioelectronic neural pixel uses organic–electronic ion pumps for delivery of neurotransmitters and conducting polymer electrodes for neuronal recording. Reproduced with permission.[103] Copyright 2016, National Academy of Sciences. D) Soft neural implant with the shape and elasticity of dura mater integrating microfluidic channel for local drug delivery with interconnects and electrodes for electrical stimulation. Reproduced with permission.[106] Copyright 2015, AAAS. E) Microimplant integrating fluidic and optical simulation modalities with electrical recording capacity. Reproduced with permission.[107] Copyright 2001, Royal Society of Chemistry. F) Soft microfluidic probe integrated with a flexible array of μ-LEDs. Reproduced with permission.[108] Copyright 2015, Elsevier. G) Multimodal fiber probes combining optical stimulation, drug delivery, and neural recording capabilities. Reproduced with permission.[109]Copyright 2015, Springer Nature.

2.2.6 Multimodal Stimulation

The electrical and chemical stimulation modalities can be combined through use of loaded conducting polymers. The metallic electrodes of implants designed for electrical stimulation are often coated with conducting polymers (e.g., polypyrrole (PPy), poly(3,4-ethylene dioxythiophene), polyterthiophene (PTTh), etc.) to reduce each interface's electrochemical impedance. Coating the electrodes with, for example, anti-inflammatory drug or growth factor-loaded conducting polymers could therefore support tissue health around neural implants through the electro-activated elution of drugs.[110]

Microfluidic channels can also be incorporated into neural stimulation devices for delivery of multiple, distinct chemical agents. Minev et al. developed soft neural implants that transmitted electrical excitation signals (via embedded interconnects and electrodes), and delivered drugs locally (via microfluidic channels called “chemotrodes”). Their implants integrated a silicone substrate, stretchable gold interconnects, platinum–silicone composite soft electrodes, and a silicone-embedded fluidic microchannel (Figure 7D).[106] Rubehn et al. introduced a polyimide-based implant incorporating an SU-8 based waveguide (for optical simulation) and fluidic channel (for chemical stimulation via transport of a gene delivery vector) (Figure 7E).[107] Jeong et al. generated a wireless optofluidic neural probe incorporating microfluidic channels (each of which enabled delivery of an independent fluid) and a cellular-scale inorganic micro-LED arrays (Figure 7F).[108] Canales et al. employed a thermal drawing process (TDP) to produce multimodal fiber probes that combined optical stimulation, drug delivery, and neural recording capabilities; these probes were used to record single action potentials in channelrhodopsin-expressing transgenic mice (Figure 7G).[111]

2.2.7 Conclusion

Taken together, these stimulation modalities offer possibilities for modulation of neural activity in human subjects beyond currently the clinically applied electrical and magnetic methods. Although careful testing is required to ensure safety and efficacy, it may be possible to improve the specificity of stimulation for anatomical regions and cell types. Indeed, clinical trials involving lentiviral vectors that could in the future be capable of introducing optical, ultrasonic, mechanical, and magnetic sensitivity to neurons are ongoing.

2.3 Power and Energy Devices

The variety of form-factors of neural-interfacing devices has necessitated the development of innovative means of powering such devices. Given the long history of use of batteries in contained and implantable medical devices (e.g., pacemakers), most neural interface device powering strategies have focused on use of batteries. However, batteries are chemically reactive, and require rigorous encapsulation. Form factor customization is also limited, increasing the size and weight of devices. Alternatively, energy converting approaches have been explored for powering implanted devices. For example, externally generated mechanical waves (i.e., ultrasound) can propagate through tissue to reach implanted devices containing piezoelectric materials for conversion of incident ultrasonic energy into electric charge. Furthermore, both piezoelectric and triboelectric materials (which respectively convert mechanical force into charge, or produce charge through contact electrification and electrostatic induction during frictional contact of surfaces with opposing polarities) can be applied to harvest the mechanical energy of human motion. The mechanical-to-electrical approach is therefore most applicable when a device is used in a region involving motion (e.g., on a peripheral nerve, or on the skin).

A similar approach can be employed to deliver power through transformation of electromagnetic energy. Electromagnetic waves can propagate through air to reach epidermal devices, or (though more attenuated) through tissue to reach implanted devices. Photovoltaic materials, which convert the energy of photons into energy of electrons, can be applied to power devices. Although electromagnetic waves can reach implanted devices, these waves must overcome absorption by the body and impedance mismatches (such as those existing between air, bone, and tissue) to do so. As a result, magnetic fields, which are only slightly affected by absorption or impedance mismatching, have also been exploited for powering. These external magnetic fields can be converted into local electric fields through inductive coils or magnetoelectric materials localized on the devices. This section will review the materials that enable the various approaches to powering neural-interfacing devices.

2.3.1 Chemical Energy

Both rechargeable and nonrechargeable batteries have been used within implantable devices. The implantable pulse generators (IPGs) that achieve deep brain stimulation are available in both fixed-life and rechargeable options, with their batteries lasting an average of three to five years, or 10+ years with 30 min of charging for two to three days per week, respectively.[112] The batteries of IPGs used for vagus nerve stimulation also require replacement; of the 1144 VNS procedures performed by a single surgeon between 1998 and 2012, 27% were performed due to generator battery depletion.[113] To limit battery size, implantable devices may employ step-up converters, which output a voltage higher than the input voltage. Azin et al. developed a 10.9 mm2 intracortical microstimulation system-on-chip that employed a dc-dc converter to generate a 5.05 V power supply from a 1.5 V battery. The converter provided a maximum DC load current of 88 μA from

5.05 V to allow for an average stimulus rate of >500 Hz on each of eight channels (Figure 8A).[114]

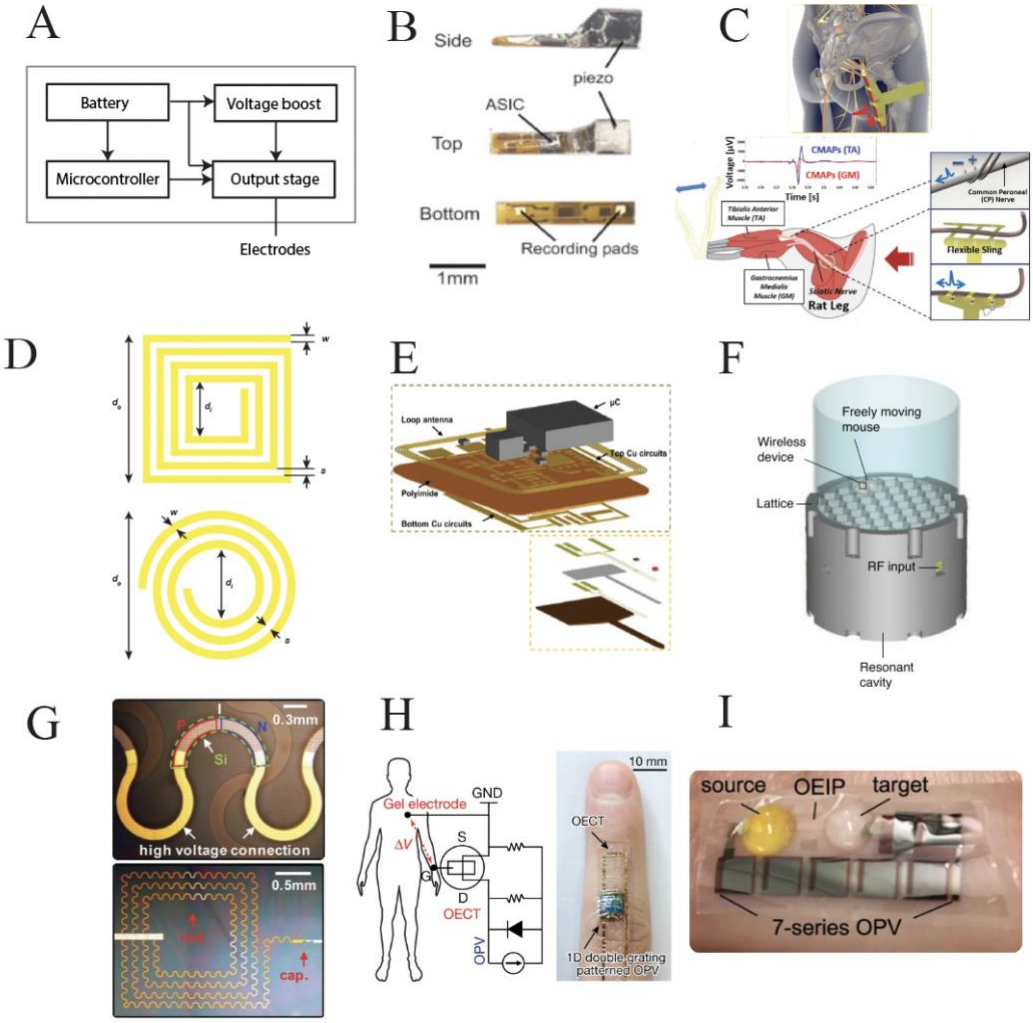

Figure 8: Power transmission strategies. A) Block diagram for typical neural stimulator. DC/DC converters boost the supply voltage to the level required by the output stage. B) Ultrasound-powered neural dust mote consists of a piezoelectric crystal, single transistor, and two recording pads. Reproduced with permission.[115] Copyright 2016, Elsevier. C) Triboelectric nanogenerator in a compressed or released state (top) generates a current (bottom). Reproduced with permission.[116] Copyright 2017, Elsevier. D) Square and circular planar spinal coils for inductive power transmission. E) Electronic (green box) and injectable modules (yellow) of a wireless oximeter. Loop antenna enables magnetic resonant coupling to an external antenna. Reproduced with permission.[117] Copyright 2019, AAAS. F) Resonant cavity for self-tracking energy transfer. Cavity is excited by a continuous-wave input. Reproduced with permission.[118] Copyright 2015, American Physical Society. G) Optical micrograph of filamentary serpentine silicon solar cell (top) and filamentary serpentine inductors and capacitors for RF operation (bottom). Reproduced with permission.[119] Copyright 2011, AAAS. H) A flexible highly stable organic solar cell as a power source for heart-rate measurements. Reproduced with permission.[120] Copyright 2018, Springer Nature. I) An organic photocapacitor is used to drive an organic ion-pump for local delivery of drug. Reproduced with permission.[121] Copyright 2019, Springer Nature.

2.3.2 Mechanical Energy

To enable wireless power transmission through mechanical waves, a piezoelectric crystal on the implanted device must receive and convert the mechanical energy into electricity. However, that crystal can also operate as a transmitter. Seo et al. devised a sub-millimeter implantable device involving a lead zirconate titanate (PZT) piezoelectric crystal, transistor, and a pair of recording electrodes. Because the PZT could both absorb and reflect ultrasonic energy, an external transducer could alternate between transmitting a series of pulses and listening for reflected pulses to power the device, or detecting the encoded electrophysiological signals (Figure 8B).[115]

Triboelectric materials have been applied to translate kinetic into electrical energy. Lee et al. investigated how a multilayer stack of triboelectric nanogenerators (TENGs) that produced an output voltage of 160 V_{pp} and short circuit current of 6.7 μA could be applied for neural stimulation. They developed sling electrodes that could be positioned around the sciatic nerve and powered with the TENG to selectively activate the tibialis anterior muscle (Figure 8C).[116]

2.2.3 Electromagnetic and Optical Energy

Electromagnetic induction has been applied to power both implantable and surface devices. Jow et al. defined a method for designing printed spiral coils geometries to maximize power transmission efficiency (Figure 8D).[122] Zhang et al. used magnetic resonant coupling to power wireless, implantable optoelectronic systems for local tissue oximetry at sites of interests, including the deep brain regions of mice. Each system's power harvesting unit included a loop antenna optimized to operate at 13.56 MHz, and a half-bridge rectifier buffered by a supercapacitor. Since the output of the power harvesting unit was also fed into a low-dropout regulator, the systems operated using a stable power supply of 3 V (Figure 8E).[117]

Ho et al. developed a resonant cavity system for wireless-powering of small-scale implants in mice (Figure 8F).[118] This system, which capitalized on the observed localization of electromagnetic energy at low gigahertz frequencies, enabled creation of implantable wireless optogenetic devices that were two orders of magnitude smaller than previously reported wireless devices.[91]

The epidermal electronics systems (EES) of Kim et al. could be powered either through induction or photovoltaic materials. Given that these systems incorporated electrodes, electronics, sensors, power supplies, and communication components into ultrathin membranes that were laminated onto the skin, material engineering techniques needed to be applied for successful integration of all components. The authors therefore developed "filamentary serpentine" (FS)-shaped components, including inductive coils and silicon photovoltaic cells, for generation of power through inductive coupling to separate transmission coils, or solar illumination, respectively. While the photovoltaic cells could generate a few tens of microwatts, generating more solar power output would have required compromising the size and mechanics of the device. Powering via inductive effects therefore was said to represent the more appealing alternative (Figure 8G).[119]

Photovoltaics have been integrated into other surface devices (Figure 8H). Jakešová et al. integrated their organic electronic ion pump (OEIP) onto a flexible carrier containing organic thin-film bilayer photovoltaic pixels; the pixels were arranged to provide the 2.5–4.5 V needed to operate the OEIP (Figure 8I).[121]

Magnetoelectric materials, which transform magnetic fields into electric fields through material properties instead of material configurations, have also been applied for wireless powering. Wickens et al. produced a magnetoelectric stimulator (ME) comprised of a magnetostrictive layer and piezoelectric layer, whereby the magnetic-field induced strain on the former exerts a force on the latter to generate a voltage. The ME could produce a variety of stimulation patterns in the 100–

200 Hz therapeutic window. The authors also demonstrated that rice-sized ME films of different resonant frequencies could be individually addressed in a human phantom when stimulated by a magnetic field of the corresponding frequency.[123]

2.4 Substrates and Encapsulation

Choosing the appropriate substrate material and geometry for a given neural interface device requires the consideration of numerous factors, such as the device's intended duration of use, cost, manufacturability, depth of recording, target neuronal population size, and function (i.e., sensing, stimulation, or both). The specific substrate used in a probe governs probe properties, most essentially the biocompatibility of the device, but also stiffness, implantability, anchoring, performance of electrical signaling (including SNR, faradic and capacitive mechanisms, sensitivity, and selectivity), compatibility with nonelectronic signaling, and ease of implementation. Chronic implants (those with applications that require use for longer than 24 h) must not trigger an inflammatory response in tissue to maintain stability over long periods of time. Acute implants, on the other hand, need only resist acute inflammatory responses and prevent infection to maintain short-term stability. Probes that will be used on the surface of the skin generally must conform to the skin and may require an adhesive in order to anchor to the soft surface. Devices recording directly from the surface of groups of neurons, such as within cortical or spinal applications, must either conform to the neural surface or anchor into a rigid reference such as bone.

2.4.1 Hard Substrates

Early studies of neural interfaces employed hard substrates such as metal, glass and silicon. Hard substrates tend to have mechanical strength, resist ingress of liquids and vapors, and display particular manufacturability due to a large thermal budget (Figure 9A–E).[124]

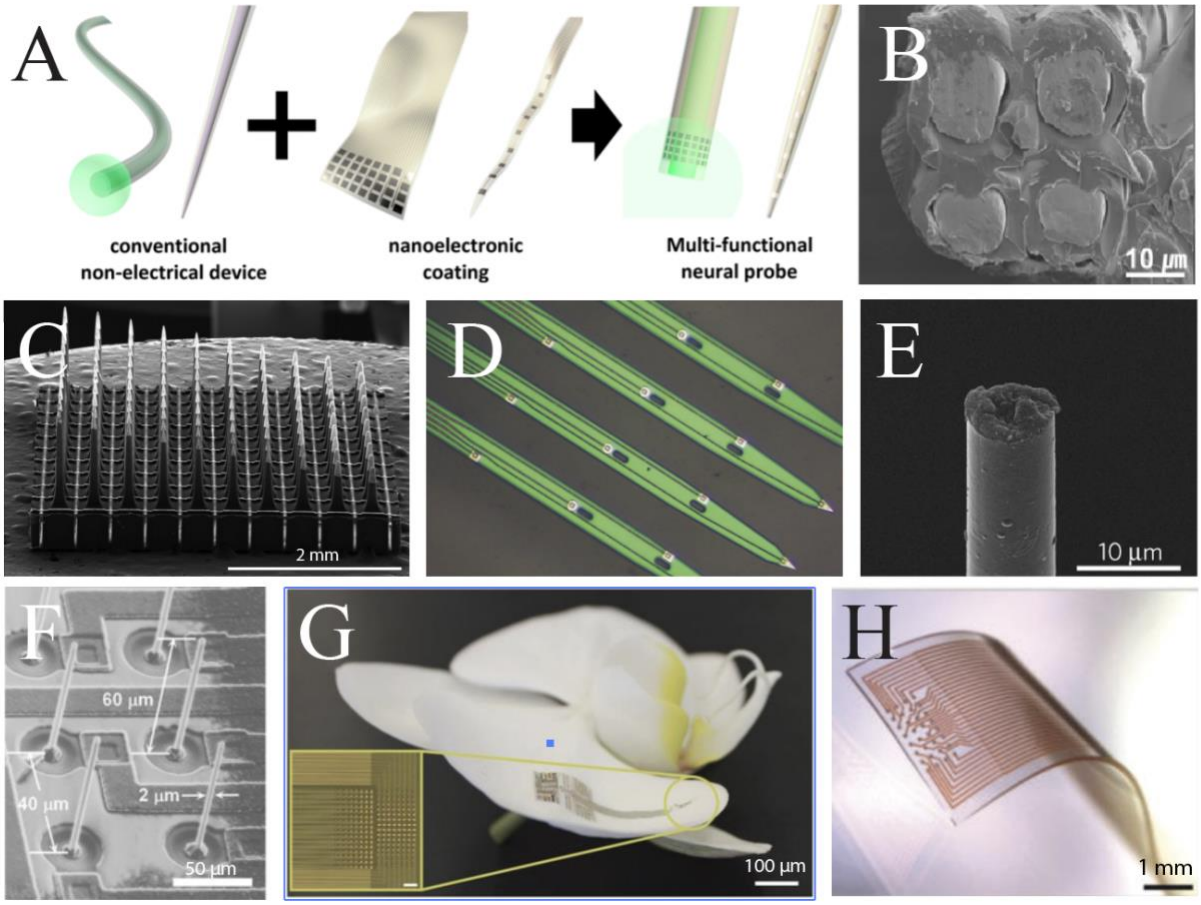

Figure 9: Examples of hard and soft substrates used in neural interfaces. A) Conventional optical fibers or glass pipettes become multifunctional neural probes upon application of nanoelectronic coatings (NECs). Reproduced with permission.[125] Copyright 2017, American Chemical Society. B) SEM of nichrome (NiCr) metal tetrode showing detail of metal substrate with polyimide insulation. Reproduced with permission.[126] Copyright 2018, The Korean Society for Brain and Neural Sciences. C) Utah Slant Electrode array with graduated penetration depths. Reproduced with permission.[127] Copyright 2014, Elsevier. D) Michigan probes, fabricated at the University of Michigan in 1994, built by bulk etching silicon substrates. E) Close-up of carbon substrate microthread with carbon core and poly(p-xylylene) coating. Reproduced with permission.[128] Copyright 2012, Springer Nature. F) Vapor-liquid-solid (VLS) silicon probes are mechanically flexible due to the growth direction and single-crystalline nature of silicon. Reproduced with permission.[129] Copyright 2010, Elsevier. G) Conformable parylene substrate with micropatterned gold electrodes and conductive traces. Reproduced with permission.[2] Copyright 2015, Springer Nature. H) Stretchable PDMS substrate with micropatterned conductive wires and electrodes. Reproduced with permission.[4] Copyright 2018, Wiley-VCH.

Metals and Metal Oxides

Metal-based microelectrodes, smaller than ≈10000 μm^2, can be used for more targeted stimulation and are generally used for ECoG and deep-brain applications. Commercially available microelectrodes, such as microwires (10–300 µm in diameter), are used for invasive neural

interfaces and come in three main categories: single wire, tetrodes, and multiwire arrays. Microwire tips can be flat or pointed, with pointed tips requiring smaller insertion forces.[130] Microwire arrays are customizable and can be obtained from manufacturers such as Blackrock Microsystems and PMT Corporation. Designed to record on the scale of individual neurons, these arrays must be carefully designed to prevent insulative layer delamination and avoid noise superimposition.[131], [132] The small conduction areas in microelectrodes are much more susceptible to degradation from permanent faradic oxidation–reduction reactions—in particular when the stimulation waveform is not charge balanced. This is a common problem in Pt and PtIr electrodes.[133] However, these metal substrates are generally good candidates for surface modification with electrode-preserving capacitive charge injection as an alternative to faradic charge injection. Surface modification with coating can also be used to improve sensing. Titanium metal electrode substrates have good compatibility with TiN, which can be grown as a fractal (high surface area) thin film.

Commonly used metal substrates have favorable properties such as efficient transmission of neural signal frequencies and low inherent impedance. They are also compatible with surface modifications for tuning impedance in order to improve SNR.[8]–[10] Metal substrates are hard, but have low risk of brittle fracture, resist ingress of gases, vapor, and liquid, and can be detectable with MRI after implantation. However, there are limitations to the use of metal substrates. Metal substrates are often the electrode itself, therefore each metal electrode is limited to one signal along the conductor ("single channel") or requires expensive special fabrication. Due to the propensity toward permanent deformation of small metal probes, accidental bending has been reported to cause deviation from intended trajectory.[134] Furthermore, these electrodes are generally susceptible to deterioration during stimulation and require a charge balanced waveform or surface

modification to enable capacitive charge injection. The inherent hardness of metal substrates makes these electrodes stiffer than surrounding tissue and has been widely observed to incite a fibrotic immune response, which also attenuates the neural signal.[64], [135] The hardness of metal substrates can also result in cell death from implantation trauma. Metal substrates are generally fabricated with traditional fabrication techniques rather than microfabrication, making continued miniaturization expensive in both reducing electrode size and connecting electrodes to backend equipment.

Silicon, Glass, and Diamond

While metal substrates have been extensively studied, silicon and glass enable finer resolution in neural interfaces. Silicon micromachining is well defined for MEMS applications, and has been used to fabricate large, dense, parallel arrays for spinal cord, peripheral nerve fibers, ECoG, and intracortical recording.[10], [136] Silicon substrates are not often used for noninvasive recordings, as they are best suited for recording microscale processes.[137] Silicon probes are generally used for recording, though monolithic circuitry built directly into silicon substrates has been used to develop two way neural interfaces.[138], [139] Silicon substrates are prevalent in the semiconductor industry, making the integration of active or computational elements straightforward. Commercially available examples of silicon neural interface arrays are Utah arrays and Michigan probes. Utah arrays are usually limited to a few square millimeters in overall recording area and are made by bulk etching of a partially doped silicon wafer to form needle-like electrodes with fixed spacing, usually 40–300 μm in diameter. When inserted, the base of the Utah array floats over the area of insertion (such as the brain or spinal cord). Michigan probes are capable of greater depth insertion, but all the electrodes lie along the plane of the probe and are oriented on one side of the probe, which can result in “backside shielding” that affects signal

processing of LFP.[6] Multiple electrodes are fabricated along the length of each comb in the array, and the implantation of these probes is largely similar to the insertion of a Utah array. The notable machinability and high-quality masking oxide material available for silicon processing also enables the formation of drug delivery cavities.[140]

Silicon probes provide considerable advantages over predecessor substrates due to silicon's inherent customizability. Silicon is arguably the most machinable substrate available for micromachining due to well-characterized processes and unique anisotropic properties. This machinability results in precise recording layouts and the ability to fabricate multiple channels along the length of a probe needle.[141] The increased number of channels allows for 3D recording at a density that was previously unattainable using metal probes. Further, the ubiquitous processes improve the consistency among probes in the array and lower production costs. Though silicon probes are widely used in neuroscience research applications, these probes must be used with caution. Silicon probes are brittle, and are prone to breaking due to handling during insertion.[134] In addition, the useful size of the array is limited by the flatness of the silicon substrate in relation to the natural curvature of physiological tissue. Large arrays will not be able to penetrate these curved surfaces at a consistent depth, and therefore have limited usefulness. Silicon arrays are often used in research of large mammals and nonhuman primates, Utah arrays are FDA-approved for research in human subjects. Uncoated silicon will degrade over time with exposure to ionic fluid, and generally chronic probes require an insulating polymer coating.[142]

Since silicon probes may be susceptible to fouling, doped diamond probes have been also explored due to their biocompatibility, low capacitance, low fouling, and high charge density properties.[171, 172] Some diamond probes are stiff like silicon, but if thinned sufficiently are somewhat flexible. However, the modulus of this material is still higher than that of adjacent tissue.[143] The

ultimate issue to overcome with rigid probes is the modulus mismatch between the probe and native tissue at the implant site. This mismatch can lead to general drift in physical position, and a signal limiting glial encapsulation immune response which significantly impairs the signal integrity for chronic recording. [10], [132], [144], [145]

2.4.2 Soft Substrates

Soft substrates are conducive to nearly all neural interface applications. For implanted probes, soft substrates have been developed with the goal of overcoming immune responses that attenuate signal, while retaining extremely small feature sizes (Figure 9F, G). Devices built on soft substrates are capable of recording high spatiotemporal resolution signals, from single neurons to micro-LFP. Commonly used soft substrates such as parylene-C, polyimide, and SU-8 have excellent compatibility with the microfabrication techniques that make silicon versatile, while having Young's moduli orders of magnitude lower.[124] The additional moldability of soft substrates can be leveraged to fabricate 3D structures with pockets to facilitate the growth of neurons into the probe or provide reservoirs for drug delivery.[146], [147] Soft implants are usually inherently dielectric and are often used as the signal isolating insulating layer on the device. The modulus of soft implants must be carefully selected: if too soft, the implant can deteriorate, but if too hard, the implant can instigate an immune response. Soft substrates tend to have lower densities and are more compliant, making them comfortable for use as wearable external neural interfaces.

Flexible

With a long history as a final coating material for implanted medical devices, parylene-C is a Class VI implant grade material deposited by a highly conformable chemical vapor deposition process. Parylene resists immune response and moisture uptake, and therefore preserves recording signal strength over long periods of time.[148] The standard thickness for parylene substrates is very thin

(<10 μm) but maintains integrity during handling. After fabrication, probes built on parylene substrates retain significant conformability, allowing them to conform on the surface of skin or neural tissue. Parylene can be coated over a hard substrate, such as a silicon wafer, and released after microfabrication of closely spaced thin film electrodes. This high-resolution fabrication process enables parylene devices to cover large areas, regardless of tissue curvature, at spike resolution.[2], [149], [150]

While polyimide has been shown to produce a lesser immune response than silicon does, it is not rated for long-term implantation. Polyimide substrates are fabricated with excellent thickness control by spin-coating precursor liquid onto the surface of a wafer, or by molding. Polyimide films can be etched slowly using photopatterning and solvent, but are more often patterned into their final shape using laser ablation, oxygen plasma or DRIE. Polyimide films require a final 400 °C baking cure step, which limits their compatibility with organic sensors that generally have a low thermal stress tolerance.[151] Once released, the polyimide substrate, usually between 10 and 50 μm thick, is still very flexible.[152] Because polyimide can be spin-coated to a range of desired thicknesses, it is often selected as a substrate for flexible neural interface devices.[12], [86], [153] Polyimide substrates are too flexible for penetration into the body without an additional "shuttle," a stiff support structure to facilitate implantation that is subsequently withdrawn.

A common soft lithography approach utilizes the photosensitive polymer SU-8 as mold material. SU-8 resist liquid comes in many spin-coating formulations to achieve thickness between 2 and 100 μm with excellent aspect ratio capability from manufacturers such as Microchem.[154], [155] SU-8 substrates can be molded or spin-coated to fabricate flexible structures that are stiff enough to penetrate tissue, such as microneedles, while retaining control of small features.[156] These stiffer structures are an alternative to the structural shuttle needed for softer materials like

polyimide and parylene.[157] However, SU-8 is not rated for long term implantation, and can be prone to breaking at the size needed to perform single neuron recording.

Stretchable

Flexible substrates are able to match the material properties of the surrounding tissue, but further material properties are necessary for interfacing with neurons in dynamic environments such as the spinal cord or peripheral nerves. Materials such as silicone derivatives can be molded and cured to form stretchable substrates (Figure 9H).[4], [86] Minev et al. demonstrated the use of a flexible silicone probe for use in the spinal column that avoids the need for fixation, due to the inherent conformation of the silicone-based material.[106] Silicone can be customized to form a range of elastomers with different properties through different crosslinking mechanisms, conferring a high degree of versatility.[156] PDMS in particular has shown promise as a stretchable substrate.[4], [158], [159] Because stretchable substrates are able to re-form after significant deformation, there are opportunities for interfacing with dynamic surfaces.[160]

2.4.3 Environmentally Dependent Substrates

Soft materials enable significantly longer-term implantation periods, but lack properties needed for ease of implantation and handling. Parylene and polyimide soft probes generally require a shuttle for deep brain access, and are at risk of folding or deforming during insertion, even when used with a support shuttle.[161] As seen with SU-8, there is a desire to forgo softness in order to fabricate a device hard enough to penetrate tissue during implantation.

Substrate materials that leverage the implant environment to dictate the stiffness of the material provide a solution to this problem. Examples of such materials are hydrogel-coated microneedles (Figure 10) [162]–[165] and thermoplastics, or thermally reactive copolymers that are implanted quickly and soften at biological temperatures.[166], [167] In some cases, the structural support

material for extremely thin probes can be used to improve manipulation during implantation, after which the support material dissolves into the water at the implant site. Kim et al. developed a device that utilized a silk support material, and was shown to conform tightly to the curvature of the brain after the support material dissolved.[168] Other dissolvable materials such as chitosan, maltose and PEG have been used as transient support structures that coat the soft device during implantation and subsequently dissolve. Recently, Rauhala et al. demonstrated the capacity to utilize chitosan for in vivo localization of neural interface devices and freestanding, stable, biocompatible films.[169] Use of these substrates opens the door to improved control over the implantation process.

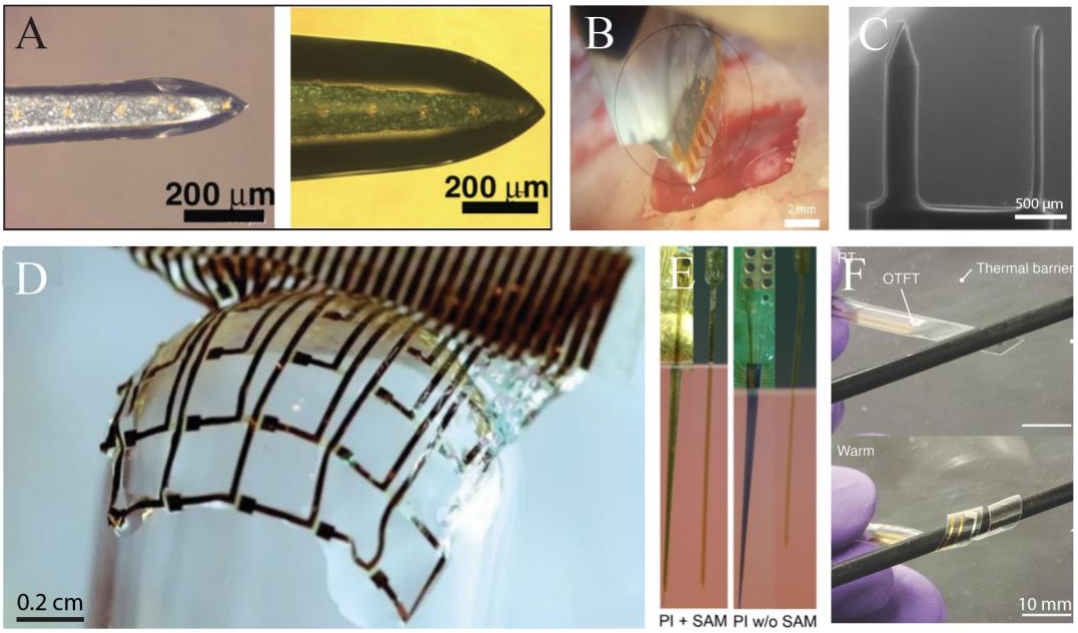

Figure 10: Environmentally dependent substrates have variable properties at different stages of use. A) Soft alginate hydrogel-coated silicon neural probe for improved early-stage integration with native tissue. Reproduced with permission.[162] Copyright 2009, Wiley-VCH. B) Thermally sensitive and water-softening neural probe with near-tissue modulus at room temperature. Reproduced with permission.[167] Copyright 2019, Springer Nature. C) Carboxymethylcellulose (CMC) dissolvable shuttle for insertion of compliant neural probes. Reproduced with permission.[170] Copyright 2014, Elsevier. D) Recording arrays made of ultrathin polyimide with silk support material. Reproduced with permission.[168]Copyright 2010, Springer Nature. E) Self-assembled monolayer (SAM)-coating of insertion shuttles improves flexible probe delamination. Reproduced with permission.[171] Copyright 2009, Elsevier. F) A planar OTFT deploys into a helix and wraps around a rod (r = 2.25 mm). Reproduced with permission.[172] Copyright 2014, Wiley-VCH.

In some cases, probes that require extensive surgery for implantation and healing will later require explant surgeries. The explant surgery puts the subject at risk of infection and necessitates the inconvenience of surgical healing a second time. The use of dissolvable metals such as Mg, Mo, Fe, and Zn—which are naturally found and essential to biological function in humans—was explored by Yin et al. [173] However, extensive studies on a completely dissolvable device have yet to be completed. Similarly, dissolvable biocompatible polymers such as polylactide, poly(ε-caprolactone), poly(polyol citrate) stretchable segmented poly-urethane, polyvinyl alcohol (PVA), poly(lactic-co-glycolic acid)(PLGA), and poly(polyol sebacate) may be used to control the lifetime of the device.[174], [175]

2.4.4 Encapsulation

Early bare electrodes used for single neuron recording were often limited to use over hours or days, due to both size and biocompatibility of material. The stable life of electrodes was extended when materials such as stainless steel, tungsten, and platinum were miniaturized into microwires coated with electrical isolation polymers that enabled recording of durations up to nearly a year in primates.[10] However, electrodes exhibited wide variation and signal quality deteriorated over time, inspiring the first encapsulation for anti-inflammatory isolation.[176] Conducting material used for interconnects and internal components of implants must be electrically isolated outside of recording regions to ensure function. Some metal and silicon electrodes will degrade in ionic solutions, but are still fabricated from these materials for ease of manufacture and high controllability. Beyond basic stability and functionality, electrodes in biological systems must resist fouling and other immune responses to prevent signal variability and degradation over time.[8], [10], [134] Therefore, encapsulation techniques are used to retain the desirable substrate properties, often related to impedance and mechanical strength, while modifying the biological

interface. Essential considerations are implant duration, substrate properties, and final form factor. Effective encapsulation prevents ingress of ions, fluids, and gases, acts as electrical isolation, and limits biological immune responses. In some applications, the encapsulation can also provide mechanical strength or promote integration with surrounding tissue. Recording devices exposed to the biological environment must interact only as necessary to provide long term, stable recordings (Figure 11).

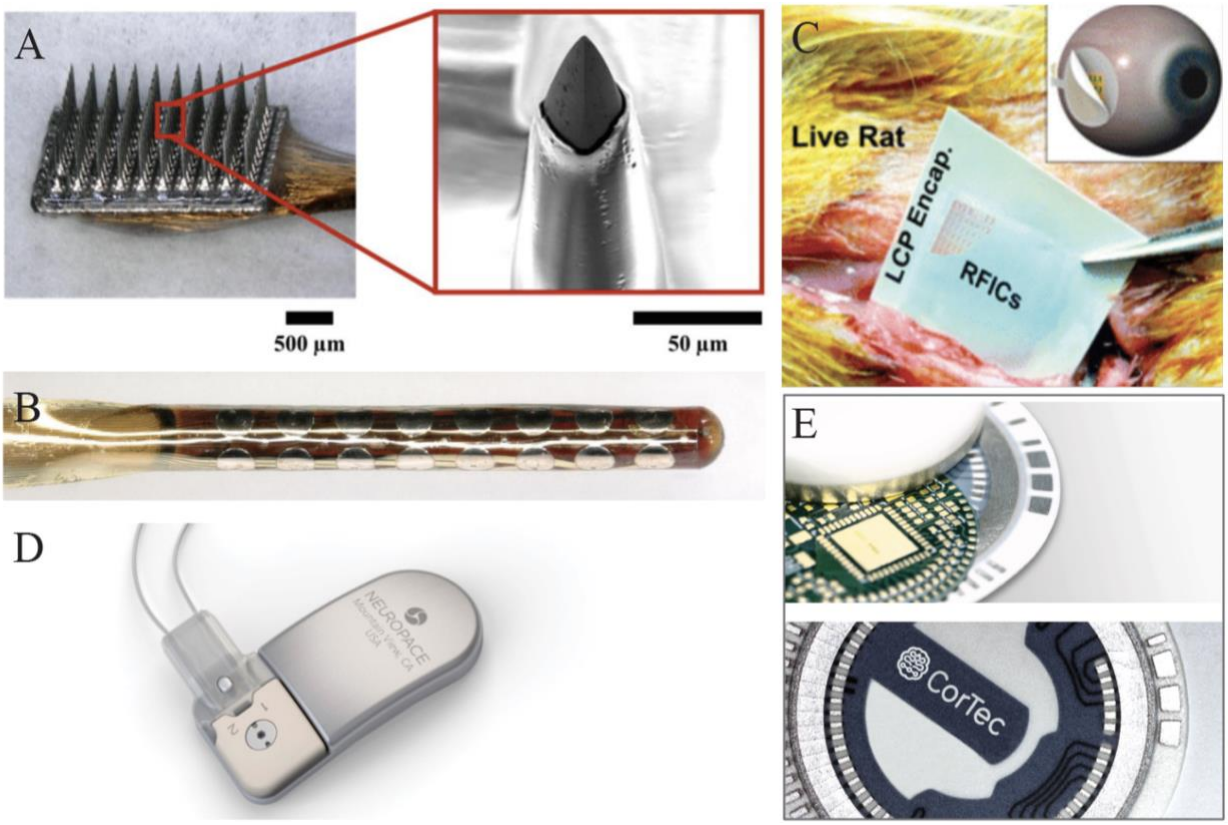

Figure 11: Encapsulation techniques for neural-interface devices. A) Parylene-C coated silicon shafts of Utah array. Reproduced with permission.[177] Copyright 2019, Springer Nature. B) Polyimide-insulated tungsten microwires. Reproduced with permission.[178] Copyright 2018, T. D. Y Kozai. C) Low-water-absorption liquid-crystal polymer (LCP) encapsulated retinal electrode. Reproduced with permission.[179] Copyright 2013, American Chemical Society. D) Metal housing used by NeuroPace, such as FDA approved biocompatible titanium. Such housings are often welded closed for a hermetic seal and further coated with parylene-C as a precautionary measure. Adapted with permission.[180] Copyright 2015, Elsevier. E) Ceramic encapsulation of flame retardant-4 (FR-4)-based printed circuit board (PCB). Feedthroughs are metal tracks on ceramic substrate.

Techniques

Encapsulation techniques include coating, molding, and encapsulation within a housing, sometimes referred to as a "can." Each technique confers unique properties related to the size of the final product, conformability of the coating material and structural support. Coating techniques such as electrospinning, spraying, dipping, chemical vapor deposition (CVD) and physical vapor deposition (PVD) result in a roughly uniform increase in size. This approach is ideal for applications where the size of the implant must be minimized. Metal coatings are often deposited with PVD, while polymers are deposited via spraying, dipping, and CVD techniques.

Molding of electrodes usually involves polymers for their low process temperature, and is generally an irreversible process. Once set, the device is permanently encapsulated. Molding techniques allow for the embedded device to take on new shapes that can involve anchors or teeth for improved fixation. The material used to make the mold must be specially selected to release the encapsulation material after setting.

Devices with complex circuity that may need to be replaced, repaired, or inspected after use take advantage of housing approaches to encapsulation. Housing is made of stiff materials, to protect potentially fragile components within, and is welded to achieve a hermetic seal. Neural interfaces that are completely implanted, such as deep brain stimulation devices, have battery and circuit components encapsulated within a housing. This housing may also act as ground or reference for some sensing devices.

Finally, encapsulation may be part of the fabrication process itself, where a biocompatible polymer is both the substrate and encapsulation of the device. Examples of such an approach include devices with integrated antennas for communication, which may be fabricated monolithically.

Organic Materials

Epoxies were one of the first encapsulation mechanisms for chronically implanted devices (Figure 12A). However, these devices were prone to corrosion and degradation if the epoxy was not completely filled or any air gaps remained in the device. For more modern encapsulation techniques, the encapsulation takes place in a dehydrated, oxygen-free environment (often replaced with nitrogen) before hermetic sealing to limit corrosion of electronics.

Silicone derivatives are a commonly used encapsulation material in commercially available medical devices (Figure 12B, C). Silicone is biocompatible, biostable, straightforward to implement and is approved for use with implanted devices. Silicone in medical applications can be coated and cured at room temperature (common one-component room temperature vulcanizing (RTV) silicones use acetoxy or alkoxy reactions) or dip coated thinly (about 100 μm) and vulcanized with heat to the final state. Thixotropic non-slump silicone is viscous and can be used to selectively coat the device surface. Self-leveling silicone is thin and can be used for potting or molding. However, silicone coatings are not perfectly conformal, tend to be somewhat thick, and may shear under pressure if not vulcanized.

Polyurethane is more expensive than other coating materials and is not rated for permanent implantation as it tends to degrade over several years. However, polyurethane is an extremely versatile polymer in which the ratios of soft backbone and hard diisocyanate components can be adjusted to create elastomers or hard plastics. It can be fabricated using a wide range of techniques including extrusion, dipping, and molding. Polyurethane has unique toughness that can be used to form strong, thin flexible cables.[181] For medical applications, polyurethanes with aromatic diisocyanates are preferred for favorable chemical resistance. The soft backbone component traditionally used in cardiac applications makes the polymer hydrophobic, but can be replaced with

another polymer such as PEG to create a biocompatible nonfouling hydrogel.[182] Polyurethane formulations have also been shown to be compatible with antimicrobial additives such as silver.[183] For neural applications, use of polyurethanes is generally found on metal probes rather than silicon.

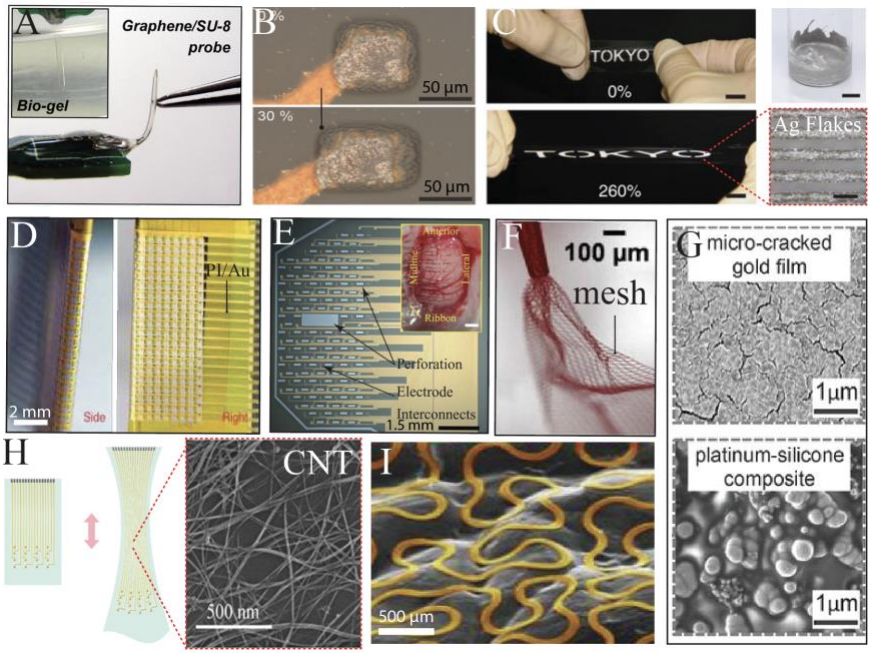

Figure 12: Flexible and stretchable interconnect. A) Flexible SU-8 probe deposited on graphene and insulated with PDMS, where graphene acts as single-signal conductor. SU-8 provides sufficient stiffness to penetrate tissue Reproduced with permission.[184] Copyright 2013, Elsevier. B) Au–TiO nanowires on stretchable PDMS substrate, shown before and after 30% extension. Reproduced with permission.[4] Copyright 2018, Wiley-VCH. C) Use of silver flakes as a conductive filler in elastomeric fluorine copolymer embedded to make conductive ink. Ink is printed onto into stretchable PDMS substrate, and retains conductivity of more than 100 S cm−1 up to 260% stretching. Reproduced with permission.[185] Copyright 2015, Springer Nature. D) Flexible polyimide device with gold conductor traces interconnecting flexible silicon nanomembrane transistors. Cable is robust enough to be folded in half and retain conductivity. Reproduced with permission.[39] Copyright 2011, Springer Nature. E) PEDOT:PSS electrodes on highly conformable ultrathin optically clear parylene substrate improves visualization of electrode placement. Highly conformable properties fix probe to location while perforations tolerated by parylene substrate allow CSF flow. Reproduced with permission.[186] Copyright 2017, AAAS. F) FET nanoprobes integrated into flexible SU-8 substrate result in injectable neural probes. Reproduced with permission.[187] Copyright 2018, Elsevier. G) Stretchable thin film cracked gold interconnects (top) and Pt–silicone stretchable composite as electrode material (bottom). Reproduced with permission.[106] Copyright 2015, AAAS. H) Stretchable PDMS ribbon with transparent carbon nanotube conductors transmitting electrode signal to recording area with electrochemical impedance below 0.4 MΩ in 7.4 pH saline for sensing compatible with optogenetic stimulation. Reproduced with permission.[188] Copyright 2018, American Chemical Society. I) Stretchable gold serpentine shapes over a skin replica material, with SEM image artificially colored to highlight conformal contact over topography. Reproduced with permission.[189] Copyright 2014, Springer Nature.

Polyimide is a biocompatible coating with excellent electrical insulation properties that can be coated as thin as 7 μm (Figure 12D). Polyimide is a common coating material for microwire electrodes, coated everywhere and then ablated in regions to be exposed. However, over time polyimide coatings show wear when exposed to aqueous environments and many formulations are not suitable for chronic implantation. [190][191] Companies such as Tucker-Davis Technologies fabricate probes with polyimide-insulated tungsten arrays.

Liquid crystal polymer (LCP) is a promising material for encapsulation with limited commercial adoption. LCP is a thermoplastic that is typically molded into a final form, such as films for coating or extruded as a coating for wires. Among LCP's favorable properties are extreme resistance to water ingress, biostability, and reliable dielectric properties. The limited adoption of LCP is often due to poor adhesion of LCP to other materials and limited encapsulation techniques, making LCP best for applications where preformed LCP can be used.[179], [192]–[195]

Finally, parylene-C is used in applications where a truly conformal coating is desired (Figure 12E). Parylene is deposited by transferring a dimeric gas directly onto the part to be coated. As parylene is deposited onto the device, thin layers are formed with low pinhole occurrence. This extremely thin layer shows excellent biocompatibility is can be used as a secondary coating after other encapsulation techniques are used.[196] Often even hermetically sealed devices have an additional parylene coating for increased reliability.

Teflon (PTFE) is a polymer that can be deposited with CVD, like parylene. Teflon is extremely nonreactive and can be used as a lubricous or nonfouling surface. Teflon has a hydrophilic surface, and can be used to generally prevent sticking between parts.

Inorganic Materials

Metals and metal oxides have been used to modify substrates in a variety of ways. From small modifications that improve the conductive tissue-device interface to sturdy encapsulation housings, certain metals enhance the device-tissue interface.[132] Metals for housings include titanium, nickel-titanium (nitinol), stainless steel, and cobalt-chrome, which have good strength and wear resistance. Gold, tantalum, and platinum are stable in the body but due to their soft nature are not usually structural elements in a device. However, tantalum can be incorporated into the encapsulation to provide detectability after implantation.

The gold standard for commercial neural devices with circuitry is a titanium can coated with parylene for additional protection. Titanium has a history of exceptional biostability and biocompatibility for chronic implantation. These shells are sealed for hermeticity to prevent moisture from affecting the circuitry inside, and often are filled with inert gas, such as nitrogen, and a desiccant for additional protection from corrosion. Brands like NeuroPace and NeuroVista build closed loop seizure detection systems that are completely implanted in the body. Both devices utilize a titanium can, embedded into the skull or chest tissue, to protect electronics from corrosion.

Glass encapsulation has not been demonstrated with modern neural probes, but has been shown to be possible in other long-term implanted medical devices. CardioMEMS, a blood pressure monitor placed within the pulmonary artery, is encased in glass using anodic bonding of two extremely flat glass surfaces.

Ceramic encapsulation is commercially available through companies such as CorTec, which are able to fabricate many electrode access holes due to superior machinability. Ceramics are ideal for applications where the encapsulation must be electromagnetically transparent, such as for devices

that rely on communication via radiofrequency or infrared, or are powered inductively. Ceramic encapsulation has also been found to outlast standard titanium housing packaging in moisture resistance.

2.5 Interconnects and Connectors Materials

Neural interfaces collect signals on the order of tens to hundreds of microvolts, which must then be amplified and filtered. Interconnects are essential parts of neural interface systems, connecting the signal collected at the electrode to backend signal acquisition, such as preamplifiers or acquisition PCBs. Signals that must traverse the interconnects can be either analog or digital, depending on the probe digitization scheme. In order to maintain the integrity of the electrode location, interconnects should be able to handle the changing relative positions of the electrodes and backend of neural interfaces. In early silicon neural interface devices, wires coated with nonreactive PTFE extended from the electrode to the backend.[134] However, the stiffness of connector wires limited connection of devices to backend electronics that were mounted to a fixed location such as the skull. The inherent mechanical forces and torque on the wire would dislodge probes recording from locations such as the spinal cord and peripheral nervous system, spurring the need for solutions to decouple these mechanical forces.[134] Furthermore, the interconnect scheme is often a bottleneck limiting the miniaturization of devices. As the number of recording sites that can be simultaneously recorded increases, the connector must be able to scale alongside the technology to transmit data to backend processing.

2.5.1 Ribbon

Ribbon cables relieve forces between electrode and backend by bending and warping to accommodate movement (Figure 13). Ribbon cables can be flexible or stretchable, usually with a dielectric insulating substrate containing a conductor able to retain conductive properties when

manipulated. The ribbon is responsible for sending electrical or optical signals over the distance between the recording electrode and backend processing.

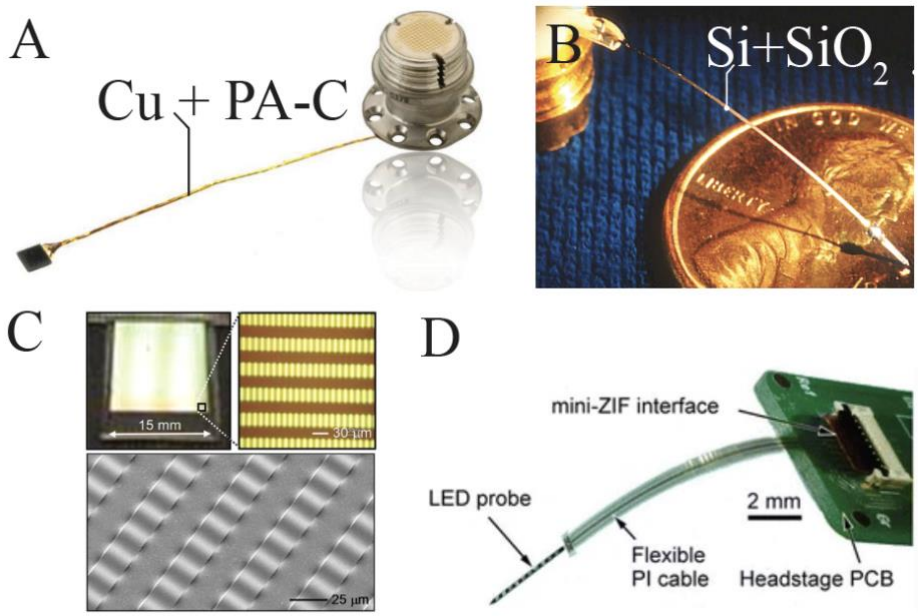

Figure 13: Examples of ribbons used to carry electrode information. A) Bundled Au wire cable with parylene insulation that does not decouple mechanical forces from connector, Reproduced with permission.[197] Copyright 2007, Elsevier. B) Array of wavy, single-crystal silicon ribbons on PDMS (top left); individual ribbons are visible (top right, bottom). Reproduced with permission.[198] Copyright 2006, AAAS. C) Fully integrated flexible polyimide ribbon cable. Reproduced with permission.[199] Copyright 2017, Springer Nature.

Flexible

Flexible ribbon cables can be built on substrates such as polyimide, parylene-C and SU-8. Ribbon cables must be robust enough to maintain integrity when bent, folded, and connected to backend equipment. Polyimide flexible interconnect cables are often integrated directly onto electrode probes, maintaining flexibility over the length of extension to backend, which can be multiple centimeters in length. The high-temperature resistance of polyimide, also known as Kapton, makes it compatible with solder-bond pads.[39], [152], [153], [200], [201] Polyimide cables also have the stiffness necessary to be used with zero insertion force (ZIF) connectors.[202] The higher thickness of polyimide provides sufficient insulation and has low likelihood of forming pinholes,

which may otherwise compromise the integrity of the signal transmission. However, because polyimide is not rated for long term implantation due to high moisture uptake (≈4 wt%),[148] benzocyclobutane has been demonstrated as an alternative by Lee at al. In this device, microfluidic channels were incorporated into the ribbon as well, making the ribbon effective for both electrical communication and fluid transfer. For applications where the environment is more dynamic, parylene-C ribbon cables are flexible and thinner than polyimide. [53], [203] In addition, parylene is rated for long-term implantation, conferring another advantage over polyimide in some situations. Using parylene, Hong et al. developed a large-scale mesh of electrodes.[187] This parylene interconnect scheme was robust enough to be forced into a needle, injected into the brain, and allowed to unfurl. The interconnect allowed signal from many recording sites to be transferred to backend processing while matching the mechanical properties of the tissue through which it traversed. For applications where optically transparent properties are necessary for the interface, the use of ITO was investigated, but was found to be unable to flex due to its brittle nature and limited by high temperature processing. Instead, the use of graphene on SU-8 and PDMS creates a conductive, optically transparent ribbon that is also capable of flexing.[16]

Stretchable

Flexible substrates are excellent for applications where mechanical properties of tissue must be matched, but these substrates generally cannot handle elongation through stretching. Stretchable ribbon cables open the door to neural interfaces in highly dynamic environments such as the spinal cord and peripheral nervous system. Standard thin film deposition, if deposited incorrectly, will delaminate and break when the stretchable substrate material is deformed.[39] However, it has been shown that some gold patterned films deposited on prestretched substrates are able to form forgiving microcracks that maintain conductivity when

stretched (Figure 12G).[147], [159] The use of nanostructures such as gold and silver nanowires can preserve conductivity of 5285 S cm−1 (original conductivity 8130 S cm−1, sheet resistance 0.25 Ω □−1) even after repeated stretching to 1.5 times the original length.[158] However, the resistance of carbon nanotubes (CNTs), gold nanowires (AuNW), silver nanowires (AgNW) and silver nanoparticles (AgNPs) will vary with respect to elongation, warping the recorded signal (Figure 12H,I). [4], [158], [185], [188], [204] Devices utilizing these technologies require characterization of impedance changes for use. Beyond stretchable materials, serpentine ribbon cables can rely on the low impedance properties of conventional metals using a serpentine shape, functioning like a spring to decouple movement. These serpentine shapes can be fabricated at many length scales, including atomic scales as shown by Tang et al. with CNT on PDMS.[205] Combinations of serpentine patterns in complementary positions elicit stretch compatibility with additional degrees of freedom.[189], [206] For applications where it is essential for the ribbon to maintain conductivity but also optical transparency during stretching, it has been shown that CNT on PDMS can be used to monitor neural circuits with both electrical and optical approaches.[188]

2.5.2 Connectors

It is necessary to create connectors that bridge the differences in conductor schemes, substrate properties, physical location, and signal postprocessing technology. Connectors represent the scheme used to transfer neural information from the interconnects to the backend recording system, and dictate the scalability, manufacturability, and integrity of the data transfer over time. Technologic advancements that produced microarrays on the 100 μm scale were able to achieve high recording site density but involved cumbersome wire bonding, bundling, and probe guiding techniques (Figure 14A–D). Hard substrates such as silicon and other MEMS

probes are compatible with fusion, eutectic, anodic, and wire bonding systems. [207]–[209] An alternative to wire bonding, which requires large equipment, is solder ball bonding. This process is heat-activated and allows a connector with well controlled dimensions to be reflowed and connect to the probe electrode.[208] However, softer substrates have limited compatibility with wire bonding equipment, especially as the contact pad sizes have decreased. Anisotropic conductive films and paste have been used to selectively connect flexible substrates with greater ease.[168] Bumps fabricated into the films make it possible to reliably connect films, but thermocompressive equipment is necessary to control the process. With proper pressure and temperature optimization, these films can be extremely reliable connectors for soft electrodes.[210] Recently, Jastrzebska-Perfect et al. introduced an organic mixed-conducting particulate composite material (MCP) that enables facile and effective electronic bonding between soft and rigid electronics (Figure 14E).[211] Ultimately, monolithic connectors in which the flexible ribbon is connected to the device during fabrication, in particular using semiconductor processes, provide the highest manufacturability. This is an extremely scalable process, and can be used to connect hundreds of electrodes in tandem. [88], [138]

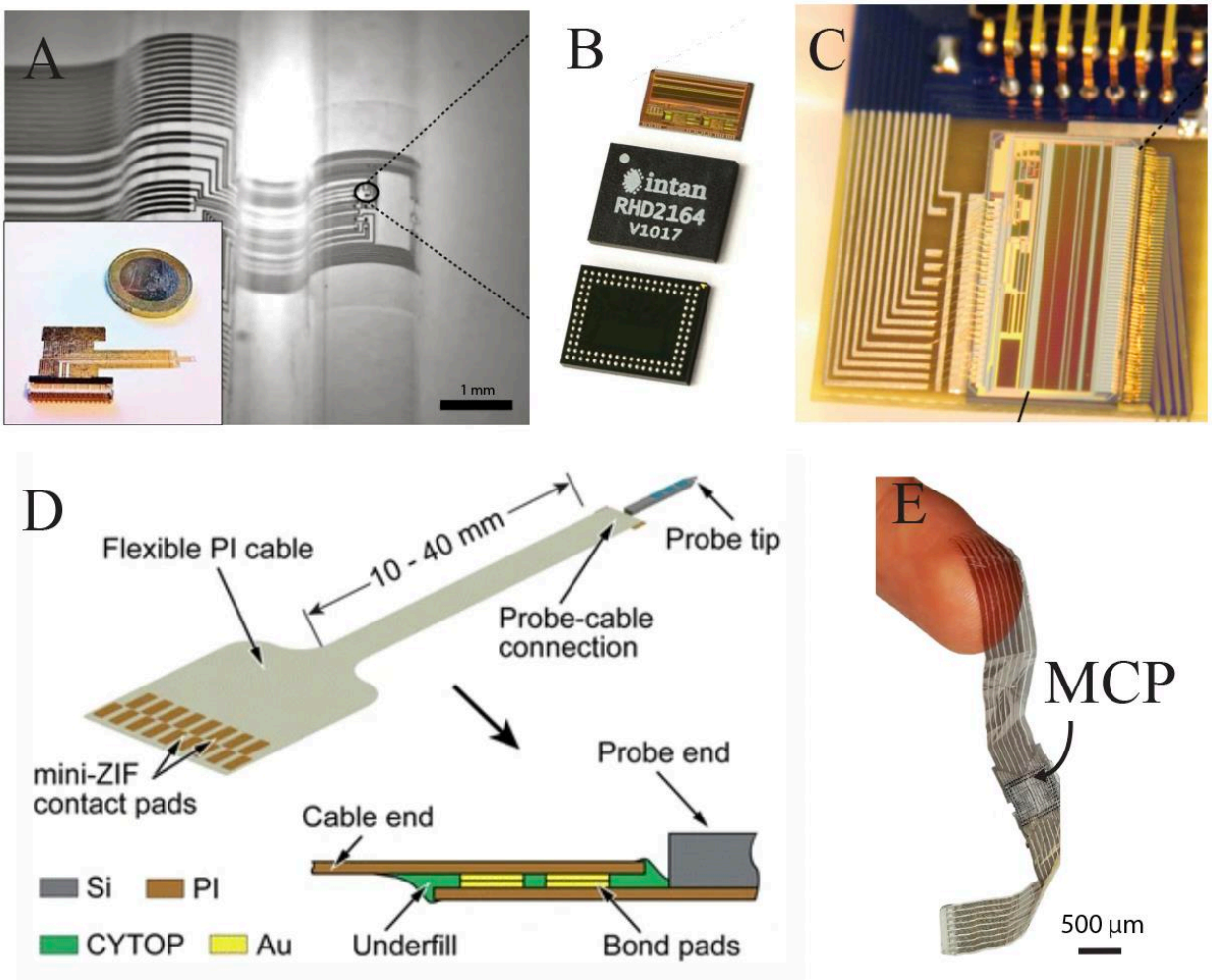

Figure 14: Examples of connectors used in neuroelectronics. A) Conformable probe with zero insertion force (ZIF) connector. Adapted with permission.[92] Copyright 2013, Springer Nature. B) Ball bonding chips (BGA) from Intan used to amplify recorded neural signals can be placed over a contact pad array and reflowed in an oven to robustly connect the chip. Adapted with permission.[260] Copyright 2020, Intan Technologies. C) Device with wire-bonded connectors on resin PCB connecting ZIF housing to backend circuitry. Reproduced with permission.[254] Copyright 2011, PLOS. D) Polyimide (PI) probe flip-chip bonded to PI cable. Probe-cable interface is underfilled with fluoropolymer CYTOP to increase mechanical stability. Reproduced with permission.[253] Copyright 2017, Springer Nature. E) Microscopy images of two conformable arrays bonded together by MCP; arrow indicates the bonding area. Reproduced with permission.[231] Copyright 2020, AAAS.

References

[1] G. Buzsáki, C. A. Anastassiou, and C. Koch, "The origin of extracellular fields and currents-EEG, ECoG, LFP and spikes," *Nat. Rev. Neurosci.*, vol. 13, no. 6, pp. 407–420, 2012, doi: 10.1038/nrn3241.

[2] D. Khodagholy *et al.*, "NeuroGrid: Recording action potentials from the surface of the brain," *Nat. Neurosci.*, vol. 18, no. 2, pp. 310–315, 2015, doi: 10.1038/nn.3905.

[3] A. J. Bard and L. R. Faulkner, *Double-Layer Structure and Adsorption*. 2001.

[4] K. Tybrandt *et al.*, "High-Density Stretchable Electrode Grids for Chronic Neural Recording," *Adv. Mater.*, vol. 30, no. 15, 2018, doi: 10.1002/adma.201706520.

[5] J. J. Jun *et al.*, "Fully integrated silicon probes for high-density recording of neural activity," *Nature*, vol. 551, no. 7679, pp. 232–236, 2017, doi: 10.1038/nature24636.

[6] G. Buzsáki *et al.*, "Tools for probing local circuits: High-density silicon probes combined with optogenetics," *Neuron*, vol. 86, no. 1, pp. 92–105, 2015, doi: 10.1016/j.neuron.2015.01.028.

[7] E. S. Lein *et al.*, "Genome-wide atlas of gene expression in the adult mouse brain," *Nature*, vol. 445, no. 7124, pp. 168–176, 2007, doi: 10.1038/nature05453.

[8] R. Chen, A. Canales, and P. Anikeeva, "Neural recording and modulation technologies," *Nat. Rev. Mater.*, vol. 2, no. 2, pp. 1–16, 2017, doi: 10.1038/natrevmats.2016.93.

[9] S. M. Wellman *et al.*, "A Materials Roadmap to Functional Neural Interface Design," *Adv. Funct. Mater.*, vol. 28, no. 12, pp. 1–38, 2018, doi: 10.1002/adfm.201701269.

[10] M. Jorfi, J. L. Skousen, C. Weder, and J. R. Capadona, "Progress towards biocompatible intracortical microelectrodes for neural interfacing applications," *J. Neural Eng.*, vol. 12, no. 1, 2015, doi: 10.1088/1741-2560/12/1/011001.

[11] R. Fiáth *et al.*, "A silicon-based neural probe with densely-packed low-impedance titanium nitride microelectrodes for ultrahigh-resolution in vivo recordings," *Biosens. Bioelectron.*, vol. 106, no. October 2017, pp. 86–92, 2018, doi: 10.1016/j.bios.2018.01.060.

[12] A. Mercanzini *et al.*, "Demonstration of cortical recording using novel flexible polymer neural probes," *Sensors Actuators A Phys.*, vol. 143, no. 1, pp. 90–96, 2008, doi: https://doi.org/10.1016/j.sna.2007.07.027.

[13] A. A. Fomani and R. R. Mansour, "Fabrication and characterization of the flexible neural microprobes with improved structural design," *Sensors Actuators, A Phys.*, vol. 168, no. 2, pp. 233–241, 2011, doi: 10.1016/j.sna.2011.04.024.

[14] M. R. Abidian, J. M. Corey, D. R. Kipke, and D. C. Martin, "Conducting-Polymer Nanotubes Improve Electrical Properties, Mechanical Adhesion, Neural Attachment, and Neurite Outgrowth of Neural Electrodes," *Small*, vol. 6, no. 3, pp. 421–429, Feb. 2010, doi: 10.1002/smll.200901868.

[15] D. Khodagholy *et al.*, "Highly Conformable Conducting Polymer Electrodes for In Vivo Recordings.," *Adv. Mater.*, pp. 1–5, Aug. 2011, doi: 10.1002/adma.201102378.

[16] D.-W. Park *et al.*, "Graphene-based carbon-layered electrode array technology for neural imaging and optogenetic applications," *Nat. Commun.*, vol. 5, p. 5258, Oct. 2014.

[17] E. Ben-Jacob and Y. Hanein, "Carbon nanotube micro-electrodes for neuronal interfacing," *J. Mater. Chem.*, vol. 18, no. 43, pp. 5181–5186, 2008, doi: 10.1039/B805878B.

[18] P. R. Troyk and S. F. Cogan, "Sensory Neural Prostheses," *Neural Eng.*, pp. 1–48, 2007, doi: 10.1007/0-306-48610-5_1.

[19] N. V. Apollo *et al.*, "Soft, Flexible Freestanding Neural Stimulation and Recording

Electrodes Fabricated from Reduced Graphene Oxide," *Adv. Funct. Mater.*, vol. 25, no. 23, pp. 3551–3559, 2015, doi: 10.1002/adfm.201500110.

[20] L. A. Geddes and R. Roeder, "Criteria for the selection of materials for implanted electrodes," *Ann. Biomed. Eng.*, vol. 31, no. 7, pp. 879–890, 2003, doi: 10.1114/1.1581292.

[21] R. Green and M. R. Abidian, "Conducting Polymers for Neural Prosthetic and Neural Interface Applications," *Adv. Mater.*, vol. 27, no. 46, pp. 7620–7637, 2015, doi: 10.1002/adma.201501810.

[22] M. R. Abidian, K. A. Ludwig, T. C. Marzullo, D. C. Martin, and D. R. Kipke, "Interfacing conducting polymer nanotubes with the central nervous system: chronic neural recording using poly(3,4-ethylenedioxythiophene) nanotubes," *Adv. Mater.*, vol. 21, no. 37, pp. 3764–3770, 2009, doi: 10.1002/adma.200900887.

[23] X. Cui and D. C. Martin, "Electrochemical deposition and characterization of poly-3-4-ethylenedioxythiophene on neural microelectrode arrays," *Sensors and Actuators*, vol. 89, pp. 92–102, 2003.

[24] D. H. Kim, J. A. Wiler, D. J. Anderson, D. R. Kipke, and D. C. Martin, "Conducting polymers on hydrogel-coated neural electrode provide sensitive neural recordings in auditory cortex," *Acta Biomater.*, vol. 6, no. 1, pp. 57–62, 2010, doi: 10.1016/j.actbio.2009.07.034.

[25] D. A. Koutsouras, P. Gkoupidenis, C. Stolz, V. Subramanian, G. G. Malliaras, and D. C. Martin, "Impedance Spectroscopy of Spin-Cast and Electrochemically Deposited PEDOT:PSS Films on Microfabricated Electrodes with Various Areas," *ChemElectroChem*, vol. 4, no. 9, pp. 2321–2327, 2017, doi: 10.1002/celc.201700297.

[26] K. A. Ludwig, J. D. Uram, J. Yang, D. C. Martin, and D. R. Kipke, "Chronic neural recordings using silicon microelectrode arrays electrochemically deposited with a poly(3,4-ethylenedioxythiophene) (PEDOT) film," *J. Neural Eng.*, vol. 3, no. 1, pp. 59–70, 2006, doi: 10.1088/1741-2560/3/1/007.

[27] P. G. Taylor *et al.*, "Orthogonal patterning of PEDOT:PSS for organic electronics using hydrofluoroether solvents," *Adv. Mater.*, vol. 21, no. 22, pp. 2314–2317, 2009, doi: 10.1002/adma.200803291.

[28] A. A. Zakhidov *et al.*, "Orthogonal processing: A new strategy for organic electronics," *Chem. Sci.*, vol. 2, no. 6, pp. 1178–1182, 2011, doi: 10.1039/c0sc00612b.

[29] D. Khodagholy *et al.*, "High speed and high density organic electrochemical transistor arrays," *Appl. Phys. Lett.*, vol. 99, no. 16, pp. 99–102, 2011, doi: 10.1063/1.3652912.

[30] M. Sessolo *et al.*, "Easy-to-fabricate conducting polymer microelectrode arrays," *Adv. Mater.*, vol. 25, no. 15, pp. 2135–2139, 2013, doi: 10.1002/adma.201204322.

[31] D. Kuzum *et al.*, "Transparent and flexible low noise graphene electrodes for simultaneous electrophysiology and neuroimaging," *Nat. Commun.*, vol. 5, no. May, pp. 1–10, 2014, doi: 10.1038/ncomms6259.

[32] C. L. Weaver, J. M. Larosa, X. Luo, and X. T. Cui, "Electrically controlled drug delivery from graphene oxide nanocomposite films," *ACS Nano*, vol. 8, no. 2, pp. 1834–1843, 2014, doi: 10.1021/nn406223e.

[33] K. A. Ng, E. Greenwald, Y. P. Xu, and N. V. Thakor, "Implantable neurotechnologies: a review of integrated circuit neural amplifiers," *Med. Biol. Eng. Comput.*, vol. 54, no. 1, pp. 45–62, 2016, doi: 10.1007/s11517-015-1431-3.

[34] B. C. Raducanu *et al.*, "Time multiplexed active neural probe with 1356 parallel recording sites," *Sensors (Switzerland)*, vol. 17, no. 10, pp. 1–20, 2017, doi: 10.3390/s17102388.

[35] R. H. Olsson, D. L. Buhl, A. M. Sirota, G. Buzsaki, and K. D. Wise, "Band-tunable and multiplexed integrated circuits for simultaneous recording and stimulation with microelectrode arrays," *IEEE Trans. Biomed. Eng.*, vol. 52, no. 7, pp. 1303–1311, 2005, doi: 10.1109/TBME.2005.847540.

[36] R. R. Harrison and C. Charles, "A low-power low-noise CMOS amplifier for neural recording applications," *IEEE J. Solid-State Circuits*, vol. 38, no. 6, pp. 958–965, 2003, doi: 10.1109/JSSC.2003.811979.

[37] R. Harrison *et al.*, "A low-power integrated circuit for a wireless 100-electrode neural recording system," *Dig. Tech. Pap. - IEEE Int. Solid-State Circuits Conf.*, vol. 38, no. 6, pp. 958–965, 2006, doi: 10.1109/isscc.2006.1696288.

[38] J. Cisneros-Fernández, M. Dei, L. Terés, and F. Serra-Graells, "Switch-less frequency-domain multiplexing of GFET sensors and low-power CMOS frontend for 1024-channel µECOG," *Proc. - IEEE Int. Symp. Circuits Syst.*, vol. 2019-May, no. c, pp. 2–6, 2019, doi: 10.1109/ISCAS.2019.8702544.

[39] J. Viventi *et al.*, "Flexible, foldable, actively multiplexed, high-density electrode array for mapping brain activity in vivo," *Nat. Neurosci.*, vol. 14, no. 12, pp. 1599–1605, 2011, doi: 10.1038/nn.2973.

[40] M. Ballini *et al.*, "A 1024-channel CMOS microelectrode array with 26,400 electrodes for recording and stimulation of electrogenic cells in vitro," *IEEE J. Solid-State Circuits*, vol. 49, no. 11, pp. 2705–2719, 2014, doi: 10.1109/JSSC.2014.2359219.

[41] J. D. M. M. Dorman, M.A.Prisbie, "A Monolithic Signal Processor for a Neurophysiological Telemetry System," *IEEE J. Solid-State Circuits*, vol. 20, no. 6, pp. 1185–1193, 1985.

[42] R. C. Kelly *et al.*, "Comparison of recordings from microelectrode arrays and single electrodes in the visual cortex," *J. Neurosci.*, vol. 27, no. 2, pp. 261–264, 2007, doi: 10.1523/JNEUROSCI.4906-06.2007.

[43] H. Fang *et al.*, "Ultrathin, transferred layers of thermally grown silicon dioxide as biofluid barriers for biointegrated flexible electronic systems," *Proc. Natl. Acad. Sci. U. S. A.*, vol. 113, no. 42, pp. 11682–11687, 2016, doi: 10.1073/pnas.1605269113.

[44] H. Fang *et al.*, "Capacitively coupled arrays of multiplexed flexible silicon transistors for long-term cardiac electrophysiology," *Nat. Biomed. Eng.*, vol. 1, no. 3, 2017, doi: 10.1038/s41551-017-0038.

[45] K. Najafi and K. D. Wise, "An Implantable Multielectrode Array with On-Chip Signal Processing," *IEEE J. Solid-State Circuits*, vol. 21, no. 6, pp. 1035–1044, 1986, doi: 10.1109/JSSC.1986.1052646.

[46] A. H. J. Müller, M. Ballini, P. Livi, Y. Chen, A. Shadmani, U. Frey, I. L. Jones, M. Fiscella, M. Radivojevic, D. J. Bakkum, A. Stettler, F. Heer, "CONFERRING FLEXIBILITY AND RECONFIGURABILITY TO A 26 , 400 MICROELECTRODE CMOS ARRAY FOR HIGH THROUGHPUT NEURAL RECORDINGS," 2013, no. June, pp. 744–747.

[47] A. Tsumura, H. Koezuka, and T. Ando, "Macromolecular electronic device: Field-effect transistor with a polythiophene thin film," *Appl. Phys. Lett.*, vol. 49, no. 18, pp. 1210–1212, 1986, doi: 10.1063/1.97417.

[48] T. A. A.Tsumura , H.Koezuka, "Polythiophene field-effect transistor: Its characteristics and operation mechanism," *Synth. Met.*, vol. 1, no. 2, pp. 12–17, 1988.

[49] H. Koezuka and A. Tsumura, "Field-effect transistor utilizing conducting polymers," *Synth. Met.*, vol. 28, no. 1–2, pp. 753–760, 1989, doi: 10.1016/0379-6779(89)90600-0.

[50] L. H. Hess *et al.*, "Graphene transistor arrays for recording action potentials from electrogenic cells," *Adv. Mater.*, vol. 23, no. 43, pp. 5045–5049, 2011, doi: 10.1002/adma.201102990.

[51] C. Hébert *et al.*, "Flexible Graphene Solution-Gated Field-Effect Transistors: Efficient Transducers for Micro-Electrocorticography," *Adv. Funct. Mater.*, vol. 28, no. 12, pp. 1–15, 2018, doi: 10.1002/adfm.201703976.

[52] E. Masvidal-Codina *et al.*, "High-resolution mapping of infraslow cortical brain activity enabled by graphene microtransistors," *Nat. Mater.*, vol. 18, no. 3, pp. 280–288, 2019, doi: 10.1038/s41563-018-0249-4.

[53] D. Khodagholy *et al.*, "In vivo recordings of brain activity using organic transistors," *Nat. Commun.*, vol. 4, 2013, doi: 10.1038/ncomms2573.

[54] D. A. Bernards and G. G. Malliaras, "Steady-state and transient behavior of organic electrochemical transistors," *Adv. Funct. Mater.*, vol. 17, no. 17, pp. 3538–3544, 2007, doi: 10.1002/adfm.200601239.

[55] G. D. Spyropoulos, J. N. Gelinas, and D. Khodagholy, "Internal ion-gated organic electrochemical transistor: A building block for integrated bioelectronics," 2019. [Online]. Available: https://www.science.org

[56] C. Cea, G. D. Spyropoulos, P. Jastrzebska-Perfect, J. J. Ferrero, J. N. Gelinas, and D. Khodagholy, "Enhancement-mode ion-based transistor as a comprehensive interface and real-time processing unit for in vivo electrophysiology," *Nat. Mater.*, vol. 19, no. 6, pp. 679–686, Jun. 2020, doi: 10.1038/s41563-020-0638-3.

[57] W. Lee *et al.*, "Transparent, conformable, active multielectrode array using organic electrochemical transistors," *Proc. Natl. Acad. Sci. U. S. A.*, vol. 114, no. 40, pp. 10554–10559, 2017, doi: 10.1073/pnas.1703886114.

[58] T. Keller and A. Kuhn, "Electrodes for transcutaneous (surface) electrical stimulation," *J. Autom. Control*, vol. 18, no. 2, pp. 35–45, 2008, doi: 10.2298/jac0802035k.

[59] G. D. Spyropoulos *et al.*, "Transcranial Electrical Stimulation and Recording of Brain Activity using Freestanding Plant-Based Conducting Polymer Hydrogel Composites," *Adv. Mater. Technol.*, vol. 5, no. 3, pp. 1–6, 2020, doi: 10.1002/admt.201900652.

[60] R. A. Green, S. Baek, L. A. Poole-Warren, and P. J. Martens, "Conducting polymer-hydrogels for medical electrode applications," *Sci. Technol. Adv. Mater.*, vol. 11, no. 1, 2010, doi: 10.1088/1468-6996/11/1/014107.

[61] Y. Liu *et al.*, "Soft and elastic hydrogel-based microelectronics for localized low-voltage neuromodulation," *Nat. Biomed. Eng.*, vol. 3, no. 1, pp. 58–68, 2019, doi: 10.1038/s41551-018-0335-6.

[62] B. Lu *et al.*, "Pure PEDOT:PSS hydrogels," *Nat. Commun.*, vol. 10, no. 1, 2019, doi: 10.1038/s41467-019-09003-5.

[63] J. Goding, C. Vallejo-Giraldo, O. Syed, and R. Green, "Considerations for hydrogel applications to neural bioelectronics," *J. Mater. Chem. B*, vol. 7, no. 10, pp. 1625–1636, 2019, doi: 10.1039/c8tb02763c.

[64] U. A. Aregueta-Robles, A. J. Woolley, L. A. Poole-Warren, N. H. Lovell, and R. A. Green, "Organic electrode coatings for next-generation neural interfaces," *Front. Neuroeng.*, vol. 7, no. MAY, pp. 1–18, 2014, doi: 10.3389/fneng.2014.00015.

[65] J. Buhlmann, L. Hofmann, P. A. Tass, and C. Hauptmanna, "Modeling of a segmented electrode for desynchronizing deep brain stimulation," *Front. Neuroeng.*, vol. 4, no. NOVEMBER, pp. 1–8, 2011, doi: 10.3389/fneng.2011.00015.

[66] A. Williamson *et al.*, "Localized Neuron Stimulation with Organic Electrochemical Transistors on Delaminating Depth Probes," *Adv. Mater.*, vol. 27, no. 30, pp. 4405–4410, Aug. 2015, doi: 10.1002/adma.201500218.

[67] C. J. Hartmann, S. Fliegen, S. J. Groiss, L. Wojtecki, and A. Schnitzler, "An update on best practice of deep brain stimulation in Parkinson's disease," *Ther. Adv. Neurol. Disord.*, vol. 12, pp. 1–20, 2019, doi: 10.1177/1756286419838096.

[68] X. Liu, M. Zhang, A. G. Richardson, T. H. Lucas, and J. Van Der Spiegel, "Design of a Closed-Loop, Bidirectional Brain Machine Interface System with Energy Efficient Neural Feature Extraction and PID Control," *IEEE Trans. Biomed. Circuits Syst.*, vol. 11, no. 4, pp. 729–742, 2017, doi: 10.1109/TBCAS.2016.2622738.

[69] A. Zhou *et al.*, "A wireless and artefact-free 128-channel neuromodulation device for closed-loop stimulation and recording in non-human primates," *Nat. Biomed. Eng.*, vol. 3, no. 1, pp. 15–26, 2019, doi: 10.1038/s41551-018-0323-x.

[70] J. Park, G. Kim, and S. D. Jung, "A 128-channel FPGA based Real-time Spike-sorting Bidirectional Closed-loop Neural Interface System," *IEEE Trans. Neural Syst. Rehabil. Eng.*, vol. PP, no. 99, p. 1, 2017.

[71] G. Pietro Seu, G. N. Angotzi, F. Boi, L. Raffo, L. Berdondini, and P. Meloni, "Exploiting All Programmable SoCs in Neural Signal Analysis: A Closed-Loop Control for Large-Scale CMOS Multielectrode Arrays," *IEEE Trans. Biomed. Circuits Syst.*, vol. 12, no. 4, pp. 839–850, 2018, doi: 10.1109/TBCAS.2018.2830659.

[72] U. Ziemann, "Transcranial Magnetic Stimulation at the Interface with Other Techniques: A Powerful Tool for Studying the Human Cortex," *Neurosci.*, vol. 17, no. 4, pp. 368–381, Feb. 2011, doi: 10.1177/1073858410390225.

[73] M. Hallett, "Transcranial magnetic stimulation and the human brain," *Nature*, vol. 406, no. 6792, pp. 147–150, 2000, doi: 10.1038/35018000.

[74] Z. De Deng, S. H. Lisanby, and A. V. Peterchev, "Electric field depth-focality tradeoff in transcranial magnetic stimulation: Simulation comparison of 50 coil designs," *Brain Stimul.*, 2013, doi: 10.1016/j.brs.2012.02.005.

[75] M. C. Romero, M. Davare, M. Armendariz, and P. Janssen, "Neural effects of transcranial magnetic stimulation at the single-cell level," *Nat. Commun.*, vol. 10, no. 1, p. 2642, 2019, doi: 10.1038/s41467-019-10638-7.

[76] G. Bonmassar, S. W. Lee, D. K. Freeman, M. Polasek, S. I. Fried, and J. T. Gale, "Microscopic magnetic stimulation of neural tissue," *Nat. Commun.*, vol. 3, no. May, p. 921, Jun. 2012, doi: 10.1038/ncomms1914.

[77] R. Chen, G. Romero, M. G. Christiansen, A. Mohr, and P. Anikeeva, "Wireless magnetothermal deep brain stimulation," *Science (80-.).*, vol. 347, no. March, pp. 6–12, Mar. 2015, doi: 10.1126/science.1261821.

[78] W. Legon *et al.*, "Transcranial focused ultrasound modulates the activity of primary somatosensory cortex in humans," *Nat. Neurosci.*, vol. 17, p. 322, Jan. 2014.

[79] S. Ibsen, A. Tong, C. Schutt, S. Esener, and S. H. Chalasani, "Sonogenetics is a non-invasive approach to activating neurons in Caenorhabditis elegans," *Nat. Commun.*, vol. 6, p. 8264, Sep. 2015.

[80] Xudong Wang, Jinhui Song, Jin Liu, and Zhong Lin Wang, "Direct-current nanogenerator driven by ultrasonic waves," *Science (80-.).*, vol. 316, no. 5821, pp. 102–105, 2007.

[81] A. Marino *et al.*, "Piezoelectric Nanoparticle-Assisted Wireless Neuronal Stimulation," *ACS Nano*, vol. 9, no. 7, pp. 7678–7689, Jul. 2015, doi: 10.1021/acsnano.5b03162.

[82] F. Marquet, Y. S. Tung, T. Teichert, V. P. Ferrera, and E. E. Konofagou, "Noninvasive, transient and selective Blood-Brain barrier opening in Non-Human primates in vivo," *PLoS One*, vol. 6, no. 7, pp. 1–7, 2011, doi: 10.1371/journal.pone.0022598.

[83] J. J. Choi, M. Pernot, S. A. Small, and E. E. Konofagou, "Noninvasive, transcranial and localized opening of the blood-brain barrier using focused ultrasound in mice," *Ultrasound Med. Biol.*, 2007, doi: 10.1016/j.ultrasmedbio.2006.07.018.

[84] K. Deisseroth, "Optogenetics - Method of the Year," *Nat. Methods*, vol. 8, no. 1, pp. 1–4, 2010, doi: 10.1038/NMETH.F.324.

[85] L. He *et al.*, "Near-infrared photoactivatable control of Ca2+ signaling and optogenetic immunomodulation," *Elife*, vol. 4, p. e10024, 2015.

[86] S. Il Park *et al.*, "Soft, stretchable, fully implantable miniaturized optoelectronic systems for wireless optogenetics," *Nat. Biotechnol.*, vol. 33, no. 12, pp. 1280–1286, 2015, doi: 10.1038/nbt.3415.

[87] M. Schwaerzle, K. Seidl, U. T. Schwarz, O. Paul, and P. Ruther, "Ultracompact optrode with integrated laser diode chips and SU-8 waveguides for optogenetic applications," in *2013 IEEE 26th International Conference on Micro Electro Mechanical Systems (MEMS)*, 2013, pp. 1029–1032. doi: 10.1109/MEMSYS.2013.6474424.

[88] F. Wu, E. Stark, P.-C. Ku, K. D. Wise, G. Buzsáki, and E. Yoon, "Monolithically Integrated μLEDs on Silicon Neural Probes for High-Resolution Optogenetic Studies in Behaving Animals," *Neuron*, vol. 88, no. 6, pp. 1136–1148, 2015, doi: https://doi.org/10.1016/j.neuron.2015.10.032.

[89] A. Mohanty *et al.*, "A Reconfigurable Nanophotonics Platform for Sub-Millisecond, Deep Brain Neural Stimulation," *arXiv Prepr. arXiv1805.11663*, 2018.

[90] J. Lee, I. Ozden, Y. K. Song, and A. V. Nurmikko, "Transparent intracortical microprobe array for simultaneous spatiotemporal optical stimulation and multichannel electrical recording," *Nat. Methods*, vol. 12, no. 12, pp. 1157–1162, 2015, doi: 10.1038/nmeth.3620.

[91] K. L. Montgomery *et al.*, "Wirelessly powered, fully internal optogenetics for brain, spinal and peripheral circuits in mice," *Nat. Methods*, vol. 12, no. 10, pp. 969–974, 2015, doi: 10.1038/nmeth.3536.

[92] J. A. Rogers, T. Someya, and Y. Huang, "Materials and mechanics for stretchable electronics," *Science (80-.).*, vol. 327, no. 5973, pp. 1603–1607, Mar. 2010, doi: 10.1126/science.1182383.

[93] H. Zhang, P. Gutruf, and J. A. Rogers, "Flexible Inorganic Light Emitting Diodes Enabled by New Materials and Designs, With Examples of Their Use in Neuroscience Research," *Inorg. Flex. Optoelectron. Mater. Appl.*, pp. 1–39, 2019.

[94] T. Sekitani *et al.*, "Stretchable active-matrix organic light-emitting diode display using printable elastic conductors," *Nat. Mater.*, vol. 8, p. 494, May 2009.

[95] C. Lu *et al.*, "Polymer Fiber Probes Enable Optical Control of Spinal Cord and Muscle Function in Vivo," *Adv. Funct. Mater.*, vol. 24, no. 42, pp. 6594–6600, 2014, doi: 10.1002/adfm.201401266.

[96] Y. Son *et al.*, "In vivo optical modulation of neural signals using monolithically integrated two-dimensional neural probe arrays," *Sci. Rep.*, vol. 5, no. September, pp. 1–11, 2015, doi: 10.1038/srep15466.

[97] M. Jakešová *et al.*, "Optoelectronic control of single cells using organic photocapacitors," *Sci. Adv.*, vol. 5, no. 4, p. eaav5265, Apr. 2019, doi: 10.1126/sciadv.aav5265.

[98] S. Yoo, S. Hong, Y. Choi, J. H. Park, and Y. Nam, "Photothermal inhibition of neural

activity with near-infrared-sensitive nanotransducers," *ACS Nano*, vol. 8, no. 8, pp. 8040–8049, Aug. 2014, doi: 10.1021/nn5020775.

[99] J. L. Carvalho-de-Souza, J. S. Treger, B. Dang, S. B. H. Kent, D. R. Pepperberg, and F. Bezanilla, "Photosensitivity of Neurons Enabled by Cell-Targeted Gold Nanoparticles," *Neuron*, pp. 1–11, 2015, doi: 10.1016/j.neuron.2015.02.033.

[100] K. Lugo, X. Miao, F. Rieke, and L. Y. Lin, "Remote switching of cellular activity and cell signaling using light in conjunction with quantum dots," *Biomed. Opt. Express*, vol. 3, no. 3, pp. 447–454, 2012, doi: 10.1364/BOE.3.000447.

[101] D. Rand *et al.*, "Direct Electrical Neurostimulation with Organic Pigment Photocapacitors," *Adv. Mater.*, vol. 30, no. 25, p. 1707292, Jun. 2018, doi: 10.1002/adma.201707292.

[102] J. Isaksson, P. Kjäll, D. Nilsson, N. D. Robinson, M. Berggren, and A. Richter-Dahlfors, "Electronic control of Ca2+ signalling in neuronal cells using an organic electronic ion pump.," *Nat. Mater.*, vol. 6, no. 9, pp. 673–9, Sep. 2007, doi: 10.1038/nmat1963.

[103] A. Jonsson *et al.*, "Erratum: Bioelectronic neural pixel: Chemical stimulation and electrical sensing at the same site (Proceedings of the National Academy of Sciences of the United States of America (2016) 113: 34 (9440-9445) DOI: 10.1073/pnas.1604231113)," *Proceedings of the National Academy of Sciences of the United States of America*, vol. 113, no. 44. p. E6903, 2016. doi: 10.1073/pnas.1615817113.

[104] R. van den Brand *et al.*, "Restoring Voluntary Control of Locomotion after Paralyzing Spinal Cord Injury," *Science (80-.).*, vol. 336, no. 6085, pp. 1182 LP – 1185, Jun. 2012, doi: 10.1126/science.1217416.

[105] S. Belverud, A. Mogilner, and M. Schulder, "Intrathecal Pumps," *Neurotherapeutics*, vol. 5, no. 1, pp. 114–122, 2008, doi: 10.1016/j.nurt.2007.10.070.

[106] I. R. Minev *et al.*, "Electronic dura mater for long-term multimodal neural interfaces," *Science (80-.).*, vol. 347, no. 6218, pp. 159 LP – 163, Jan. 2015, doi: 10.1126/science.1260318.

[107] B. Rubehn, S. B. E. Wolff, P. Tovote, A. Lüthi, and T. Stieglitz, "A polymer-based neural microimplant for optogenetic applications: design and first in vivo study," *Lab Chip*, vol. 13, no. 4, pp. 579–588, 2013.

[108] J. W. Jeong *et al.*, "Wireless Optofluidic Systems for Programmable In Vivo Pharmacology and Optogenetics," *Cell*, vol. 162, no. 3, pp. 662–674, 2015, doi: 10.1016/j.cell.2015.06.058.

[109] P. Anikeeva, "Optoelectronic fibers interrogate brain function," *SPIE Newsroom*, pp. 2–4, 2015, doi: 10.1117/2.1201510.006102.

[110] M. Asplund, C. Boehler, and T. Stieglitz, "Anti-inflammatory polymer electrodes for glial scar treatment: bringing the conceptual idea to future results ," *Frontiers in Neuroengineering* , vol. 7. p. 9, 2014.

[111] A. Canales *et al.*, "Multifunctional fibers for simultaneous optical, electrical and chemical interrogation of neural circuits in vivo," *Nat. Biotechnol.*, vol. 33, p. 277, Jan. 2015.

[112] T. Khaleeq, H. Hasegawa, M. Samuel, and K. Ashkan, "Fixed-Life or Rechargeable Battery for Deep Brain Stimulation: Which Do Patients Prefer?," *Neuromodulation*, vol. 22, no. 4, pp. 489–492, 2019, doi: 10.1111/ner.12810.

[113] J. D. Couch, A. M. Gilman, and W. K. Doyle, "Long-term Expectations of Vagus Nerve Stimulation: A Look at Battery Replacement and Revision Surgery," *Neurosurgery*, vol. 78, no. 1, pp. 42–46, Aug. 2015, doi: 10.1227/NEU.0000000000000985.

[114] M. Azin, D. J. Guggenmos, S. Barbay, R. J. Nudo, and P. Mohseni, "A battery-powered

activity-dependent intracortical microstimulation IC for brain-machine-brain interface," *IEEE J. Solid-State Circuits*, vol. 46, no. 4, pp. 731–745, 2011, doi: 10.1109/JSSC.2011.2108770.

[115] D. Seo *et al.*, "Wireless Recording in the Peripheral Nervous System with Ultrasonic Neural Dust," *Neuron*, vol. 91, no. 3, pp. 529–539, 2016, doi: 10.1016/j.neuron.2016.06.034.

[116] S. Lee *et al.*, "Development of battery-free neural interface and modulated control of tibialis anterior muscle via common peroneal nerve based on triboelectric nanogenerators (TENGs)," *Nano Energy*, 2017, doi: 10.1016/j.nanoen.2016.12.038.

[117] H. Zhang *et al.*, "Wireless, battery-free optoelectronic systems as subdermal implants for local tissue oximetry," *Sci. Adv.*, vol. 5, no. 3, p. eaaw0873, Mar. 2019, doi: 10.1126/sciadv.aaw0873.

[118] J. S. Ho *et al.*, "Self-tracking energy transfer for neural stimulation in untethered mice," *Phys. Rev. Appl.*, vol. 4, no. 2, pp. 1–6, 2015, doi: 10.1103/PhysRevApplied.4.024001.

[119] D.-H. Kim *et al.*, "Epidermal Electronics," *Science (80-.).*, vol. 333, no. 6044, pp. 838 LP – 843, Aug. 2011, doi: 10.1126/science.1206157.

[120] S. Park *et al.*, "Self-powered ultra-flexible electronics via nano-grating-patterned organic photovoltaics," *Nature*, vol. 561, no. 7724, pp. 516–521, 2018, doi: 10.1038/s41586-018-0536-x.

[121] M. Jakešová *et al.*, "Wireless organic electronic ion pumps driven by photovoltaics," *npj Flex. Electron.*, vol. 3, no. 1, 2019, doi: 10.1038/s41528-019-0060-6.

[122] U. M. Jow and M. Ghovanloo, "Design and optimization of printed spiral coils for efficient inductive power transmission," *Proc. IEEE Int. Conf. Electron. Circuits, Syst.*, vol. 1, no. 3, pp. 70–73, 2007, doi: 10.1109/ICECS.2007.4510933.

[123] A. Wickens *et al.*, "Magnetoelectric materials for miniature, wireless neural stimulation at therapeutic frequencies," *bioRxiv*, p. 461855, Jan. 2018, doi: 10.1101/461855.

[124] K. Scholten and E. Meng, "Materials for microfabricated implantable devices: A review," *Lab on a Chip*, vol. 15, no. 22. Royal Society of Chemistry, pp. 4256–4272, 2015. doi: 10.1039/c5lc00809c.

[125] Z. Zhao *et al.*, "Nanoelectronic Coating Enabled Versatile Multifunctional Neural Probes," *Nano Lett.*, vol. 17, no. 8, pp. 4588–4595, 2017, doi: 10.1021/acs.nanolett.7b00956.

[126] D. Lee *et al.*, " Characterization of Tetrodes Coated with Au Nanoparticles (AuNPs) and PEDOT and Their Application to Thalamic Neural Signal Detection in vivo ," *Exp. Neurobiol.*, vol. 27, no. 6, p. 593, 2018, doi: 10.5607/en.2018.27.6.593.

[127] M. B. Christensen, S. M. Pearce, N. M. Ledbetter, D. J. Warren, G. A. Clark, and P. A. Tresco, "The foreign body response to the Utah Slant Electrode Array in the cat sciatic nerve," *Acta Biomater.*, vol. 10, no. 11, pp. 4650–4660, 2014, doi: 10.1016/j.actbio.2014.07.010.

[128] T. D. Yoshida Kozai *et al.*, "Ultrasmall implantable composite microelectrodes with bioactive surfaces for chronic neural interfaces," *Nat. Mater.*, vol. 11, no. 12, p. 1065, Nov. 2012, doi: 10.1038/nmat3468.

[129] T. Kawano *et al.*, "Electrical interfacing between neurons and electronics via vertically integrated sub-4mu;m-diameter silicon probe arrays fabricated by vapor-liquid-solid growth," *Biosens. Bioelectron.*, vol. 25, no. 7, pp. 1809–1815, 2010, doi: 10.1016/j.bios.2009.12.037.

[130] A. A. Sharp, A. M. Ortega, D. Restrepo, D. Curran-Everett, and K. Gall, "In vivo penetration mechanics and mechanical properties of mouse brain tissue at micrometer

scales," *IEEE Trans. Biomed. Eng.*, vol. 56, no. 1, pp. 45–53, Jan. 2009, doi: 10.1109/TBME.2008.2003261.

[131] A. Prasad *et al.*, "Comprehensive characterization and failure modes of tungsten microwire arrays in chronic neural implants," *J. Neural Eng.*, vol. 9, no. 5, Oct. 2012, doi: 10.1088/1741-2560/9/5/056015.

[132] K. M. Szostak, L. Grand, and T. G. Constandinou, "Neural interfaces for intracortical recording: Requirements, fabrication methods, and characteristics," *Frontiers in Neuroscience*, vol. 11, no. DEC. Frontiers Media S.A., Dec. 2017. doi: 10.3389/fnins.2017.00665.

[133] A. Prasad and J. C. Sanchez, "Quantifying long-term microelectrode array functionality using chronic in vivo impedance testing," *J. Neural Eng.*, vol. 9, no. 2, Apr. 2012, doi: 10.1088/1741-2560/9/2/026028.

[134] J. C. Barrese *et al.*, "Failure mode analysis of silicon-based intracortical microelectrode arrays in non-human primates," *J. Neural Eng.*, vol. 10, no. 6, Dec. 2013, doi: 10.1088/1741-2560/10/6/066014.

[135] D. Prodanov and J. Delbeke, "Mechanical and Biological Interactions of Implants with the Brain and Their Impact on Implant Design.," *Front. Neurosci.*, vol. 10, p. 11, 2016, doi: 10.3389/fnins.2016.00011.

[136] K. D. Wise, "Silicon microsystems for neuroscience and neural prostheses," *IEEE Engineering in Medicine and Biology Magazine*, vol. 24, no. 5. pp. 22–29, Sep. 2005. doi: 10.1109/MEMB.2005.1511497.

[137] G. Buzsáki, "Large-scale recording of neuronal ensembles.," *Nat. Neurosci.*, vol. 7, no. 5, pp. 446–51, May 2004, doi: 10.1038/nn1233.

[138] C. Pang, S. Musallam, Y.-C. Tai, J. W. Burdick, and R. a Andersen, *Novel Monolithic Silicon Probes with Flexible Parylene Cables for Neural Prostheses*, no. May. 2006, pp. 64–67. doi: 10.1109/MMB.2006.251491.

[139] A. Stett, B. Müller, and P. Fromherz, "Two-way silicon-neuron interface by electrical induction," *Phys. Rev. E - Stat. Physics, Plasmas, Fluids, Relat. Interdiscip. Top.*, vol. 55, no. 2, pp. 1779–1782, 1997, doi: 10.1103/PhysRevE.55.1779.

[140] S. T. Retterer *et al.*, "Model neural prostheses with integrated microfluidics: A potential intervention strategy for controlling reactive cell and tissue responses," *IEEE Trans. Biomed. Eng.*, vol. 51, no. 11, pp. 2063–2073, Nov. 2004, doi: 10.1109/TBME.2004.834288.

[141] D. A. Henze, Z. Borhegyi, J. Csicsvari, A. Mamiya, K. D. Harris, and G. Buzsáki, "Intracellular features predicted by extracellular recordings in the hippocampus in vivo," *J. Neurophysiol.*, vol. 84, no. 1, pp. 390–400, 2000, doi: 10.1152/jn.2000.84.1.390.

[142] S. F. Cogan, D. J. Edell, A. A. Guzelian, Y. Ping Liu, and R. Edell, "Plasma-enhanced chemical vapor deposited silicon carbide as an implantable dielectric coating.," *J. Biomed. Mater. Res. A*, vol. 67, no. 3, pp. 856–67, Dec. 2003, doi: 10.1002/jbm.a.10152.

[143] H. Chan, D. M. Aslam, J. A. Wiler, and B. Casey, "A Novel Diamond Microprobe for Neuro-Chemical and -Electrical Recording in Neural Prosthesis," *J. Microelectromechanical Syst.*, vol. 18, no. 3, pp. 511–521, 2009, doi: 10.1109/JMEMS.2009.2015493.

[144] N. F. Nolta, M. B. Christensen, P. D. Crane, J. L. Skousen, and P. A. Tresco, "BBB leakage, astrogliosis, and tissue loss correlate with silicon microelectrode array recording performance.," *Biomaterials*, vol. 53, pp. 753–62, 2015, doi:

10.1016/j.biomaterials.2015.02.081.
[145] T. D. Y. Kozai, J. R. Eles, A. L. Vazquez, and X. T. Cui, "Two-photon imaging of chronically implanted neural electrodes: Sealing methods and new insights," *J. Neurosci. Methods*, vol. 258, pp. 46–55, Jan. 2016, doi: 10.1016/j.jneumeth.2015.10.007.
[146] S. Takeuchi, D. Ziegler, Y. Yoshida, K. Mabuchi, and T. Suzuki, "Parylene flexible neural probes integrated with microfluidic channels.," vol. 5, no. 5, May 2005, doi: 10.1039/b417497f.
[147] S. P. Lacour, J. Jones, S. Wagner, T. Li, and Z. Suo, "Stretchable Interconnects for Elastic Electronic Surfaces," *Proc. IEEE*, vol. 93, no. 8, pp. 1459–1467, 2005, doi: 10.1109/JPROC.2005.851502.
[148] P. Hesketh, H.-S. Noh, K.-S. Moon, A. Cannon, P. J. Hesketh, and C. P. Wong, "Wafer bonding using microwave heating of parylene intermediate layers," *Artic. J. Micromechanics Microengineering*, 2004, doi: 10.1088/0960-1317/14/4/025.
[149] T. D. Y. Kozai *et al.*, "Ultrasmall implantable composite microelectrodes with bioactive surfaces for chronic neural interfaces," *Nat. Mater.*, vol. 11, p. 1065, Nov. 2012.
[150] B. A. Wester, R. H. Lee, and M. C. LaPlaca, "Development and characterization of in vivo flexible electrodes compatible with large tissue displacements.," *J. Neural Eng.*, vol. 6, no. 2, p. 024002, Apr. 2009, doi: 10.1088/1741-2560/6/2/024002.
[151] H. P. Schwan, "ELECTRODE POLARIZATION IMPEDANCE AND MEASUREMENTS IN BIOLOGICAL MATERIALS," *Ann. N. Y. Acad. Sci.*, vol. 148, no. 1, pp. 191–209, 1968, doi: 10.1111/j.1749-6632.1968.tb20349.x.
[152] S. Takeuchi, T. Suzuki, K. Mabuchi, and H. Fujita, "3D flexible multichannel neural probe array," *J. Micromechanics Microengineering*, vol. 14, no. 1, pp. 104–107, 2003, doi: 10.1088/0960-1317/14/1/014.
[153] Y.-Y. Chen *et al.*, "Design and fabrication of a polyimide-based microelectrode array: Application in neural recording and repeatable electrolytic lesion in rat brain," *J. Neurosci. Methods*, vol. 182, no. 1, pp. 6–16, 2009, doi: https://doi.org/10.1016/j.jneumeth.2009.05.010.
[154] E. Kim, J. Y. Kim, and H. Choi, "An SU-8-based microprobe with a nanostructured surface enhances neuronal cell attachment and growth," *Micro and Nano Systems Letters*, vol. 5, no. 1. Society of Micro and Nano Systems, Dec. 2017. doi: 10.1186/s40486-017-0062-x.
[155] B. Tian *et al.*, "Macroporous nanowire nanoelectronic scaffolds for synthetic tissues," *Nat. Mater.*, vol. 11, no. 11, pp. 986–994, 2012, doi: 10.1038/nmat3404.
[156] A. Colas and J. Curtis, "Silicone Biomaterials: History and Chemistry & Medical Applications of Silicones."
[157] M. Tijero *et al.*, "SU-8 microprobe with microelectrodes for monitoring electrical impedance in living tissues," *Biosens. Bioelectron.*, vol. 24, no. 8, pp. 2410–2416, 2009, doi: https://doi.org/10.1016/j.bios.2008.12.019.
[158] F. Xu and Y. Zhu, "Highly Conductive and Stretchable Silver Nanowire Conductors," *Adv. Mater.*, vol. 24, no. 37, pp. 5117–5122, Sep. 2012, doi: 10.1002/adma.201201886.
[159] S. P. Lacour, D. Chan, S. Wagner, T. Li, and Z. Suo, "Mechanisms of reversible stretchability of thin metal films on elastomeric substrates," *Appl. Phys. Lett.*, vol. 88, no. 20, p. 204103, May 2006, doi: 10.1063/1.2201874.
[160] C. Hassler, T. Boretius, and T. Stieglitz, "Polymers for neural implants," *J. Polym. Sci. Part B Polym. Phys.*, vol. 49, no. 1, pp. 18–33, Jan. 2011, doi: 10.1002/polb.22169.
[161] A. Altuna *et al.*, "SU-8-based microneedles forin vitroneural applications," *J.*

Micromechanics Microengineering, vol. 20, no. 6, p. 64014, 2010, doi: 10.1088/0960-1317/20/6/064014.
[162] M. R. Abidian and D. C. Martin, "Multifunctional nanobiomaterials for neural interfaces," *Adv. Funct. Mater.*, vol. 19, no. 4, pp. 573–585, Feb. 2009, doi: 10.1002/adfm.200801473.
[163] A. E. Hess *et al.*, "Development of a stimuli-responsive polymer nanocomposite toward biologically optimized, MEMS-based neural probes," *J. Micromechanics Microengineering*, vol. 21, no. 5, May 2011, doi: 10.1088/0960-1317/21/5/054009.
[164] K. Shanmuganathan, J. R. Capadona, S. J. Rowan, and C. Weder, "Biomimetic mechanically adaptive nanocomposites," *Progress in Polymer Science (Oxford)*, vol. 35, no. 1–2. pp. 212–222, Jan. 2010. doi: 10.1016/j.progpolymsci.2009.10.005.
[165] N. A. Peppas, J. Z. Hilt, A. Khademhosseini, and R. Langer, "Hydrogels in Biology and Medicine: From Molecular Principles to Bionanotechnology**," 2006, doi: 10.1002/adma.200501612.
[166] T. Ware *et al.*, "Fabrication of Responsive, Softening Neural Interfaces," *Adv. Funct. Mater.*, p. n/a-n/a, May 2012, doi: 10.1002/adfm.201200200.
[167] A. Zátonyi *et al.*, "A softening laminar electrode for recording single unit activity from the rat hippocampus," *Sci. Rep.*, vol. 9, no. 1, Dec. 2019, doi: 10.1038/s41598-019-39835-6.
[168] D.-H. Kim *et al.*, "Dissolvable films of silk fibroin for ultrathin conformal bio-integrated electronics.," *Nat. Mater.*, vol. 9, no. 6, pp. 511–7, Jun. 2010, doi: 10.1038/nmat2745.
[169] O. J. Rauhala *et al.*, "Chitosan-Based, Biocompatible, Solution Processable Films for In Vivo Localization of Neural Interface Devices," *Adv. Mater. Technol.*, vol. 5, no. 3, pp. 1–7, 2020, doi: 10.1002/admt.201900663.
[170] T. D. Y. Kozai *et al.*, "Chronic tissue response to carboxymethyl cellulose based dissolvable insertion needle for ultra-small neural probes," *Biomaterials*, vol. 35, no. 34, pp. 9255–9268, 2014, doi: 10.1016/j.biomaterials.2014.07.039.
[171] T. D. Y. Kozai and D. R. Kipke, "Insertion shuttle with carboxyl terminated self-assembled monolayer coatings for implanting flexible polymer neural probes in the brain," *J. Neurosci. Methods*, vol. 184, no. 2, pp. 199–205, 2009, doi: 10.1016/j.jneumeth.2009.08.002.
[172] J. Reeder *et al.*, "Mechanically adaptive organic transistors for implantable electronics," *Adv. Mater.*, vol. 26, no. 29, pp. 4967–4973, 2014, doi: 10.1002/adma.201400420.
[173] L. Yin *et al.*, "Dissolvable metals for transient electronics," *Adv. Funct. Mater.*, vol. 24, no. 5, pp. 645–658, Feb. 2014, doi: 10.1002/adfm.201301847.
[174] E. Bat, Z. Zhang, J. Feijen, D. W. Grijpma, and A. A. Poot, "Biodegradable elastomers for biomedical applications and regenerative medicine part of," *Regen. Med*, vol. 9, no. 3, pp. 385–398, 2014, doi: 10.2217/RME.14.4.
[175] J. Pas *et al.*, "A bilayered PVA/PLGA-bioresorbable shuttle to improve the implantation of flexible neural probes," *J. Neural Eng.*, vol. 15, no. 6, Sep. 2018, doi: 10.1088/1741-2552/aadc1d.
[176] E. M. Schmidt, M. J. Bak, and J. S. McIntosh, "Long-term chronic recording from cortical neurons," *Exp. Neurol.*, vol. 52, no. 3, pp. 496–506, 1976, doi: 10.1016/0014-4886(76)90220-X.
[177] S. N. & F. S. Moritz Leber, Julia Körner, Christopher F. Reiche, Ming Yin, Rajmohan Bhandari, Robert Franklin, "Neural Interface: Frontiers ans Apllications," in *Advances in Penetrating Multichannel Microelectrodes Based on the Utah Array Platform*, vol. 1101, 2019, pp. 207–223. doi: 10.1007/978-981-13-2050-7_8.
[178] T. D. Y. Kozai, "The history and horizons of microscale neural interfaces," *Micromachines*,

vol. 9, no. 9, pp. 1–17, 2018, doi: 10.3390/mi9090445.
[179] G. T. Hwang *et al.*, "In vivo silicon-based flexible radio frequency integrated circuits monolithically encapsulated with biocompatible liquid crystal polymers," *ACS Nano*, vol. 7, no. 5, pp. 4545–4553, May 2013, doi: 10.1021/nn401246y.
[180] B. Lee *et al.*, "A Single-Center Experience with the NeuroPace RNS System: A Review of Techniques and Potential Problems," *World Neurosurg.*, vol. 84, no. 3, pp. 719–726, 2015, doi: 10.1016/j.wneu.2015.04.050.
[181] R. J. Zdrahala and I. J. Zdrahala, "Biomedical Applications of Polyurethanes: A Review of Past Promises, Present Realities, and a Vibrant Future".
[182] L. Rao, H. Zhou, T. Li, C. Li, and Y. Y. Duan, "Polyethylene glycol-containing polyurethane hydrogel coatings for improving the biocompatibility of neural electrodes," *Acta Biomater.*, vol. 8, no. 6, pp. 2233–2242, Jul. 2012, doi: 10.1016/j.actbio.2012.03.001.
[183] N. Roohpour *et al.*, "Development of bacterially resistant polyurethane for coating medical devices," *Biomed. Mater.*, vol. 7, no. 1, 2012, doi: 10.1088/1748-6041/7/1/015007.
[184] C.-H. Chen *et al.*, "A flexible hydrophilic-modified graphene microprobe for neural and cardiac recording," *Nanomedicine Nanotechnology, Biol. Med.*, vol. 9, no. 5, pp. 600–604, 2013, doi: https://doi.org/10.1016/j.nano.2012.12.004.
[185] N. Matsuhisa *et al.*, "Printable elastic conductors with a high conductivity for electronic textile applications," *Nat. Commun.*, vol. 6, p. 7461, Jun. 2015.
[186] D. Khodagholy, J. N. Gelinas, and G. Buzsáki, "Learning-enhanced coupling between ripple oscillations in association cortices and hippocampus," *Science (80-.).*, vol. 372, no. October, pp. 369–372, Oct. 2017.
[187] G. Hong, X. Yang, T. Zhou, and C. M. Lieber, "Mesh electronics: a new paradigm for tissue-like brain probes," *Curr. Opin. Neurobiol.*, vol. 50, pp. 33–41, 2018, doi: https://doi.org/10.1016/j.conb.2017.11.007.
[188] J. Zhang *et al.*, "Stretchable Transparent Electrode Arrays for Simultaneous Electrical and Optical Interrogation of Neural Circuits in Vivo," *Nano Lett.*, vol. 18, no. 5, pp. 2903–2911, May 2018, doi: 10.1021/acs.nanolett.8b00087.
[189] J. A. Fan *et al.*, "Fractal design concepts for stretchable electronics," *Nat. Commun.*, vol. 5, p. 3266, Feb. 2014.
[190] R. DeIasi and J. Russell, "Aqueous degradation of polyimides," *J. Appl. Polym. Sci.*, vol. 15, no. 12, pp. 2965–2974, 1971, doi: 10.1002/app.1971.070151206.
[191] P. Takmakov, K. Ruda, K. Scott Phillips, I. S. Isayeva, V. Krauthamer, and C. G. Welle, "Rapid evaluation of the durability of cortical neural implants using accelerated aging with reactive oxygen species," *J. Neural Eng.*, vol. 12, no. 2, Apr. 2015, doi: 10.1088/1741-2560/12/2/026003.
[192] J. Jeong, S. Hyun Bae, J. M. Seo, H. Chung, and S. June Kim, "Long-term evaluation of a liquid crystal polymer (LCP)-based retinal prosthesis," *J. Neural Eng.*, vol. 13, no. 2, Feb. 2016, doi: 10.1088/1741-2560/13/2/025004.
[193] J. Jeong, K. S. Min, and S. J. Kim, "Microfabrication process for long-term reliable neural electrode arrays using liquid crystal polymer (LCP)," *Microelectron. Eng.*, vol. 216, p. 111096, Aug. 2019, doi: 10.1016/j.mee.2019.111096.
[194] S. W. Lee, F. Fallegger, B. D. F. Casse, and S. I. Fried, "Implantable microcoils for intracortical magnetic stimulation," *Sci. Adv.*, vol. 2, no. 12, Dec. 2016, doi: 10.1126/sciadv.1600889.
[195] C. Jae Lee, S. Jae Oh, J. Keun Song, and S. June Kim, "Neural signal recording using

microelectrode arrays fabricated on liquid crystal polymer material", doi: 10.1016/j.msec.2003.09.143.

[196] J.-M. Hsu, L. Rieth, R. a Normann, P. Tathireddy, and F. Solzbacher, "Encapsulation of an integrated neural interface device with Parylene C.," *IEEE Trans. Biomed. Eng.*, vol. 56, no. 1, pp. 23–9, Jan. 2009, doi: 10.1109/TBME.2008.2002155.

[197] S. Musallam, M. J. Bak, P. R. Troyk, and R. A. Andersen, "A floating metal microelectrode array for chronic implantation," *J. Neurosci. Methods*, vol. 160, no. 1, pp. 122–127, 2007, doi: 10.1016/j.jneumeth.2006.09.005.

[198] D.-Y. Khang, H. Jiang, Y. Huang, and J. A. Rogers, "A Stretchable Form of Single-Crystal," *Science (80-.).*, vol. 311, no. January, pp. 208–212, 2006.

[199] S. Ayub *et al.*, "Hybrid intracerebral probe with integrated bare LED chips for optogenetic studies," *Biomed. Microdevices*, vol. 19, no. 3, pp. 1–12, 2017, doi: 10.1007/s10544-017-0190-3.

[200] Wei Mong Tsang *et al.*, "Flexible Split-Ring Electrode for Insect Flight Biasing Using Multisite Neural Stimulation," *IEEE Trans. Biomed. Eng.*, vol. 57, no. 7, pp. 1757–1764, Jul. 2010, doi: 10.1109/TBME.2010.2041778.

[201] P. J. Rousche, D. S. Pellinen, D. P. Pivin, J. C. Williams, R. J. Vetter, and D. R. Kipke, "Flexible polyimide-based intracortical electrode arrays with bioactive capability.," *IEEE Trans. Biomed. Eng.*, vol. 48, no. 3, pp. 361–71, Mar. 2001, doi: 10.1109/10.914800.

[202] F. Pothof *et al.*, "Chronic neural probe for simultaneous recording of single-unit, multi-unit, and local field potential activity from multiple brain sites Chronic neural probe for recording of SUA, MUA, and LFP activity 2," 2017.

[203] W. Li *et al.*, "Parylene-based integrated wireless single-channel neurostimulator," *Sensors Actuators A Phys.*, vol. 166, no. 2, pp. 193–200, 2011, doi: https://doi.org/10.1016/j.sna.2010.03.003.

[204] M. Park, J. Park, and U. Jeong, "Design of conductive composite elastomers for stretchable electronics," *Nano Today*, vol. 9, no. 2, pp. 244–260, 2014, doi: https://doi.org/10.1016/j.nantod.2014.04.009.

[205] J. Tang *et al.*, "Highly Stretchable Electrodes on Wrinkled Polydimethylsiloxane Substrates," *Sci. Rep.*, vol. 5, Nov. 2015, doi: 10.1038/srep16527.

[206] W. Wu, "Stretchable electronics: functional materials, fabrication strategies and applications," *Science and Technology of Advanced Materials*, vol. 20, no. 1. Taylor and Francis Ltd., pp. 187–224, Jan. 2019. doi: 10.1080/14686996.2018.1549460.

[207] P. Norlin, M. Kindlundh, A. Mouroux, K. Yoshida, and U. G. Hofmann, "A 32-site neural recording probe fabricated by DRIE of SOI substrates," *J. Micromechanics Microengineering*, vol. 12, no. 4, pp. 414–419, 2002, doi: 10.1088/0960-1317/12/4/312.

[208] H. G. Kim *et al.*, "Recent Progress on Microelectrodes in Neural Interfaces," *Materials* , vol. 11, no. 10. 2018. doi: 10.3390/ma11101995.

[209] C. K. Bjune *et al.*, "Package architecture and component design for an implanted neural stimulator with closed loop control," in *Proceedings of the Annual International Conference of the IEEE Engineering in Medicine and Biology Society, EMBS*, Nov. 2015, vol. 2015-Novem, pp. 7825–7830. doi: 10.1109/EMBC.2015.7320206.

[210] Dong-Hyun Baek *et al.*, "Interconnection of Multichannel Polyimide Electrodes Using Anisotropic Conductive Films (ACFs) for Biomedical Applications," *IEEE Trans. Biomed. Eng.*, vol. 58, no. 5, pp. 1466–1473, May 2011, doi: 10.1109/TBME.2010.2102020.

[211] P. Jastrzebska-Perfect *et al.*, "Mixed-conducting particulate composites for soft

electronics," *Sci. Adv.*, vol. 6, no. 17, pp. 1–10, 2020, doi: 10.1126/sciadv.aaz6767.

Chapter 3: Mixed-Conducting Particulate Composites for Soft Electronics

Soft and biocompatible materials constitute an effective solution for interfacing electronic devices with biological tissue[1], [2]. A wide variety of organic materials are inherently flexible, chemically inert, non-toxic, and have tunable physical properties, making them optimal for this function[3], [4]. In addition, conducting and semi-conducting organics can form non-linear electronic components (such as transistors and diodes) capable of biological signal sensing and transduction[5]–[7]. Bioelectronic devices often require advanced signal processing to implement diagnostic and therapeutic operations, from differential amplification and time division multiplexing, to analog to digital conversion and high-speed digital communication[2]. Silicon-based electronics can accomplish each of these functions, with a large repository of pre-existing designs, fabrication processes, and experiential knowledge[8]. These technologies are rigid and incompatible with ion-rich physiologic environments [9], [10]. A device with organic material at the abiotic/biotic interface to perform signal preprocessing, and advanced silicon-based circuits for subsequent signal communication and analysis would combine the beneficial properties of both approaches. However, two substantial challenges hinder realization of such devices: i) lack of stable, high performance, independently addressable organic components for integrated circuits, ii) absence of scalable, biocompatible processes to seamlessly integrate soft, organic materials with rigid silicon-based circuits. Because conducting polymers are mixed (ionic and electronic) conductors[11], [12], they offer the possibility of ion-based modulation of electronic charge carriers within a single material, in contrast to inorganics, where multiple different materials need to be precisely combined to accomplish these operations.

Here, we introduce a novel, soft, biocompatible composite material (MCP) composed of mixed-conducting polymer particles and an electronically insulating, ion-conducting scaffolding polymer matrix. It can be used to create different electronic components based on the size and density of its constituent particles. The physical processes to generate MCP are scalable, solvent-free, and preserve the electrical properties of the conducting polymer. We determined that MCP can form functional anisotropic films, independently addressable transistors, resistors, and diodes. MCP permits anisotropic, high spatiotemporal resolution sensing and transmission, and enabled recording of high-quality neurophysiological data from the surface of the human brain. We also used MCP to directly interface with human skin, and were able to sense spatially localized nerve action potentials non-invasively from a small surface area. Therefore, MCP can form multiple different electronic components, with potential applicability to enhancing safety and efficacy of a wide range of bioelectronic devices.

3.1 Mixed-Conducting Particles (MCP)

We hypothesized that by manipulating the sparsity and size of mixed-conducting particles within a scaffolding polymer matrix that has controllable ionic conductivity, we could create films with various regimes of electronic operation (Figure 1A). This approach would allow a single material to function as multiple different principle electronic components, eliminating the need for several bonded layers of patterned conducting, semiconducting, and insulating materials. The key properties of the mixed-conducting particles are their mean diameter (α) and density (ρ) in solution, which interact to determine the longest electrically conducting length that the particles can form (mean-free-path, λ). The relationship of these parameters with the distance between electrical terminals in both the horizontal (d_1 and d_2) and vertical plane (h) results in five major functional modes of operation:

i) anisotropic conductors: when α and ρ result in a λ that is shorter than the distance between electrical terminals in the horizontal plane (d), the possibility of lateral electric conduction is eliminated because no continuous electrical path can be formed by the particles. If α is also approximately equal to the distance between electrical terminals in the vertical plane (h), selective vertical conduction will occur.

ii) electrochemical transistor: increasing α or ρ to create a λ that is longer than d_1 in the absence of a terminal in the vertical plane generates an electrochemical transistor architecture. Particles bridging d_1 form the transistor channel that can be de/doped by the ionic conducting scaffolding polymer matrix when voltage is applied.

iii) resistor: when λ surpasses d_1 by orders of magnitude, resistive electronic properties will dominate the interaction, and the mixed conducting particles will approach the properties of a conducting polymer.

iv) independently-gated electrochemical transistors: in this case, an additional electrical terminal is added in the horizontal plane at d_2. Increasing α or ρ to create a λ that is longer than d_1 but shorter than d_2 allows for independent gating of the electrochemical transistor. Particles bridging d_1 form the transistor channel, which has ionic interaction with the gate electrode located at d_2 through the scaffolding polymer matrix. In this manner, addressable transistors can be formed without channel patterning.

v) diode: when α is substantially less than d_1, but λ is approximately equal to d_1, a diode is created. Particle chains that are in contact with both electrical terminals and span d_1 (bridging particle chains) will permit electronic conduction to occur between the terminals. However, the particle chains that are in contact with just one terminal and omnidirectionally distributed within the scaffolding polymer matrix will act as a conducting polymer gate terminal and can de/dope the

bridging particle chains through inducing ionic current in the matrix. These interactions result in a nonlinear relationship between applied voltage and conduction.

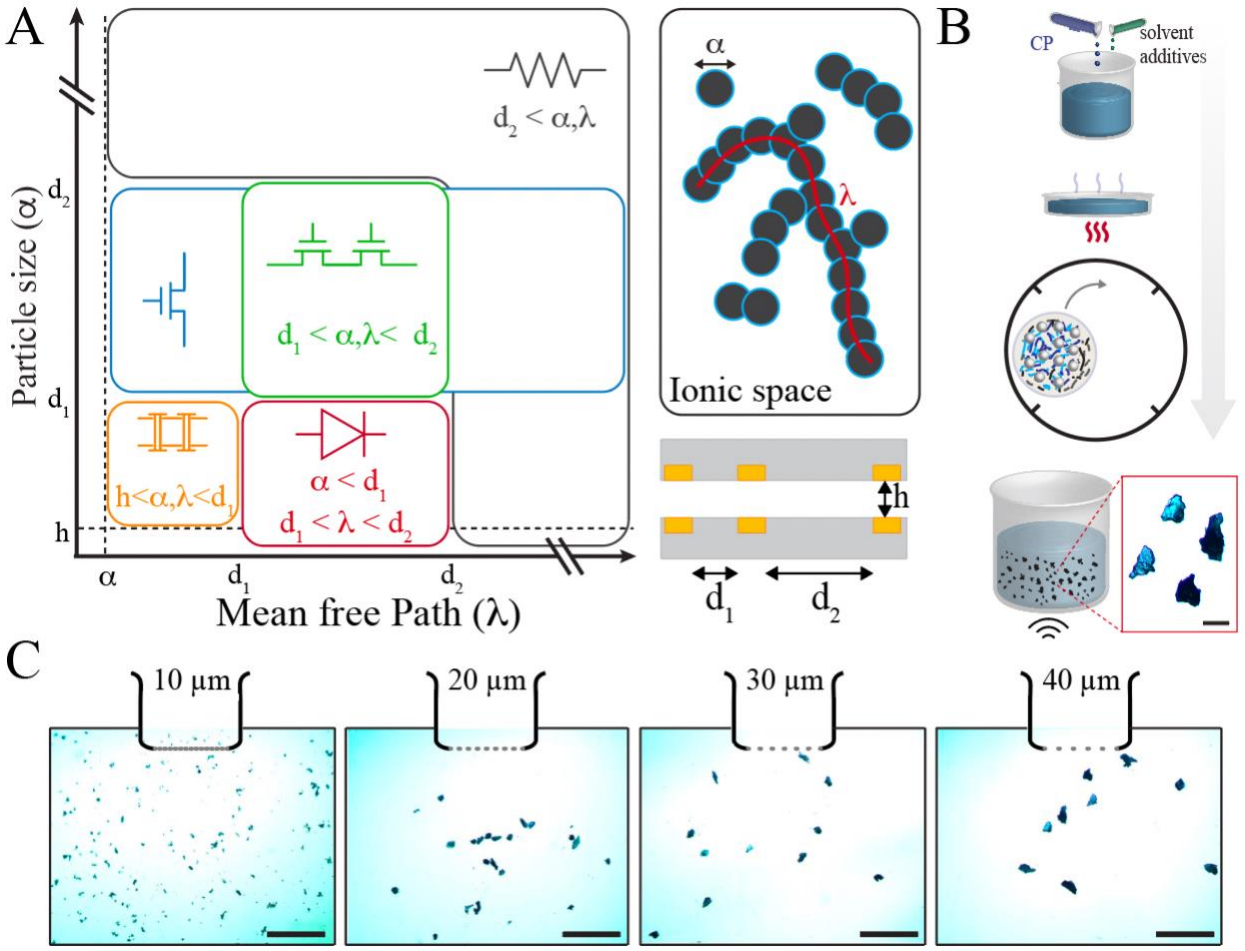

Figure 1: IC enables fully implantable, noninvasive, ultralow power, stable, and high-speed communication for implantable devices. A) Power consumption of IC as a function of data rate and TX electrode impedance (1, 10, and 100 kilohms dark to light). The shaded areas highlight the required data communication bandwidth for using the denoted neural interface devices. B) Efficiency of implantable communication systems derived as the ratio of bandwidth to power consumption for RF waves, mechanical waves (ME), and IC. C) Simplified schematic of the placement and location of the implant in a rat (top left). Complete embedded system with conformable probe and battery before implantation (right; black scale bar, 5 mm; white scale bar, 50 µm). Location of incision for positioning IC electrode 1 week after surgery (bottom left). RX is aligned transcutaneously via the fiducial magnet of the implanted TX array.

To test this hypothesis, we developed particulate mixed-conducting composites that permitted investigation of all theorized functional regimes. We first prepared a highly conducting dispersion of the conducting polymer poly(3,4-ethylenedioxythiophene)-poly(styrenesulfonate)

(PEDOT:PSS) [13], [14], including additives and crosslinkers to maximize conductivity and stability (see Methods). This dispersion was evaporated over a large surface area to create dried, highly conductive PEDOT:PSS sheets with < 50 μm thickness. The films were cut into small pieces, weighed, and mixed with milling medium in a ball-mill machine. The resulting particles were further broken-down using sonication and sieved into solutions with well-defined particle sizes (Figure 1B-C). Next, we used chitosan (CS)-based polymers to create an ion-conducting scaffolding polymer matrix. CS is optimal for this purpose because its ion conductivity (water-uptake) and adhesiveness can be tuned [15]–[17]. Combining the mixed-conducting particles with the scaffolding polymer matrix generated the particulate mixed conducting composites (MCP).

We found that the composite provided reliable, flexible mechanical bonding between conformable substrates due to the bio-adhesive properties of chitosan (Figure 2A). The distinct color contrast between mixed-conducting particles (dark blue) and the scaffolding polymer matrix (light yellow) enabled direct optical imaging, though the auto fluorescence of CS can also be leveraged for visualization (Figure 2B). To investigate the homogeneity of the particle distribution, we evaluated composites with a low and high density (ρ) of mixed-conducting particles. Optical analysis of same-sized areas blade-coated with each composite revealed that the majority of the pixels in the low-density composite reflected an absence of particles, while the distribution of pixel intensity of the high-density composite was shifted to the left (darker), indicating the presence of numerous particles. These results suggest that increasing the density of particles yields a homogeneous composite that is uniformly darker when visualized, with consistent film thickness across multiple samples. If particles instead tended to coagulate into focal areas, a multi-peaked distribution would occur as particle density was increased (Figure 2C). Using similar optical methods, we found that

the sieving process was highly selective, creating particles ranging from 10 – 40 µm with a narrow size distribution (Figure 2D).

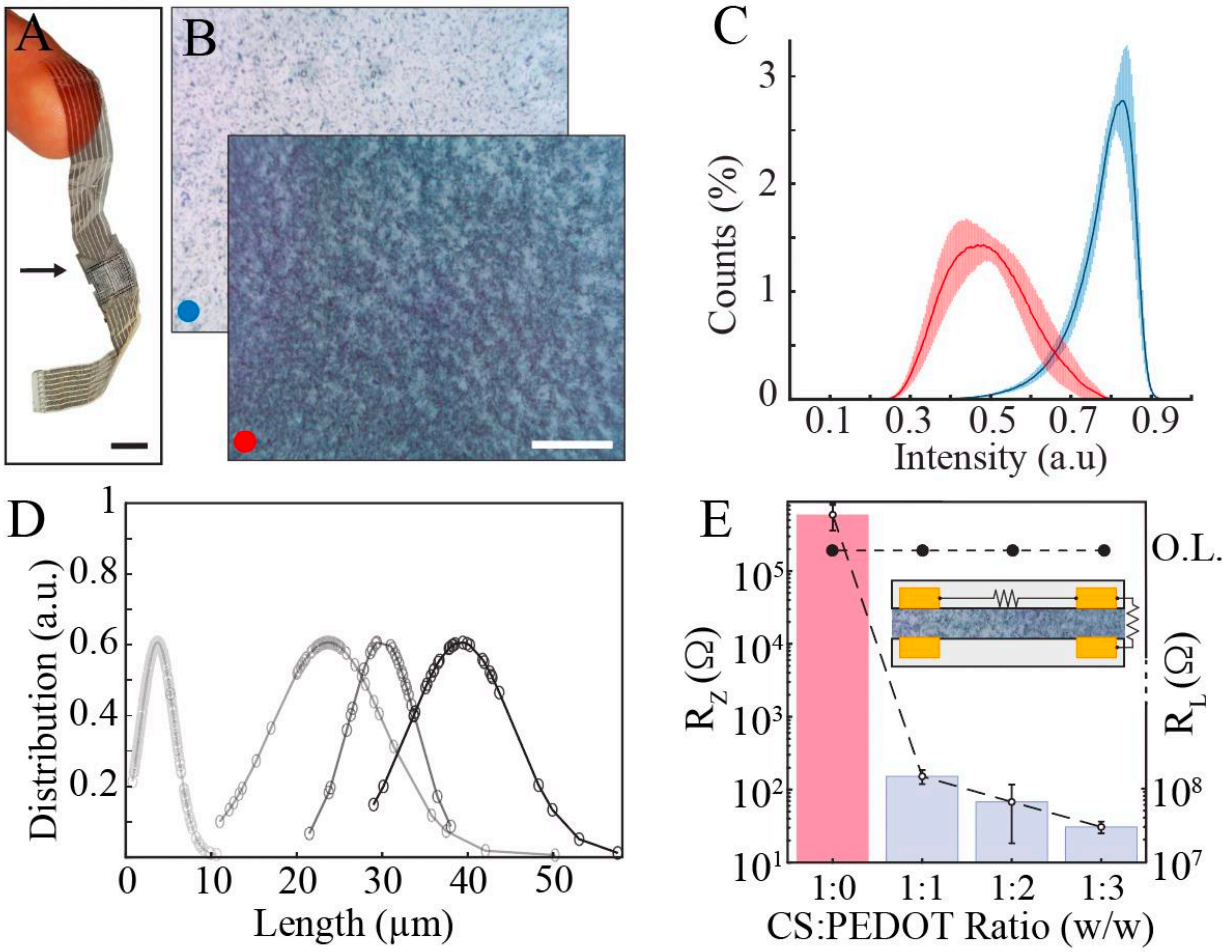

Figure 2: MCP forms uniform films with controllable particle size and conductivity. (A) Micrograph of two conformable arrays bonded together by MCP; arrow indicates the bonding area. Scale bar, 500 µm. Photo credit: Patricia Jastrzebska-Perfect, Columbia University. (B) Optical micrographs of blade-coated MCP films. Concentration [% (w/v)] of conducting polymer particles in nonconducting medium of CS, sorbitol, and glycerol is 6.1 (blue dot) or 18 (red dot). Distinct particles are visible in the nonconducting matrix (top right). Scale bar, 100 µm. (C) Pixel intensity distribution (where black = 0) of MCP; concentration [% (w/v)] of PEDOT:PSS particles in blade-coated solution is 6.1 (blue) or 18 (red). Data are represented as mean darkness (n = 6) ± SEM. Note that a higher concentration of particles produces a darker and wider distribution of pixel intensity. a.u., arbitrary units. (D) Optically measured distributions conducting polymer particle size in MCP (from left to right, using 1 and 10 µm, 10 and 20 µm, 20 and 30 µm, and 30 and 40 µm sieves). (E) Vertical (left axis, open circles) resistance of MCP is proportional to conducting polymer particle density in CS (particle size = 40 µm). Inset shows measurement configuration of vertical and horizontal resistances. O.L., overload.

To characterize the conductivity of the MCPs, we prepared composites with various particle densities, including one without particles (control). These composites were sandwiched between two substrates that consisted of multiple horizontally spaced, vertically aligned strips of Au (1 mm wide and 100 μm spacing, 100 nm thick; Figure 2E, inset). The MCPs exhibited < 100 Ω electrical contact resistance between the aligned Au strips. This vertical resistance (R_Z) was proportional to particle density, whereas resistance between horizontally spaced Au strips remained high ($R_L > 10^{10}$ Ω) (Figure 2E). These features suggest that the particles remain homogenously distributed within the MCP when sandwiched between the substrates, without focal coagulation that would cause increased horizontal conduction. Thus, the physical processes used to prepare the MCP offers several key advantages: (i) highly controllable generation of particles with specific size and density, (ii) homogeneous distribution of particles within the composite, even after lamination, (iii) preservation of electrical properties of the conducting polymer, (iv) ability to include additives that enhance electrical performance of the composite, (v) solvent-free synthesis, enhancing compatibility with organic materials, and (vi) scalability for a variety of production volumes [18]. We next tested the ability of MCP to perform the operations described in Figure 1. Firstly, we examined whether MCP had sufficient anisotropy to form high-density vertical interconnects between electronic components without patterning. We fabricated Au-based electronic pads on rigid (SiO_2) and conformable (parylene-C) substrates with geometrically varying inter-electrode spacing. The MCP was deposited onto the bottom substrate using typical solution processible techniques (spin coating and blade coating) and then covered by the top substrate. Because CS is intrinsically adhesive, MCP established strong mechanical bonds between layers of both rigid and conformable substrates, without requiring elevated temperatures (maximum 70°C) or application of pressure. Anisotropy of the interface (A) was determined by calculating the ratio of the

horizontal (R_L) and vertical (R_Z) resistances between the pads ($A=R_L / R_Z$, Figure 3A). Ensuring that the MCP used had a smaller λ than the electrode pitch, we were able to achieve anisotropy values as high as 10^{10} at 50 μm resolution (Figure 3B). These anisotropy values were consistent for more than 100 days, highlighting the stability of MCP's electrical and mechanical bonding.

Next, we made MCP-based independently-gated electrochemical transistors by blade-coating MCP onto three Au-based pads (Figure 3C). This configuration functioned as a depletion-mode, high-transconductance, individually addressable organic electrochemical transistor. Application of positive gate voltage to the Au pads directed cations of the ion-conducting scaffolding polymer matrix into the bridging mixed-conducting particles of the channel, resulting in de-doping. The electrical characteristics of the transistor were comparable to those generated by PEDOT:PSS dispersion (Figure 3D) [14], [19], [20]. We utilized the independent gating of these devices to create logic circuits with series and parallel connectivity between transistor terminals (such as a NOR gate; Figure 3E) and found that MCP-based transistors performed the appropriate digital logic (Figure 3F) over extended time periods in physiological conditions [21]–[24]. Therefore, MCP can be used to produce independent transistors that maintain the properties of their constituent conducting polymer without requiring any channel patterning.

Lastly, we explored the ability of the MCP to operate as a diode. We coated MCP with appropriate α and ρ onto two Au-based pads and applied voltage between the terminals (Figure 3G). This arrangement created particle chains that contacted both terminals ("bridging particle chains") and particle chains that contacted one terminal with their free ends omnidirectionally distributed in the ion conducting scaffolding polymer matrix ("omnidirectional particle chains"). The application of voltage to the terminals resulted in both (i) electronic current through the bridging particle chains, and (ii) ionic current in the scaffolding polymer matrix in the region between the omnidirectional

particle chains and bridging particle chains. When negative voltage was applied, the omnidirectional chains at the opposite terminal were at positive potentials. The ionic current caused cations of the matrix to de-dope the bridging particle chains and lower the charge carrier density. Conversely, when omnidirectional chains were at negative potentials, the bridging particles chains were maximally doped and unaffected by the ionic current within the matrix. Together, these interactions generated the non-linear voltage-current relationship characteristic of a diode (Figure 3H). This working mechanism is akin to a diode-connected transistor [25].

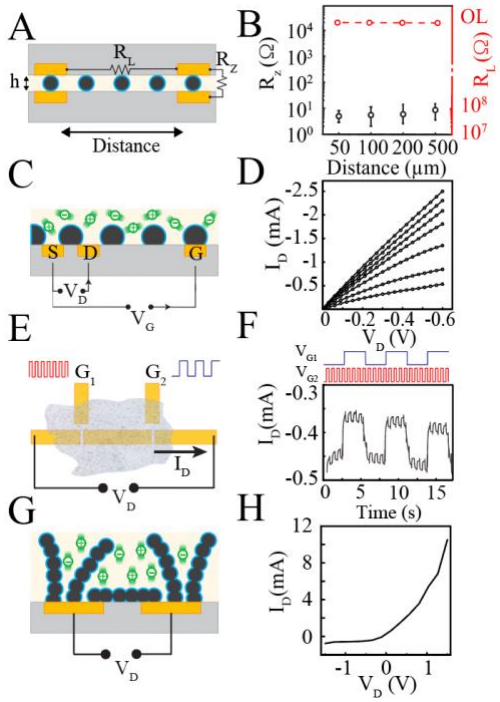

Figure 3: MCP creates high-performance anisotropic films, independently addressable transistors, and diodes by varying conducting polymer particle size and density. A) MCP operating as an anisotropic conductive film. λ is smaller than electrode spacing. Scaffolding polymer matrix (light yellow), conducting polymer particles (dark blue), Au contacts (gold), and substrate (gray) are visible. B) Adjacent MCP-bonded electrodes have consistently low vertical resistance (left axis) and high horizontal resistance (right axis) across a wide range of horizontal electrode pitch. C) MCP operating as an independently gated transistor. λ is longer than d1 but shorter than d2. Mobile ions (green), and Au contacts forming the source (S), drain (D), and gate (G) are visible. D) Output characteristics of MCP-based transistor operating in depletion mode (L = 250 μm, W = 5 mm, particle size = 30 μm), with VG varying from 0 to 0.6 V, in increments of 0.1 V (top to bottom). E) NOR gate generated using un-patterned MCP-based transistors. Input signals are applied at gates 1 and 2 (G1 and G2, respectively). F) Temporal response of MCP-based NOR gate (L = 100 μm, W = 500 μm, particle size = 30 μm) with gate pulse amplitudes of 0.5 V. G) MCP operating as a diode. α is substantially less than d1, but λ is approximately equal to d1. H) Output characteristic of MCP-based diode [same dimensions as (D), particle size = 10 μm].

3.2 MCP as Anisotropic Interface for Electrophysiologic Signal Acquisition

We created devices that harnessed the anisotropic properties of MCP to address challenges in physiological signal transmission and biopotential sensing. High spatiotemporal resolution conformable probes are increasingly being used to acquire signals from biological tissues, and similar resolution rigid electronics exist to process these signals. However, current techniques to enable transmission of signals between the soft probe and hard electronics (thermal bonding or sonic metal-metal bonding, metal/epoxy composite pastes) are neither biocompatible nor scalable, and introduce additional rigidity and bulk to the device. We hypothesized that the characteristics of MCP would enable high spatiotemporal resolution, biocompatible multi-channel electrical contact between soft and hard electronic device components with a facile fabrication process that is adaptable to a wide range of materials. We fabricated conformable (parylene-C) and flexible (polyethylene naphthalate, PEN) high-density neural interface devices for integration with flexible (polyethylene terephthalate, PET) and rigid (flame retardant glass epoxy, FR4) neural acquisition electronic circuits. MCP was applied to the back-end (where the interconnects transform into contact pads) of the probe using a blade-coater. MCP formed an adhesive film (through evaporation of excess water) within 120 s at room temperature. We then aligned the mating board (a geometrically matched board containing hard electronics) and established mechanical contact using a manual cotton-based roller with negligible application of pressure (0.15 N). We found that MCP was able to establish a reliable electrical interface between all combinations of conformable, flexible, and rigid neural probes and acquisition electronics (Figure 4A), permitting higher density connectivity compared to traditional connector or bonding processes [26], [27]. To validate the functionality of these MCP-bonded devices, we used them to acquire high spatiotemporal resolution electrophysiological signals in various experimental conditions. MCP-bonded surface

electrocorticography (ECoG) arrays (NeuroGrid [26]; 128 channels) and penetrating probes (32 channels) were implanted chronically into freely moving rodents. NeuroGrid recordings demonstrated spatially localized high gamma oscillations[28], [29] (Figure 4B-C), confirming the absence of crosstalk between adjacent channels. Insertion of penetrating probes into the dorsal CA1 of the hippocampus allowed high fidelity acquisition of characteristic high frequency hippocampal oscillations[30], [31] (Figure 4D; ripples, 100-250 Hz) and individual neuronal action potentials (Figure 4D inset). Taken together, these results demonstrate that MCP bonding can be used to create scalable, multi-channel neural interface devices that are capable of acquiring signals at the spatiotemporal resolution of individual neurons.

We also leveraged the biocompatibility of MCP to generate neural interface devices for intra-operative neural recording in human patients undergoing implantation of deep brain stimulation (DBS) electrodes. During a DBS procedure, clinical electrodes are inserted through a burr hole (14 mm diameter) to reach the appropriate subcortical target [32], [33]. We recorded from the exposed cortex with our MCP-bonded device during the surgical procedure. In order to record from the small exposed cortical area, the probe and amplifier components must be miniaturized and flexible, precluding use of conventional surface ECoG arrays. We demonstrated that MCP-bonded NeuroGrids could be placed within the burr hole (Figure 4E) and acquired spatially resolved, high signal-to-noise-ratio (SNR) neurophysiological data in the intra-operative environment. These data revealed characteristic signals associated with transition from anesthesia to waking, as well as localized epochs of gamma oscillations (Figure 4F-G). Thus, MCP-bonded neural interface devices can be safely and effectively translated to use in human subjects.

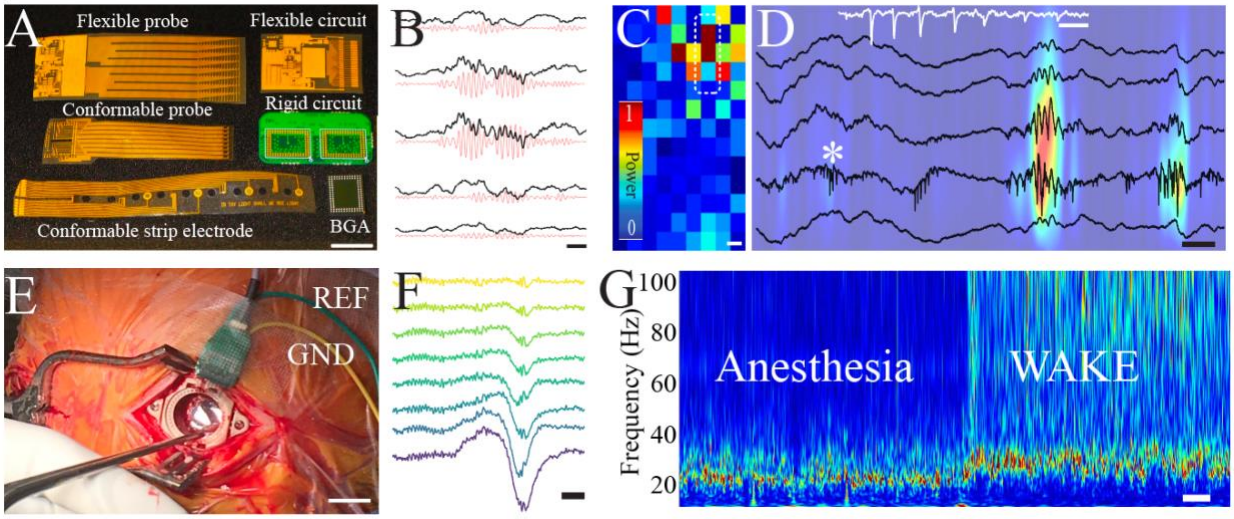

Figure 4: MCP creates an anisotropic interface for high–spatiotemporal resolution electrophysiologic signal transmission. A) Photograph of conformable, flexible, and rigid neural probes with electronic circuits that can be bonded together using MCP to acquire neurophysiological signals in vivo. Scale bar, 5 mm. BGA, ball grid array. Photo credit: Dion Khodagholy, Columbia University. B) High gamma oscillations are differentiable across electrodes of an MCP-bonded array placed on cortical surface of a freely moving rat [unfiltered local field potential (LFP) traces (black) and corresponding filtered traces (red, 60 to 100 Hz)]. Scale bar, 40 ms. C) Trigger-averaged gamma band power is spatially confined across array placed on cortical surface of a freely moving rat. Scale bar, 1 mm. The white dashed rectangle indicates the electrodes that generated the traces in (B). D) MCP-bonded flexible probe inserted into rat hippocampus permits recording of characteristic ripple oscillations in dorsal CA1 [sample wide-band traces (black, 0.1 to 20 kHz) superimposed on a heat map highlighting the instantaneous power in the ripple band (100 to 150 Hz); scale bar, 50 ms] as well as individual action potential waveforms (burst firing of putative pyramidal cell, white trace, zoomed in from location denoted by white star, 0.1 to 20 kHz; scale bar, 5 ms). Color bar same as (C). E) Intraoperative photograph showing conformable MCP-bonded neural probe on the surface of human cortex with associated amplifier circuits. Scale bar, 10 mm. Photo credit: Dion Khodagholy, Columbia University. REF, reference; GND, ground. F) Sample wide-band LFP (0.1 to 1250 Hz) acquired during intraoperative human recording demonstrating spatially diverse activity patterns acquired by MCP-bonded neural probe. Scale bar, 100 ms. G) Spectrogram of neural data acquired by MCP-bonded neural probe revealing transition from anesthetized to awake state intraoperatively. Scale bar, 10 s. Color bar same as (C).

Next, we investigated MCP for direct biopotential sensing. Because MCP is biocompatible, with tunable electronic and ionic properties and a versatile fabrication process, we hypothesized that it could effectively interface directly with the human body and enable high spatiotemporal resolution, mechanically stable sensing (Figure 5A, left). The bonding strength and electrochemical impedance of the MCP interface with tissue was enhanced by D-sorbitol, a biocompatible sugar alcohol, within the composite. The D-sorbitol facilitates uptake and

maintenance of water within the matrix [21], [34]. Conventional electrodes designed to acquire electrophysiologic signals from the skin typically rely on ionic gels to form an appropriate impedance interface with the skin. These gels are not amenable to patterning and their spread across the skin surface is difficult to control, limiting the spatial resolution of activity that can be acquired non-invasively. When higher resolution signals are required, such as with clinical electromyography (EMG), needle electrodes are inserted through the skin. Au-based electrodes coated with a layer of MCP (200 μm diameter) were placed over the biceps muscle and wrist of healthy volunteers (n = 3) to acquire EMG and ECG signals (Figure 5A, right). The SNR of both EMG and ECG acquired by MCP-based interface were comparable with that of conventional, larger gel-based electrodes (Figure 5A, bottom). To evaluate the possibility of higher spatial resolution biopotential acquisition, we fabricated a conformable array of electrodes (64 channels, 250 μm electrode diameter, 4×7 mm^2 effective surface area), applied a thin layer of MCP to a similar surface area of skin over the wrist of a human subject, and placed the array on top. Voluntary flexion of each finger resulted in differentiable patterns of neural activity across the electrode array (Figure 5B). In addition, it was possible to localize independent nerve action potentials with well-defined waveforms and firing rates (Figure 5C). Multiple adjacent electrodes on the array captured the same action potential with waveforms reflecting the source and propagation of the activity (Figure 5D). Simple application of a biocompatible MCP layer enables high spatiotemporal resolution, non-invasive acquisition of electrophysiologic potentials from human skin.

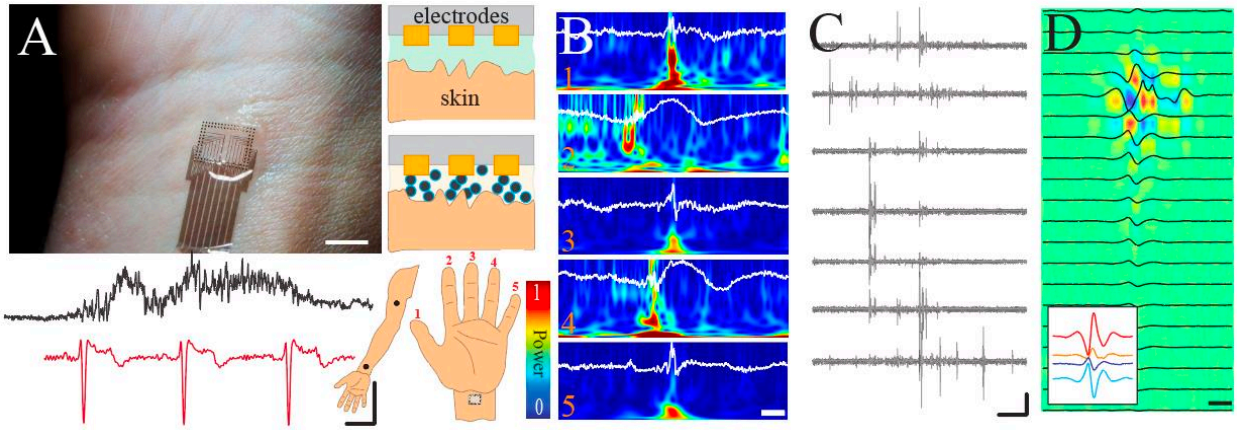

Figure 5: MCP creates an anisotropic interface for high spatiotemporal biopotential sensing. A) Micrograph of a high-density, conformable EMG array adhered to the wrist of a human participant using MCP (top left; scale bar, 10 mm). Cross-sectional schematic (top right) comparing gel (upper) and MCP interfaces (lower) between skin and electronics. Sample traces of MCP-acquired EMG (black) and ECG (red) signals are shown with their corresponding recording site on biceps and the wrist. Scale bar, 1 s; 4 mV. Photo credit: George Spyropoulos, Columbia University. B) Spectrograms of EMG signals acquired using MCP-adhered conformable array placed over the wrist (bottom left schematic) reveal distinct patterns during voluntary flexion of each finger. Scale bar, 80 ms. C) MCP-adhered conformable array permits noninvasive recording of independent nerve action potentials. Scale bar, 100 ms; 4 mV. D) Current source density heat map of a sample nerve action potential from (C) as visualized across adjacent electrodes reveals the source localization and propagation. Scale bar, 5 ms. Color bar same as (B).

References

[1] J.-W. W. Jeong, G. Shin, S. I. Il Park, K. J. J. Yu, L. Xu, and J. A. A. Rogers, "Soft materials in neuroengineering for hard problems in neuroscience," *Neuron*, vol. 86, no. 1, pp. 175–186, 2015, doi: 10.1016/j.neuron.2014.12.035.

[2] R. Chen, A. Canales, and P. Anikeeva, "Neural recording and modulation technologies," *Nat. Rev. Mater.*, vol. 2, no. 2, pp. 1–16, 2017, doi: 10.1038/natrevmats.2016.93.

[3] T. Someya, Z. Bao, and G. G. Malliaras, "The rise of plastic bioelectronics," *Nature*, vol. 540, no. 7633, pp. 379–385, 2016, doi: 10.1038/nature21004.

[4] M. Berggren and A. Richter-Dahlfors, "Organic Bioelectronics," *Adv. Mater.*, vol. 19, no. 20, pp. 3201–3213, Sep. 2007, doi: 10.1002/adma.200700419.

[5] B. Crone *et al.*, "Large-scale complementary integrated circuits based on organic transistors," *Nature*, vol. 403, p. 521, Feb. 2000.

[6] M. Kaltenbrunner *et al.*, "An ultra-lightweight design for imperceptible plastic electronics," *Nature*, vol. 499, no. 7459, pp. 458–463, Jul. 2013, doi: 10.1038/nature12314.

[7] S. H. Kim *et al.*, "Electrolyte-gated transistors for organic and printed electronics," *Adv. Mater.*, vol. 25, no. 13, pp. 1822–1846, 2013, doi: 10.1002/adma.201202790.

[8] E. Krook-Magnuson, J. N. Gelinas, I. Soltesz, and G. Buzsáki, "Neuroelectronics and biooptics: Closed-loop technologies in neurological disorders," *JAMA Neurol.*, vol. 72, no. 7, pp. 823–829, 2015, doi: 10.1001/jamaneurol.2015.0608.

[9] H. Fang *et al.*, "Ultrathin, transferred layers of thermally grown silicon dioxide as biofluid barriers for biointegrated flexible electronic systems," *Proc. Natl. Acad. Sci.*, vol. 113, no. 42, pp. 11682–11687, Oct. 2016, doi: 10.1073/pnas.1605269113.

[10] H. Fang *et al.*, "Capacitively coupled arrays of multiplexed flexible silicon transistors for long-term cardiac electrophysiology," *Nat. Biomed. Eng.*, vol. 1, p. 38, Mar. 2017.

[11] B. D. Paulsen, K. Tybrandt, E. Stavrinidou, and J. Rivnay, "Organic mixed ionic–electronic conductors," *Nat. Mater.*, 2019, doi: 10.1038/s41563-019-0435-z.

[12] I. Zozoulenko, A. Singh, S. K. Singh, V. Gueskine, X. Crispin, and M. Berggren, "Polarons, Bipolarons, And Absorption Spectroscopy of PEDOT," *ACS Appl. Polym. Mater.*, vol. 1, no. 1, pp. 83–94, 2019, doi: 10.1021/acsapm.8b00061.

[13] X. Crispin *et al.*, "The Origin of the High Conductivity of (PEDOT:PSS) Plastic Electrodes," *Chem. Mater.*, vol. 18, no. 4, pp. 4354–4360, 2006, doi: 10.1021/cm061032+.

[14] D. Khodagholy *et al.*, "High transconductance organic electrochemical transistors," *Nat. Commun.*, vol. 4, 2013, doi: 10.1038/ncomms3133.

[15] S. Wang *et al.*, "Chitosan/gelatin porous scaffolds assembled with conductive poly(3,4-ethylenedioxythiophene) nanoparticles for neural tissue engineering," *J. Mater. Chem. B*, vol. 5, no. 24, pp. 4774–4788, 2017, doi: 10.1039/c7tb00608j.

[16] X. Meng, Z. Wang, L. Wang, M. Pei, W. Guo, and X. Tang, "Electrosynthesis of pure poly(3,4-ethylenedioxythiophene) (PEDOT) in chitosan-based liquid crystal phase," *Electron. Mater. Lett.*, vol. 9, no. 5, pp. 605–608, 2013, doi: 10.1007/s13391-012-2171-2.

[17] M. N. V. Ravi Kumar and R. K. MNV., "A review of chitin and chitosan applications," *React. Funct. Polym.*, vol. 46, no. 1, pp. 1–27, 2000, doi: 10.1016/S1381-5148(00)00038-9.

[18] N. Sani *et al.*, "All-printed diode operating at 1.6 GHz," *Proc. Natl. Acad. Sci. U. S. A.*, vol. 111, no. 33, pp. 11943–11948, 2014, doi: 10.1073/pnas.1401676111.

[19] J. Rivnay, S. Inal, A. Salleo, R. M. Owens, M. Berggren, and G. G. Malliaras, "Organic

electrochemical transistors," *Nat. Rev. Mater.*, vol. 3, p. 17086, 2018, doi: 10.1038/natrevmats.2017.86.

[20] D. A. Bernards and G. G. Malliaras, "Steady-state and transient behavior of organic electrochemical transistors," *Adv. Funct. Mater.*, vol. 17, no. 17, pp. 3538–3544, 2007, doi: 10.1002/adfm.200601239.

[21] G. D. Spyropoulos, J. N. Gelinas, and D. Khodagholy, "Internal ion-gated organic electrochemical transistor: A building block for integrated bioelectronics," 2019. [Online]. Available: https://www.science.org

[22] A. C. Arias, J. D. MacKenzie, I. McCulloch, J. Rivnay, and A. Salleo, "Materials and applications for large area electronics: solution-based approaches.," *Chem. Rev.*, vol. 110, no. 1, pp. 3–24, Jan. 2010, doi: 10.1021/cr900150b.

[23] D. Braga, N. C. Erickson, M. J. Renn, R. J. Holmes, and C. D. Frisbie, "High-Transconductance Organic Thin-Film Electrochemical Transistors for Driving Low-Voltage Red-Green-Blue Active Matrix Organic Light-Emitting Devices," *Adv. Funct. Mater.*, vol. 22, no. 8, pp. 1623–1631, Feb. 2012, doi: 10.1002/adfm.201102075.

[24] J. Lee, M. J. Panzer, Y. He, T. P. Lodge, and C. D. Frisbie, "Ion gel gated polymer thin-film transistors.," *J. Am. Chem. Soc.*, vol. 129, no. 15, pp. 4532–3, Apr. 2007, doi: 10.1021/ja070875e.

[25] A. S. Sedra, D. E. A. S. Sedra, K. C. Smith, and K. C. Smith, *Microelectronic circuits*. New York: Oxford University Press, 1998.

[26] D. Khodagholy *et al.*, "NeuroGrid: Recording action potentials from the surface of the brain," *Nat. Neurosci.*, vol. 18, no. 2, pp. 310–315, 2015, doi: 10.1038/nn.3905.

[27] D. Khodagholy *et al.*, "Organic electronics for high-resolution electrocorticography of the human brain," *Sci. Adv.*, vol. 2, no. e1601027, 2016.

[28] A. Sirota *et al.*, "Entrainment of neocortical neurons and gamma oscillations by the hippocampal theta rhythm.," *Neuron*, vol. 60, no. 4, pp. 683–97, Nov. 2008, doi: 10.1016/j.neuron.2008.09.014.

[29] D. Khodagholy, J. N. Gelinas, and G. Buzsáki, "Learning-enhanced coupling between ripple oscillations in association cortices and hippocampus," *Science (80-.).*, vol. 372, no. October, pp. 369–372, Oct. 2017.

[30] G. Buzsaki, "Hippocampal Sharp Wave-Ripple : A Cognitive Biomarker for Episodic Memory and Planning," *Hippocampus*, vol. 25, no. 10, pp. 1073–1188, 2015, doi: 10.1002/hipo.22488.

[31] G. Buzsaki, Z. Horvath, R. Urioste, J. Hetke, and K. Wise, "High-frequency network oscillation in the hippocampus," *Science (80-.).*, vol. 256, no. 5059, pp. 1025–1027, 1992.

[32] M. K. Mian, M. Campos, S. A. Sheth, and E. N. Eskandar, "Deep brain stimulation for obsessive-compulsive disorder: Past, present, and future," *Neurosurg. Focus*, vol. 29, no. 2, pp. 1–9, 2010, doi: 10.3171/2010.4.FOCUS10107.

[33] D. Benninger and M. Schüpbach, "Deep brain stimulation," *Ther. Umschau*, vol. 75, no. 7, pp. 425–431, Jun. 2018, doi: 10.1024/0040-5930/a001019.

[34] G. D. Spyropoulos *et al.*, "Organic and perovskite solar modules innovated by adhesive top electrode and depth-resolved laser patterning," *Energy Environ. Sci.*, vol. 9, no. 7, pp. 2302–2313, 2016, doi: 10.1039/c6ee01555g.

Chapter 4: Enhancement-Mode Ion-Based Transistor as a Comprehensive Interface and Real-Time Processing Unit for Neuroelectronics

To understand and modulate brain function, bioelectronic devices capable of forming physiologically safe circuits to capture, amplify, process, and stimulate neurons are required[1]–[4]. Because signals of communication between neurons can be read out from minute changes in the ionic flux within brain tissue[5], [6], organic mixed-conducting materials that transduce ions to electrons can most effectively convert physiologic signals to those suitable for input to electronics[7]. Transistors form the backbone of circuits that can perform complex operations. However, a lack of both suitable materials and transistor architectures limits use of ion-based devices in applications that require stable interactions with neural networks. There is an enormous need to develop bioelectronic components that can merge biocompatibility, ion transduction, high speed, and reliable operation in physiological environments.

Spyropoulos et al. developed internal ion-gated organic electrochemical transistors (IGTs) that combine many of these properties[8]. These transistors maintain hydrated ion reservoirs within a conducting polymer channel, reducing the transit time of ions participating in the dedoping process and thereby enabling high speed of operation. They are individually addressable due to the incorporation of an ion membrane between the channel and gate electrode. Therefore, IGTs can serve as biocompatible, high performance bioelectronic transistors. However, these IGTs function only in depletion mode (normally ON), and optimal building blocks for bioelectronic devices should include both depletion and enhancement mode (normally OFF) transistors. Because most integrated circuits are currently designed based on enhancement mode transistors, the development

of enhancement mode IGTs would permit seamless integration with these preexisting designs. In addition, having equally high performance enhancement and depletion mode devices would enable unique integrated circuit design opportunities that could enhance the diversity of functions executed by bioelectronic devices.

Enhancement mode operation is commonly employed across different transistor architectures. Silicon field effect transistors (Si-FETs) typically operate in enhancement mode due to increased performance and ease of fabrication compared to their depletion mode counterparts. However, Si-FETs are rigid and require strong encapsulation in physiologic environments because ion diffusion damages the silicon components, precluding their use in long-term bioelectronic applications[9], [10]. These properties also restrict the abiotic/biotic coupling to capacitive interaction between the surface of the gate material and electrolyte in such devices. Nanoparticles of zinc oxide and organic semiconductors can form channels to create electrolyte-gated enhancement mode transistors that permit direct coupling of ions in the electrolyte with the channel through a large double electric layer capacitance. These transistors have been employed as sensors, invertors, and ring oscillators[11]–[17]. Organic electrochemical transistors (OECTs) further increase capacitance by using hydrophilic conducting polymer channels that can undergo bulk redox reactions, resulting in volumetric capacitance[18]. In contrast to depletion mode OECTs composed of poly(2,3-dihydrothieno-1,4-dioxin)-poly(styrenesulfonate) (PEDOT:PSS), enhancement mode OECTs are often unstable and based on non-biocompatible solvents, limiting their use in biological applications[19]–[21]. Furthermore, the electrolyte is an integral part of electrolyte-gated and electrochemical transistors, such that the transient response of these transistor architectures is defined by the “time of flight” of ions through the gate-electrolyte-channel circuit[22]. Operation speeds are therefore dictated by ion mobility and cannot be improved by enhancing the electronic

performance of the channel material[23]. Although such speeds may suffice for limited sensing applications, they are inadequate for creation of advanced integrated bioelectronics[24], [25]. Building blocks of these devices must merge high speed and high amplification while maintaining biocompatibility and independent gating.

Here, we developed an easily synthesizable, biocompatible material that enables creation of enhancement mode IGTs (e-IGTs). The channel is composed of a mixture of PEDOT:PSS and polyethylenimine (PEI). E-IGTs have high transconductance, exhibit volumetric capacitance, and can be stably operated over extended periods of time. Temporal responses of e-IGTs are faster than all other ion-based transistors, due to the shortened ionic transit time enabled by hydrated ion reservoirs within the e-IGT channel, and are best described by hole mobility. E-IGTs possess both high transconductance and speed, resulting in a measure of gain bandwidth product several orders of magnitude above other ion-based transistors. We deployed e-IGTs in a wide range of neurophysiological applications, including the first use of an ion-based transistor to acquire action potentials from individual neurons and real-time detection of epileptic discharges *in vivo*. Therefore, these enhancement mode transistors are optimal for creation of integrated circuits in bioelectronic devices.

4.1 Operating Mechanism, Structure, Steady-State Characteristics and Stability of an E-IGT

The channel material of e-IGT is composed of PEDOT:PSS, PEI, D-sorbitol and cross linking additives (see Methods). PEDOT:PSS is a highly stable and versatile conducting polymer that can achieve high conductivities and convert ions to electrons within the composite material[26]. D-sorbitol is a sugar alcohol that stretches the PEDOT:PSS-rich domains, thereby enhancing the electronic conductivity of the PEDOT:PSS film[27]. In addition, D-sorbitol facilitates

maintenance and movement of mobile ions within the channel by forming hydrated ion reservoirs[8]. The amine groups of PEI serve as reducing agents through electron transfer to PEDOT:PSS and decrease the intrinsic conductivity of the channel by several orders of magnitude [28]–[30]. Mixing PEDOT:PSS with PEI also results in decrease in absorption in the near infrared (due to fewer polarons) and emergence of an absorption peak at 600 nm (associated with a color change to cobalt blue (Figure 1A) . These changes in optical properties support the occurrence of a redox reaction between PEDOT:PSS and PEI[31], [32].

We hypothesized that a reduced-PEDOT:PSS film that contains excess PEI and PSS, combined with ease of ion movement within the channel material, could carry out repeatable and reversible ion-based doping to create an enhancement mode (normally OFF) transistor. Such a transistor would function as follows: during the initial OFF-state of the device ($V_G = 0$ V), the conducting polymer is in its reduced ($PEDOT^0$) state due to electron transfer from PEI. The now protonated PEI^+ establishes ionic bonds with PSS^- to maintain charge balance. This process is naturally facilitated by the presence of sulfonic acid groups in PSS and the basic nature of PEI (Figure 1B top)[30], [31]. During the ON state, the application of a negative V_G ($V_G < 0$) will compensate the PEI^+ in the channel and release the bonded PSS^-, which then recombines with PEDOT (Figure 1B, bottom). This formation of $PEDOT^+$:PSS^- increases the channel conduction, providing the mechanism whereby application of gate voltage modulates the channel current. The embedded hydrated reservoirs established by D-sorbitol within the channel facilitate these ion exchanges and eliminate the need for external electrolyte to operate the device (Figure 1B).

The PEDOT:PSS-PEI composite was effectively created either by direct mixing and filtration of the solutions or layer-by-layer deposition. It was formed into a film and then patterned between Au-based source and drain electrodes to generate a transistor channel. To allow independent

control of individual transistors, the gate electrode must have efficient ionic, but not electronic, conduction with the transistor channel. We chose chitosan to function as the transistor's ion membrane due to its biocompatibility, stability, and processability[33], [34]. It is also critical for the ion membrane not to disrupt the charge balance of the PEDOT:PSS-PEI composite. Alternative biopolymers, such as gelatin, PVA, and PVA:PSS were also able to serve as the ion membrane.

The device was fabricated using established microfabrication processes capable of creating large-scale conformable transistors and circuits (Figure 1C). As anticipated, the transistor operated in enhancement mode, wherein increase in negative potential of V_G resulted in higher drain current (Figure 1D). We found that these e-IGTs can achieve high transconductances, exceeding the majority of electrolyte-gated and electrochemical transistors with similar or larger geometries (Figure 1E)[8], [35]–[38]. We hypothesize that these characteristics are attributable to the high geometrical flexibility in transistor design combined with efficient doping of the reduced PEDOT by internally available PEI. Next, we sought to confirm that this composite material contains all the required elements for self-doping without the need for an external ionic source, such as electrolyte. We deposited Au-based source and drain electrodes onto a 90 nm thick thermally grown SiO_2 silicon wafer. The SiO_2 served as an ideal ion barrier and the channel was formed by spin coating the composite materials in between source and drain electrodes. It was possible to enhance drain current by a gate pulse applied through the bulk of Si, suggesting that the PEDOT:PSS-PEI-based composite is capable of self-doping (Figure 1F).

We characterized how the amount of excess PEI in the channel affects device function. Higher amounts of excess PEI resulted in lower OFF-state current, but simultaneously reduced the ON-state current and lowered transconductance (Figure 2A).

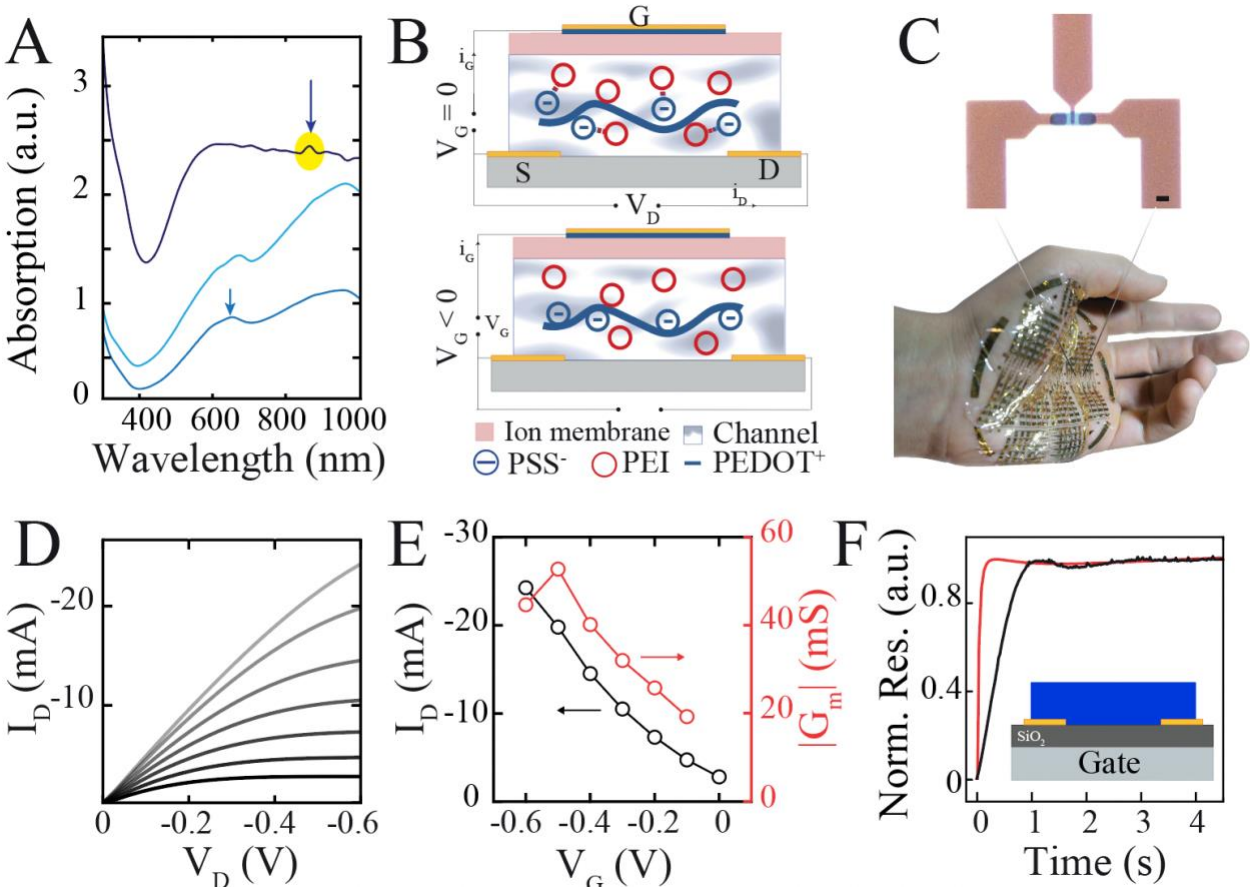

Figure 1: Operating mechanism, structure, and steady-state characteristics of an e-IGT. A) Representative absorption spectra of PEDOT:PSS and PEDOT:PSS treated with D-sorbitol and PEI (n = 4). Black arrow shows peak indicating the existence of polarons in untreated PEDOT:PSS that is reduced when PEI is added. Light blue (PEDOT:PSS–PEI) and red (diluted PEDOT:PSS–PEI in sorbitol) arrows indicate the emergence of a 600 nm peak. B) Schematic illustration of e-IGT cross-section and wiring diagram for device operation. Protonated PEI (red) bonds with PSS– (blue), de-doping the PEDOT chain (VG = 0 V, top). Under a negative applied gate voltage (VG < 0 V, bottom), PEI+ is deprotonated and releases PSS, which then recombines with PEDOT and increases channel conductivity. D-sorbitol creates hydrated ion reservoirs within the channel. PEDOT-rich regions are shown in light blue and PSS lamellas in white (G, S and D denote gate, source and drain terminals, respectively). C) Optical micrograph displaying the top view of an individual e-IGT (top right). Scale bar, 5 µm. Ultra-flexible, ultra-thin e-IGT array conforming to the surface of a human hand (bottom left). D) Output characteristics (ID–VD) of the e-IGT device (length (L) = 5 µm, width (W) = 500 µm, thickness of PEDOT:PSS = 300 nm) for VG varying from 0 V (bottom curve) to −0.6 V (top curve) with a step of −0.1 V; colour intensity corresponds to VG amplitude. E) Transfer curve for VD = −0.6 V (black) with corresponding transconductance (red), Gmmax = 52.74 mS. F) Normalized response of drain current with respect to gate voltage pulse of a PEDOT:PSS–PEI channel gated through chitosan (red; VD = −0.6 V and VG varying from 0 V to −0.3 V) versus a PEDOT:PSS–PEI channel gated through a 90 nm thick SiO2 layer (black; VD = −10 V and VG varying from 0 V to −20 V). Inset shows schematic cross-sectional illustration of PEDOT:PSS–PEI channel with a SiO2 ion barrier layer. Channel dimensions for both devices were L = 5 mm and W = 10 mm, with a thickness of PEDOT:PSS = 300 nm (representative data from n = 3 experiments).

The e-IGT transconductance also increased systematically with channel thickness (Figure 2B). This result implies that the PEI distributed throughout the conducting polymer was able to uniformly reduce the entire channel. Hydrated ion reservoirs inside the channel created by D-sorbitol facilitate engagement of the entire bulk of the channel into this efficient ion-based doping process. Increasing the amount of PEI relative to PEDOT:PSS in the channel also shifts the threshold voltage of the transistor to more negative values, as minimal PEDOT:PSS is available for further dedoping at positive gate voltages. To further assess the effect of channel geometry and optimize the e-IGT design for various electrophysiological applications, we fabricated an array of e-IGTs that scaled channel length and width from 5 – 500 μm. We found that the transconductance of e-IGTs increased proportionally with respect to gate area and channel volume (Figure 2C-D). In order for such a transistor to operate stably over time, it must i) maintain protons localized within the channel despite the absence of an ionic barrier between the channel and ion membrane, and ii) preserve the channel in its reduced form without gradual oxidation. We enabled these properties within e-IGTs by incorporating excess PEI and PSS in the channel. E-IGTs demonstrated stable, constant modulation of drain current in response to a train of gate voltage pulses (both at high V_G pulse amplitude and when biased at maximum transconductance) delivered for 4 days in physiological conditions (Figure 2E) and under mechanical stress. The duration of these stability experiments was defined based on requirements for electrophysiology rather than device failure.

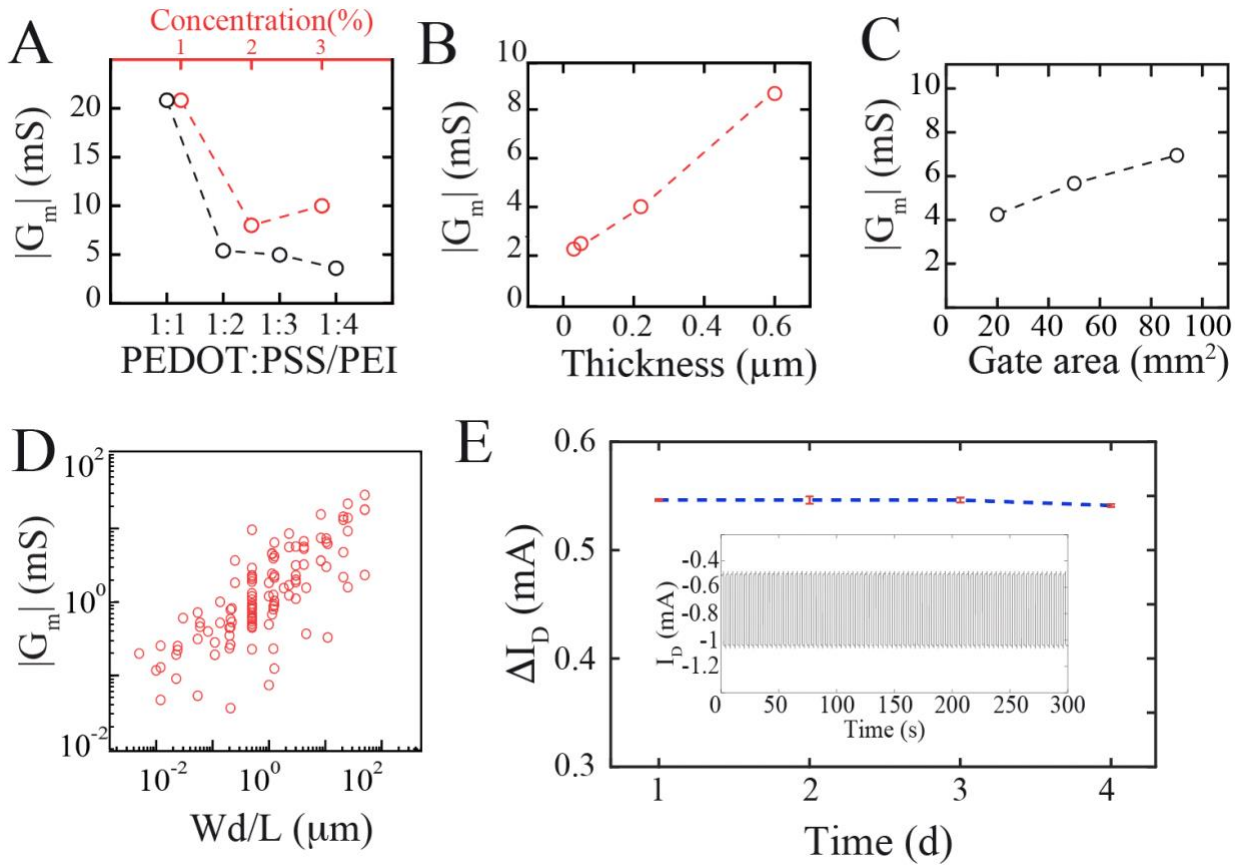

Figure 2: PEDOT:PSS–PEI composite creates long-term, stable, volumetric capacitance for the operation of an enhancement-mode transistor. A) Maximum transconductance as a function of PEI solution concentration (top) and PEDOT:PSS to PEI layer ratio (bottom, PEI solution concentration = 1%). Transconductance was calculated based on a transfer curve for $V_D = -0.6$ V and V_G varying from 0 V to −0.6 V (L = 5 mm, W = 10 mm, representative data from n = 3 experiments). B) Maximum transconductance increases proportionally with channel thickness. Transconductance was calculated from a transfer curve for $V_D = = -0.6$ V and V_G varying from 0 V to −0.6 V (L = 5 mm, W = 10 mm, representative data from n = 3 experiments). C) Maximum transconductance increases proportionally with gate area. Transconductance was estimated from a transfer curve with $V_D = -0.6$ V and V_G varying from 0 V to −0.6 V (L = 250 μm, W = 10 mm, representative data from n = 3 experiments). D) Maximum transconductance increases proportionally with channel volume. Transconductance was calculated for a 6 × 6 array of e-IGTs with logarithmically increasing channel length and width (5–500 μm) from a transfer curve with $V_D = -0.6$ V and $V_G = 0$ V to −0.6 V (d denotes channel thickness, n = 113 transistors). E) Drain-current (ID) modulation of an e-IGT over a period of four days with pulsed gate voltages (VD = −0.4 V and V_G varying from 0 V to −0.6 V; W = 500 μm, L = 30 μm, thickness of PEDOT:PSS = 150 nm). Each point represents the average modulation of the transistor under continuous operation for 50 min. Error bars (red) represent the maximum and minimum value for each data point. Inset shows the temporal response of the drain current (I_D) of the e-IGT under continuous operation for 300 s (n = 3,000 pulses, day 1 = 0.546 mA ± 0.915 μA, day 2 = 0.546 mA ± 3.387 μA, day 3 = 0.546 mA ± 2.250 μA, day 4 = 0.541 mA ± 1.256 μA; mean ± standard deviation).

4.2 E-IGTs High Speed of Operation.

High speed of operation is required for use of transistors in bioelectronic devices for many neurophysiologic applications, such as recording of neural action potentials (complex waveform duration 1-2 ms[39]) or performing signal processing for responsive neurostimulation[40]–[42]. The time constant (τ) of operation for electrochemical transistors and electrolyte-gated FETs is defined by device geometry and ionic mobility because the transient dynamics of such devices are described using an ionic-based RC circuit between gate and channel[22]. We previously showed that maintaining mobile ionic species within the polymeric channel decreases the "time-of-flight" of ions engaged in the dedoping process by reducing the average traveling distance of the ions[8]. An e-IGT with 5 μm channel length had a rise time of 2.9 μs while maintaining ~1.5 mS transconductance (Figure 3A). This speed of operation is several orders of magnitude faster than reported enhancement mode ion-based (electrochemical or electrolyte-gated, organic or inorganic) transistors. To better understand the transient dynamics of the e-IGT, we systematically fabricated devices with various channel lengths and measured the rise time and hole mobility using constant gate voltage and current pulses, respectively (Figure 3B). In contrast to OECTs and EGOFETs, e-IGT transient responses fall within the range of hole mobility (0.1-10 $cm^2\ V^{-1}s^{-1}$) [43]–[45]rather than ion mobility values (10^{-2}-10^{-4} $cm^2\ V^{-1}s^{-1}$)[23] in conducting polymers (Figure 3B). This result suggests that the e-IGT architecture can leverage the higher hole mobility of conducting polymers to increase operation speed compared to other organic electrochemical devices where speed is dictated by ion mobility.

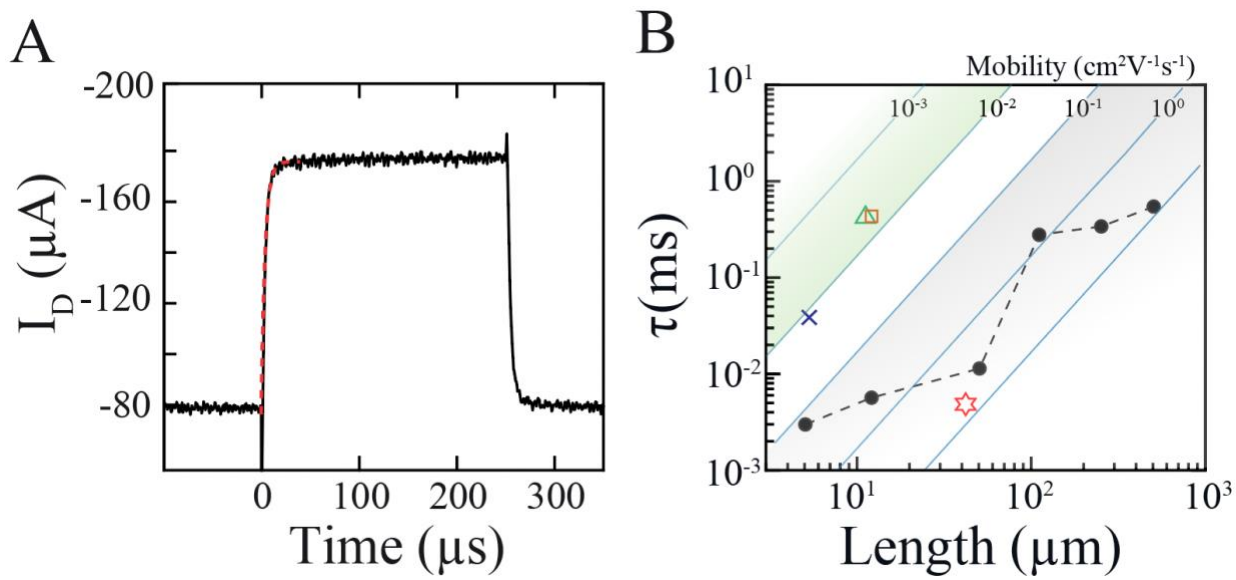

Figure 3:High-speed transient response of an e-IGT is a function of hole rather than ion mobility. A) Temporal response of the drain current (I_D) of an e-IGT device with L = 5 μm, W = 5 μm (thickness of PEDOT:PSS = 100 nm) biased at $V_D = -0.6$ V and $V_G = -0.4$ V, with pulse amplitude of 0.2 V. Exponential fit of the e-IGT drain current (red) resulted in a time constant of 2.9 μs (n = 256 pulses). B) Rise time for e-IGTs with different channel lengths (black circles) fall within the theoretical ranges governed by hole mobility (grey shaded area). Blue lines show the theoretical achievable rise time based on the corresponding carrier mobilities ranging from 10^{-3} to 10 $cm^2 V^{-1} s^{-1}$. Rise times of other ion-based transistors (cross[36], triangle[19], rectangle[46]) fall within ranges governed by ion mobility (green shaded area); the poly-Si-based enhancement-mode transistor (star[47]) falls in the hole-mobility regime. Note, n = 256 pulses per data point.

4.3 E-IGT Based Integrated Circuits

However, transistors must have both high speed and amplification to function effectively in bioelectronic circuits[48], [49], and these parameters are often inversely related due to geometrical design and material composition of the device. To evaluate this trade-off in e-IGTs, we characterized transistor performance based on the ratio of transconductance and rise-time as a measure of gain bandwidth product. E-IGTs performed favorably compared with most organic transistor architectures, and surpassed the majority of enhancement mode transistors by several orders of magnitude (Figure 4A).

We next investigated the feasibility of using e-IGTs for integrated circuits. A key factor that limits integrated circuit design is cross-talk and current leakage between adjacent transistors.

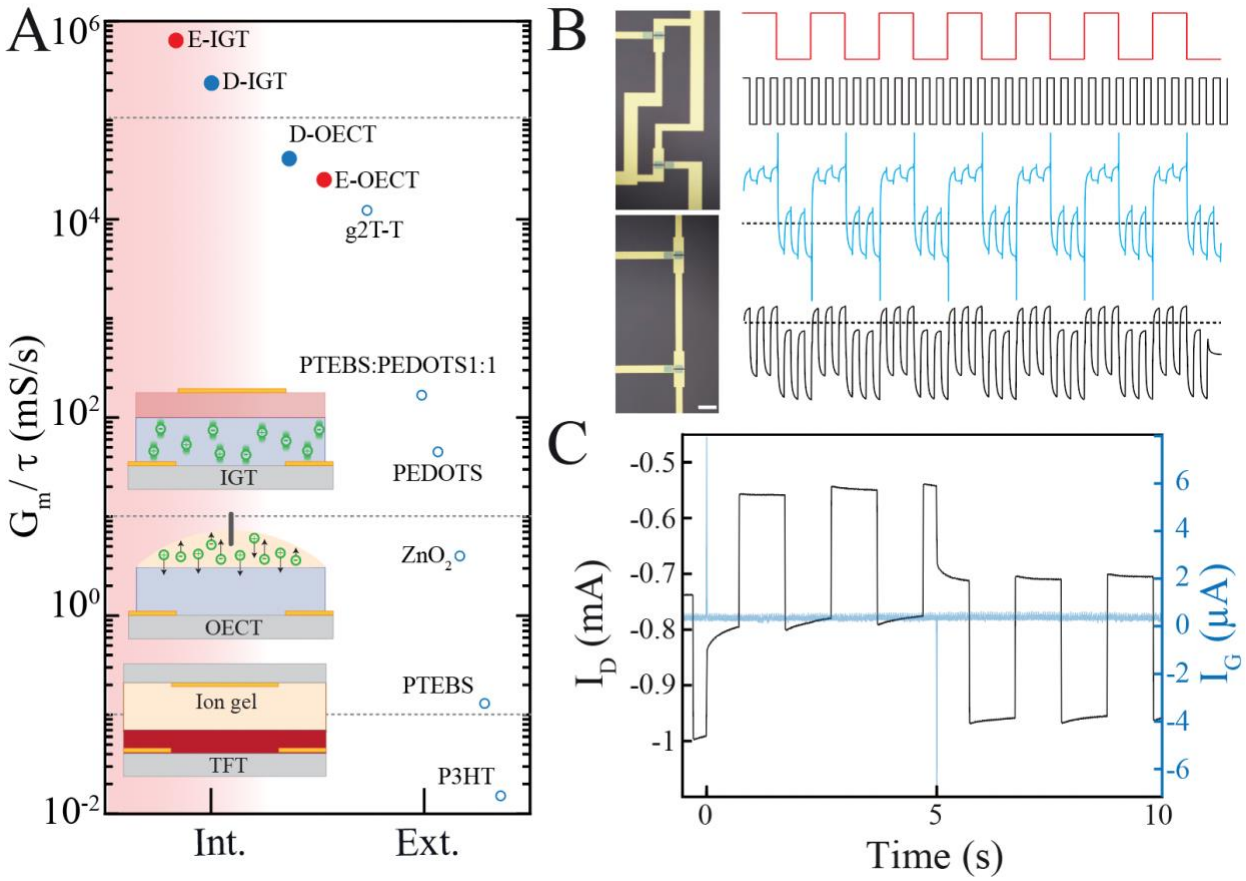

Figure 4: E-IGTs have a high gain–bandwidth product and create low-leakage, effective integrated circuits. A) Ratio of transconductance to rise time for different ion-based transistors. Internal mobile ions enable higher Gm/τ compared with external ions supplied by an electrolyte. PEDOT:PSS–PEI based OECTs and IGTs are marked in red. Filled circles denote devices that were fabricated in this study g2T-T denotes poly(2-(3,3′-bis(2-(2-(2-methoxyethoxy)ethoxy)ethoxy)-[2,2'-bithiophen]-5-yl) [3,2-b]thiophene)[20], PTEBS denotes sodium poly(2-(3-thienyl)-ethoxy-4-butylsulfonate), PEDOTS denotes poly(4-(2,3-dihydrothieno-(3,4-b)-(1,4)dioxin-2-yl-methoxy)-1-butanesulfonic acid[50], sodium salt, and P3HT referes to poly(3-hexylthiophene-2,5-diyl)[11]. B) Optical micrographs of OR (left, top) and AND (left, bottom) logic gates; scale bar, 150 μm. Input signals (red and black) are the top two traces. Response of AND (light blue) and OR (dark blue) logic gate are the bottom two traces. Dashed lines mark the threshold of high and low logics (representative data from n = 5 experiments). C) E-IGTs perform digital logic with minimal leakage current. The drain current of the e-IGT is shown in black, and the leakage current between the source and gate of an adjacent e-IGT is shown in blue (representative data from n = 5 experiments).

Depletion mode transistors have high conductivity in the unbiased channel, necessitating complex patterning processes to eliminate high current leakage between adjacent transistors. This feature often poses a significant fabrication challenge because organic electronic materials are highly sensitive to photolithographic chemicals, which include strong bases and solvents. Although peel-

off techniques can enable appropriate patterning in some cases, the deposition layer must be substantially thinner than the peel-off layer, limiting the design and material possibilities[24], [51]. In contrast to depletion mode devices, the low OFF-current (high-resistance) of the e-IGT in its unbiased state allows for high resistance paths between adjacent transistors in the absence of any channel patterning. We fabricated digital logic gates (AND, OR gates) that accurately performed the corresponding arithmetic, and exhibited minimal gate leakage current (I_G), confirming that e-IGTs can function as scalable, low-leakage bioelectronic computational modules (Figure 4B-C).

4.4 High-Quality Electrophysiological Signal Acquisition with E-IGTs

We designed a series of experiments to evaluate the applicability of e-IGTs to a broad range of electrophysiological measurements, including non-invasive electromyography (EMG) and electrocardiography (ECG) from surface of human skin, as well as chronic intracranial encephalography (iEEG) from the surface of the brain and deeper structures in freely moving rats. We were able to create e-IGT-based devices with various form factors to accommodate the different mechanical and electrical requirements of each application due to the e-IGT's versatile architecture and fabrication process. Specifically, the devices adequately surveyed the entire electrophysiological frequency spectrum (0.1 - 10^4 Hz) with appropriate signal-to-noise ratio (SNR) for each signal's amplitude (Figure 5A).

We performed e-IGT-based EMG and ECG recording from the skin over the right biceps muscle and left chest of healthy volunteers (n = 3), respectively. E-IGTs required minimal force to maintain contact with the skin due to their lightweight and conformable design (Figure 5B). The e-IGT was placed in a common-source configuration with an adhesive electrode on the left forearm serving as a ground for measurement with a source measure unit in both cases (Figure 5C). We recorded low noise, high SNR, muscle compound action potentials triggered by voluntary flexion

of the biceps muscle (Figure 5C). ECG recording revealed typical waveform morphology with well-distinguished QRS complexes, comparable to signal obtained with commercially available medical electrodes connected to a differential amplifier. These results confirm the ability of the e-IGT to effectively function as a non-invasive electrophysiological transducer.

We next used e-IGTs to perform chronic, invasive brain recording in an animal model. We fabricated two types of devices to mimic the electrode configurations typically employed to record from brain networks: i) conformable surface arrays of e-IGTs for placement on the cortical surface, and ii) strips with e-IGTs at the tip for insertion into deep cortical layers. A craniotomy was opened over rat somatosensory cortex, and e-IGT arrays were placed on the cortical surface. The device conformed to the curvilinear surface of the brain and maintained mechanical contact. Two surgical stainless-steel screws implanted in the cerebellum served as the e-IGT gate and the ground for the acquisition amplifier and recording was initiated using a common-source configuration while the rat was freely moving. We computed the time-frequency spectrogram of e-IGT-based local field potentials (LFP) recorded two weeks after implantation (Figure 5D). Characteristic spectral features of non-rapid eye movement (NREM) sleep, rapid eye movement (REM) sleep, and wakefulness were identifiable in the recordings. Being able to identify well-characterized behavioral states (such as NREM and REM sleep) confirms the ability of e-IGTs to accurately detect neurophysiologic signals that can be interpreted by neurophysiologists using conventional analysis methods and is often required during evaluation of neural signals for clinical purposes. To evaluate the fidelity of the device performance at higher frequencies, we investigated cross-frequency coupling, a phenomenon that is linked to neural computation and information transfer within cortical networks. The cross-frequency coupling demonstrated temporal co-occurrence of brain oscillations across a wide frequency spectrum[52]. This analysis replicated the temporal

coupling between cortical sleep spindles (10-20 Hz) and both low gamma (20-30 Hz) and high gamma (>40 Hz) oscillations previously identified using conventional intracranial electrodes (Figure 5E)[39], [53]. Therefore, e-IGTs are capable of acquiring consistently high-quality LFP data from the cortical surface over a period of two weeks, demonstrating stability in a physiological environment. Post-mortem histological analysis revealed lack of macroscopic tissue damage, neuronal loss, or gliosis in the vicinity of the implanted e-IGTs, supporting device biocompatibility. Although the highly protonated form of PEI may cause cytotoxicity, charge-balanced PEI and its combination with chitosan has been demonstrated to be an effective biocompatible cell scaffolding material[34], [54].

Neural spiking provides key insight into the mechanisms of brain function[52], [55]. We assessed the capacity of e-IGTs to acquire *in vivo* neural spiking activity from deep cortical layers, an experimental procedure that is only possible if a neural interface device provides high speed and amplification simultaneously. To ensure an appropriate sampling rate (20 kHz) for acquisition of action potentials, we converted the drain current of the e-IGT to voltage and digitized it with a 1 kΩ resistor in series between the channel and electrophysiological amplifier (Figure 5F). E-IGT strips were fabricated onto a narrow, conformable parylene-C substrate with an anchor point at the tip to facilitate placement into the cortex (Figure 5G). This design allowed the device to be wrapped around a 50 μm-wide tungsten microwire to guide device insertion (Figure 5G). High pass filtering (>250 Hz) of neural signals acquired by implanted e-IGTs revealed large amplitude transients suggestive of action potentials (Figure 5H). Transients detected from individual e-IGTs had consistent waveform morphology (Figure 5I, top and left) and autocorrelation of their occurrence times demonstrated a pattern consistent with the physiologic refractory period of a

neuron (Figure 5K, right). These results validate the ability of e-IGTs to record the spiking activity of individual neurons *in vivo*.

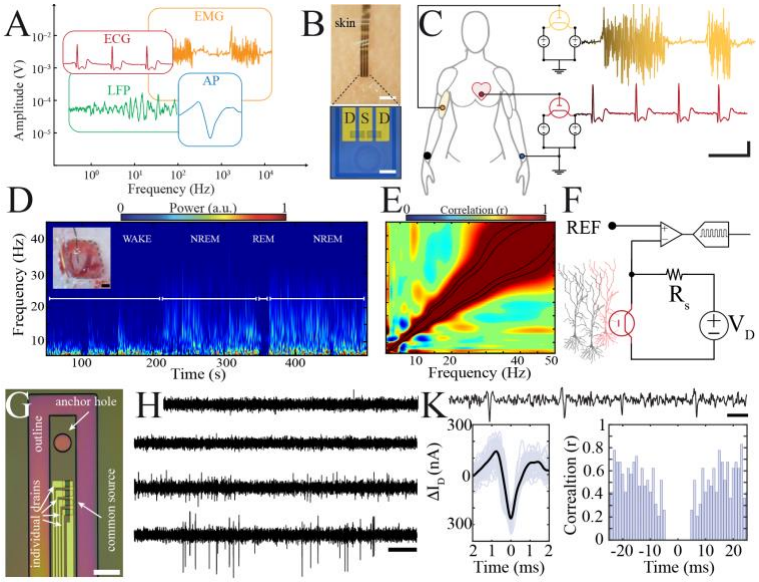

Figure 5: E-IGTs enable high-quality electrophysiological signal acquisition across a broad range of frequencies and amplitudes. A) Sample traces of in vivo signals acquired by e-IGTs plotted to reflect the wide span of frequency and amplitude characteristics (representative data from n = 4 rats). B) Micrograph of an e-IGT-based device used for ECG and EMG signal acquisition in contact with human skin (top; scale bar, 150 µm). Optical micrograph of e-IGT devices with two recording channels (bottom; scale bar, 100 µm). The middle source electrode (S) and the two drain electrodes (D) are denoted. C) Wiring diagram of EMG and ECG recording using an e-IGT-based device at $V_D = -0.3$ V and $V_G = 0$ V. The gate electrode was at the wrist (blue circle), and e-IGTs were placed on the right biceps for EMG recording (yellow circle) and chest for ECG recording (red circle). Sample traces of e-IGT-acquired EMG (yellow) and ECG (red) signals are shown. The black, filled dot on the right hand denotes ground (GND). Scale bar 1 s, 200 µA (representative data from n = 3 healthy subjects). D) Time–frequency spectrogram of an e-IGT-based chronic LFP recording from a cortical surface with behavioral states marked. Inset shows a photograph of e-IGT-based device placement on rat cortex; scale bar, 500 µm. Warmer colors represent a higher relative power in arbitrary units (representative data from n = 4 rats). E) Comodulogram showing cross-frequency coupling of cortical LFP at spindle, low-gamma and high-gamma frequency bands. Warmer colours represent a higher relative correlation ($P < 0.05$ after the Bonferroni–Holm correction for multiple comparisons that were considered statistically significant; representative data from n = 4 rats). F) Wiring diagram of action potential recording using an e-IGT-based implantable device. The drain current was converted to voltage using a series resistor, then digitized using a neurophysiological amplifier (VDS = −0.4 V, VGS = −0.5 V, while VG = 0 V, REF refers to reference voltage). G) Optical micrograph of an e-IGT-based device with four transistors for LFP and spike recording. The anchor hole facilitates insertion of the conformable device using a microwire guide into deep layers of rat cortex. The potential generated by neurons serves as the small-signal VG. Scale bar, 80 µm. h, High-pass filtered traces (250–2,500 Hz) from four e-IGTs in deep layers of rat cortex revealing waveforms suggestive of neural action potentials. Scale bar, 300 nA, 500 ms. i, High-pass filtered trace showing neural action potential waveforms (top; scale bar, 300 nA, 25 ms). Trigger averaging (n = 50, spikes are aligned at waveform trough, t = 0 s) of waveforms demonstrates consistent action potential morphology (black line, bottom left). Autocorrelogram indicative of neural firing refractory period (bottom right, n = 9,357 spikes).

4.5 Real-Time Detection of Epileptic Discharges using IGTs.

Bioelectronic devices are increasingly required to not only acquire biologic signals, but also to process them in real-time[42]. For a subset of patients with epilepsy, responsive neurostimulation approaches with implanted neural interface devices are the most promising form of treatment[56]. However, the only components capable of performing these functions at present are silicon-based, non-biocompatible, bulky, and need rigid encapsulation in physiologic environments. We sought to use IGT-based circuitry to create soft, biocompatible, chronically implantable neural processing units. A key function of these responsive neurostimulation devices is accurate detection of epileptic discharges, which is typically accomplished using bandpass filters or amplitude thresholding[57]. This detection can be challenging due to the variable amplitude of the neural potentials based on the location of the recording electrode with respect to local dipoles and the reference electrode[6], [58]. Non-linear rectification could improve detection by suppressing lower but variable amplitude non-target signals, but this strategy is not practical to implement using a single transistor type. We combined a d-IGT with an e-IGT to create an IGT-based non-linear rectification circuit (Figure 6A). This device was used to process signals acquired from the hippocampus of a freely moving epileptic rat (Figure 6B-C). The IGT-based non-linear rectification circuit accurately detected epileptic discharges (Figure 6D), with receiver operating characteristics that surpassed traditional amplitude or bandpass filter thresholding methods (Figure 6E). Therefore, IGTs and their ability to efficiently integrate enhancement and depletion mode devices within individual circuits can improve real-time processing of disease-relevant neurophysiological signals and have the potential to form fully implantable, conformable acquisition and processing units for bioelectronic devices.

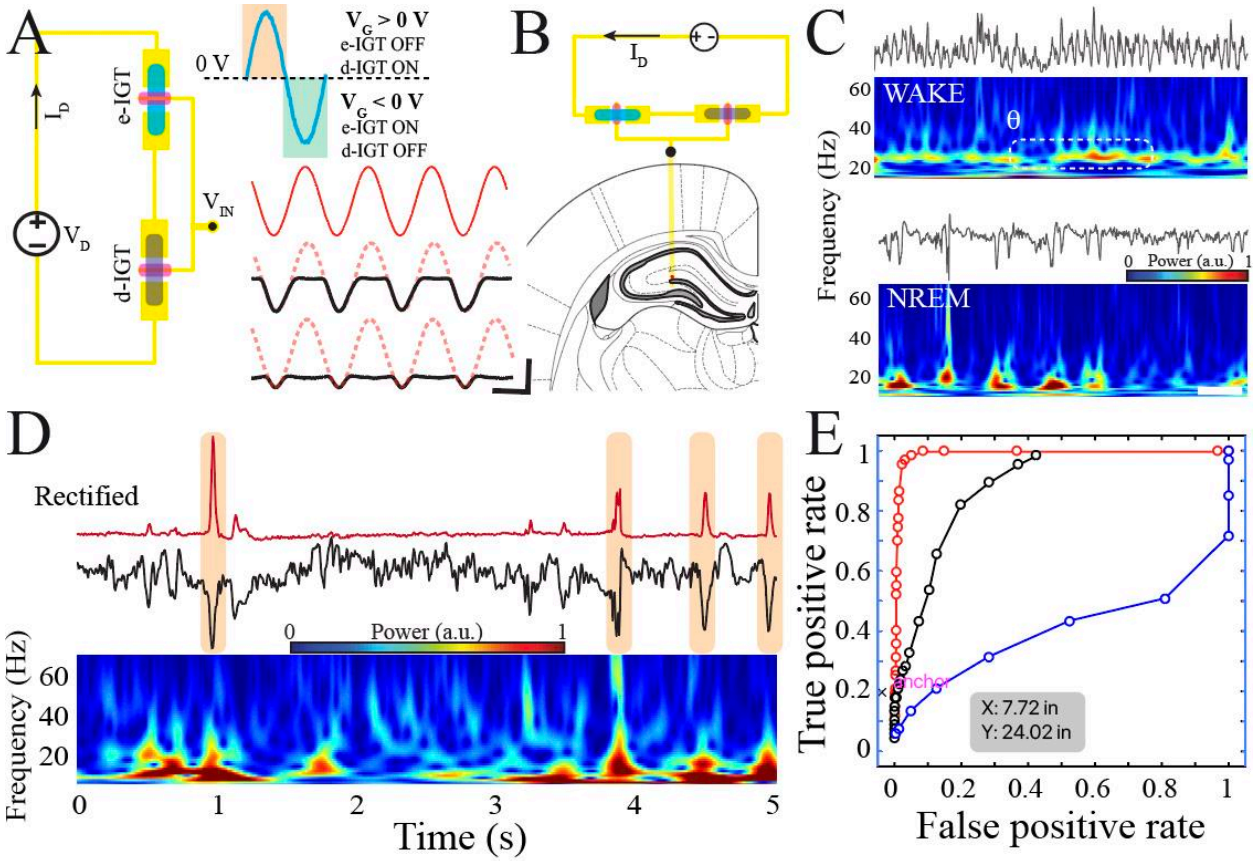

Figure 6: E-IGTs in combination with d-IGTs enable real-time non-linear signal rectification for the accurate detection of epileptic discharges in vivo. A) Schematic of a non-linear signal rectification circuit composed of a d-IGT and an e-IGT (left). Non-linearity of the IGT-based circuit output is accomplished by varying the geometry of the d-IGT relative to the e-IGT; a 1 Hz sine wave input provided to the IGT-based circuitry (top red trace) results in thresholding at 0 V when the d-IGT and e-IGT have equivalent geometries (middle black trace), but thresholding at negative voltages when the d-IGT is smaller than the e-IGT (lower black trace). Scale bar, 500 ms, 200 µA; note that the IGT-based circuit output is not to scale relative to the input trace, for visualization purposes. B) Anatomical schematic of a coronal slice of rat brain demonstrating the source of the neural recording in the hippocampus (red dot) with the circuit diagram for IGT-based real-time detection. C) Sample raw traces and accompanying spectrograms of neural signals recorded using an e-IGT implanted in a freely moving rat during wakefulness (top; scale bar, 500 nA, 500 ms) and NREM sleep (bottom; scale bar, 1 µA, 500 ms). Prominent theta band activity is present during the rat's locomotion (white dashed box). Warmer colors represent a higher relative power in arbitrary units. D) The IGT-based non-linear rectifier shown in a provides high signal-to-noise real-time detection of epileptic discharges. Sample raw trace (black; scale bar, 1 µA, 500 ms) and accompanying spectrogram reveal several epileptic discharges (orange boxes) that are transformed into easily detectable peaks by the IGT-based circuit (red). Warmer colors represent a higher relative power in arbitrary units. E) Receiver operating curves demonstrating the superior detection of epileptic discharges using the IGT-based circuit (red; area under curve = 0.96) compared with traditional detection approaches based on bandpass filtered power thresholding (black; area under curve = 0.62) and amplitude thresholding (blue; area under curve = 0.43; n = 167 interictal epileptiform discharges (IEDs)).

References

[1] R. Chen, A. Canales, and P. Anikeeva, "Neural recording and modulation technologies," *Nat. Rev. Mater.*, vol. 2, no. 2, pp. 1–16, 2017, doi: 10.1038/natrevmats.2016.93.

[2] G. G. Malliaras, K. Deisseroth, H. Wang, J. Rivnay, and L. Fenno, "Next-generation probes, particles, and proteins for neural interfacing," *Sci. Adv.*, vol. 3, no. 6, p. e1601649, 2017, doi: 10.1126/sciadv.1601649.

[3] J. W. Jeong, G. Shin, S. Il Park, K. J. Yu, L. Xu, and J. A. Rogers, "Soft materials in neuroengineering for hard problems in neuroscience," *Neuron*, vol. 86, no. 1, pp. 175–186, 2015, doi: 10.1016/j.neuron.2014.12.035.

[4] G. Buzsáki *et al.*, "Tools for probing local circuits: High-density silicon probes combined with optogenetics," *Neuron*, vol. 86, no. 1, pp. 92–105, 2015, doi: 10.1016/j.neuron.2015.01.028.

[5] G. Buzsaki and A. Draguhn, "Neuronal oscillations in cortical networks," *Science (80-.).*, vol. 304, no. 5679, pp. 1926–1929, 2004, doi: 10.1126/science.1099745.

[6] G. Buzsáki, C. a. Anastassiou, and C. Koch, "The origin of extracellular fields and currents — EEG, ECoG, LFP and spikes," *Nat. Rev. Neurosci.*, vol. 13, no. 6, pp. 407–420, May 2012, doi: 10.1038/nrn3241.

[7] T. Someya, Z. Bao, and G. G. Malliaras, "The rise of plastic bioelectronics," *Nature*, vol. 540, no. 7633, pp. 379–385, 2016, doi: 10.1038/nature21004.

[8] G. D. Spyropoulos, J. N. Gelinas, and D. Khodagholy, "Internal ion-gated organic electrochemical transistor: A building block for integrated bioelectronics," 2019. [Online]. Available: https://www.science.org

[9] H. Fang *et al.*, "Ultrathin, transferred layers of thermally grown silicon dioxide as biofluid barriers for biointegrated flexible electronic systems," *Proc. Natl. Acad. Sci.*, vol. 113, no. 42, pp. 11682–11687, Oct. 2016, doi: 10.1073/pnas.1605269113.

[10] D.-H. Kim *et al.*, "Stretchable and Foldable Silicon Integrated Circuits," *Nature*, vol. 320, no. April, pp. 507–511, Apr. 2008.

[11] J. H. Cho, J. Lee, Y. He, B. Kim, T. P. Lodge, and C. D. Frisbie, "High-capacitance ion gel gate dielectrics with faster polarization response times for organic thin film transistors," *Adv. Mater.*, vol. 20, no. 4, pp. 686–690, Feb. 2008, doi: 10.1002/adma.200701069.

[12] S. H. Kim *et al.*, "Electrolyte-gated transistors for organic and printed electronics," *Adv. Mater.*, vol. 25, no. 13, pp. 1822–1846, 2013, doi: 10.1002/adma.201202790.

[13] M. J. Panzer and C. D. Frisbie, "Polymer electrolyte-gated organic field-effect transistors: low-voltage, high-current switches for organic electronics and testbeds for probing electrical transport at high charge carrier density.," *J. Am. Chem. Soc.*, vol. 129, no. 20, pp. 6599–607, May 2007, doi: 10.1021/ja0708767.

[14] F. Zare Bidoky *et al.*, "Sub-3 V ZnO Electrolyte-Gated Transistors and Circuits with Screen-Printed and Photo-Crosslinked Ion Gel Gate Dielectrics: New Routes to Improved Performance," *Adv. Funct. Mater.*, vol. 0, no. 0, p. 1902028, May 2019, doi: 10.1002/adfm.201902028.

[15] M. Ha *et al.*, "Printed , Sub-3V Digital Circuits on Inks," *ACS Nano*, vol. 4, no. 8, pp. 4388–4395, Aug. 2010, doi: 10.1021/nn100966s.

[16] D. Braga, N. C. Erickson, M. J. Renn, R. J. Holmes, and C. D. Frisbie, "High-Transconductance Organic Thin-Film Electrochemical Transistors for Driving Low-Voltage Red-Green-Blue Active Matrix Organic Light-Emitting Devices," *Adv. Funct.*

Mater., vol. 22, no. 8, pp. 1623–1631, Feb. 2012, doi: 10.1002/adfm.201102075.
[17] E. Song *et al.*, "Flexible electronic/optoelectronic microsystems with scalable designs for chronic biointegration," *Proc. Natl. Acad. Sci. U. S. A.*, vol. 116, no. 31, pp. 15398–15406, 2019, doi: 10.1073/pnas.1907697116.
[18] J. Rivnay, S. Inal, A. Salleo, R. M. Owens, M. Berggren, and G. G. Malliaras, "Organic electrochemical transistors," *Nat. Rev. Mater.*, vol. 3, p. 17086, 2018, doi: 10.1038/natrevmats.2017.86.
[19] A. Giovannitti *et al.*, "Controlling the mode of operation of organic transistors through side-chain engineering," *Proc. Natl. Acad. Sci.*, vol. 113, no. 43, pp. 12017 LP – 12022, Oct. 2016, doi: 10.1073/pnas.1608780113.
[20] C. B. Nielsen *et al.*, "Molecular Design of Semiconducting Polymers for High-Performance Organic Electrochemical Transistors," *J. Am. Chem. Soc.*, vol. 138, no. 32, pp. 10252–10259, Aug. 2016, doi: 10.1021/jacs.6b05280.
[21] P. Schmode, D. Ohayon, P. M. Reichstein, A. Savva, S. Inal, and M. Thelakkat, "High-Performance Organic Electrochemical Transistors Based on Conjugated Polyelectrolyte Copolymers," *Chem. Mater.*, vol. 31, no. 14, pp. 5286–5295, Jul. 2019, doi: 10.1021/acs.chemmater.9b01722.
[22] D. A. Bernards and G. G. Malliaras, "Steady-state and transient behavior of organic electrochemical transistors," *Adv. Funct. Mater.*, vol. 17, no. 17, pp. 3538–3544, 2007, doi: 10.1002/adfm.200601239.
[23] E. Stavrinidou *et al.*, "Direct measurement of ion mobility in a conducting polymer.," *Adv. Mater.*, vol. 25, no. 32, pp. 4488–93, Aug. 2013, doi: 10.1002/adma.201301240.
[24] D. Khodagholy *et al.*, "High speed and high density organic electrochemical transistor arrays," *Appl. Phys. Lett.*, vol. 99, no. 16, pp. 99–102, 2011, doi: 10.1063/1.3652912.
[25] D. Khodagholy *et al.*, "Highly Conformable Conducting Polymer Electrodes for In Vivo Recordings.," *Adv. Mater.*, pp. 1–5, Aug. 2011, doi: 10.1002/adma.201102378.
[26] X. Crispin *et al.*, "The Origin of the High Conductivity of (PEDOT:PSS) Plastic Electrodes," *Chem. Mater.*, vol. 18, no. 4, pp. 4354–4360, 2006, doi: 10.1021/cm061032+.
[27] G. D. Spyropoulos *et al.*, "Organic and perovskite solar modules innovated by adhesive top electrode and depth-resolved laser patterning," *Energy Environ. Sci.*, vol. 9, no. 7, pp. 2302–2313, 2016, doi: 10.1039/c6ee01555g.
[28] Y. Zhou *et al.*, "A Universal Method to Produce Low–Work Function Electrodes for Organic Electronics," vol. 873, no. April, pp. 327–332, 2012, doi: 10.1126/science.1218829.
[29] Z. Lin, J. Chang, J. Zhang, C. Jiang, J. Wu, and C. Zhu, "A work-function tunable polyelectrolyte complex (PEI:PSS) as a cathode interfacial layer for inverted organic solar cells," *J. Mater. Chem. A*, vol. 2, no. 21, pp. 7788–7794, 2014, doi: 10.1039/C4TA00289J.
[30] Y. Xuan, M. Sandberg, M. Berggren, and X. Crispin, "An all-polymer-air PEDOT battery," *Org. Electron. physics, Mater. Appl.*, vol. 13, no. 4, pp. 632–637, 2012, doi: 10.1016/j.orgel.2011.12.018.
[31] Y. Van De Burgt *et al.*, "A non-volatile organic electrochemical device as a low-voltage artificial synapse for neuromorphic computing," *Nat. Mater.*, vol. 16, no. 4, pp. 414–418, 2017, doi: 10.1038/NMAT4856.
[32] I. Zozoulenko, A. Singh, S. K. Singh, V. Gueskine, X. Crispin, and M. Berggren, "Polarons, Bipolarons, And Absorption Spectroscopy of PEDOT," *ACS Appl. Polym. Mater.*, vol. 1, no. 1, pp. 83–94, 2019, doi: 10.1021/acsapm.8b00061.

[33] M. N. V. Ravi Kumar and R. K. MNV., "A review of chitin and chitosan applications," *React. Funct. Polym.*, vol. 46, no. 1, pp. 1–27, 2000, doi: 10.1016/S1381-5148(00)00038-9.

[34] H. L. Jiang *et al.*, "Chitosan-graft-polyethylenimine as a gene carrier," *J. Control. Release*, vol. 117, no. 2, pp. 273–280, 2007, doi: 10.1016/j.jconrel.2006.10.025.

[35] D. Khodagholy *et al.*, "In vivo recordings of brain activity using organic transistors," *Nat. Commun.*, vol. 4, 2013, doi: 10.1038/ncomms2573.

[36] D. Khodagholy *et al.*, "High transconductance organic electrochemical transistors," *Nat. Commun.*, vol. 4, 2013, doi: 10.1038/ncomms3133.

[37] J. Rivnay *et al.*, "High-performance transistors for bioelectronics through tuning of channel thickness," *Sci. Adv.*, no. May, pp. 1–5, 2015.

[38] S. Inal, G. G. Malliaras, and J. Rivnay, "Benchmarking organic mixed conductors for transistors," *Nat. Commun.*, vol. 8, no. 1, pp. 1–6, 2017, doi: 10.1038/s41467-017-01812-w.

[39] D. Khodagholy *et al.*, "NeuroGrid: Recording action potentials from the surface of the brain," *Nat. Neurosci.*, vol. 18, no. 2, pp. 310–315, 2015, doi: 10.1038/nn.3905.

[40] A. Fernández-Ruiz, A. Oliva, E. F. de Oliveira, F. Rocha-Almeida, D. Tingley, and G. Buzsáki, "Long-duration hippocampal sharp wave ripples improve memory," *Science*, vol. 364, no. 6445, pp. 1082–1086, 2019, doi: 10.1126/science.aax0758.

[41] R. D. Wimmer *et al.*, "Sustaining sleep spindles through enhanced SK2-channel activity consolidates sleep and elevates arousal threshold," *J Neurosci*, vol. 32, no. 40, pp. 13917–13928, 2012, doi: 10.1523/JNEUROSCI.2313-12.2012.

[42] E. Krook-Magnuson, J. N. Gelinas, I. Soltesz, and G. Buzsáki, "Neuroelectronics and biooptics: Closed-loop technologies in neurological disorders," *JAMA Neurol.*, vol. 72, no. 7, pp. 823–829, 2015, doi: 10.1001/jamaneurol.2015.0608.

[43] H. H. Choi, K. Cho, C. D. Frisbie, H. Sirringhaus, and V. Podzorov, "Critical assessment of charge mobility extraction in FETs," *Nat. Publ. Gr.*, vol. 17, no. 1, pp. 2–7, 2018, doi: 10.1038/nmat5035.

[44] J. Rivnay *et al.*, "Structural control of mixed ionic and electronic transport in conducting polymers," *Nat. Commun.*, vol. 7, pp. 1–9, Apr. 2016, doi: 10.1038/ncomms11287.

[45] V. Podzorov, "Organic single crystals: Addressing the fundamentals of organic electronics," *MRS Bull.*, vol. 38, no. 1, pp. 15–24, 2013, doi: 10.1557/mrs.2012.306.

[46] S. Inal *et al.*, "A high transconductance accumulation mode electrochemical transistor," *Adv. Mater.*, vol. 26, no. 44, pp. 7450–7455, 2014, doi: 10.1002/adma.201403150.

[47] J. Viventi *et al.*, "Flexible, foldable, actively multiplexed, high-density electrode array for mapping brain activity in vivo," *Nat. Neurosci.*, vol. 14, no. 12, pp. 1599–1605, 2011, doi: 10.1038/nn.2973.

[48] B. Crone *et al.*, "Large-scale complementary integrated circuits based on organic transistors," *Nature*, vol. 403, p. 521, Feb. 2000.

[49] Y. Kim *et al.*, "A bioinspired flexible organic artificial afferent nerve," *Science*, vol. 360, no. 6392, pp. 998–1003, 2018, doi: 10.1126/science.aao0098.

[50] E. Zeglio *et al.*, "Conjugated Polyelectrolyte Blends for Electrochromic and Electrochemical Transistor Devices," *Chem. Mater.*, vol. 27, no. 18, pp. 6385–6393, Sep. 2015, doi: 10.1021/acs.chemmater.5b02501.

[51] M. Sessolo *et al.*, "Easy-to-fabricate conducting polymer microelectrode arrays," *Adv. Mater.*, vol. 25, no. 15, pp. 2135–2139, 2013, doi: 10.1002/adma.201204322.

[52] D. Khodagholy, J. N. Gelinas, and G. Buzsáki, "Learning-enhanced coupling between ripple oscillations in association cortices and hippocampus," *Science (80-.).*, vol. 372, no. October, pp. 369–372, Oct. 2017.

[53] A. Peyrache, F. P. Battaglia, and A. Destexhe, "Inhibition recruitment in prefrontal cortex during sleep spindles and gating of hippocampal inputs," *Proc. Natl. Acad. Sci.*, vol. 108, no. 41, pp. 17207–17212, 2011, doi: 10.1073/pnas.1103612108.

[54] F. Khan, R. S. Tare, R. O. C. Oreffo, and M. Bradley, "Versatile biocompatible polymer hydrogels: Scaffolds for cell growth," *Angew. Chemie - Int. Ed.*, vol. 48, no. 5, pp. 978–982, 2009, doi: 10.1002/anie.200804096.

[55] G. Buzsaki, "Hippocampal Sharp Wave-Ripple : A Cognitive Biomarker for Episodic Memory and Planning," *Hippocampus*, vol. 25, no. 10, pp. 1073–1188, 2015, doi: 10.1002/hipo.22488.

[56] M. J. Morrell, "Responsive cortical stimulation for the treatment of medically intractable partial epilepsy," *Neurology*, vol. 77, no. 13, pp. 1295–1304, 2011, doi: 10.1212/WNL.0b013e3182302056.

[57] K. A. González Otárula, Y. Mikhaeil-Demo, E. M. Bachman, P. Balaguera, and S. Schuele, "Automated seizure detection accuracy for ambulatory EEG recordings," *Neurology*, vol. 92, no. 14, pp. e1540–e1546, 2019, doi: 10.1212/WNL.0000000000007237.

[58] J. N. Gelinas, D. Khodagholy, T. Thesen, O. Devinsky, and G. Buzsáki, "Interictal epileptiform discharges induce hippocampal–cortical coupling in temporal lobe epilepsy," *Nat. Med.*, vol. 22, no. 6, pp. 641–648, Jun. 2016, doi: 10.1038/nm.4084.

Chapter 5: Ionic Communication for Implantable Bioelectronics

Implanted bioelectronic devices are increasingly being used to monitor and treat disease [1]–[3]. Signal transmission from the implanted device to the external electronics is a major challenge for safe, effective, long-term use. Physiologic signals are robustly transmitted by cables due to their simplicity and high data rate capacity, but this approach requires permanent tissue traversing components that limit their use in chronic applications. Wireless data transmission from implanted devices has been accomplished using radio frequency (RF) and ultrasound-based communication [4]–[10]. The complex, high-power consumption, non-biocompatible, and rigid RF electronic components combined with the high ionic conductivity of biological tissue place severe restrictions on its signal transmission capabilities [11]–[13]. As a result, the majority of RF-based systems require tissue extruding components that interface with a transmitter placed outside the body [14], [15]. Although ultrasound has better tissue penetration than RF, communication is strongly dependent on the coupling factor between the transmitter and receiver, allowing tissue inhomogeneity and mechanical movements to introduce instability [5], [7], [8], [10], [16]. Optical methods have high power consumption, and are limited by light scattering within tissue [17]. Therefore, approaches that harmonize with the properties of biological tissue to facilitate simple, yet reliable, data transmission are lacking. Intra-body communication that utilizes ion-conducting tissue as the medium to transmit information has been proposed. Signals have been transmitted across the tissue surface using externally applied electric potential, and this circuit is completed by capacitive coupling with the surrounding environment (air) [18], [19]. Therefore, this approach cannot be utilized for transmission from a fully implanted device, because a permanent conduit with the environment is required to complete the circuit. Because the signal is transmitted by ion

transport between transmitter and receiver, speed of communication is also dictated by ion mobility [20].

Neuroelectronic devices have some of the most demanding requirements for data transmission due to the high spatial and temporal sampling required to interpret and modulate brain activity[21]. Sampling neural activity at several kHz per second from multiple electrodes improves representation of activity patterns and allows targeted feedback [22]–[24]. Such devices are currently used to diagnose and treat neuropsychiatric disorders [25]–[27], decode neural representations for brain-machine-interfaces [28], [29], and establish the functional relevance of neural activity [30]. However, data transmission challenges complicate clinical device implementation. For instance, brain machine interfaces to enable control of assistive movement and communication devices in paralyzed patients require a chronically implanted, bulky, and rigid transcutaneous port that transmits high spatiotemporal resolution neural signals from a microelectrode array to external processors [28]. Bioelectronics for responsive neurostimulation to abort seizures (NeuroPace) are fully implanted and communicate using RF, but necessitate a large, rigidly encapsulated processing unit and the number of transmitted channels is limited [31]. Here, we introduce ionic communication (IC) that leverages ions in biologic tissue to propagate MHz-range signals. We demonstrate that IC operates by generating and sensing stored electrical potential energy within polarizable media in a frequency-dependent manner. We determined the geometric properties that govern IC transmission depth and controlled transmission radius to permit multi-line parallel communication. We integrated IC with advanced neural interfaces to create a fully implantable device capable of acquisition and non-invasive transmission of neurophysiologic data from freely moving rats over a period of weeks. IC enabled a stable, efficient link with implanted components, and had communication efficiency (data rate/power

consumption) several orders of magnitude above other approaches employed with implantable bioelectronics. We used IC for real-time transmission of multi-channel local field potential (LFP) and neural spiking data, with data quality sufficient for clustering of individual neuronal action potentials. IC creates a high-speed, low-power link between implanted and external electronics with the potential to enhance the safety and efficiency of a wide range of bioelectronic devices.

5.1 Configuration and Characterization of Ionic Communication (IC)

Polarizability governs a material's dielectric constant (also known as relative permittivity) and reflects the frequency-dependent ability to store potential energy under the influence of an electric field. Electromagnetic waves are efficiently generated and propagated within low relative permittivity materials. As the relative permittivity increases, more energy is stored in the material and the transmission efficiency decreases [11]–[13]. When materials contain charge carriers, such as electrons or ions, electromagnetic energy is also converted into conduction currents, impeding generation and limiting propagation to the material's specific skin depth in a frequency-dependent manner [32]. Therefore, the ion-rich, aqueous nature of biological tissue limits use of radio frequency technologies in implantable devices. We hypothesized that we could transmit electrical signals by sensing the stored electrical potential energy within the tissue, rather than relying on an implanted antenna. Application of alternating potential across a pair of implanted electrodes would transfer energy into the tissue, with efficiency dictated by the material's conductivity and polarizability, as well as the frequency of the applied potential.

To test this hypothesis, we first developed an experimental setup consisting of two pairs of Au-based electrodes with identical geometry placed parallel to each other across a medium to simulate tissue (Figure 1A). In this manner, one pair serves as signal transmitter (TX, implanted) that is connected to a constant amplitude frequency sweep signal from 1 Hz – 10 MHz and the second

pair functions as a receiver (RX, on the surface), permitting differential amplification of the transmitted potential across its constituent electrodes. To evaluate the capacity of such a device to establish a communication link across tissue, we performed frequency response measurements from the RX in media with varying ion concentrations of phosphate buffer saline (10^{-3}, 10^{-2}, 10^{-1} and 1×, PBS (Figure 1B). Each frequency response curve was characterized by an inverted U pattern, with increasing response between 1 Hz – 1 KHz, an intervening plateau, and decreasing response above 10 KHz – 100 MHz. Increasing ion concentration shifted the curve to the right, resulting in maximal response at higher frequencies relative to lower ion concentrations. We attributed these responses to a combination of properties derived from the i) electrode/electrolyte interface; ii) material composition of the electrolyte. We investigated this electrode/electrolyte interface, which is modeled by a resistive-capacitive (RC) circuit due to existence of electric double layer capacitance (EDL)[33], by performing electrochemical impedance spectroscopy (EIS) using the same electrodes and media. At low frequencies (< 1 KHz), the interface is dominated by the capacitive component of the EDL, and we found that the impedance (Z) was independent of the medium's ion concentration (Figure 1C). At higher frequencies, the contribution of this capacitance to the impedance becomes negligible ($Z \sim 1/C$); and the impedance is governed by the resistive component. In keeping with this notion, higher ion concentrations resulted in lower impedance at these frequencies (Figure 1C; red shading). The material composition of the electrolyte can also be modeled as an RC, with the resistive component arising from strength of ionic conduction, and the capacitive component determined by the polarizability (quantified by relative permittivity, ε_r)[34]. These results suggest that the frequency response curves of IC can be separated into two regimes: i) EDL-RC dominated (yellow) at low frequencies; and ii) medium-RC dominated at higher frequencies (red), generating a medium-specific bandpass

of maximal IC response (Figure 1D). Consistent with this model, media with very low ion concentration (deionized water, DI) exhibited less response than ionic electrolytes and a further left-shifted frequency response curve (Figure 1B, gray). Media with low polarizability (isopropyl alcohol, IPA) had the lowest response across the spectrum (Figure 1B, red). Ionic aqueous solutions, such as those that comprise the extracellular space of tissue, are therefore optimally situated to maximally transmit alternating potential at high frequencies.

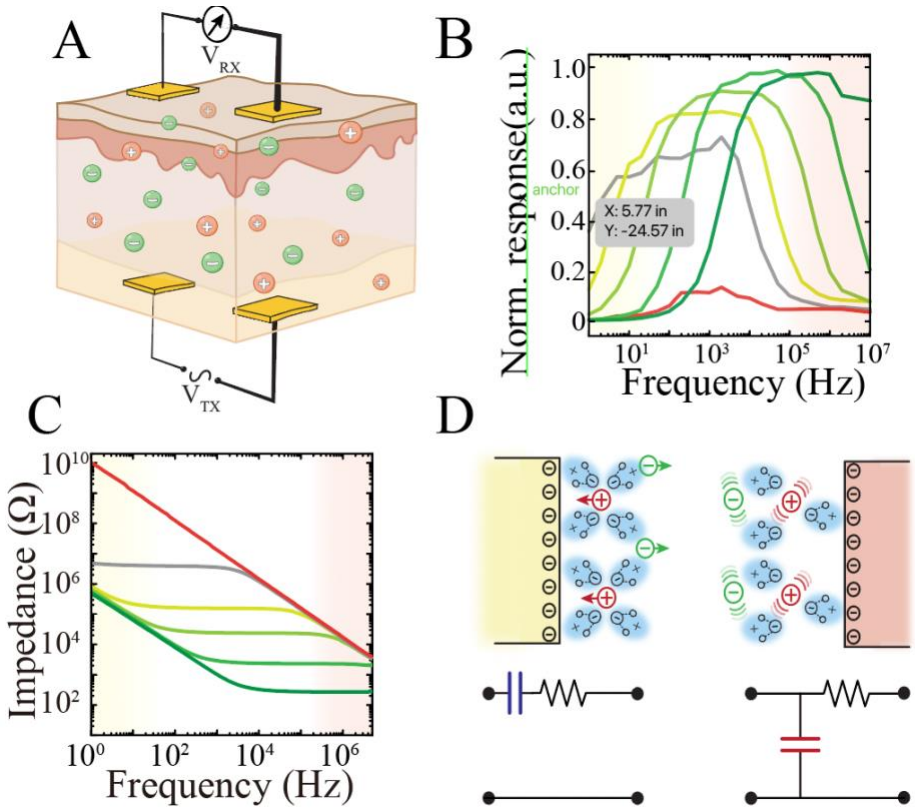

Figure 1: Configuration and characterization of IC. A) Cross sectional schematic illustration of an IC device consisting of an implanted transmitter (TX) electrode pair inside biological tissue with ionic charge carriers (anions (green) and cations (red)), and a receiver electrode pair (RX) on the surface of the tissue. VTX denotes the transmitter signal while VRX represents the measured voltage from the RX outside of tissue. B) Frequency responses of IC acquired in 10-3, 10-2, 10-1 and 1× PBS (darker shades represent higher concentrations), deionized water (DI; gray) and isopropanol (IPA; red) with a 1 Hz – 10MHz VTX sweep signal . Interelectrode spacing as well as distance between TX and RX arrays was fixed at 25 mm. C) Electrochemical impedance of an IC electrode as a working electrode in the same media as (B); color scheme as per (B). Ag/AgCl electrodes were used as counter and reference electrodes. D) Schematic of EDL capacitance (yellow; top left) at electrode/electrolyte interface and its corresponding simplified series RC model (bottom left). Schematic of capacitance resulting from media polarizability (red; top right) and its parallel RC model (bottom right).

Next, we established that IC is distinct from intra-body communication approaches both in regards to its operating mechanism and performance. We designed experiments that directly compared the performance of IC with capacitive coupling and galvanic coupling-based communication for implantable devices. Intra-body capacitive coupling (CC) utilizes cutaneous tissue and the environment (air) between RX and TX terminals as communication medium **(**Figure 2A; top**).** As its name implies, this circuit is comprised of a capacitor formed by the air /environment as dielectric between RX and TX terminals **(**Figure 2A; top highlighted in yellow**)** [18], [35]. Therefore, the simplified circuit diagram of CC is composed of two paths between TX (source) and RX (measure): (i) a lateral cutaneous path consisting of the tissue impedance (Z_T) in series with the electrode/tissue interface impedance, defined by the tissue's electrochemical properties, electrode materials, and effective electrode area; and (ii) an environmental path consisting of the environmental capacitance (C_{env}), defined by the size of RX and TX electrodes and the dielectric properties of the environment and air **(**Figure 2A; middle**)**. The value of C_{env} plays a critical role in feasibility and stability of communication between RX and TX. Higher values of C_{env} result in lower impedance of the environmental path and robust communication via CC. Even when C_{env} is high (Figure 2A, blue zone), only short-term exchange of small data packets, such as business card information, is possible because changes in the environment (e.g. air flow, lighting) directly affect C_{env} and as such the stability of the link. In order to create an implantable device based on CC, the environmental path must be within the body. However, the high ion concentration of body tissue reduces the capacitance of the environmental path to several orders of magnitude lower than that required for CC-based communication **(**Figure 2A; bottom). To increase the stability of the environmental path, intra-body galvanic coupling (GC) was introduced [36]. GC replaced the environmental path of CC with another cutaneous path by placing both pairs of RX and TX on the

tissue surface (Figure 2B; top). The simplified circuit model of GC is composed of four electrode/tissue interface impedances connected to a network of tissue impedances. When the electrode/tissue interface impedance is low relative to the tissue impedance, a practical voltage division is established that allows communication. Low interface impedance is typically accomplished by using large electrodes. In this manner, the circuit impedances can also remain constant and independent of the environment, providing more communication stability compared to CC. An implantable device based on GC requires the TX to be moved from a position on the tissue surface, where tissue impedance is high (Figure 2B; bottom, blue zone), to within the tissue, where impedance is much lower [37], [38] (Figure 2B; bottom, red zone). Tissue impedance in this arrangement only sufficiently exceeds interface impedance at low frequencies (~ KHz regime) and when interface impedance is maximally decreased (e.g. by increasing electrode size; Figure 2B, lighter shaded curves), precluding practical use.

In contrast to CC and GC, IC is specifically designed for use with fully implantable devices, where TX is within tissue and RX is on the surface (Figure 2C; top). Based on electrochemical impedance and frequency measurements performed in the presence of varying ion concentrations and media polarizability (Figure 1), we defined the IC simplified circuit model as a band-pass filter. The electric double layer capacitance between the tissue and electrode (Figure 2C; middle, series blue capacitor) accounts for the high-pass regime (rising section of curves in Figure 1B), whereas the capacitance due water polarization in the presence of physiologic concentrations of ions (Figure 2c; middle, parallel red capacitor) defines the low-pass regime (falling section of curves in Figure 1B). The high ion concentration and water content of tissue results in an effective bandpass (flat area of the curves in Figure 1B) between 10^5-10^7 Hz, optimal for high speed communication (Figure 2C; bottom, green trace).

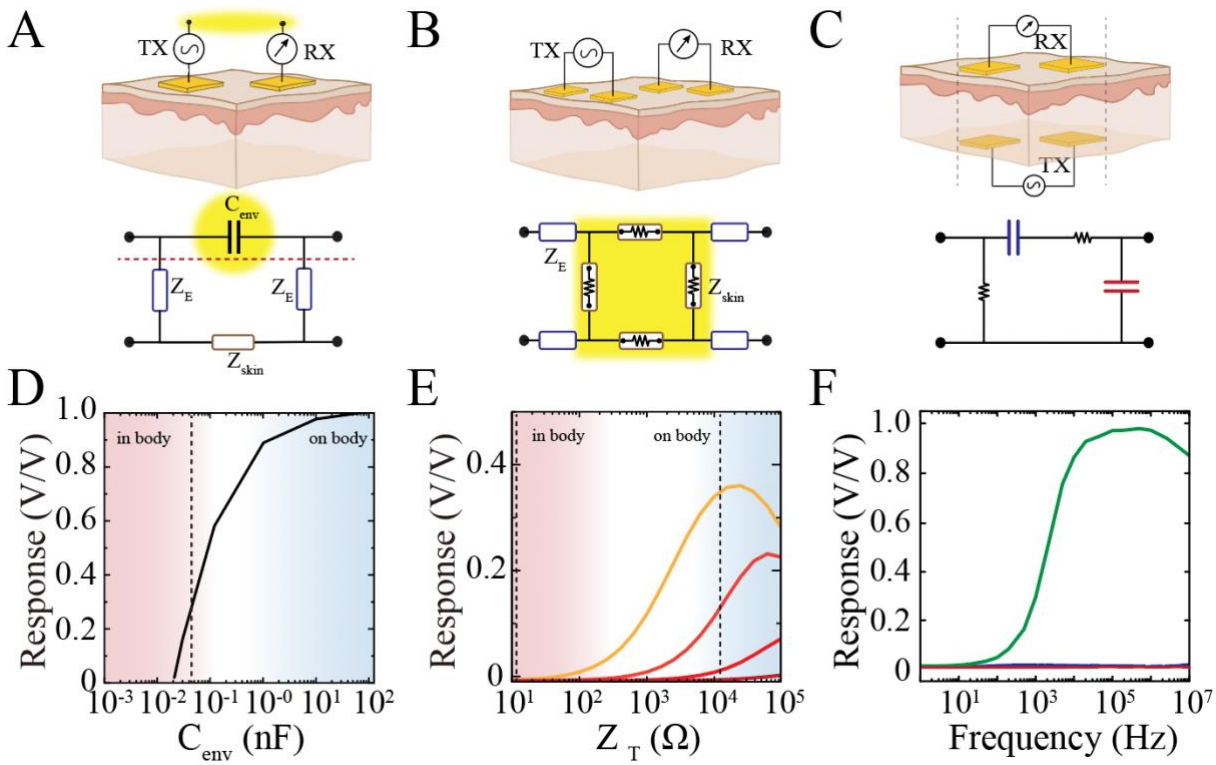

Figure 2: Comparison of IC with capacitive (CC) and galvanic (GC) intrabody communication. A) Cross-sectional schematic illustrating location and arrangement of TX and RX for CC. Highlighted area illustrates the environmental capacitance (Cenv) between RX and TX via shared environment (top). Corresponding simplified circuit model of CC; ZE = electrode/body interface impedance, Zskin = tissue impedance. Yellow highlighted area emphasizes the necessity of a capacitive return path through the environment (middle). Normalized response defined by the ratio of VTX and VRX as a function of Cenv. Blue area localizes the range of achievable capacitance values when the electrodes are on a tissue surface or outside body. Red area marks the effective capacitance when electrodes are placed within tissue. B) Cross-sectional schematic illustrating location and arrangement of TX and RX for GC. Corresponding simplified circuit model of GC with similar notation as (A). The highlighted area emphasizes the necessity of high overall tissue impedance to create a voltage divider (middle). Normalized response, as in (A), as a function of tissue impedance (ZT). The superimposed curves show TX with 103 to 106 ohms (orange to red, respectively) impedances (ZE). Blue area localizes the range impedances for the tissue surface. Red area marks impedance ranges within tissue. C) Cross-sectional schematic illustrating location of TX and RX for IC. TX is implanted within tissue, and RX is placed on the external tissue surface. The dashed lines indicate that TX and RX are aligned (top). Corresponding simplified circuit model of IC that accounts for EDL capacitance in blue and capacitance from polarizability of water in red (middle). Frequency responses of IC (black), as well as implanted configurations of CC (red) and GC (blue). Au-based TX and RX electrodes (25 mm) were used in PBS for all experiments.

We directly and experimentally compared the performance of CC, GC and IC in a fully implanted configuration. All electrodes and geometries were kept constant across the communication methods. We found that IC (Figure 2C; bottom, green trace) maintained a high constant response

at MHz frequencies, whereas CC (red) and GC (blue) exhibited negligible responses across the frequency spectrum, with no effective signal received **(**Figure 2C; bottom**)**. Therefore, CC and GC cannot serve as data transmission methods for fully implantable devices, and IC is a practically and mechanistically distinct, effective method for this purpose.

5.2 IC Operation Frequencies

After establish IC as a potentially viable strategy for implantable device communication, we began investigating electrode/electrolyte interface by examining the effect of TX/RX electrode material composition and geometry on the IC frequency response. We fabricated Au and conducting polymer-based (Poly–3,4-ethylenedioxythiophene–polystyrenesulfonate, PEDOT:PSS) IC electrode pairs spanning two orders of magnitude in size. It is known that conducting polymers reduce the electrochemical impedance of noble metals [39]. This impedance reduction is primarily mediated by increased uptake of ions across the bulk of the hydrophilic PEDOT:PSS film, which enlarges the electrode/electrolyte capacitance[40], [41]. We found that the conducting polymer resulted in higher capacitance (lower impedance) than Au for a given electrode size at low frequencies, and that the impedances became equivalent at high frequencies. However, the corner frequency (f_c) of the EIS curves was left-shifted for a PEDOT:PSS compared to a Au electrode of the same size. Larger electrode size was associated with decreased impedance across the frequency spectrum (Figure 3A). We observed that the EIS f_c was equivalent to the corner frequency of the IC frequency response curve (f_{IC}; Figure 3B), suggesting that the EDL plays a critical role in the effective bandwidth for IC operation. Extracting f_{IC} for the electrodes characterized in Figure 3a revealed that use of conducting polymer as TX/RX electrode material extends the bandwidth for IC by 2 orders of magnitude for any given electrode size (**Figure 3c**). Therefore, even though

improving the electrochemical capacitance of the TX/RX does not directly affect the signal response for IC, it enables a wider range of IC operating frequencies with smaller electrodes.

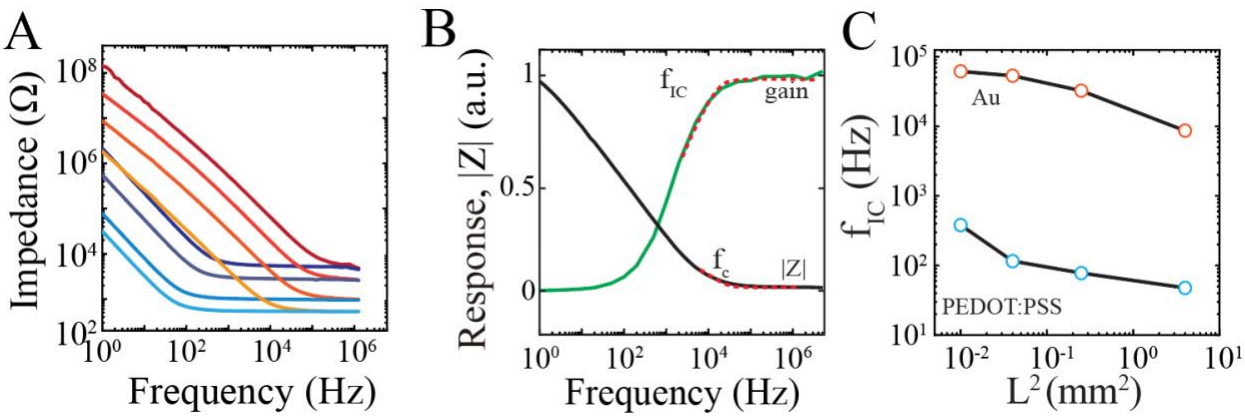

Figure 3: Use of conducting polymers lowers electrochemical impedance to expand the range of effective IC operation frequencies. (A) Electrochemical impedance of conducting polymer–based (shades of blue) and Au-based (shades of red) IC electrodes with 0.5-, 1-, 2-, and 5-mm length (darker shades represent shorter lengths). (B) Normalized IC response (green) and electrochemical impedance (black) spectrum of an IC electrode (W, L, D = 5 mm) highlighting the alignment of Fc and FIC. The red dashed superimposed lines are exponential fits of the response and impedance curves that resulted into fc = 8.63 KHz and fIC = 8.71 KHz. (C) Turning frequency of Au and PEDOT:PSS–based electrodes as a function of their area. The larger capacitance of PEDOT:PSS results in lower turning frequencies.

5.3 IC Parallel High-Bandwidth Logic Data Transmission

We next asked across what tissue distance IC could effectively transmit. We fabricated IC RX/TX pairs with geometries spanning 2 orders of magnitude in their length (L), distance between electrodes in a pair (W), and the distance between the TX and RX pairs (D), and measured the frequency response curves for each configuration. IC response was linearly and independently correlated with each measure, increasing proportionally with L and W, but decreasing with D (Figure 4A-B). As such, any combination of L and W that resulted in the same multiplicative product was associated with the same D. Effective signal acquisition at the RX is also affected by the voltage of signal applied to the TX. To understand the relationship between these factors, we determined the maximal D across which signals could be reliably acquired at each combined geometry (L × W) for 4 different TX signal voltages (Figure 4C). At an operating voltage of 50

mV, a combined geometry of 9 mm^2 (which could be achieved, for example, by a configuration of 3a mm RX/TX electrode length (L) with 3 mm between the electrodes of the TX (W)) resulted in a transmission depth of 50 mm. At the lowest operating voltage tested (1 mV), a transmission depth of 50 mm necessitated increasing the combined geometry to 200 mm^2 (which could be achieved, for example, by a configuration of L = 10 mm and W = 20 mm). Therefore, a range of IC electrode geometries compatible with implantation were capable of communicating across distances required to target a variety of tissue, from human skin to visceral organs. We furthermore directly compared the transmission depth of IC (L = 1 mm) with a Bluetooth Low Energy protocol and found that the RF-based system had dramatically higher signal attenuation in physiological environments. RF, in contrast to IC, was unable to establish a transmission link at distances further than 50 mm and the RF signal attenuation at the smallest measurable depth was greater than IC signal attenuation at a depth of 100 mm.

Digital communication is often an optimal approach because it preserves signal quality, as well as allowing for error correction, encryption, and narrow bandwidth transmission. Because IC effectively transmits high frequency signals, it is primed for use with digital communication protocols. To explore this application, we used a set of TX/RX electrodes across electrolyte to transmit digital pulses. To convert the received signals into a digital stream and simultaneously eliminate amplitude variations due to changes in electrode/electrolyte potential, we employed an automatic variable gain differential amplifier at the RX. This design maintained a constant signal root-mean-square (RMS) over a defined window (10 μs), which was substantially longer than individual pulses transmitted (0.1-1 μs). We found that the rise/fall time of the pulse (τ) after differential amplification was 7.1 ns (Figure 5A). Therefore, using a practical consideration for transmission fidelity of $10 \times \tau$, it would be practically possible to reach 14 MHz communication

(1 / (10 × τ)) with a single IC line. With currently available commercial, discrete amplifiers, we were able to effectively receive and decode digital pulses transmitted up to 6 MHz.

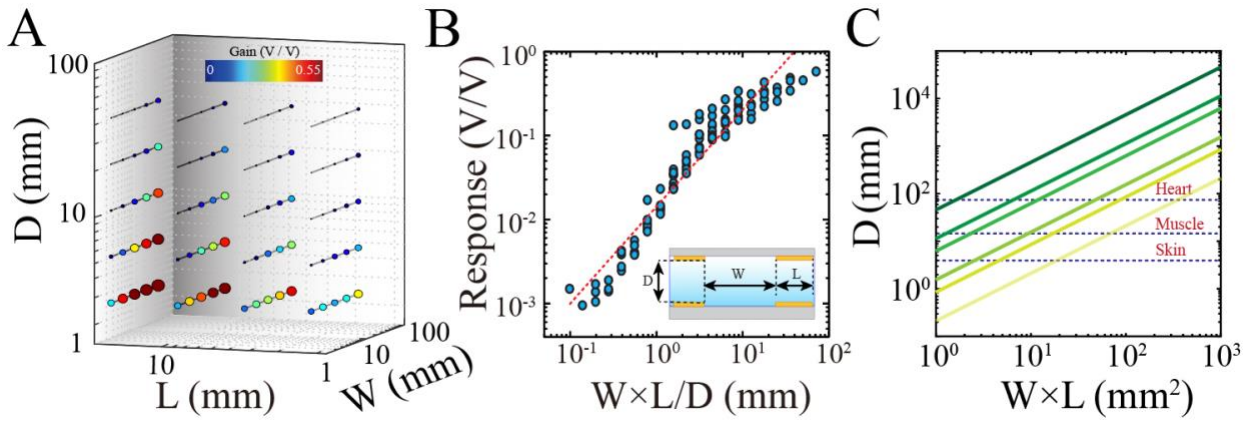

Figure 4: IC transmission depth scales with TX array geometry and operating voltage to enable low-voltage, long-range, and geometrically scalable communication in physiological environments. A) Effect of electrode geometry (W, D, and L) on IC response above fIC frequencies. Larger and warmer colored symbols correspond to larger responses. Each datapoint is determined by extracting the average response of 256 cycles per frequency. B) IC response is linearly positively correlated with the product of W and L, and linearly negatively correlated with D. Inset: Cross-sectional schematic illustrating geometrical parameters of IC device. The blue medium between TX and RX arrays represents the biological tissue; D is the depth of TX inside tissue, W is the interelectrode distance of TX or RX pairs, and L is the length of square electrodes. C) Estimated communication depth of IC based on electrode geometry and operating voltage (1, 5, 10, 50, 100, and 500 mV; darker shades denote higher voltages). The dashed lines denote the approximate distances between the surface and implants in various human tissues**.**

Many bioelectronic devices require multiple parallel lines of data communication, so we explored whether this functionality could be attained using IC. With parallel lines, the rate of data communication can be dramatically increased without necessitating higher operating frequency. This approach would only be feasible if individual IC links (RX and TX pairs) could maintain independent transmission in the absence of cross-talk. We therefore designed an experiment where the physical location of the RX pair could be offset with respect to the TX pair (Figure 5B, inset). The most effective communication (highest response across frequency range) was observed when the RX and TX electrodes were directly aligned. Upon reaching misalignments larger than the electrode geometry (L) a dramatic decay in response was observed (Figure 5B-C). Because the response dropped sharply at the boundary of TX/RX electrode overlap, it is theoretically possible

to create a densely packed conformable array of IC transmitters in co-axial format without introducing cross-talk between the independent transmitters. To test this notion, we next fabricated a conformable array of 10 miniaturized IC TX-RX arrays on a parylene C substrate and bonded them directly to rigid or flexible printed circuits (Figure 5D). Each IC channel was able to operate independently at approximately 6 MHz with minimal crosstalk in this setting (Figure 5E, red). We then combined operation of all ten channels to achieve an overall digital communication speed of up to 60 Mbps (Figure 5E, green). To evaluate signal transmission quality in a physiologic environment, we concurrently operated IC while recording the noise level across the physiologic frequency spectrum using a conventional neural acquisition system sampling from the same medium (Figure 5F). We used a Manchester coding protocol, in which data bits are represented by either a low then high, or a high then low, state for equal time. This approach creates charge-balanced transmission signals and minimizes direct current (DC) components of these signals. The presence of IC components within the medium did not introduce noise into the electrophysiological recordings, suggesting potential for integration into implanted devices designed to assay a variet of biological signals.

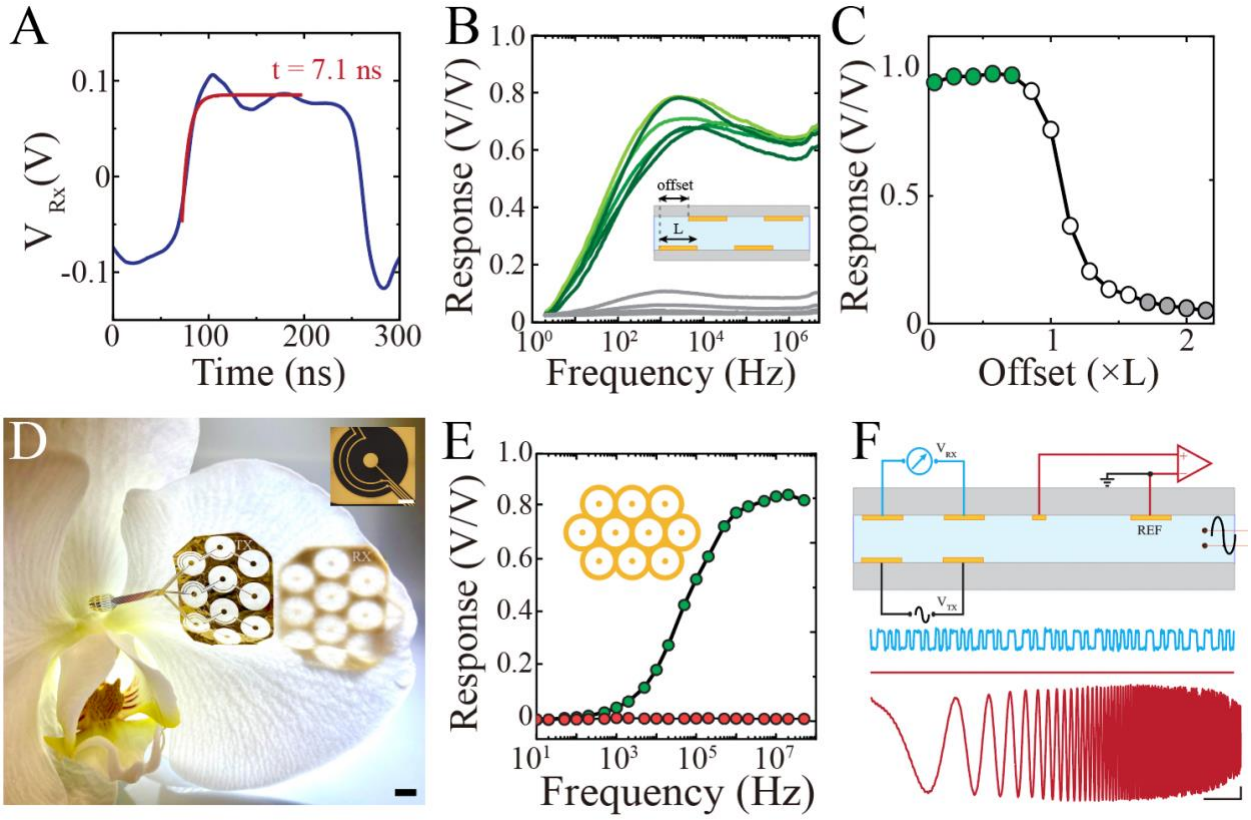

Figure 5: IC establishes high-bandwidth, digital, parallel data communication using conformable electronic substrates. A) Received square pulse at the RX before slicing and digitization. The red trace is the exponential fit of the IC RX voltage before digitization, resulting in a time constant of 7.1 ns (W, L, D = 5 mm). B) Comparison of frequency responses acquired when RX and TX arrays were positioned inside (green) and outside (gray) line of sight. Inset: Cross-sectional schematic illustrating the experimental setup for measuring IC response at various offsets between TX and RX pairs. C) The response of IC as a function of RX and TX positional offset. Green markers show IC response for positions where the RX is within TX's line of sight, whereas unfilled and gray markers indicate partial alignment or full misalignments of TX and RX, respectively (L = 25 mm). D) Four-micrometer-thick, parallelized (10 links) IC TX and RX arrays conforming to the surface of an orchid petal; scale bar, 5 mm. Optical micrograph of one of the coaxial-shaped IC links; scale bar, 500 µm. E) Frequency response of 10-link IC-based communication resulting in stable high response at ~60 MHz bandwidth (black). The red trace shows the absence of cross-talk between two nearby RX and TX pairs. F) Cross-sectional schematic of simultaneous electrophysiological recording and digital IC signal transmission (with 2-MHz, 50-mV amplitude VTX). Lower blue traces show the extracted digital at RX before digitization, and the two red traces are concurrent electrophysiological measurements of ground (top) or a sweep signal (bottom; 1 to 10 KHz; scale bar, 1 mV amplitude). The RMS noise of electrophysiologic (0.1 to 7500 Hz) recordings during operation of IC was 2.7 µVrms compared to 2.4 µVrms without IC operation.

5.4 Low Power, Wireless, High-Speed Ionic Communication for High Spatio-Temporal Resolution Chronic *in-vivo* Electrophysiology

Low power consumption is a critical feature for implanted bioelectronic devices. We determined that IC power consumption remains constant across frequency for a given impedance, with higher TX/RX impedance resulting in lower consumption across all data rates (Figure 6A). Given these properties, IC would be capable of transmitting data from a range of clinical and research implanted devices with low power consumption. We compared IC communication efficiency (defined by power consumption relative to operation speed) to other data transmission approaches. Because IC efficiently operates at low voltages, its communication efficiency surpassed the majority of wireless communication protocols used for such devices (Figure 6B**)**. IC operates by application of MHz-range signals to tissue; thus, we also took the guidelines for power injection based on the International Commission on Non-Ionizing Radiation Protection into consideration [43]. We found that the maximum operating voltages as a function of i) TX array area and ii) distance between TX electrodes within a pair were well within safety boundaries for induced electric fields in tissue.

To test the ability of IC to practically transmit high sampling rate, multichannel data such as would be required for advanced bioelectronic devices, we first devised a surgical protocol to enable chronic implantation in a rodent model **(**Figure 6C**)**. In addition, IC must be compatible with existing Si-based data acquisition and processing devices. We use mixed conducting particulate composite [44] to bond a conformable electrode array to a printed circuit board (PCB) with a neurophysiological acquisition chip (Intan) and a microprocessor to organize acquired data into packets delivered to the attached conformable TX electrodes, each equipped with a nearby encapsulated magnet. A miniaturized battery was used to supply power (Figure 6C). The

conformable shank was implanted into the brain through a scalp incision and craniotomy. Using a trocar-based surgical approach [45], the TX array and battery were tunneled into the subcutaneous space over the dorsal aspect of the rat's neck. All surgical incisions were then closed, resulting in a fully implanted device capable of transcutaneous data transmission. Two miniaturized external magnets were used both as RX electrodes and for fiducial alignment with the implanted TX electrodes. Signals were decoded by a differential amplifier attached to the RX electrodes.

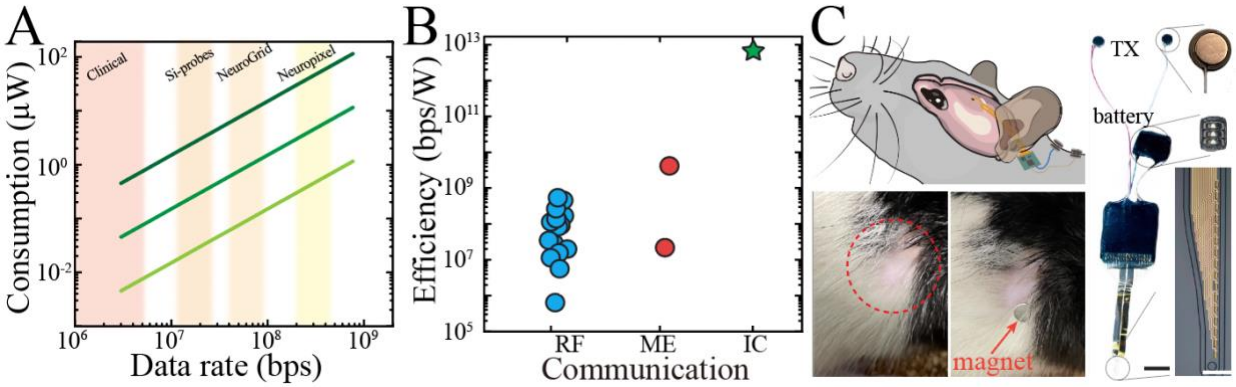

Figure 6: IC enables fully implantable, noninvasive, ultralow power, stable, and high-speed communication for implantable devices. A) Power consumption of IC as a function of data rate and TX electrode impedance (1, 10, and 100 kilohms dark to light). The shaded areas highlight the required data communication bandwidth for using the denoted neural interface devices. B) Efficiency of implantable communication systems derived as the ratio of bandwidth to power consumption for RF waves, mechanical waves (ME), and IC. C) Simplified schematic of the placement and location of the implant in a rat (top left). Complete embedded system with conformable probe and battery before implantation (right; black scale bar, 5 mm; white scale bar, 50 μm). Location of incision for positioning IC electrode 1 week after surgery (bottom left). RX is aligned transcutaneously via the fiducial magnet of the implanted TX array.

With this set-up, we designed a series of experiments to evaluate the ability of IC to transmit chronic intracranial encephalography (iEEG) signals from multi-channel implantable probes in freely moving rats. Rats implanted with IC devices had normal behavior without indications of discomfort, and neural signals were transmitted via IC while the animals successfully performed behavioral tasks on an open field maze. IC established high-speed communication for simultaneous real-time transmission of 32 channels data across intact cutaneous tissue with minimum distortion *in vivo*. The RX array was attached and detached repetitively without

adversely affecting signal quality. Transmitted local field potential (LFP) exhibited identifiable state-dependent time-frequency characteristics (Figure 7A-B) and typical waveform features corresponding to hippocampal area CA1 layers (Figure 7C). We also compared quality of signals transmitted via IC and conventional SPI cables. We found that neural activity patterns did not differ in regards to frequency or duration between the methods. Power spectral density of the wideband transmitted signals were also indistinguishable, demonstrating that IC does not introduce additional noise or spurious signals into neural data.

Furthermore, IC supported data sampled at 20 KHz, permitting acquisition of neural spiking data. Identifying action potentials originating from individual neurons (spike sorting) is precisely dependent on the shape of each action potential waveform (1-2 ms duration), and as such any signal contamination would prevent identification of spiking clusters. We used a conventional spike sorting algorithm and were able to identify multiple putative individual neurons with stable waveforms and typical physiologic firing patterns (Figure 7D-E). These data support the ability of IC to reliably transmit some of the most exacting biological signals.

To evaluate the stability of IC *in vivo*, we performed multiple recording sessions in freely moving rodents over a period of 3 weeks post-device implantation. Physiologic spectral features of the transmitted signals were maintained across these sessions (Figure 7A), and detected neural activity patterns exhibited consistent amplitude, duration, and frequency over weeks. Taken together, these results indicate that IC is fully capable of high quality and long-term signal transmission in naturalistic *in vivo* environments, suggesting broad applicability to a range of implanted devices.

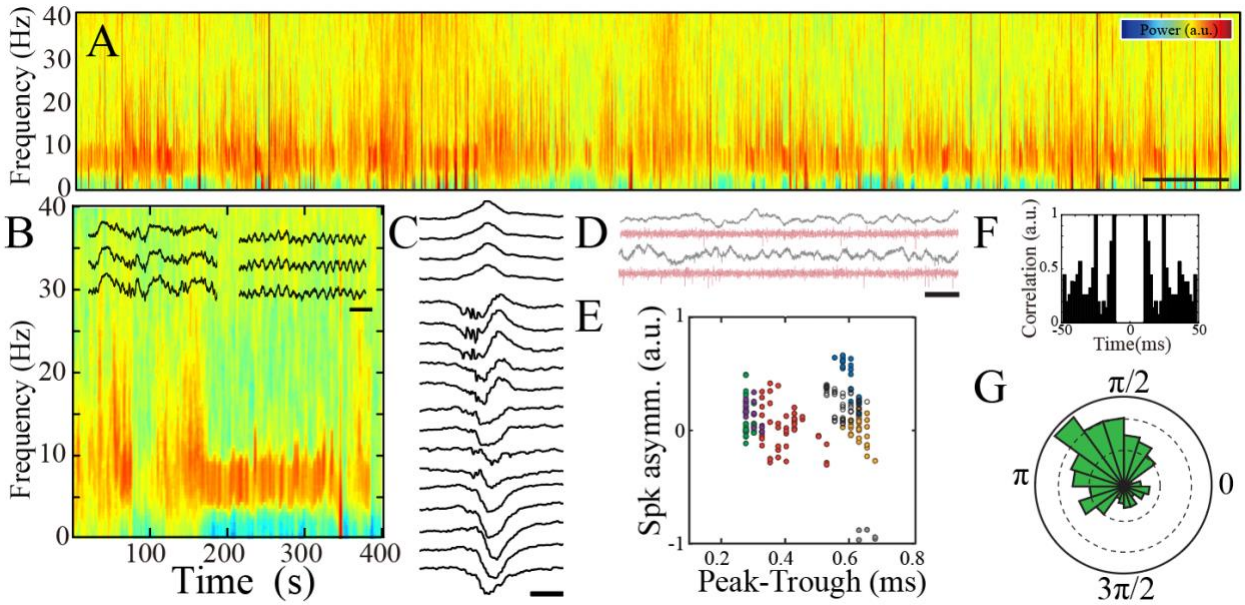

Figure 7: IC enables stable, chronic communication for implantable devices at the resolution of single neurons in vivo. A) Long-term, time-frequency spectrogram of LFP transmitted by IC from a freely moving rat. Each block notated by dashed lines represents data extracted from a separate recording session (scale bar, 15 s). Superimposed white traces illustrate waveform traces of sleep spindles (scale bar, 250 μV, 100 ms). B) Spectrogram of NREM transitioning to REM sleep with superimposed traces of delta waves and sleep spindles during NREM, as well as theta oscillation during REM sleep (scale bar, 200 ms). C) Sample ripple with clear spatial profile across hippocampal CA1 layers (scale bar, 50 ms). D) Sample LFP traces (top) and their corresponding filtered traces (>500 Hz; bottom) with visible neural spiking activity; scale bar, 50 ms. E) Scatterplot of waveform characteristics of putative single units transmitted by the IC in a freely moving rat. Each symbol corresponds to an average spike waveform of 20 spikes from a putative isolated neuron; colors represent different clustered neurons. F) Sample autocorrelation of a putative clustered neuron transmitted by the IC in a freely moving rat. G) Phase-locking of sample putative single unit's spikes to cortical gamma oscillation ($P < 0.01$, circular mean statistics mu = 0.005, $\kappa = 2.33 \times 104$).

References

[1] E. Krook-Magnuson, J. N. Gelinas, I. Soltesz, and G. Buzsáki, "Neuroelectronics and biooptics: Closed-loop technologies in neurological disorders," *JAMA Neurol.*, vol. 72, no. 7, pp. 823–829, 2015, doi: 10.1001/jamaneurol.2015.0608.

[2] P. Jastrzebska-Perfect *et al.*, "Translational Neuroelectronics," *Adv. Funct. Mater.*, vol. 30, no. 29, pp. 1–31, 2020, doi: 10.1002/adfm.201909165.

[3] T. Someya, Z. Bao, and G. G. Malliaras, "The rise of plastic bioelectronics," *Nature*, vol. 540, no. 7633, pp. 379–385, 2016, doi: 10.1038/nature21004.

[4] T. A. Szuts *et al.*, "A wireless multi-channel neural amplifier for freely moving animals," *Nat. Neurosci.*, vol. 14, no. 2, pp. 263–270, 2011, doi: 10.1038/nn.2730.

[5] S. M. Won, L. Cai, P. Gutruf, and J. A. Rogers, "Wireless and battery-free technologies for neuroengineering," *Nat. Biomed. Eng.*, Mar. 2021, doi: 10.1038/s41551-021-00683-3.

[6] C. Y. Kim *et al.*, "Soft subdermal implant capable of wireless battery charging and programmable controls for applications in optogenetics," *Nat. Commun.*, vol. 12, no. 1, pp. 1–13, 2021, doi: 10.1038/s41467-020-20803-y.

[7] D. Seo *et al.*, "Wireless Recording in the Peripheral Nervous System with Ultrasonic Neural Dust," *Neuron*, vol. 91, no. 3, pp. 529–539, 2016, doi: 10.1016/j.neuron.2016.06.034.

[8] D. K. Piech *et al.*, "A wireless millimetre-scale implantable neural stimulator with ultrasonically powered bidirectional communication," *Nat. Biomed. Eng.*, vol. 4, pp. 207–222, 2020, doi: 10.1038/s41551-020-0518-9.

[9] D. A. Borton, M. Yin, J. Aceros, and A. Nurmikko, "An implantable wireless neural interface for recording cortical circuit dynamics in moving primates," *J. Neural Eng.*, vol. 10, no. 2, p. 026010, Apr. 2013, doi: 10.1088/1741-2560/10/2/026010.

[10] P. Jin *et al.*, "A flexible, stretchable system for simultaneous acoustic energy transfer and communication," *Sci. Adv.*, vol. 7, no. 40, pp. 1–13, Oct. 2021, doi: 10.1126/sciadv.abg2507.

[11] L. J. Challis, "Mechanisms for interaction between RF fields and biological tissue," *Bioelectromagnetics*, vol. 26, no. S7, pp. S98–S106, 2005, doi: 10.1002/bem.20119.

[12] E. R. Adair and R. C. Petersen, "Biological effects of radiofrequency/microwave radiation," *IEEE Trans. Microw. Theory Tech.*, vol. 50, no. 3, pp. 953–962, Mar. 2002, doi: 10.1109/22.989978.

[13] "IEEE Standard for Safety Levels with Respect to Human Exposure to Radio Frequency Electromagnetic Fields, 3 kHz to 300 GHz," vol. 16, pp. 1–83, 1999, doi: 10.1109/IEEESTD.1999.89423.

[14] A. Zhou *et al.*, "A wireless and artefact-free 128-channel neuromodulation device for closed-loop stimulation and recording in non-human primates," *Nat. Biomed. Eng.*, vol. 3, no. 1, pp. 15–26, 2019, doi: 10.1038/s41551-018-0323-x.

[15] M. Yin *et al.*, "Wireless neurosensor for full-spectrum electrophysiology recordings during free behavior," *Neuron*, vol. 84, no. 6, pp. 1170–1182, 2014.

[16] A. Khalifa *et al.*, "The Microbead: A Highly Miniaturized Wirelessly Powered Implantable Neural Stimulating System," *IEEE Trans. Biomed. Circuits Syst.*, vol. 12, no. 3, pp. 521–531, 2018, doi: 10.1109/TBCAS.2018.2802443.

[17] I. V Meglinski and S. J. Matcher, "Quantitative assessment of skin layers absorption and skin reflectance spectra simulation in the visible and near-infrared spectral regions," *Physiol. Meas.*, 2002.

[18] T. G. Zimmerman, “Personal area networks: Near-field intrabody communication,” *IBM Syst. J.*, vol. 35, no. 3–4, pp. 609–617, 1996, doi: 10.1147/sj.353.0609.

[19] S. Il Chang, K. Alashmouny, M. McCormick, Y. C. Chen, and E. Yoon, “BioBolt: A minimally-invasive neural interface for wireless epidural recording by intra-skin communication,” *IEEE Symp. VLSI Circuits, Dig. Tech. Pap.*, pp. 146–147, 2011.

[20] E. Stavrinidou *et al.*, “Direct measurement of ion mobility in a conducting polymer.,” *Adv. Mater.*, vol. 25, no. 32, pp. 4488–93, Aug. 2013, doi: 10.1002/adma.201301240.

[21] G. Buzsáki *et al.*, “Tools for probing local circuits: High-density silicon probes combined with optogenetics,” *Neuron*, vol. 86, no. 1, pp. 92–105, 2015, doi: 10.1016/j.neuron.2015.01.028.

[22] K. D. Harris, D. A. Henze, J. Csicsvari, H. Hirase, and G. Buzsáki, “Accuracy of tetrode spike separation as determined by simultaneous intracellular and extracellular measurements.,” *J. Neurophysiol.*, vol. 84, no. 1, pp. 401–14, Jul. 2000, doi: 10.1152/jn.2000.84.1.401.

[23] J. J. Jun *et al.*, “Fully integrated silicon probes for high-density recording of neural activity,” *Nature*, vol. 551, no. 7679, pp. 232–236, 2017, doi: 10.1038/nature24636.

[24] D. Khodagholy *et al.*, “NeuroGrid: Recording action potentials from the surface of the brain,” *Nat. Neurosci.*, vol. 18, no. 2, pp. 310–315, 2015, doi: 10.1038/nn.3905.

[25] B. Lee *et al.*, “A Single-Center Experience with the NeuroPace RNS System: A Review of Techniques and Potential Problems,” *World Neurosurg.*, vol. 84, no. 3, pp. 719–726, 2015, doi: 10.1016/j.wneu.2015.04.050.

[26] B. C. Jobst *et al.*, “Brain-responsive neurostimulation in patients with medically intractable seizures arising from eloquent and other neocortical areas,” *Epilepsia*, vol. 58, no. 6, pp. 1005–1014, 2017, doi: 10.1111/epi.13739.

[27] U. Topalovic *et al.*, “Wireless Programmable Recording and Stimulation of Deep Brain Activity in Freely Moving Humans,” *Neuron*, vol. 108, no. 2, pp. 322-334.e9, 2020, doi: 10.1016/j.neuron.2020.08.021.

[28] L. R. Hochberg *et al.*, “Neuronal ensemble control of prosthetic devices by a human with tetraplegia,” *Nature*, vol. 442, no. 7099, pp. 164–171, 2006, doi: 10.1038/nature04970.

[29] M. Velliste, S. Perel, M. C. Spalding, A. S. Whitford, and A. B. Schwartz, “Cortical control of a prosthetic arm for self-feeding,” *Nature*, vol. 453, no. 7198, pp. 1098–1101, 2008, doi: 10.1038/nature06996.

[30] G. Buzsáki, “Large-scale recording of neuronal ensembles.,” *Nat. Neurosci.*, vol. 7, no. 5, pp. 446–51, May 2004, doi: 10.1038/nn1233.

[31] M. J. Morrell, “Responsive cortical stimulation for the treatment of medically intractable partial epilepsy,” *Neurology*, vol. 77, no. 13, pp. 1295–1304, 2011, doi: 10.1212/WNL.0b013e3182302056.

[32] R. W. P. King, B. S. Trembly, and J. W. Strohbehn, “The Electromagnetic Field of an Insulated Antenna in a Conducting Or Dielectric Medium,” *IEEE Trans. Microw. Theory Tech.*, vol. 31, no. 7, pp. 574–583, 1983, doi: 10.1109/TMTT.1983.1131547.

[33] D. C. Grahame, “The Electrical Double Layer and the Theory of Electrocapillarity.,” *Chem. Rev.*, vol. 41, no. 3, pp. 441–501, Dec. 1947, doi: 10.1021/cr60130a002.

[34] J. Israelachvili, *Intermolecular and Surface Forces*. Elsevier, 2011. doi: 10.1016/C2009-0-21560-1.

[35] J. Li, Y. Dong, J. H. Park, and J. Yoo, “Body-coupled power transmission and energy harvesting,” *Nat. Electron.*, vol. 4, no. 7, pp. 530–538, 2021, doi: 10.1038/s41928-021-

00592-y.
[36] K. Hachisuka, T. Takeda, Y. Terauchi, K. Sasaki, H. Hosaka, and K. Itao, "Intra-body data transmission for the personal area network," *Microsyst. Technol.*, vol. 11, no. 8–10, pp. 1020–1027, Aug. 2005, doi: 10.1007/s00542-005-0500-1.
[37] J. Rosell, J. Colominas, P. Riu, R. Pallas-Areny, and J. G. Webster, "Skin impedance from 1 Hz to 1 MHz," *IEEE Trans. Biomed. Eng.*, vol. 35, no. 8, pp. 649–651, 1988.
[38] C. Gabriel, "Compilation of the dielectric properties of body tissues at RF and microwave frequencies.," King's Coll London (United Kingdom) Dept of Physics, 1996.
[39] X. Cui and D. C. Martin, "Electrochemical deposition and characterization of poly(3,4-ethylenedioxythiophene) on neural microelectrode arrays," *Sensors Actuators B Chem.*, vol. 89, no. 1, pp. 92–102, 2003, doi: https://doi.org/10.1016/S0925-4005(02)00448-3.
[40] K. Tybrandt, I. V Zozoulenko, and Berggren M, "Chemical potential–electric double layer coupling in conjugated polymer–polyelectrolyte blends," *Science Advances*. advances.sciencemag.org, 2017.
[41] D. Khodagholy *et al.*, "In vivo recordings of brain activity using organic transistors," *Nat. Commun.*, vol. 4, 2013, doi: 10.1038/ncomms2573.
[42] A. Burton *et al.*, "Wireless, battery-free, and fully implantable electrical neurostimulation in freely moving rodents," *Microsystems Nanoeng.*, vol. 7, no. 1, 2021, doi: 10.1038/s41378-021-00294-7.
[43] "Guidelines for Limiting Exposure to Electromagnetic Fields (100 kHz to 300 GHz).," *Health Phys.*, vol. 118, no. 5, pp. 483–524, 2020, doi: 10.1097/HP.0000000000001210.
[44] P. Jastrzebska-Perfect *et al.*, "Mixed-conducting particulate composites for soft electronics," *Sci. Adv.*, vol. 6, no. 17, pp. 1–10, 2020, doi: 10.1126/sciadv.aaz6767.
[45] Z. Zhao, C. Cea, J. N. Gelinas, and D. Khodagholy, "Responsive manipulation of neural circuit pathology by fully implantable, front-end multiplexed embedded neuroelectronics," *Proc. Natl. Acad. Sci.*, vol. 118, no. 20, p. e2022659118, May 2021, doi: 10.1073/pnas.2022659118.

Chapter 6: Integrated Internal Ion-Gated Organic Electrochemical Transistors for Stand Alone Conformable Bioelectronics

It is increasingly appreciated that individual variability can strongly affect response to clinical treatments, motivating approaches that enable long-term monitoring of physiologic signals and delivery of responsive therapeutics[1]–[3]. Implanted bioelectronic devices are often critical components of such approaches, but implementation challenges hinder widespread use. The incompatibility of traditional electronic components with physiologic media, risk of device-related tissue disruption, and limited means by which to interface and power implanted devices are key hurdles [4][5].

The most widely used building block for active electronic circuitry is the metal oxide semiconductor field effect transistor (MOSFET). It combines diverse functionality with capacity for miniaturization and rapid computation, creating a performance profile that is unmatched by other materials and architectures. However, these transistors possess a mechanically rigid, Si-based channel and when used to create integrated circuits require >1 V supply voltage. As a result, defects or damage to the device can pose a risk to biological tissue and approaches to powering are limited. Furthermore, the channels of these transistors are susceptible to ion contamination and oxidation, entailing careful isolation from physiologic media in the form of hard and bulky metallic enclosures that cause a large mechanical mismatch between the implant and body. Lastly, the ion to electron conversion process in these transistors is limited to the surface of the gate electrode or oxide layer, dampening the interface charge storage capacity as quantified by the electric double layer (EDL) capacitance[6], [7].

Organic transistors, such as electrolyte gated field effect transistors (EGOFETs)[8] or organic electrochemical transistors (OECTs)[9] leverage water-stable semiconducting materials in lieu of

Si to improve the biocompatibility, conformability, and physical footprint of transistors targeted for function in physiologic environments. These devices operate by directly interfacing with ions, and use of hydrophilic and ion permeable polymers as channel material (such as poly(2,3-dihydrothieno-1,4-dioxin)-poly(styrenesulfonate) PEDOT:PSS) can enhance the EDL capacitance, leading to high transconductance. These advantages come at the cost of longer device time constants, because the temporal dynamics are defined by ion mobility, and inability to perform independent gating, due to the requisite function of external electrolyte for transistor operation. We previously developed the internal ion-gated organic electrochemical transistors (IGTs) to address these limitations of OECTs[10]. The conducting polymer-based channel of an IGT contains ion reservoirs that are sufficient for effective de/doping of the channel, eliminating dependence on external electrolyte and reducing the transit time of ions participating in the de/doping process. IGTs therefore operate at a bandwidth up to several hundreds of KHz and can be independently gated to form functional circuits. Yet, Si-based transistors operate at higher speeds, particularly for the purposes of operations such as multiplexing and data communication. In addition, when immersed in an ion-conducting medium, such as physiologic tissue, operation of an IGT can induce a potential in the medium that modulates the gate of a neighboring IGT and results in cross-talk.

At a systems level, stand-alone bioelectronic devices require components for signal acquisition, processing and data transmission as well as powering. Traditionally, an implanted device with these capabilities would require multiple rigid and non-biocompatible components, including complex RF circuity for data communication, and batteries for power, and a series of interfacing boards to establish physical and electrical connections between these modules. Transiently powered and wireless bioelectronics eliminate the need for bulky batteries and cables by harvesting

an externally propagated energy source such as RF, ultrasound, and magnetic, or ionic waves. However, these approaches still require implanted rigid encapsulated electronics to convert this energy to a usable form for the signal acquisition, processing and transmission modules, precluding the realization of fully conformable stand-alone bioelectronics.

Here, we address these issues directly by introducing a scalable, self-contained, sub-micron IGT architecture, the vIGT. We incorporate a vertical channel arrangement that augments the intrinsic speed of the IGT architecture by optimizing channel geometry and permits high-density integration capacity. We also deployed a vertical hydration access conduit (H-via) that maintains device hydration but prevents cross-talk even when immersed in an ion-rich medium. The combination of these features resulted in an organic transistor that is able to operate in the MHz signal range while concurrently maintaining high amplification, with performance surpassing any flexible transistor (including Si-based devices). vIGTs are stable in physiologic conditions for over 1 year without the need for encapsulation, and were effectively fabricated in conformable arrays with a density of 155k transistor/cm^2. The reduction state of the channel can be chemically tuned to permit device operation in both enhancement and depletion modes. The combination of these features enabled creation of vIGT-based high gain multi-stage amplifiers, oscillators, multiplexers, and rectifiers. We then realized that vIGT properties could be leveraged to permit development of conformable, wireless circuitry capable not only of acquiring and transmitting physiologic signals, but simultaneously providing power to the implanted circuitry through an intact tissue interface. We demonstrated this capacity by performing high spatiotemporal resolution *in vivo* electrophysiology in a rodent model using only fully conformable implanted v-IGT-based circuitry in the absence of any rigid or Si-based components. vIGTs therefore represent a convergence of

high electronic performance, scalability, stability, and conformability capable of serving as the foundation for stand-alone organic bioelectronic devices.

6.1 Structure, Steady State and High-Frequency Characteristics of v-IGTs

We hypothesized that incorporating the operational principles of IGTs with 2 novel material and design elements would generate high-performance, high-speed transistors that could form large-scale integrated circuits with minimal cross-talk, even when fully implanted in physiologic media: (i) vertical channel orientation; (ii) introduction of a hydration access conduit (H-via) that attenuates ionic interaction of the gate and any external medium (Figure 1A).

To test the feasibility of these concepts, we first fabricated vertical IGTs (vIGTs) guided by processes developed for horizontal IGTs. vIGTs were similarly composed of a PEDOT:PSS-based channel containing sugar alcohol (D-sorbitol) to create a depletion mode (normally ON) transistor, with the addition of poly-ethylamine (PEI) to generate an enhancement mode (normally OFF) transistor [11]–[13]. These additives are highly biocompatible and preserved the electrical properties of the PEDOT:PSS [14][15], [16][17]. We exploited the facile solution processability of these channel material dispersions to orient the channel vertically. The length of this vertical channel was defined by the thickness of the interlayers (800 nm). Gate electrodes were composed of PEDOT:PSS to increase charge capacity compared to Au[18]–[20]. We maintained a polysaccharide-based (chitosan) ion membrane (IM) to establish ionic, but prevent electronic, conduction between the gate and channel. Due to the vertical channel arrangement, the gate and IM were now between source and drain contacts and completely isolated from the external environment. To allow for hydration of the transistor channel, we etched a vertical H-via across the IM layer (Figure 1B-C). The entire fabrication process was implemented at wafer scale and used for creation of both depletion and enhancement mode transistors.

We first characterized the steady state characteristics of vIGTs. They possessed high transconductance and ON channel current similar to their horizontal IGT counterparts, establishing capacity for preserved ON current despite channel miniaturization, a property observed with Si-based MOSFETs (Figure 1D). Temporal responses were in the sub-microsecond domain, which represented an improvement upon previous IGTs (Figure 1D**)**. This high-speed operation was achieved for both depletion and enhancement mode vIGTs. We found that the overall performance of vIGTs characterized by their rate of transconductance vs. rise time ratio surpassed all other organic transistors and compared favorably with top performing inorganic flexible transistors such as indium gallium zinc oxide (IGZO) and Si-based foundry produced transistors (Figure 1E).

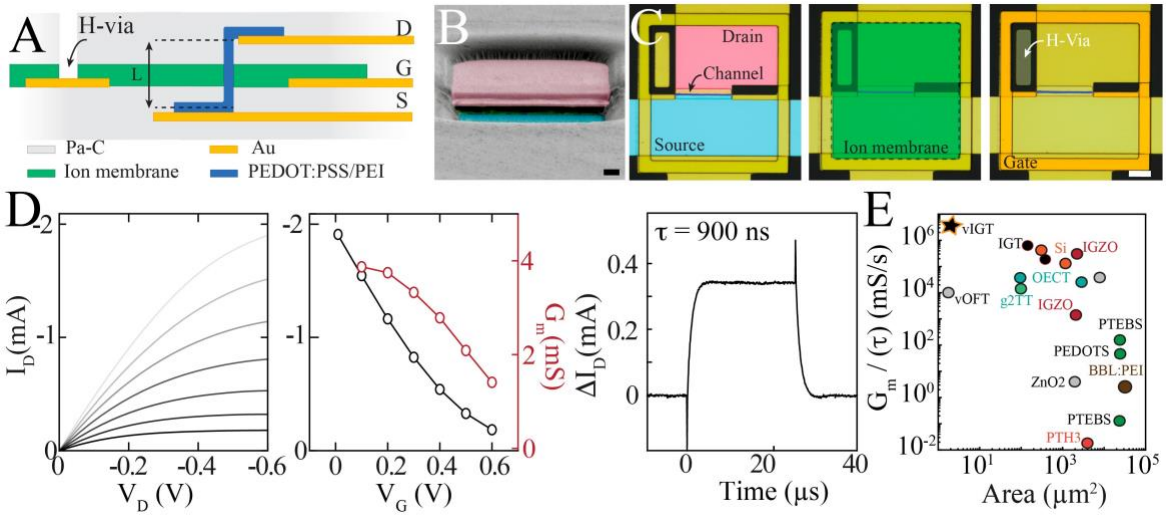

Figure 1. Physical structure and electrical characteristics of vIGTs. A) Schematic illustration of vIGT cross-section consisting of a vertical channel length (L) defined by the thickness of interlayers between source and drain contacts. Channel hydration was ensured by the H-via, providing a micro-conduit from the surface of the device through the ion membrane layer. B) Colorized cross-section scanning electron microscopy (SEM) image of vIGT after defining the channel area. The pink and blue regions are source and drain contacts, respectively (scale bar, 800 nm). C) Optical micrograph displaying the top view of an individual vIGT. Each part of the transistor is highlighted with a different color (blue = source contact; pink = drain contact; ion membrane = green; H-via = dark green; scale bar, 5 μm). D) Output characteristics of a depletion mode vIGT device (W/L = 5/ 0.8 μm, thickness (d) = 100 nm) for VG varying from 0 V (top curve) to 0.6 V (bottom curve) with a step of 0.1 V (left). Transfer (black) and transconductance (red) curves for VD = −0.6 V (center). Corresponding temporal response of the drain current (ID) for VD = −0.6 V and VG pulse amplitude of 0.1 V; exponential fit of the vIGT drain current resulted in a time constant of 0.9 μs (right). E) Performance of flexible transistors as characterized by the ratio of transconductance and rise time vs. channel area..

To investigate the mechanism underlying the vIGT operation and inter-transistor crosstalk in ion-rich environments, we focused on the effect of the H-via on transistor operation. We found that the H-via established a large electrochemical impedance between the channel and the external electrolyte compared to architectures that directly expose the channel to the electrolyte (Figure 2A). This impedance appeared to act as a large series attenuator that minimized the spread of gate potential into the electrolyte. Despite the presence of this large impedance, the H-via did not alter the transfer curve of the transistor (Figure 2B). Taken together, these findings indicate that the H-via does not serve as a substantive source for ions to operate the transistor; in this case, its high electrochemical impedance would deteriorate transistor performance. Instead, we hypothesized that the H-via permits osmotic movement of water to hydrate the channel, but mobile ions internal to the channel material mediate transistor operation, in line with previous mechanistic investigation of horizontal IGTs[10], [21].

We next aimed to determine whether vIGT design was effective in eliminating cross-talk in an ion-conducting environment. We fabricated vIGTs with different inter-transistor spacing and monitored the cross-talk by observing the drain current of a biased transistor ($T_{2;}$ red) while operating its adjacent transistor ($T_{1;}$ black) using a squared gate voltage (Figure 2C-D). There was no observable leakage at any pitch size achievable with contact lithography (Figure 2E). Critically, vIGT performance (time constant and transconductance) was maintained across all multi-transistor configurations. Lastly, the vIGT equipped with H-via exhibited consistent modulation for over 1 year, emphasizing the chemical stability of the channel material and the persistent functionality of the H-via (Figure 2F). Therefore, the H-via enables stable, long-term, crosstalk-free operation of densely packed vIGTs.

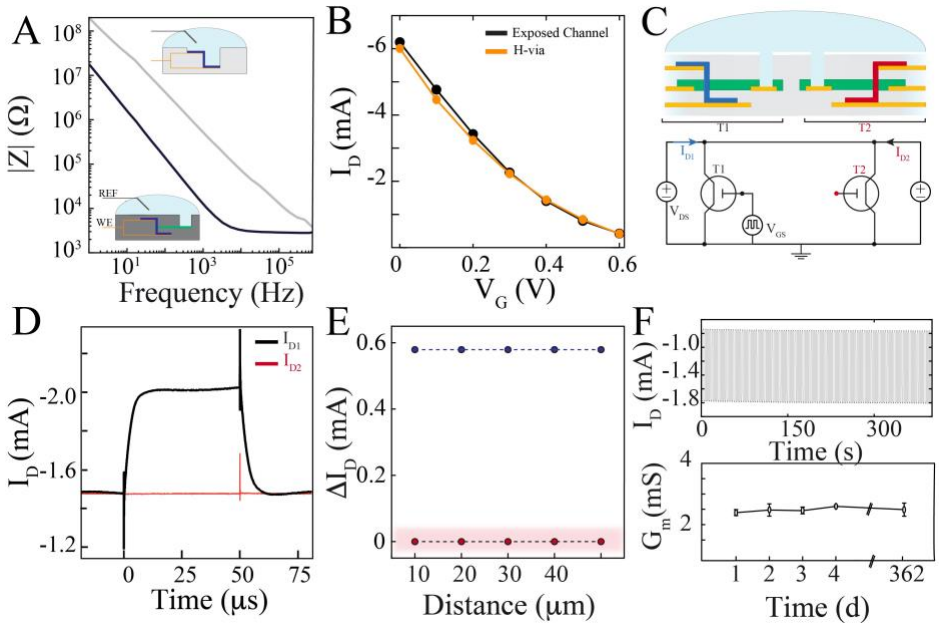

Figure 2. Crosstalk-free and stable operation of densely packed vIGTs in physiologic media. A) Electrochemical impedance spectrum (EIS) of a vIGT (W/L = 5/0.8 µm, d = 200 nm) fabricated to expose the full channel area to electrolyte (black). EIS of a similar vIGT channel hydrated through only the H-via (gray). Insets shows wiring diagrams of a vIGT with exposed channel interfacing the electrolyte (top) and of a vIGT with H-via only (bottom). In both cases, the vIGT channel was used as the working electrode with source and drain contacts connected to each other. Ag/AgCl and Pt electrodes were used as reference and counter electrodes, respectively. B) Transfer curves of vIGT with full channel exposed to electrolyte (black) and vIGT with H-via only (orange) demonstrating that the H-via does not impede vIGT performance (W/L = 5/0.8 µm, d = 100 nm, VD = – 0.6 V). C) Cross-sectional schematic of two adjacent vIGTs immersed in physiologic media demonstrating the increased channel-electrolyte impedance introduced by the H-via to eliminate cross-talk between closely adjacent transistors (top). Wiring diagram of two adjacent vIGTs used for crosstalk characterization; both transistors were powered and T1 received a pulsed voltage to VG while T2 was monitored in the absence of input to its own gate (bottom). D) Transient response of the drain current (ID1, black) of a vIGT (T1), operating at VD = – 0.6 V, with pulsed VG between 0 - 0.6 V. Transient response of the drain current (ID2, red) of T2, during T1 operation with pulsed gate voltage. Transistors had identical geometry (W/L = 5/0.8 µm, d = 100 nm). E) Input applied to the gate of an individual vIGT results in drain current modulation of this specific transistor (black) without inducing modulation of neighboring transistors at varying distances (red). Measurements were obtained simultaneously using operating parameters and device geometry as in (d). Red highlighted area indicates limit of instrument sensitivity. F) Maximum transconductance (Gmmax) of a vIGT over a period of 362 days under continuous pulsed gate voltages (VD = −0.4 V and VG pulses from 0 V to 0.4 V; same geometry as in (D)). Each point represents the average transconductance under continuous operation for 50 min. Error bars represent the standard deviation value (top). vIGT ID temporal response during continuous operation for 400 s (bottom).

By miniaturizing the channel through vertical stacking of the terminals rather than complex projection or electron-based lithographic techniques, fabrication was substantially simplified and highly consistent wafer scale manufacturing of vIGTs was possible. However, the remaining

components of the transistor were defined by the resolution of the proximity lithography, resulting in channel contact areas that were larger than the channel itself. This ratio of component sizes could potentially deteriorate the temporal response of the vIGT by forming parasitic capacitances. Therefore, we investigated the temporal response of these devices as a function of their contact size. We first modeled the contacts as a series resistance (R_C) and a parallel resistive-capacitive (R_P, C_C) circuit between the Au-based ohmic contacts of the drain and gate. A similar approach was taken for the gate interface (R_G, C_G). Fitting the impedance electrochemical spectroscopy measurements of these contacts revealed that the value of R_p is several orders of magnitude larger than the series resistances and can be neglected for derivation of total resistance and capacitance (Figure 3A, top)[22], [23]. Therefore, the time constant ($\tau = RC$) resulting from these circuits was proportional to the sum of the series resistances and the parallel sum of the gate and contact capacitances (Figure 3a, top). In this arrangement, the time constant therefore also depends on the magnitude of the contact area relative to the gate area. If the gate area was larger than the contact area ($C_G > C_C$), the total capacitance was controlled by the contact capacitance (Figure 3B). Increasing the contact area in this regime gave rise to an overall increase in the time constant ($\uparrow\tau = (R_G+R_C)\ C_C\uparrow$). If the contact area was larger than the gate area ($C_G < C_C$), the overall capacitance was dictated by the gate capacitance (Figure 3B). In this case, increasing the contact area lowered the overall resistance of the circuit and enabled a faster time constant ($\downarrow \tau = \downarrow(R_G+R_C)\ C_G$). Of note, this set of relationships is only valid when the temporal response of the channel itself is substantially smaller than that of the contacts. Because IGTs rely on internal mobile ions for operation, the temporal response of the channel is dictated by hole rather than ion mobility and the ensuing fast channel dynamics support applicability of these parameters. To demonstrate these relationships experimentally, we fabricated an array of horizontal IGTs with variable contact (H)

but constant gate areas. Horizontal IGTs were used to permit facile modification of the channel area (maintaining similar proportions) to accommodate contact area that varied by two orders of magnitude. The overall time constant of these IGTs (L = W = 100 μm) was on the order of 10-15 μs, which is close to the limit of hole mobility (1 cm^2/Vs) and approximately 100 times faster than conventional OECTs with similar geometries[24], [25]. As predicted by the model, the time constant of these devices expressed an inverted U pattern with the rise and fall of the curve corresponding to larger gate and contact areas, respectively. We then leveraged vIGT design to increase the contact area while maintaining a proportionally smaller gate. This modification led to a decrease in the overall response time with no significant effect on transconductance (Figure 3C). However, substantially larger contact areas also resulted in lower overall electrochemical impedance and consequently a higher OFF current (Figure 3D). This effect occurs because IGTs (similar to OECTs) are able to completely dedope the PEDOT:PSS channel of electronic carriers. As such, the OFF current is equal to the ionic drift current across the source and drain contacts, which is governed by the drain voltage and the overall electrochemical impedance of the contacts. Given these properties of individual vIGTs, we hypothesized that it would be possible to generate large, conformable vIGT arrays with high transistor density. Using the scalable vIGT fabrication process with its intrinsic multi-layer metallization, we created a 3 μm thick, conformable integrated circuit with ~155k transistor/cm^2 density in a common source matrix structure comprised of a total of half a million transistors (Figure 4A-B). This transistor density surpasses other flexible transistors, including those with high throughput production capacity and photo-patternable semiconducting channels (Figure 4C). We next demonstrated the functionality of vIGTs by developing several circuit components. Because physiologic signals are often low amplitude, we created a multi-stage, high speed amplifier with a gain exceeding 650 at an operating

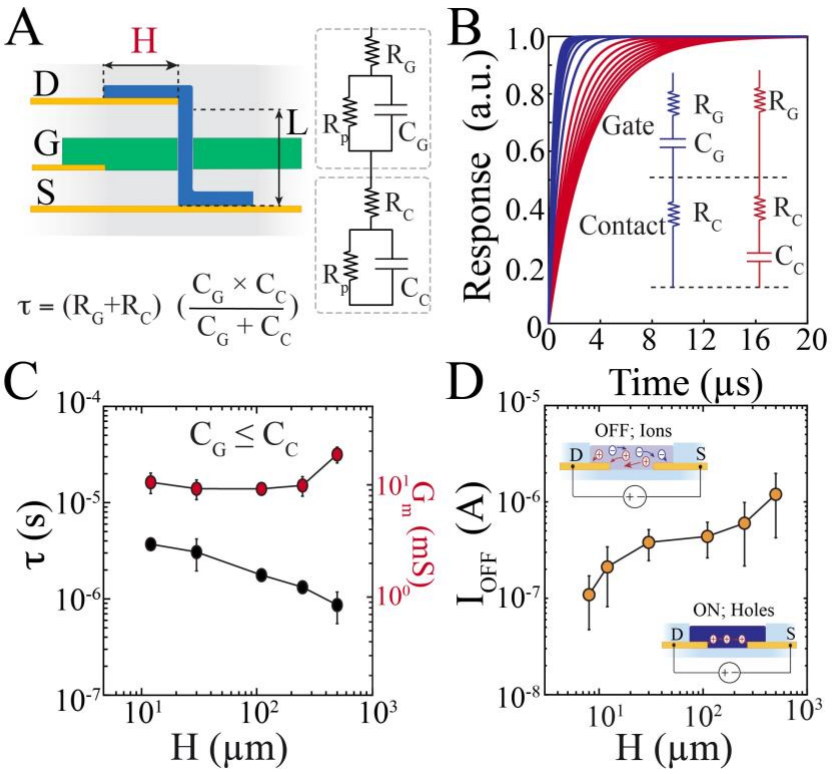

Figure 3. Contact area has non-linear effects on temporal response. A) Schematic illustration of a vIGT displaying channel length (L) and contact area (H; left). Circuit diagram of the model showing electrical characteristics of the gate (RG, CG) and channel contacts (RC, CC and RP; right). Time constant equation of the series gate and contact circuits (RP >> RG, Rc; lower). B) Simulated transient behavior of a vIGT in response to a square step of the gate voltage. If CG > CC, the transient response depends only on CC, RC, and RG; hence, larger contacts result in a slower transient response (red). If CG ≤ CC, the transient response depends on CG, RG, and RC; hence larger contact result in a faster transient response (blue). C) Transient response of vIGTs with a range of contact areas (spanning from smaller to larger than the gate area; black circles). vIGT transconductance shows a small increase with the largest contact areas (red circles). D) Off-current of vIGT is defined by the impedance and geometry of the contacts (inset schematics). Increasing contact area results in larger off-current (yellow circles).

voltage of 600 mV to facilitate safe, effective amplification even in direct contact with biologic tissue (Figure 4D). To highlight the consistency and precision of vIGT fabrication, we also generated a ring oscillator at 15 KHz (Figure 4E). Multiplexers are key components of multi-channel acquisition devices because they increase the number of signals that can be sampled relative to number of interconnects. vIGTs formed high performance multiplexing switches with low cross-talk (< - 60 dB; Figure 4F). Another advantage of vIGTs is the ability to control the reduction state of the channel, permitting creation of diodes and rectifying circuitry using a single

channel material (Figure 4G, top). The threshold voltage (V_t) of these organic diodes could be tuned from –0.2 to 0.2 V depending on the concentration of PEI in the PEDOT:PSS channel, which is substantially lower than the hydrolysis potential as well as V_t of Si-based diodes (Figure 4G; bottom).

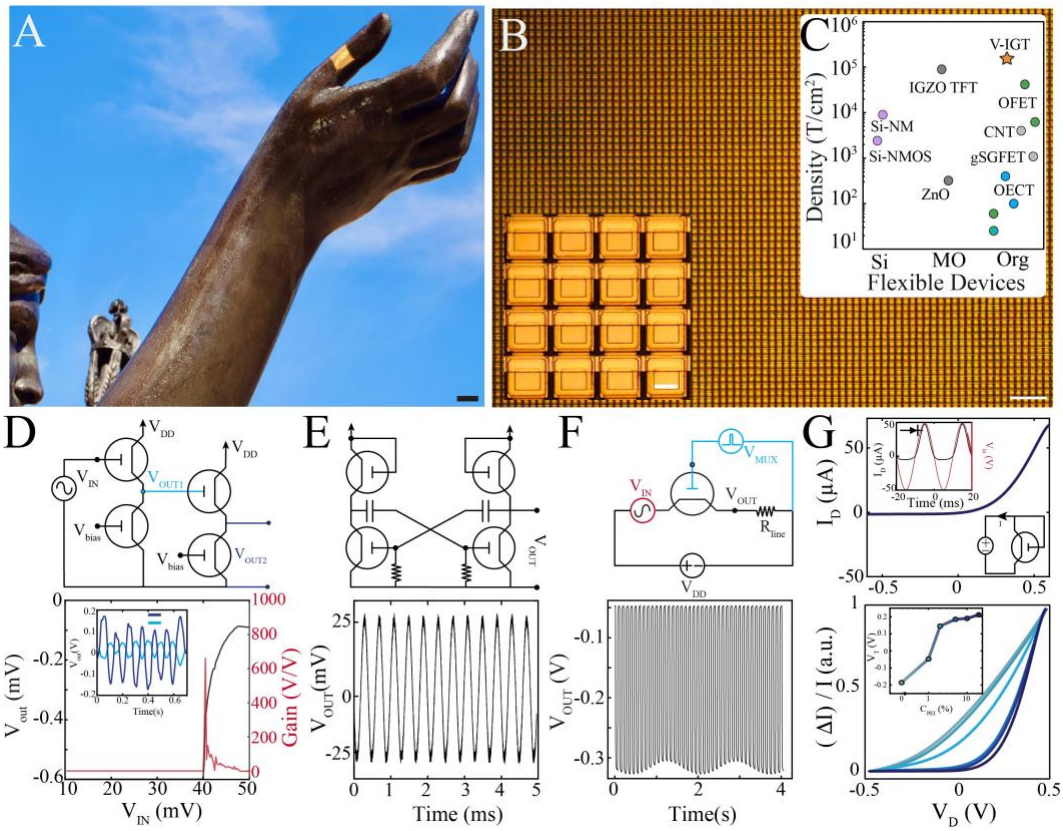

Figure 4. Conformable, high-density vIGT-based integrated circuits. A) 3μm thick vIGT array conforming to a complex curvilinear surface. Scale bar 10 mm. B) Optical micrograph of 1 million vIGTs with 155,586 transistors/cm2 density (scale bar, 30 μm). Inset shows magnified image of the vIGT array (scale bar, 4 μm). C) Fabrication density of flexible transistors based on channel material (Si = silicon; MO = metal oxide; Org = organic; see Supplementary Table 2 for device details). D) Circuit diagram of active load, multistage, cascaded vIGT-based inverter (top) with corresponding input/output and gain (G = 650; bottom). Inset shows application of the circuit as a voltage amplifier for 25μVPP sine wave input signals. E) A phase shifter-based oscillator constructed by two active load vIGT inverters (top). Output voltage of the vIGT based oscillator operating at 1.5 Khz (bottom). F) Circuit diagram of vIGT-based multiplexer switch (top) and the corresponding output signal of the switch performing time division multiplexing of a sinewave input signal (bottom; VD = -0.6 V and VG = 100 mVPP). G) Current-voltage (IV) characteristics of vIGT operating as a diode. Insets demonstrate the vIGT as a diode-connected transistor rectifying an altering sign wave (top). Superimposed IV characteristics of vIGT configured as a diode-connected transistor with different threshold voltages. Darker colors represent high concentration of PEI; Inset shows modulation of the threshold voltage of diode-connected transistor as a function of PEI concentration (Bottom).

6.2 Integration of vIGTs with IC.

The combination of high-speed, efficient ion to electron conversion and low-operating voltage characteristic of vIGTs opened unique possibilities for device integration. We hypothesized that we could create a fully conformable stand-alone vIGT-based bioelectronic implant that acquires and amplifies physiological data, transmits this data wirelessly to the external environment, and operates via wireless power. Traditionally, an implanted device with these capabilities would require multiple rigid and non-biocompatible components, including complex RF circuity for power harvesting, Si-based amplifiers, and a series of interfacing boards to establish physical and electrical connections between these modules. We aimed to bypass these requirements by expanding the principles underlying ionic communication (IC)[26] to concurrently power and transmit data from vIGTs. To accomplish this, we needed to power a vIGT using fast alternating current (AC) rather than direct current (DC). It has been previously shown that high frequency electrical signals applied between a pair of contacts efficiently propagate through ion-rich media, including intact biological tissue[26], [27]. Based on this concept, it would be theoretically possible to bias an implanted transistor by electric potentials applied non-invasively at a distance. Because vIGTs can operate at high frequencies, we could bias the transistor at a desired set point once per cycle of the applied AC waveform. For example, a 500 mV amplitude, 1MHz frequency sine wave would set the channel potential to – 500 mV at the trough of each cycle (which occurs every microsecond). In turn, the vIGT amplifies the physiological activity at its gate (input) and modulates the amplitude of the received sine wave to encode this signal. The amplified and modulated sine wave can then be transmitted back across the ion-rich medium using a third contact. This signal is received and differentially amplified with respect to the initially transmitted sine wave to permit extraction of the physiological signal (Figure 5A).

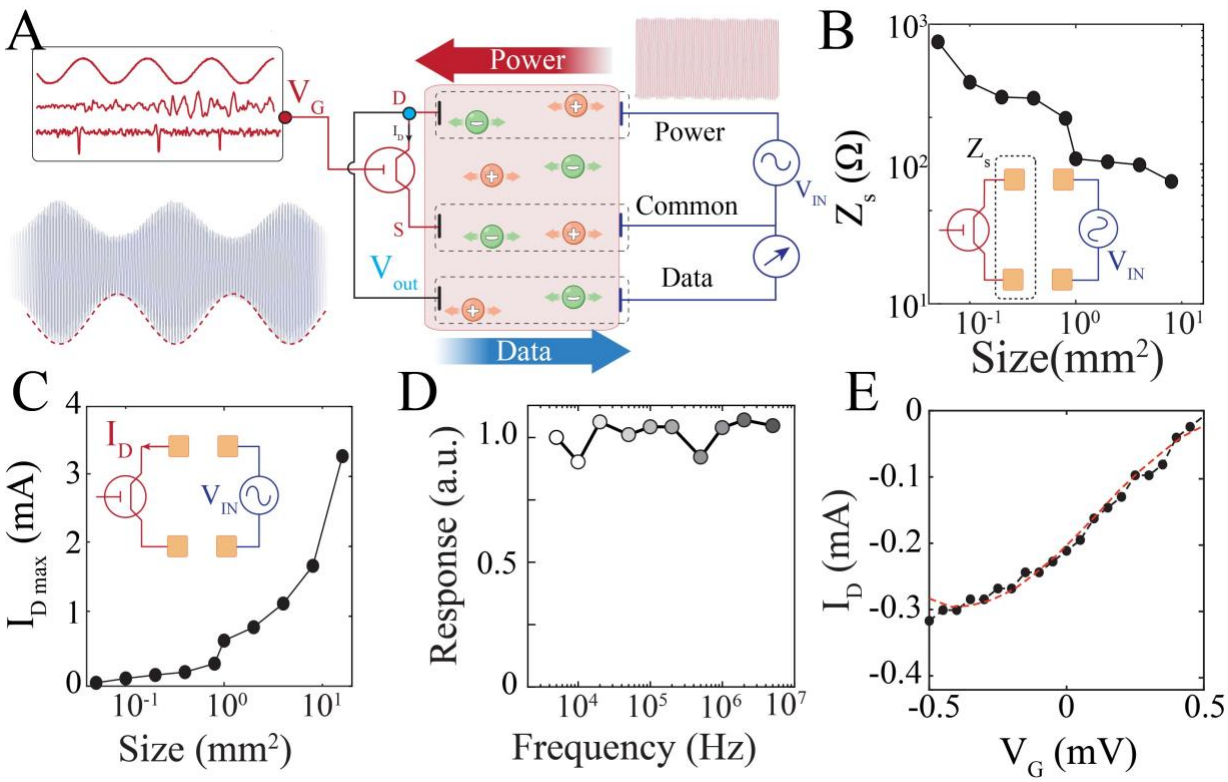

Figure 5: Integration of vIGT with ionic communication (IC) establishes a fully conformable, stand-alone device with wireless powering and data transmission. A) Schematic of working principles permitting vIGT powering via an alternating sine wave (red) transmitted across a physiologic medium using two sets of aligned power contacts (power and common). The vIGT modulates this sine wave according to the electrophysiological signal at its gate. This encoded signal (blue) is then routed to the data contact for transmission back across the medium. At the receiver, the data is acquired and demodulated with respect to the common electrode potential to decode the electrophysiologic signal. B) Two terminal electrochemical impedance (at 100 KHz) varies relative to the geometry of the power contacts (as shown in the inset). as function of data and common electrodes. These impedance values correspond to the overall power source impedance (Zs) at each geometry. C) Maximum current delivery capacity varies relative to the power contact size (VDS = 500 mVPP). This current represents the maximum possible ID that can be delivered to the vIGT via IC at each geometry. D) Normalized modulation of vIGT is stable across a range of carrier frequencies up to 5 MHz. E) vIGT transfer curves are similar when provided with DC (red dashed line; VDS = -500 mV) and AC power (black circles; VDS = -500 mVpp; 1 MHZ).

We first determined the amount of power that could be delivered to the vIGT in this configuration. Because the power was transmitted to the vIGT via alternating potential applied across two distant power contacts, the geometry of these contacts was critical. We used two-terminal electrochemical impedance spectroscopy to measure the impedance as power contact dimensions were varied. With application of 500 mV across the contacts, we found that approximately 500 μA/mm^2 normalized current per power contact area was delivered to the vIGT (Figure 5B-C). This current capacity

directly translates into the drain current of the vIGT and is on par with typical I_D in DC operation mode. Thus, IC can supply sufficient power to operate vIGTs. Next, we investigated the range of carrier frequencies over which vIGTs could maintain amplification. We previously established that the effective carrier frequency range for ionic communication is between 50 KHz – 5 MHz for ion concentrations equivalent to that found in biologic tissue. The vIGT demonstrated consistent current modulation and voltage gain (ratio of input/output voltage) across this frequency range, and values were similar to those obtained via application of DC potentials (Figure 5D-E).

To test these concepts in a realistic setting, we developed a stand-alone device that utilized a vIGT to acquire and amplify neurophysiologic signals, and IC to power the vIGT and transmit data to the external environment. This device contained only conformable, biocompatible materials and was fully implanted in a freely moving rodent. We fabricated a parylene-C implantable shank with a vIGT at the tip, allowing neural activity patterns to be monitored from the vicinity of the transistor gate (Figure 6A). Interconnects were extended from the vIGT source and drain contacts to connect with two conducting polymer-based power contacts placed on the surface of the rat's skull. The power contact connected to the source was designated as the common contact, because it also served as the integration point for the reference signal from the cerebellum (Figure 6B). The transistor was therefore configured as a common-source amplifier and the output potential was extracted from the node between the drain and power contact by a third conducting polymer-based electrode (the data contact). Interestingly, we found that the power contact effectively served as the load for the vIGT-based amplifier in this circuit design. A matching 3 contact array was fabricated and aligned over the intact tissue interface to transmit power and data. The vIGT shank was placed on the surface of rat somatosensory cortex with the power/data contacts laminated to the surface of the skull. To validate the neural data acquired by this device, we also placed a

conventional device (neural probe attached to Si-based amplifiers with cables for data transmission) on the adjacent cortical tissue. We generated somatosensory evoked potentials (SSEPs) by electrical stimulation of the hindlimb and monitored responses with both devices. The vIGT-based device was able to acquire the SSEPs with similar SNR to the conventional device, and accurately conveyed the known relationship between applied current and SSEP amplitude (Figure 6B-C). We then monitored the performance of these devices in a chronic set-up. In freely moving rats, we recorded spontaneous neural activity across behavioral state transitions. We identified characteristic patterns in the local field potential (LFP) corresponding to wakefulness, rapid eye movement (REM) and non-rapid eye movement (NREM) sleep. Furthermore, power spectra from the vIGT-based device and the conventional device were not significantly different, highlighting the ability of the vIGT-based device to accurately sample and transmit neurophysiologic data (Figure 6D-E).

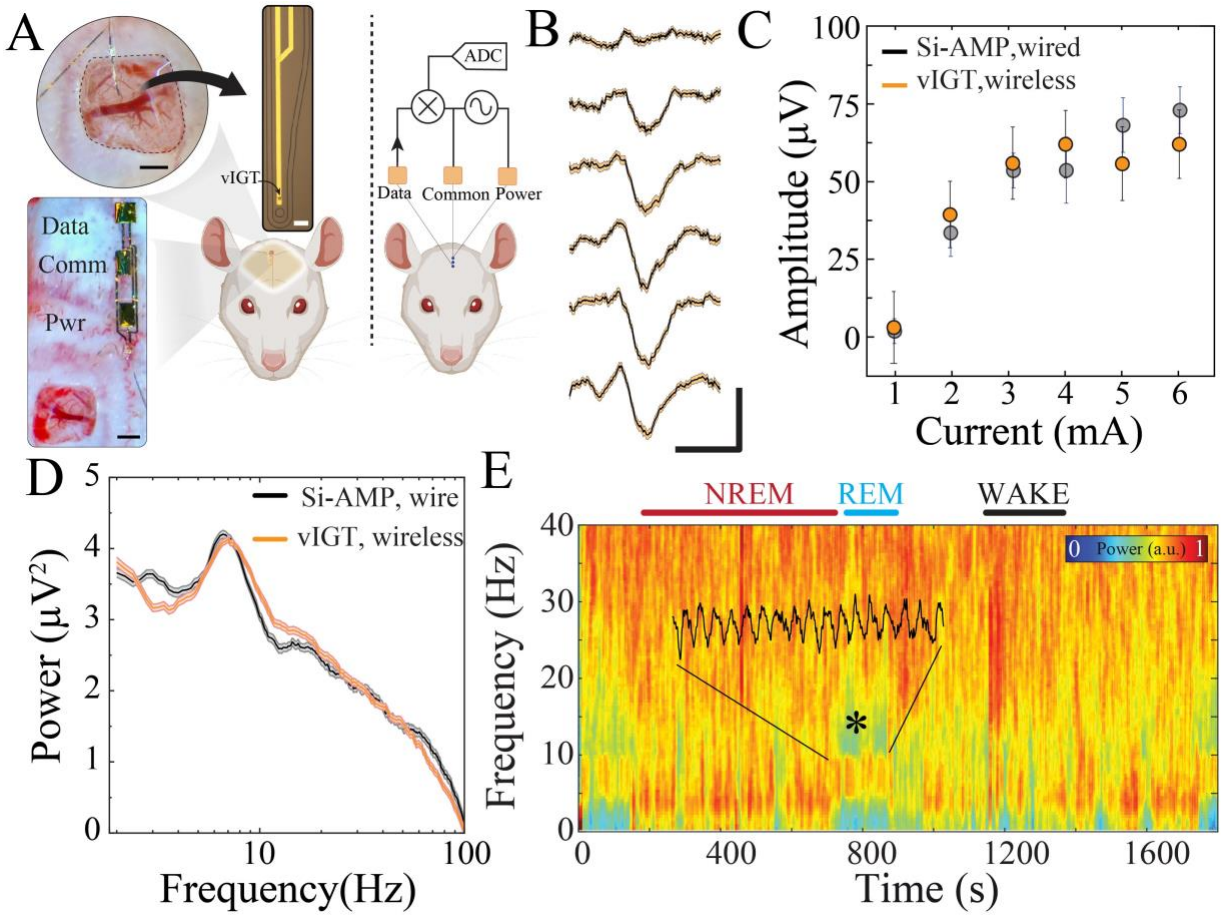

Figure 6: Fully conformable, implanted, vIGT-based stand-alone device performs in vivo acquisition and wireless signal transmission of neurophysiological activity. A) Intraoperative micrograph of a conformable vIGT-based neural shank being placed on somatosensory cortex (top left; scale bar, 500 μm). Optical micrograph of a vIGT-based shank and its interconnects (top right; scale bar, 20 μm). Intraoperative micrograph of the power, data, and common contacts laminated on the surface of the skull adjacent to the craniotomy through which the vIGT is implanted (bottom left; scale bar, 500 μm). Schematic illustration of the power generator and data receiver electrodes placed on top of the scalp (right). B) Somatosensory evoked potentials (SSEPs) recorded and wirelessly transmitted using a vIGT-based stand-alone device as peripheral stimulation intensity is increased from 1 to 6 mA (top to bottom; Line traces and shaded error bars show mean standard deviation; n = 120 trials). C) Relationship between peripherally applied stimulation current and SSEP amplitude for vIGT-based stand-alone device (orange) and conventional neural interface device (black). D) Power spectra extracted from an epoch of rapid-eye-movement (REM) sleep traces by vIGT-based stand-alone device (red) and conventional neural interface device (black). E) Continuous time-frequency spectrogram of neural data acquired and wirelessly transmitted using vIGT-based stand-alone device demonstrates characteristic LFP patterns corresponding to wakefulness, REM sleep, and NREM sleep. Superimposed raw time trace highlights theta oscillations during REM sleep.

References

[1] D. Khodagholy, J. J. Ferrero, J. Park, Z. Zhao, and J. N. Gelinas, "Large-scale, closed-loop interrogation of neural circuits underlying cognition," *Trends Neurosci.*, vol. 45, no. 12, pp. 968–983, 2022, doi: 10.1016/j.tins.2022.10.003.

[2] K. W. Scangos *et al.*, "Closed-loop neuromodulation in an individual with treatment-resistant depression," *Nat. Med.*, vol. 27, no. 10, pp. 1696–1700, 2021, doi: 10.1038/s41591-021-01480-w.

[3] E. Krook-Magnuson, J. N. Gelinas, I. Soltesz, and G. Buzsáki, "Neuroelectronics and biooptics: Closed-loop technologies in neurological disorders," *JAMA Neurol.*, vol. 72, no. 7, pp. 823–829, 2015, doi: 10.1001/jamaneurol.2015.0608.

[4] J. W. Jeong, G. Shin, S. Il Park, K. J. Yu, L. Xu, and J. A. Rogers, "Soft materials in neuroengineering for hard problems in neuroscience," *Neuron*, vol. 86, no. 1, pp. 175–186, 2015, doi: 10.1016/j.neuron.2014.12.035.

[5] P. Jastrzebska-Perfect *et al.*, "Translational Neuroelectronics," *Adv. Funct. Mater.*, vol. 30, no. 29, Jul. 2020, doi: 10.1002/ADFM.201909165.

[6] T. Someya, Z. Bao, and G. G. Malliaras, "The rise of plastic bioelectronics," *Nature*, vol. 540, no. 7633, pp. 379–385, 2016, doi: 10.1038/nature21004.

[7] J. Rivnay, R. M. Owens, and G. G. Malliaras, "The rise of organic bioelectronics," *Chem. Mater.*, vol. 26, no. 1, pp. 679–685, 2014, doi: 10.1021/cm4022003.

[8] F. Torricelli *et al.*, "Electrolyte-gated transistors for enhanced performance bioelectronics," *Nat. Rev. Methods Prim.*, vol. 1, no. 1, 2021, doi: 10.1038/s43586-021-00065-8.

[9] J. Rivnay, S. Inal, A. Salleo, R. M. Owens, M. Berggren, and G. G. Malliaras, "Organic electrochemical transistors," *Nat. Rev. Mater.*, vol. 3, p. 17086, 2018, doi:

10.1038/natrevmats.2017.86.

[10] G. D. Spyropoulos, J. N. Gelinas, and D. Khodagholy, "Internal ion-gated organic electrochemical transistor: A building block for integrated bioelectronics," *Sci. Adv.*, vol. 5, no. 2, 2020, doi: 10.1126/SCIADV.AAU7378.

[11] C. Cea, G. D. Spyropoulos, P. Jastrzebska-Perfect, J. J. Ferrero, J. N. Gelinas, and D. Khodagholy, "Enhancement-mode ion-based transistor as a comprehensive interface and real-time processing unit for in vivo electrophysiology," *Nat. Mater.*, vol. 19, no. 6, pp. 679–686, Jun. 2020, doi: 10.1038/s41563-020-0638-3.

[12] Y. Van De Burgt *et al.*, "A non-volatile organic electrochemical device as a low-voltage artificial synapse for neuromorphic computing," *Nat. Mater.*, vol. 16, no. 4, pp. 414–418, 2017, doi: 10.1038/NMAT4856.

[13] S. T. Keene *et al.*, "Enhancement-Mode PEDOT:PSS Organic Electrochemical Transistors Using Molecular De-Doping," *Adv. Mater.*, vol. 32, no. 19, 2020, doi: 10.1002/adma.202000270.

[14] H. L. Jiang *et al.*, "Chitosan-graft-polyethylenimine as a gene carrier," *J. Control. Release*, vol. 117, no. 2, pp. 273–280, 2007, doi: 10.1016/j.jconrel.2006.10.025.

[15] D. Bitas and V. Samanidou, "Chitosan-Based (Nano)Materials for Novel Biomedical Applications," *Liq. Extr.*, pp. 683–723, 2019, doi: 10.1016/B978-0-12-816911-7.00023-2.

[16] O. J. Rauhala *et al.*, "Chitosan-Based, Biocompatible, Solution Processable Films for In Vivo Localization of Neural Interface Devices," *Adv. Mater. Technol.*, vol. 5, no. 3, pp. 1–7, 2020, doi: 10.1002/admt.201900663.

[17] M. N. V. Ravi Kumar and R. K. MNV., "A review of chitin and chitosan applications," *React. Funct. Polym.*, vol. 46, no. 1, pp. 1–27, 2000, doi: 10.1016/S1381-5148(00)00038-

9.

[18] G. D. Spyropoulos *et al.*, "Transcranial Electrical Stimulation and Recording of Brain Activity using Freestanding Plant-Based Conducting Polymer Hydrogel Composites," *Adv. Mater. Technol.*, vol. 5, no. 3, pp. 1–6, 2020, doi: 10.1002/admt.201900652.

[19] R. Green and M. R. Abidian, "Conducting Polymers for Neural Prosthetic and Neural Interface Applications," *Adv. Mater.*, vol. 27, no. 46, pp. 7620–7637, 2015, doi: 10.1002/adma.201501810.

[20] M. R. Abidian and D. C. Martin, "Experimental and theoretical characterization of implantable neural microelectrodes modified with conducting polymer nanotubes," *Biomaterials*, vol. 29, no. 9, pp. 1273–1283, 2008, doi: 10.1016/j.biomaterials.2007.11.022.

[21] S. Y. Yeung, A. Veronica, Y. Li, and I. M. Hsing, "High-Performance Internal Ion-Gated Organic Electrochemical Transistors for High-Frequency Bioimpedance Analysis," *Adv. Mater. Technol.*, vol. 2201116, pp. 1–12, 2022, doi: 10.1002/admt.202201116.

[22] D. A. Koutsouras, P. Gkoupidenis, C. Stolz, V. Subramanian, G. G. Malliaras, and D. C. Martin, "Impedance Spectroscopy of Spin-Cast and Electrochemically Deposited PEDOT:PSS Films on Microfabricated Electrodes with Various Areas," *ChemElectroChem*, vol. 4, no. 9, pp. 2321–2327, 2017, doi: 10.1002/celc.201700297.

[23] J. Rivnay *et al.*, "High-performance transistors for bioelectronics through tuning of channel thickness," *Sci. Adv.*, no. May, pp. 1–5, 2015.

[24] D. Khodagholy *et al.*, "High transconductance organic electrochemical transistors," *Nat. Commun.*, vol. 4, 2013, doi: 10.1038/ncomms3133.

[25] P. Andersson Ersman *et al.*, "All-printed large-scale integrated circuits based on organic electrochemical transistors," *Nat. Commun.*, vol. 10, no. 1, pp. 1–9, 2019, doi:

10.1038/s41467-019-13079-4.

[26] Z. Zhao, G. D. Spyropoulos, C. Cea, J. N. Gelinas, and D. Khodagholy, "Ionic communication for implantable bioelectronics," *Sci. Adv.*, vol. 8, no. 14, pp. 1–12, 2022, doi: 10.1126/sciadv.abm7851.

[27] T. G. Zimmerman, "Personal area networks: Near-field intrabody communication," *IBM Syst. J.*, vol. 35, no. 3–4, pp. 609–617, 1996, doi: 10.1147/sj.353.0609.

Conclusions

In this work, a comprehensive organic-material based bioelectronic system for neurelectronics is presented. Each component of such device including the front-end, the processing unit, the powering and data transmission system is conformable and biocompatible.

First, an innovative, soft, biocompatible composite material (MCP) that can form various electronic components such as transistors, resistors, and diodes is presented. MCP addresses key challenges in electrophysiological signal acquisition and processing by permitting anisotropic, high–spatiotemporal resolution sensing and transmission. A layer of MCP can bond soft and rigid electronics, thereby eliminating the need for bulky or nonbiocompatible interfaces between these device components. Also, MCP can directly interface with human skin, overcoming the trade-off between electrode size and impedance to allow high-fidelity acquisition of ECG and EMG, as well as sensing of spatially localized nerve action potentials noninvasively from a small surface area.

Secondly, organic electrochemical internal ion-gated transistors (IGTs) are described. IGTs were used in a wide range of neurophysiological applications, including EMG, ECG, intracranial encephalography and action potential (AP) recording. In all cases, signals acquired by IGTs had a high SNR and spatiotemporal resolution, comparable with the quality of signals generated using conventional electrodes with silicon-based amplifiers. However, IGTs bring key advantages compared with such systems. Amplification is local and does not require an external amplifier, allowing for the miniaturization and conformability of sensors. Furthermore, IGTs were used as a real time processing unit to accurately detected epileptic discharges *in vivo*, with receiver operating characteristics that surpassed traditional amplitude or bandpass filter thresholding methods. Finally, the ionic communication (IC) is presented as a data transmission system. IC uses ions to effectively propagate megahertz-range signals across a range of biologically relevant tissue depths

and operates by generating and sensing electrical potential energy within polarizable media without interfering with concurrent use of other bioelectronics. An integration of IGTs technology with IC is employed to create a fully conformable bioelectric implant that can receive power wirelessly, acquire and amplify neurophysiological data and transmit this data wireless to the outside body.